



ADVANCES IN CHEMICAL ENGINEERING

Volume 13

James Wei

ADVANCES IN CHEMICAL ENGINEERING

Volume 13

This Page Intentionally Left Blank

ADVANCES IN CHEMICAL ENGINEERING

Editor-in-Chief

JAMES WEI

*Department of Chemical Engineering
Massachusetts Institute of Technology
Cambridge, Massachusetts*

Editors

JOHN L. ANDERSON

*Department of Chemical Engineering
Carnegie-Mellon University
Pittsburgh, Pennsylvania*

KENNETH B. BISCHOFF

*Department of Chemical Engineering
University of Delaware
Newark, Delaware*

MORTON M. DENN

*Department of Chemical Engineering
University of California
Berkeley, California*

JOHN H. SEINFELD

*Department of Chemical Engineering
California Institute of Technology
Pasadena, California*

Volume 13

1987



ACADEMIC PRESS, INC.

Harcourt Brace Jovanovich, Publishers

Orlando San Diego New York Austin
Boston London Sydney Tokyo Toronto

COPYRIGHT © 1987 BY ACADEMIC PRESS, INC.
ALL RIGHTS RESERVED.
NO PART OF THIS PUBLICATION MAY BE REPRODUCED OR
TRANSMITTED IN ANY FORM OR BY ANY MEANS, ELECTRONIC
OR MECHANICAL, INCLUDING PHOTOCOPY, RECORDING, OR
ANY INFORMATION STORAGE AND RETRIEVAL SYSTEM, WITHOUT
PERMISSION IN WRITING FROM THE PUBLISHER.

ACADEMIC PRESS, INC.
Orlando, Florida 32887

United Kingdom Edition published by
ACADEMIC PRESS INC. (LONDON) LTD.
24-28 Oval Road, London NW1 7DX

LIBRARY OF CONGRESS CATALOG CARD NUMBER: 56-6600

ISBN 0-12-008513-5 (alk. paper)

PRINTED IN THE UNITED STATES OF AMERICA

87 88 89 90 9 8 7 6 5 4 3 2 1

CONTENTS

PREFACE	vii
-------------------	-----

Future Opportunities in Chemical Engineering

EDWARD G. JEFFERSON

Text	1
----------------	---

Analysis of Transport Phenomena Using Scaling and Physical Models

ELI RUCKENSTEIN

I. Introduction	11
II. Dimensional Analysis Based on Two Kinds of Scales	12
III. The Algebraic Method	15
IV. Turbulent Heat and Mass Transfer	54
V. Closing Remarks	109
References	109

Mathematical Modeling of Packed Bed Reactors: Numerical Solutions and Control Model Development

ROHIT KHANNA AND JOHN H. SEINFELD

I. Introduction	113
II. Packed Bed Reactor Models	114
III. Reaction System	115
IV. Formulation of the Mathematical Model	118
V. Numerical Solution	129
VI. Analysis of Model Behavior	139
VII. Orthogonal Collocation on Finite Elements	152
VIII. Evaluation of Common Physical Simplifications in Packed Bed Modeling	160
IX. Control Model Development	170
X. Dimensionality of the Linearized Model	178
XI. Nomenclature	189
References	190

**KINPTR (Mobil’s Kinetic Reforming Model): A Review of
Mobil’s Industrial Process Modeling Philosophy**

**MICHAEL P. RAMAGE, KENNETH R. GRAZIANI, PAUL H. SCHIPPER,
FREDERICK J. KRAMBECK, AND BYUNG C. CHOI**

I.	Introduction	193
II.	Reforming Process	194
III.	Development of Reforming Kinetics	206
IV.	Experimental Design and Parameter Estimation	226
V.	C ₆ Reforming Kinetics for R16H Bimetallic Catalyst	232
VI.	Structure of Reforming Process Model	240
VII.	Predictions with the Complete Reforming Kinetics	249
VIII.	Examples of Model Applications	259
IX.	Nomenclature	265
	References	266
INDEX	267

PREFACE

The world of chemical engineering is entering a turbulent period of change. Some of the mature areas of the chemical and petroleum industries are retrenching and could benefit greatly from the application of the latest scientific and engineering advances to reduce costs and thus remain competitive. Many new high-tech areas are "waiting to be born" (from "Second Coming" by William Butler Yeats) and need engineering innovations to solve pioneering problems. Concerns about the environment and about safety and health must be satisfied so that our industries are accepted by the public. In fact, we should declare our willingness to become the guardians of the cradle-to-grave responsibility of potentially toxic chemicals. To solve these pressing problems, we need to develop more fundamental concepts and tools that are powerful and applicable.

The research community of chemical engineering has a responsibility to address and to solve problems that bolster the health of the chemical and petroleum industries, as well as that of many emerging high-tech and environmental industries. *Advances in Chemical Engineering* has a responsibility to publish articles that would shorten the gap between research results found in primary journals on the one hand, and the stimulation of new research, the teaching of graduate courses, and the practice of engineering on the other hand.

Four articles are contained in this volume. The first one, "Future Opportunities in Chemical Engineering," represents the Warren K. Lewis Lecture of Edward Jefferson at Massachusetts Institute of Technology in November 1985. It draws on his experience as Chief Executive Officer of DuPont and architect of the transformation of the company into new areas. The second article, "Analysis of Transport Phenomena Using Scaling and Physical Models" by Eli Ruckenstein, gives insight into chemical engineering in the microscale. "Mathematical Modeling of Packed Bed Reactors" by Khanna and Seinfeld gives a vigorous account of the workhorse of chemical engineering reactors. The last article, "KINPTR (Mobil's Kinetic Reforming Model)" by Ramage *et al.*, summarizes the much acclaimed refinery model developed over a long period of time, and contains parameter values that are suitable for the initiation of simulation efforts.

Future issues of *Advances in Chemical Engineering* will include articles in all the major subjects of support frontiers of mature areas, development of high-tech areas, protection of environment and health, and development of new engineering science concepts and tools.

James Wei

FUTURE OPPORTUNITIES IN CHEMICAL ENGINEERING

Edward G. Jefferson

**Retired Chairman of the Board
Chairman of the Finance Committee
E. I. du Pont de Nemours and Company, Inc.
1007 Market Street
Wilmington, Delaware 19898**

In many respects we have outgrown the traditional definition of the chemical industry. Changes in worldwide business conditions are having their impact on all of industry, and I shall look at what this means for companies with chemical products and for the people who work for them—especially scientists and engineers.

There is growing recognition of broad opportunities for the application of chemistry and chemical engineering. Chemistry, interacting with other disciplines, provides the fundamental knowledge required to deal with many of society's needs. These include new materials for aerospace, automotive, and electronics industries; basic data for the design of effective environmental controls; and the understanding of life processes important to agriculture and health care. A report by the National Academy of Sciences entitled "Opportunities in Chemistry"—also called the 'Pimentel Report'—helps us to crystallize our thoughts about the central importance of chemistry and chemical engineering and the wide bounds of their application.

The maturing of commodity chemicals, plastics, and apparel fibers businesses; growing international competition; and problems with environmental quality and toxic materials have led many to a defensive view of our industry. If we are not careful, such a view could stultify creativity. In point of fact, the opportunities are bright for new businesses based on the chemical sciences. But to take advantage of these opportunities, we must be prepared to depart from traditional fields into new areas.

Consider Du Pont as a case in point. From the company's founding to the beginning of the twentieth century, Du Pont was primarily a producer of

explosives. But by the end of World War I, management was already aware that future growth in explosives was limited, and the company therefore used its strong cash position to diversify into businesses that would provide greater long-term growth. During the 1920s and 1930s Du Pont made substantial investments in General Motors, purchased rayon and ammonia technology from the French, and acquired dyes, pigments, electrochemicals, and photographic businesses in the United States. As a consequence, by the late 1930s explosives accounted for less than 10% of sales.

While pursuing growth opportunities during that period, management also tried a new strategy: basic research. As it turned out, Du Pont was very successful at both the basic work and its translation to new product development. Commercial products evolved rapidly and included neoprene synthetic rubber and, of course, nylon. These successes encouraged the company to continue research in polymer science and to become a world leader in the field.

This technology base led to many more fiber, plastic, and elastomer products. By the 1960s, Du Pont comprised more than 50 businesses, which were organized into 14 largely autonomous departments. About three-quarters of the products were based on high polymers. Du Pont had grown through a combination of research and development, purchase of technology, and the driving force of market opportunity.

By the early 1970s, it once again became necessary for Du Pont to look for new growth areas. It had strong commodity chemical businesses; a very large fibers business; leading positions in engineering plastics, packaging, and engineering films; automotive paints; and numerous specialty and consumer products. But the company was already losing proprietary positions for many of the products it had invented. Companies in other countries became competitors in many product areas. The fibers business, which in the early 1970s accounted for a third of Du Pont's sales, was cyclical and only marginally profitable in the down part of the business cycle. More than 80% of Du Pont's product portfolio was dependent on petroleum-based raw materials, and it was hurt in the mid-1970s by the oil price volatility and the recession that followed the Arab oil embargo.

The company also had to deal with declining industrial growth. From 1955 to 1973, growth in industrial production averaged 4.5% annually. The compound real growth in industrial production from 1980 to 1985 has been less than 2%. The drop in growth of the chemical industry has been even more dramatic. From 1955 to 1973, the chemical industry grew more than 8% per year—almost double the growth rate of the economy. The compound real growth rate fell to 4% per year in the period 1973 to 1979 and dropped to only 1.8% per year from 1980 to 1985.

Other competitive developments have taken place in the world markets Du Pont serves. Commodity petrochemical production in the Middle East has increased, with the Saudis and other oil producers using their exceptional petroleum position to gain advantage.

During the early 1980s the abnormally strong dollar made it difficult for American manufacturers to compete in world markets while making it easier for foreign manufacturers to export their products to the United States. Du Pont suffered the negative effects of import penetration in markets for many products including commodity chemicals, plastics, and fibers. It was necessary to idle plants that were fully competitive in scale and efficiency.

Since the 1970s American industry has faced a series of special challenges: oil shocks, a dramatic falloff in industrial growth, recession, trade difficulties, and serious economic policy problems that have yet to be resolved. In light of these factors, Du Pont's management established a set of broad goals.

First, it wanted to secure hydrocarbon assets to lend stability to its mainstay businesses, because while many of the businesses were maturing, management knew that they would have to remain healthy to generate cash for years to come.

The second goal was that the company should seek to be the lowest-cost producer in the more mature businesses. These include oil and gas exploration and production, coal production, commodity fibers and plastics, automotive finishes, plastic films, and titanium dioxide white pigment. Extensive process and productivity improvements have been achieved.

Many of Du Pont's chemical products are made in reactions employing catalysts. Great progress has been made in understanding and advancing both homogeneous and heterogeneous catalysis used in manufacture. Biological systems, of course, accomplish complex syntheses under very mild conditions. As more is learned from life processes, new and more powerful catalytic methods for synthesis will be developed. Du Pont expects to remain in the vanguard of this work.

Third, the company has divested assets that cannot be brought up to good economic performance and those that do not fit our long-range strategy. From 1982 to 1985, Du Pont sold or withdrew from more than 20 such businesses, including consumer paint, colored pigments, and a number of commodity chemicals.

Fourth, Du Pont's management has given strong support to diversification into businesses where substantial growth is expected and in which the company has now achieved or can expect to achieve a strong competitive position. Such businesses include electronics, health care and agricultural products, specialty fibers, engineering plastics, and composite structures. Du Pont is not generally thought of as an important factor in electronics or

businesses based on the life sciences, such as agricultural products and health care. Yet these have already become very substantial businesses for the company.

Du Pont's fifth goal has been to achieve new growth through discovery. The company has remained convinced that science and engineering is a means for developing new opportunities for long-term growth and profitability. From 1981 to 1985, Du Pont invested nearly \$4 billion in research and development and about \$13 billion in capital projects and petroleum exploration. This is a large investment in the future to sustain and build the competitiveness of our businesses in world markets.

Perhaps of particular interest are the efforts in the last two areas mentioned: diversification into higher-growth businesses and some current research and development interests. In these businesses Du Pont is generally moving downstream closer to the consumer—and in so doing is adding more value.

Let us consider first electronics. With sales of roughly \$1.2 billion per year, Du Pont is one of the largest worldwide suppliers of materials to the electronics industry. The company's sales in this area have grown at a 20% compound rate since 1972, and Du Pont expects them to reach \$3 billion by the mid-1990s. The latest development in this area is reflected in the announcement of a joint venture with N. V. Philips of the Netherlands. Philips brings its strong position in compact discs and video discs to the venture. Du Pont brings technology for high-density information storage discs. The Du Pont research in advanced materials is important to the overall venture.

In another major area, biomedical products, Du Pont has annual sales of medical diagnostic and therapeutic products of \$1 billion. The company is second only to Abbot Laboratories worldwide in clinical diagnostic sales.

Du Pont's medical diagnostics and pharmaceutical businesses are underpinned by substantial basic research in molecular biology and biochemistry. For example, Du Pont recently announced an improved, more reliable test for detection of antibodies to the virus that causes acquired immunodeficiency syndrome. In another program the protein interleukin-2 produced in Du Pont's laboratories by recombinant DNA methods is being used in some very promising cancer research.

Sales of agricultural products were \$600 million in 1984. Du Pont expects to double this amount by 1990. There are many new products in the pipeline. Several of these new products are weed killers based on sulfonylurea chemistry. This family of weed killers is characterized by very low toxicity to mammals and high herbicidal activity at very low application rates in the field—often less than an ounce per acre of cropland.

Another key opportunity is in engineering plastics, which accounted for over \$700 million in sales in 1985. Du Pont has a 12% share of a 3-billion-pound market that is expected to double by the turn of the century. The

market for exterior automobile parts is just beginning to develop, and it alone could reach 5 billion pounds per year by the year 2000. Du Pont's sales for such applications could be \$500 million by the middle of the next decade.

Advanced composites represent another major growth market. It is expected to reach \$10 billion by the end of the next decade. Du Pont recently announced the formation of a new composites division to consolidate operations and business-planning functions. The company intends to participate in every step of the composites process, from the manufacture of reinforcing fibers and resins to the design and fabrication of finished products to replace metals in aeronautic, aerospace, and automotive applications. Du Pont's families of engineering resins and industrial fibers give it an excellent springboard for this opportunity.

As can be seen from this quick sketch, Du Pont's activities in new business areas are replete with opportunities for the chemical engineer. The businesses just discussed are supported by developments in two broad areas, materials science and the life sciences. Let us look at some of the specific intellectual challenges for the chemical engineer offered by these categories of inquiry.

Of the high-growth businesses foreseen for companies in the chemical industry, many opportunities are the result of advances in materials science. In electronics, the demand exists for new materials in semiconductor technology, photovoltaics, optical media for data storage, and (longer range) electro-optical materials for data transmission. These applications require complex compounds—gallium arsenide and lithium niobate in semiconductors, for example—of very high purity. Their design and manufacture present numerous engineering challenges even in small-scale batch processing using laboratory techniques, the current mode of manufacture. We have yet to develop larger-scale continuous industrial processes for their manufacture, which will be necessary to take full advantage of these materials.

In the area of specialty polymers, we are seeing an explosion of new polymer blends, alloys, and composites. The properties of novel polymer alloys, for example, are significantly better than those of the materials from which they are blended, but many aspects of these alloys are not well understood. Most of the materials consist of multiple polymer phases. But there is still uncertainty as to the desired characteristics and size of the polymer domains and the mechanisms by which forces are transferred through the material. All of these questions will benefit from the chemical engineering approach.

Another important area of materials development is related to the life sciences and concerns the development of materials to serve as replacements for body parts. There are challenges in replacing hard tissues such as hip and knee joints as well as soft tissues such as vascular tissue and ligaments. These implants will require very sophisticated composite materials if they are to model the properties of living tissues successfully.

Of course, specialized materials constitute only one aspect of chemical engineering in the life sciences. The term *life sciences* has become about as vague as the term *biotechnology*. But in the industrial context life sciences for the chemical engineer can be divided into at least two areas: processes to synthesize compounds and systems applied for biological results.

The reader is probably already familiar with the most common area of chemical engineering in the life sciences: the application of classic chemical engineering techniques to the manufacture of compounds with biological activity. At present, this includes most agricultural chemicals and many drugs. Another life science technology is the design and control of systems for microbial processing to produce chemicals by biological processes. Alcohols, sugars, and penicillin are typical products in this field. Switching from processes to raw materials, both microbial and traditional reactor processing can emphasize renewable resources. Light hydrocarbons from low-value trees and brush or from crop residues are excellent examples. A final compound-directed example is the much publicized work to produce interferon and human insulin by recombinant DNA methods.

A different but very important area of chemical engineering in the life sciences involves the design and manufacture of health care systems for diagnostic or therapeutic purposes. Consider the example of controlled release drugs or dermal penetration drugs. Here the emphasis is on the system rather than on the compound. The design of these systems requires an understanding of reactions, kinetics, fluid mechanics, and membrane systems.

Another good example is a diagnostic system that Du Pont manufactures and sells called the automatic clinical analyzer. These instruments process blood and other body fluids and quickly perform a wide range of diagnostic tests on a single sample. Although some models are compact enough to sit on a physician's desk, they are small chemical plants. They employ reaction technology, separation columns, and other elements in their design and function.

Over 20 years ago, when I was responsible for research in the plastics business, I learned that chemical engineering principles are just as applicable to polymer synthesis, isolation, and processing as they are in the technology of lower-molecular-weight conventional compounds. Above all, control of reactant purity, good instrumentation and measurement, thorough material and heat balances, control of mixing, and understanding of rates and equilibria will pay handsome dividends. Extension to the macromolecules of biological systems will require similar rigorous application of basic principles.

Some of the businesses that we are developing are by no means typical of what was traditionally thought of as the chemical industry. Yet they are very much based on chemical science and fall well within the scope of chemistry described in the Pimentel Report. More than 4000 of the nearly 16,000

technically trained people working in Du Pont operations are chemical engineers, and there will be plenty of opportunities for them to apply their skills and insights in these new areas.

Nevertheless, those beginning or contemplating the study of chemical engineering are no doubt asking themselves certain questions: What generally will be the demand for the chemical engineer in the future? Is my course of study preparing me for an industry that is obsolete or moving off shore? Will I be expected to become specialized in order to obtain employment? Will there be genuine challenges for the chemical engineer in the new industries that are on the horizon, or will I have to take a back seat to other engineering and science disciplines?

To a certain extent, answers to these questions are implicit in what I have already discussed. But these are all serious concerns, and I would like to make a few general observations about chemical engineering in response to them.

First, I do not believe that any engineering discipline is vocational training pure and simple. The engineer learns to think about physical concepts, systems design, and problem solving. A properly educated engineer has a world view that equips the individual well for living and working in the modern industrial world.

The chemical engineer is particularly well suited to working on the problems at hand. It is not enough to say that the growth areas for chemical engineering parallel the growth areas of the chemical industry. It is more fundamental than that. Chemical engineering preparation will be broadly useful in the future of industry because many of the developments we expect in the life sciences, electronics, and other fields will actually be developments in *chemistry*, and their application will require the contributions of chemical engineers.

Second, even with new areas opening up, some very traditional chemical engineering will require attention. Process technology is a good example. The challenge to make existing and future plants as safe, as environmentally acceptable, and as efficient as possible has never been more critical. The established products of the chemical industry find uses throughout the industrial system, and the need for them will endure. Also, the engineer will be required to deliver more plant construction for the money as efficiency and productivity become key to the profitability and perhaps the competitive survival of segments of our industry.

Third, because the chemical engineer will be useful in proportion to how well he or she helps other disciplines solve problems, it will become necessary for chemical engineers to broaden their training and expectations. Although the baccalaureate degree will continue to be very good preparation for positions in marketing and plant supervision, the time may be passing when the bachelor's degree is sufficient for entry-level chemical engineering

positions in research and process development. Just as positions in chemistry and biology traditionally have required an advanced degree—often a doctorate—similar credentials may be required of the chemical engineer in the future. In other words, the role of the chemical engineer will become less a matter of running plants and more a matter of interdisciplinary problem solving.

Fourth, the chemical engineer will be squarely in the middle of developments in many of the high-technology industries. We must transcend the image of the chemical engineer as the guy in the hard hat standing on the catwalk of a refinery surveying his world-scale plant.

In fact, “he” may well be “she” these days. But more to the point, the whole notion of a change of scale is one of the more intriguing and challenging developments in chemical engineering at the present time. This change is occurring on two fronts. One is that the scale of the physical piece of equipment on which engineers will work in some of the new fields may be much smaller; instead of thinking in thousands of square feet or gallons, they will be thinking in square inches and milliliters. Quantities of material moving through the equipment may no longer be measured in tons or hundreds of pounds, but in ounces and grams.

The other change in scale is more conceptual but still quite real in impact. It has to do with increasing the effectiveness of chemical products. We live during an era of “smart” chemicals. This is seen at Du Pont with supertough nylon, “Kevlar” aramid fiber, high-covering-power coatings, superfine denier textiles, and high-activity agricultural chemicals, such as Du Pont’s “Glean” sulfonyleurea weed killer. In end-use applications, these products result in the same or better job performance with fewer pounds of chemicals than the products they replace. To the extent that we can make these new products in existing facilities, we have effectively added new capacity—and certainly more value in use. Consequently, rather than sinking expensive capital into new facilities, it will become important to be able to retrofit existing facilities.

Chemical engineering in the years ahead will be practiced increasingly in a retrofit world. For new facilities it will be necessary to consider retrofit options up front. This approach conserves capital while allowing faster, more flexible response to changing markets and worldwide conditions.

There are, undoubtedly, other generalizations that one might make concerning the outlook for chemical engineering. It has been my aim to emphasize that companies with chemical businesses are applying advanced technology to existing products and are moving beyond traditional chemical lines into areas that offer new growth prospects. These are businesses that depend on chemical sciences, and they will have an essential need for chemical engineering.

However, the demands made of the discipline and those who practice it are changing. The challenge before us is to prepare chemical engineers who think in terms of the overall solution to a problem, including product, processing, marketing, economic, and human resource considerations. Appropriate changes in curricula are evident, suggesting that our chemical engineering departments are adjusting to these new realities as they have historically to other changes. The chemical sciences and chemical engineering have helped make our industry competitive on the world scene, a competitiveness reflected in a positive balance of trade in chemical products, even under the challenging economic circumstances of recent years.

The study and practice of chemistry and chemical engineering will continue to be excellent preparations for a variety of operational, management, and research assignments in the modern corporation. And the beauty of it is that it is exciting, challenging, and rewarding work. In many ways I wish that I myself was just beginning.

This Page Intentionally Left Blank

ANALYSIS OF TRANSPORT PHENOMENA USING SCALING AND PHYSICAL MODELS

Eli Ruckenstein

**Department of Chemical Engineering
State University of New York at Buffalo
Buffalo, New York 14260**

I. Introduction

The purpose of this chapter is to provide a comprehensive discussion of some simple approaches that can be employed to obtain information on the rate of heat and mass transfer for both laminar and turbulent motion. One approach is based on dimensional scaling and hence ignores the transport equations. Another, while based on the transport equations, does not solve them in the conventional way. Instead, it replaces them by some algebraic expressions, which are obtained by what could be called physical scaling. The constants involved in these expressions are determined by comparison with exact asymptotic solutions. Finally, the turbulent motion is represented as a succession of simple laminar motions. The characteristic length and velocity scales of these laminar motions are determined by dimensional scaling. It is instructive to begin the presentation with an outline of the basic ideas.

Conventional dimensional analysis uses single length and time scales to obtain dimensionless groups. In the first section, a new kind of dimensional analysis is developed which employs two kinds of such scales, the microscopic (molecular) scale and the macroscopic scale. This provides some physical significance to the exponent of the Reynolds number in the expression of the Sherwood number, as well as some bounds of this exponent for both laminar and turbulent motion.

In developing the boundary layer concept, Prandtl suggested an order-of-magnitude evaluation of the terms in the Navier–Stokes equations, which provides an expression (with an unknown proportionality constant) for the

thickness of the hydrodynamic boundary layer. Such order-of-magnitude evaluations are transformed here into a computational tool, which can provide expressions for the mass transfer coefficient in complex cases in terms of the mass transfer coefficients for simpler cases. The terms of the convective diffusion equation are replaced by algebraic expressions in terms of scaling quantities but multiplied by constants. Thus, an algebraic equation containing a number of constants is obtained for the mass transfer coefficient. The undetermined constants are determined from the solutions available for simpler limiting cases. This approach is termed "algebraic" because the convective diffusion equation is replaced by an algebraic equation.

Third, turbulent transport is represented as a succession of simple laminar flows. If the boundary is a solid wall, then one considers that elements of liquid proceed short distances along the wall in laminar motion, after which they dissolve into the bulk and are replaced by other elements, and so on. The path length and initial velocity in the laminar motion are determined by dimensional scaling. For a liquid–fluid interface, a roll cell model is employed for turbulent motion as well as for interfacial turbulence.

The essential point of the treatments discussed here is that simple procedures based on scaling (either dimensional or physical) or physical models can be used to interpret some complex cases of transport in terms of simpler ones.

II. Dimensional Analysis Based on Two Kinds of Scales

For dimensional analysis one needs to identify the physical quantities upon which the transfer coefficients depend. The number of dimensionless groups equals the number of physical quantities involved minus the number of independent dimensions. In this procedure, the dimensionless groups are constructed without involving the transport equations. They can also be formed on the basis of the similarity method applied to the transport equations [1]. The latter method extends the concept of similitude from geometry to the transport equations. By using scaling transformations for all the quantities involved, the conditions for two temperature or concentration fields to be similar are derived. The resulting dimensionless groups are the same as the ones obtained by dimensional analysis.

Conventional dimensional analysis employs single length and time scales. Correlations are thus obtained for the mass or heat transfer coefficients in terms of the minimum number of independent dimensionless groups; these can generally be represented by power functions such as

$$\text{Sh} = A \text{Re}^m \text{Sc}^n \quad (1)$$

and

$$\text{Nu} = A \text{Re}^m \text{Pr}^n \quad (2)$$

where

$$\text{Sh} \quad (\text{the Sherwood number}) \equiv kd/D \quad (3)$$

$$\text{Nu} \quad (\text{the Nusselt number}) \equiv hd/k' \quad (4)$$

$$\text{Re} \quad (\text{the Reynolds number}) \equiv Ud/\nu \quad (5)$$

$$\text{Sc} \quad (\text{the Schmidt number}) \equiv \nu/D \quad (6)$$

and

$$\text{Pr} \quad (\text{the Prandtl number}) \equiv \nu/a \quad (7)$$

Here k is the mass transfer coefficient, d is a characteristic length of the system (e.g., the diameter of the tube), U is a characteristic velocity, ν is the kinematic viscosity, D is the diffusion coefficient, h is the heat transfer coefficient, k' is the thermal conductivity, a is the thermal diffusivity, and A , m , and n are constants.

The present approach to dimensional analysis is based on the observation that, in both laminar and turbulent flows, two kinds of quantities are involved: the physical properties, such as D , ν , and a , and the macrodimensions and macrovelocity of the system, such as d and U . For this reason, two kinds of length and time scales should characterize the process: the micro- and macroscales. The microlength l and microtime t are associated with molecular phenomena and can therefore be used to express the dimensions of the molecular diffusion coefficient, of the thermal diffusivity, and of the kinematic viscosity. The macrolength L and macrotime T can be used to express the diameter and length of the tube and the velocity of the fluid. The mass transfer coefficient depends, however, on both micro- and macroquantities. It is, therefore, necessary to include both these kinds of scales in its dimensions. Denoting the exponent of the macrolength by α and that of the macrotime by β , the dimensions of the mass transfer coefficient k become

$$[k] = L^\alpha l^{1-\alpha} / T^\beta t^{1-\beta} \quad (8)$$

The dimensions of the other relevant quantities can be written as

$$[d] = L, \quad [U] = LT^{-1}, \quad [D] = l^2 t^{-1}, \quad \text{and} \quad [\nu] = l^2 t^{-1} \quad (9)$$

Assuming, as usual, a power relation between the variables

$$k = AU^\alpha d^\nu \nu^z D^v \quad (10)$$

then, the dimensional analysis in which the macro- and microscales are treated separately, leads to

$$kd/D = A(Ud/\nu)^\beta (\nu/D)^{1-\beta} \quad (11)$$

where

$$\beta = (1 + \alpha)/2 \quad (12)$$

Equation (11) has the same form as Eq. (1). The exponent m of the Reynolds number,

$$m = \beta = (1 + \alpha)/2 \quad (13)$$

acquires, however, some physical meaning, because β is a measure of the participation of the macrotime scale and α is a measure of the participation of the macrolength scale in the dimensional structure of the mass transfer coefficient. Since one expects the participation of the macroscales to be greater in turbulent motion than in laminar motion, the value of m should be larger in the former case.

In the extreme case of $Re \rightarrow \infty$ (strong turbulence), no microparticipation is expected to occur because the molecular processes do not play any role in the transport rate. In this case, $\alpha = \beta = 1$ [see Eq. (8)]. In the other extreme case, such as the vanishingly small Reynolds number flows around a sphere or the mass transfer in laminar flow in a long tube, the Sherwood number is constant. In this case, the microparticipation dominates and $\alpha = -1$ and $\beta = 0$. In turbulent flows involving sufficiently large Reynolds numbers, some microparticipation will arise because the molecular quantities do play a role in the rate of the process. The macroparticipation still remains more important than the microparticipation, however. Similarly, at the other extreme, such as the laminar flow past a sphere at not too large Reynolds numbers, the microparticipation is expected to decrease in comparison to that for $Re \rightarrow 0$, but will still be greater than the macroparticipation. Extrapolating in both directions, it is plausible to consider that the macroparticipation is greater than or equal to the microparticipation for turbulent motion and that the opposite is valid for laminar flow. Thus, for the turbulent flow,

$$\alpha > 1 - \alpha \quad \text{and} \quad \beta > 1 - \beta \quad (14)$$

Since α and β are not independent quantities, being related via Eq. (12), the preceding two inequalities are simultaneously satisfied only if

$$0.5 \leq \alpha < 1 \quad \text{and} \quad 0.75 \leq \beta < 1 \quad (15)$$

Similarly, for the laminar case,

$$1 - \alpha > \alpha \quad \text{and} \quad 1 - \beta > \beta \quad (16)$$

These inequalities are satisfied without contradicting Eq. (12) only if

$$\beta \leq 0.5 \quad \text{and} \quad \alpha \leq 0 \quad (17)$$

Equations (15) and (17) show that the exponent of the Reynolds number is

greater than or equal to 0.75 for turbulent flow and smaller than or equal to 0.5 for laminar flow. Indeed, in turbulent flow, the exponent of the Reynolds number is equal or larger than 0.75 [2]. In laminar flow, the exponent of the Reynolds number is 1/2 for sufficiently large Reynolds number flows along a plate or around a sphere, to become 1/3 for a Stokes flow around a sphere and zero for vanishingly small Reynolds number flows around a sphere or for laminar motion in a long tube [2].

One may also note from Eq. (11) that the exponent of the Schmidt number is independent of the exponents of the macro- and microscales. In other words, the exponent of ν/D should be the same for both laminar and turbulent flows. Experiment indeed indicates that the value of 1/3 for this exponent is valid for many laminar and turbulent flows along solid interfaces and that the value of 1/2 is valid for laminar and turbulent motions along fluid–fluid interfaces. It is interesting to note that there is a jump from 0.5 to 0.75 in the value of the bound of the exponent m with the transition from laminar to turbulent flow, a result which is in agreement with experimental observations [2].

III. The Algebraic Method

A. PRANDTL'S EVALUATION PROCEDURE

In order to familiarize the reader with Prandtl's evaluation procedure [3–5] on which the algebraic method is based, let us examine the steady laminar motion of a fluid along a plate and denote by x the coordinate along the plate, by y the distance to the plate, by u and v the x and y components of the velocity, and by p the pressure. The equations of motion of an incompressible fluid of density ρ and kinematic viscosity ν have the form

$$u \frac{\partial u}{\partial x} + v \frac{\partial u}{\partial y} = -\frac{1}{\rho} \frac{\partial p}{\partial x} + \nu \left(\frac{\partial^2 u}{\partial x^2} + \frac{\partial^2 u}{\partial y^2} \right) \quad (18)$$

and

$$u \frac{\partial v}{\partial x} + v \frac{\partial v}{\partial y} = -\frac{1}{\rho} \frac{\partial p}{\partial y} + \nu \left(\frac{\partial^2 v}{\partial x^2} + \frac{\partial^2 v}{\partial y^2} \right) \quad (19)$$

where u and v are related via the continuity equation

$$\frac{\partial u}{\partial x} + \frac{\partial v}{\partial y} = 0 \quad (20)$$

As suggested by Prandtl, the entire zone of motion can be subdivided into two regions: a boundary layer region near the plate of thickness $\delta_h = \delta_h(x)$, in

which the viscosity plays a role, and a region of inviscid motion further from the plate, in which the effect of viscosity can be neglected and hence Euler's equations can be used. The Navier–Stokes equations can be simplified within the boundary layer because the thickness of this layer is small compared with the length l of the plate. In order to evaluate the terms of the equations of motion, it is useful to scale the coordinates x and y with l and δ_h , respectively, by introducing the dimensionless variables

$$X = x/l \quad \text{and} \quad Y = y/\delta_h \quad (21)$$

Equations (18) to (20) are thus transformed into

$$\frac{u}{l} \frac{\partial u}{\partial X} + \frac{v}{\delta_h} \frac{\partial u}{\partial Y} = -\frac{1}{\rho l} \frac{\partial p}{\partial X} + \frac{v}{l^2} \frac{\partial^2 u}{\partial X^2} + \frac{v}{\delta_h^2} \frac{\partial^2 u}{\partial Y^2} \quad (22)$$

$$\frac{u}{l} \frac{\partial v}{\partial X} + \frac{v}{\delta_h} \frac{\partial v}{\partial Y} = -\frac{1}{\rho \delta_h} \frac{\partial p}{\partial Y} + \frac{v}{l^2} \frac{\partial^2 v}{\partial X^2} + \frac{v}{\delta_h^2} \frac{\partial^2 v}{\partial Y^2} \quad (23)$$

and

$$\frac{1}{l} \frac{\partial u}{\partial X} + \frac{1}{\delta_h} \frac{\partial v}{\partial Y} = 0 \quad (24)$$

Denoting by u_o the value of u at the outer edge of the boundary layer and taking into account that $0 < X < 1$ and $0 < Y < 1$, one can write

$$\frac{1}{l} \frac{\partial u}{\partial X} \sim \frac{u_o}{l} \quad (25a)$$

and hence, using the continuity equation (24), that

$$v \sim \frac{\delta_h}{l} u_o \quad (25b)$$

where the sign \sim means of the order of. Similarly, one can write that

$$\frac{\partial u}{\partial X} \sim \frac{\partial^2 u}{\partial X^2} \sim u_o, \quad \frac{\partial v}{\partial X} \sim \frac{\partial^2 v}{\partial X^2} \sim \frac{\delta_h}{l} u_o \quad (25c)$$

$$\frac{\partial u}{\partial Y} \sim \frac{\partial^2 u}{\partial Y^2} \sim u_o, \quad \frac{\partial v}{\partial Y} \sim \frac{\partial^2 v}{\partial Y^2} \sim \frac{\delta_h}{l} u_o \quad (25d)$$

$$\frac{v}{l^2} \frac{\partial^2 u}{\partial X^2} \sim \frac{v u_o}{l^2}, \quad \frac{v}{l^2} \frac{\partial^2 v}{\partial X^2} \sim \frac{v \delta_h u_o}{l^3} \quad (25e)$$

$$\frac{v}{\delta_h^2} \frac{\partial^2 u}{\partial Y^2} \sim \frac{v u_o}{\delta_h^2}, \quad \frac{v}{\delta_h^2} \frac{\partial^2 v}{\partial Y^2} \sim \frac{v u_o}{\delta_h l} \quad (25f)$$

Replacing the terms of the equation of motion with their evaluations, one

concludes that $\partial^2 u / \partial y^2 \gg \partial^2 u / \partial x^2$ because $\delta_h / l \ll 1$ and that the thickness δ_h of the boundary layer is given by the expression

$$\delta_h \propto (\nu x / u_o)^{1/2} \quad (26)$$

The exact solution of the problem leads to the same expression with a proportionality constant between 3 and 5, depending on the definition of the thickness of the boundary layer. In the following sections, the preceding evaluation procedure is applied to a large number of problems, particularly to complex cases for which limiting solutions can be obtained. As already noted in the introduction, the terms in the transport equations will be replaced by their evaluating expressions multiplied by constants. The undetermined constants will then be determined from solutions available for some asymptotic cases.

B. THICKNESS OF THE HYDRODYNAMIC BOUNDARY LAYER FOR A VISCOELASTIC FLUID

We show here that the preceding scaling procedure can be extremely useful in complex cases involving viscoelastic liquids. Various authors [6–8] have extended Prandtl's boundary layer approach to a viscoelastic fluid, their treatments being summarized by Schowalter [9]. However, these authors have used the boundary layer approach solely to simplify the equations of motion. It will be employed here to obtain an expression for the thickness of the boundary layer, which will be used to extract insights concerning some experimental results. The following approximate equation is assumed to be valid for the flow of a viscoelastic fluid along a plate [9]:

$$u \frac{\partial u}{\partial x} + v \frac{\partial u}{\partial y} = \nu \frac{\partial^2 u}{\partial y^2} + v\theta \left[u \frac{\partial^3 u}{\partial x \partial y^2} + v \frac{\partial^3 u}{\partial y^3} + \frac{\partial u}{\partial x} \frac{\partial^2 u}{\partial y^2} - \frac{\partial u}{\partial y} \frac{\partial^2 u}{\partial x \partial y} \right] \quad (27)$$

where θ is a constant characterizing the relaxation of polymer chains. Extending the procedure used for the viscous fluids to Eq. (27), one can write

$$u \frac{\partial u}{\partial x} \sim \frac{u_o^2}{x}, \quad v \frac{\partial u}{\partial y} \sim \frac{\delta_h u_o}{x} \frac{u_o}{\delta_h} = \frac{u_o^2}{x} \quad (28a)$$

$$\nu \frac{\partial^2 u}{\partial y^2} \sim \frac{\nu u_o}{\delta_h^2} \quad (28b)$$

and

$$v\theta \left[u \frac{\partial^3 u}{\partial x \partial y^2} + v \frac{\partial^3 u}{\partial y^3} + \frac{\partial u}{\partial x} \frac{\partial^2 u}{\partial y^2} - \frac{\partial u}{\partial y} \frac{\partial^2 u}{\partial x \partial y} \right] \sim \frac{\nu \theta u_o^2}{x \delta_h^2} \quad (28c)$$

Replacing the terms of Eq. (27) by their corresponding evaluations multiplied

by constants, one obtains

$$\delta_h^2 = A(vx/u_o) + Bv\theta \quad (29)$$

where A and B are constants. One must emphasize the fact that the possibility of evaluating a boundary layer thickness does not necessarily mean that a similarity solution exists. Equation (29) indicates only the existence of a region near the wall where viscosity and elasticity play a role. This simple expression, however, has some interesting implications. First, one may note that, in contrast to the case of a viscous fluid, the thickness of the hydrodynamic boundary layer has a finite value at the origin. Second, for large values of the free stream velocity, the thickness of the boundary layer caused by viscosity, which is of the order of $(vx/u_o)^{1/2}$, becomes small compared to that caused by elasticity, which is proportional to $(v\theta)^{1/2}$, and the thickness of the hydrodynamic boundary layer becomes independent of velocity. As a result, the drag coefficient and the heat transfer coefficient are expected to become independent of velocity when the ratio $(v\theta)^{1/2}/(vl/u_o)^{1/2}$ of the thicknesses becomes sufficiently large. This ratio contains the so-called Deborah number [10], $De \equiv \theta u_o/l$, which compares the relaxation time θ to the residence time l/u_o . It is interesting to note that experiments have shown [11] that when a viscoelastic fluid flows past a cylinder, the heat transfer coefficient and the drag coefficient become independent of velocity at large values of the latter. However, the experiments of James and Acosta [11] have been carried out at relatively low Reynolds numbers ($Re < 50$), while the boundary layer approximation is valid for large Reynolds numbers. Thus, while no quantitative agreement between the preceding considerations and experiment is expected, the boundary layer approach still provides insight into the problem.

Let us now use this evaluating procedure to obtain an expression for the drag coefficient at large velocities. In order to calculate the drag coefficient, the expressions of the stress tensor corresponding to Eq. (27) must be written explicitly. They are

$$\frac{\tau_{yx}}{\rho} = v \frac{\partial u}{\partial y} + v\theta \left[u \frac{\partial^2 u}{\partial x \partial y} + v \frac{\partial^2 u}{\partial y^2} + 2 \frac{\partial u}{\partial x} \frac{\partial u}{\partial y} \right] \quad (30)$$

and

$$\sigma_{xx} \approx -\sigma_{yy} = -v\rho\theta \left(\frac{\partial u}{\partial y} \right)^2 \quad (31)$$

where τ_{yx} is the shear stress component and σ_{xx} and σ_{yy} are the normal components of the stress tensor. The components of the stress tensor at the surface of the cylinder, which are marked with the superscript o , can be evaluated as follows:

$$\tau_{yx}^o/\rho u_o^2 = C'(v/u_o\delta_h) + C''(v\theta/x\delta_h) \quad (32)$$

and

$$\sigma_{yy}^o/\rho u_o^2 = C''' v\theta/\delta_h^2 \quad (33)$$

where C' , C'' , and C''' are constants.

For sufficiently large values of u_o , $\delta_h \propto (v\theta)^{1/2}$ and, as a result,

$$\tau_{yx}^o/\rho u_o^2 \propto (v\theta)^{1/2}/x, \quad \text{and} \quad \sigma_{yy}^o/\rho u_o^2 = \text{const} \quad (34)$$

Neglecting the presence of the wake, the drag coefficient C_D is given by the expression

$$C_D = \left(\int_0^\pi \tau_{yx}^o \sin \phi \, d\phi + \int_0^\pi \sigma_{yy}^o \cos \phi \, d\phi \right) \bigg/ \frac{1}{2} \rho u_o^2 \quad (35)$$

where $\phi = 2x/d$, d being the diameter of the cylinder. For large values of u_o , one thus obtains

$$C_D \propto (v\theta)^{1/2}/d \quad (36)$$

Regarding the heat transfer coefficient, let us write that the thickness δ of the thermal boundary layer is related, for sufficiently large Prandtl numbers, to that of the hydrodynamic boundary layer by

$$\delta = \delta_h \text{Pr}^{-1/3}$$

This expression, which is valid for Newtonian fluids only, is extended here to viscoelastic fluids only because it eventually leads to a satisfactory correlation of the experimental data.

The heat transfer coefficient h_x can therefore be evaluated from

$$h_x = \frac{k'}{\delta} \equiv \frac{k' \text{Pr}^{1/3}}{\{A(vx/u_o) + Bv\theta\}^{1/2}} \quad (37a)$$

and

$$\text{Nu}_x \equiv \frac{h_x x}{k'} = \frac{\text{Pr}^{1/3}}{\{A(v/u_o x) + Bv\theta/x^2\}^{1/2}} \quad (37b)$$

For sufficiently large values of u_o , h_x becomes independent of both x and u_o , since Eq. (37a) leads to

$$h_x = k' \text{Pr}^{1/3}/(Bv\theta)^{1/2} \quad (38)$$

Consequently, the boundary layer approach suggests that the drag coefficient and the heat transfer coefficient should indeed become independent of the velocity at sufficiently high velocities.

In addition, Eq. (37b) can be modified to correlate the data of James and Acosta using the observation that in the lower range of Reynolds numbers employed by them the exponent of the Reynolds number is nearer to 1/3 than

to $1/2$ [5]. Experiment has shown that in the viscous limit [12]

$$hd/k' = 0.965 \text{Pr}^{0.3} \text{Re}^{0.28} \quad \text{for } 0.08 < \text{Re} < 8 \quad (38a)$$

where h is the average heat transfer coefficient over the surface of the cylinder. This suggests that Eq. (37b) should be replaced by the equation

$$\frac{hd}{k'} = \frac{\text{Pr}^{1/3}}{\{A(v/u_o d) + B(v\theta/d^2)\}^{0.28}} \quad (38b)$$

Determining the constant A by means of Eq. (38a), to which Eq. (38b) should reduce for $\theta = 0$, and the constant B from the experimental data, one obtains the expression

$$\frac{hd}{k'} = \frac{\text{Pr}^{1/3} \text{Re}^{0.28}}{\{1.035 + 22.3(u_o \theta/d)\}^{0.28}} \quad (38c)$$

which constitutes a satisfactory representation of the experimental data of James and Acosta.

In what follows, the preceding evaluation procedure is employed in a somewhat different mode, the main objective now being to obtain expressions for the heat or mass transfer coefficient in complex situations on the basis of information available for some simpler asymptotic cases. The order-of-magnitude procedure replaces the convective diffusion equation by an algebraic equation whose coefficients are determined from exact solutions available in simpler limiting cases [13,14]. Various cases involving free convection, forced convection, mixed convection, diffusion with reaction, convective diffusion with reaction, turbulent mass transfer with chemical reaction, and unsteady heat transfer are examined to demonstrate the usefulness of this simple approach. There are, of course, cases, such as the one treated earlier, in which the constants cannot be obtained because exact solutions are not available even for simpler limiting cases. In such cases, the procedure is still useful to correlate experimental data if the constants are determined on the basis of those data.

C. LAMINAR FREE CONVECTION FROM A VERTICAL PLATE OVER THE ENTIRE RANGE OF PRANDTL NUMBERS

The laminar free convection from a vertical plate can be described by the equations

$$\frac{\partial u}{\partial x} + \frac{\partial v}{\partial y} = 0 \quad (39)$$

$$u \frac{\partial u}{\partial x} + v \frac{\partial u}{\partial y} = g\beta(T - T_\infty) + \nu \frac{\partial^2 u}{\partial y^2} \quad (40)$$

and

$$u \frac{\partial T}{\partial x} + v \frac{\partial T}{\partial y} = a \frac{\partial^2 T}{\partial y^2} \quad (41)$$

Here u and v are the x and y components of the velocity, x is the distance up the plate, y is the distance to the plate, T is the temperature, T_∞ is the ambient temperature, g is the acceleration due to gravity, and β is the volumetric coefficient of expansion. It has already been argued that convective momentum and energy transport dominate diffusive processes in the flow direction.

The velocity field is caused in free convection by the temperature field. Therefore, the thickness δ of the thermal boundary layer can be used as the single length scale that characterizes both the temperature and velocity fields. Denoting the velocity scale in the x direction by u_o , the continuity equation [Eq. (39)] shows that the velocity scale v_o in the y direction is of the order of $u_o \delta / x$.

The terms of Eqs. (40) and (41) are evaluated by replacing u and ∂u by u_o , ∂x by x , ∂y by δ , ∂T and $T - T_\infty$ by $\Delta T = T_w - T_\infty$ (where T_w is the wall temperature). This yields

$$u \frac{\partial u}{\partial x} + v \frac{\partial u}{\partial y} \sim \frac{u_o^2}{x} \quad (42a)$$

$$v \frac{\partial^2 u}{\partial y^2} \sim \frac{v u_o}{\delta^2}, \quad a \frac{\partial^2 T}{\partial y^2} \sim \frac{a \Delta T}{\delta^2} \quad (42b)$$

and

$$u \frac{\partial T}{\partial x} + v \frac{\partial T}{\partial y} \sim \frac{u_o \Delta T}{x} \quad (42c)$$

Replacing each term by the corresponding evaluation multiplied by a constant, Eqs. (40) and (41) are replaced by

$$A'(u_o^2/x) + B'(v u_o/\delta^2) = g\beta \Delta T \quad (43)$$

and

$$C'(u_o/x) = a/\delta^2 \quad (44)$$

where A' , B' , and C' are constants.

Eliminating the velocity scale u_o between Eqs. (43) and (44) yields

$$\delta^4 = \frac{a^2 x [A + B(v/a)]}{g\beta \Delta T} \quad (45)$$

where A and B are constants. Since the local heat transfer coefficient h_x is given

by

$$h_x = k'/\delta \quad (46)$$

Eq. (45) becomes [15]

$$\begin{aligned} \text{Nu}_x &\equiv \frac{h_x x}{k'} = \left(\frac{g\beta \Delta T x^3}{\nu a} \right)^{1/4} \left(\frac{\nu}{a} \right)^{1/4} \left(A + B \frac{\nu}{a} \right)^{-1/4} \\ &\equiv \text{Ra}_x^{1/4} \text{Pr}^{1/4} (A + B \text{Pr})^{-1/4} \end{aligned} \quad (47)$$

where $\text{Ra}_x \equiv g\beta \Delta T x^3 / \nu a$ is the Rayleigh number. For the extreme cases $\text{Pr} \rightarrow 0$ and $\text{Pr} \rightarrow \infty$, expression (47) acquires the forms of the exact relations given subsequently. The constants A and B are determined from these exact relations.

For an isothermal plate, the solutions derived by LeFevre [16] are

$$\text{Nu}_x = 0.6(\text{Ra}_x \text{Pr})^{1/4} \quad \text{for } \text{Pr} \rightarrow 0 \quad (48a)$$

and

$$\text{Nu}_x = 0.5 \text{Ra}_x^{1/4} \quad \text{for } \text{Pr} \rightarrow \infty \quad (48b)$$

while for uniform heat flux, they have the form [17]

$$\text{Nu}_x = 0.7(\text{Ra}_x \text{Pr})^{1/4} \quad \text{for } \text{Pr} \rightarrow 0 \quad (49a)$$

and

$$\text{Nu}_x = 0.56 \text{Ra}_x^{1/4} \quad \text{for } \text{Pr} \rightarrow \infty \quad (49b)$$

Employing the above asymptotic solutions, one can calculate the constants A and B , and Eq. (47) becomes [15]

$$\text{Nu}_x = \text{Ra}_x^{1/4} \text{Pr}^{1/4} (7.7 + 15.7 \text{Pr})^{-1/4} \quad (50)$$

for uniform wall temperature and

$$\text{Nu}_x = \text{Ra}_x^{1/4} \text{Pr}^{1/4} (4.36 + 10 \text{Pr})^{-1/4} \quad (51)$$

for uniform heat flux.

Equations (50) and (51) are in good agreement with the empirical correlations suggested by Churchill and Ozoe [17] to represent their numerical solution of the governing transport equations. Tables I and II compare the results.

D. MASS TRANSFER COEFFICIENT IN A SEMIINFINITE LIQUID THAT MOVES ALONG A PLANAR FLUID BOUNDARY

This case was treated by Potter [18] by means of the integral method. Since for high values of the Schmidt number only the region in the vicinity of the planar fluid boundary contributes appreciably to the value of the mass

TABLE I

CONSTANT WALL TEMPERATURE CASE ($Nu_x/Ra_x^{1/4}$ VERSUS Pr)

Pr	Present equation (50)	Churchill's equation
0.01	0.1889	0.1812
0.05	0.2771	0.2548
0.10	0.3224	0.2901
0.20	0.3687	0.3257
0.50	0.4236	0.3704
1.00	0.4549	0.4004
2.00	0.4758	0.4259
5.00	0.4911	0.4521
10.00	0.4967	0.4667
20.00	0.4997	0.4775
50.00	0.5015	0.4872
100.00	0.5021	0.4921
200.00	0.5024	0.4956
500.00	0.5026	0.4985
1000.00	0.5026	0.5000

TABLE II

CONSTANT WALL HEAT FLUX CASE ($Nu_x/Ra_x^{1/4}$ VERSUS Pr)

Pr	Present equation (51)	Churchill's equation
0.01	0.2176	0.2083
0.05	0.3185	0.2919
0.10	0.3696	0.3315
0.20	0.4212	0.3712
0.50	0.4810	0.4206
1.00	0.5141	0.4534
2.00	0.5358	0.4810
5.00	0.5513	0.5091
10.00	0.5570	0.5247
20.00	0.5600	0.5361
50.00	0.5618	0.5464
100.00	0.5624	0.5516
200.00	0.5627	0.5552
500.00	0.5629	0.5583
1000.00	0.5629	0.5598

transfer coefficient, one can use for the velocity components u and v the expressions valid near that boundary:

$$\frac{u}{u_\infty} = \frac{u_o}{u_\infty} + 2 \left(1 - \frac{u_o}{u_\infty} \right) \frac{y}{\delta_h} \quad (52)$$

and

$$v = \frac{2v}{u_\infty} \frac{630(u_\infty - u_o)}{74 + 115(u_o/u_\infty)} \frac{y^2}{\delta_h^3} \quad (53)$$

where

$$\delta_h^2 = \frac{4vx}{u_\infty} \frac{630}{74 + 114(u_o/u_\infty)} \quad (54)$$

u_o being the velocity at the fluid–fluid boundary and u_∞ the velocity of the liquid at large distance from the fluid–fluid boundary.

The convective diffusion equation has the form

$$u \frac{\partial c}{\partial x} + v \frac{\partial c}{\partial y} = D \frac{\partial^2 c}{\partial y^2} \quad (55)$$

where c is the concentration.

The terms of Eq. (55) can be evaluated as follows:

$$u \frac{\partial c}{\partial x} \sim \left[u_o + 2(u_\infty - u_o) \frac{\delta}{\delta_h} \right] \frac{\Delta c}{x} \quad (56a)$$

$$v \frac{\partial c}{\partial y} \sim \frac{2v}{u_\infty} \frac{630(u_\infty - u_o)}{74 + 115(u_o/u_\infty)} \frac{\delta^2}{\delta_h^3} \frac{\Delta c}{\delta} \quad (56b)$$

and

$$D \frac{\partial^2 c}{\partial y^2} \sim D \frac{\Delta c}{\delta^2} \quad (56c)$$

where the thickness δ of the diffusion boundary layer is related to the mass transfer coefficient k_x via

$$k_x = D/\delta \quad (57)$$

Replacing each of the terms of Eq. (55) by its algebraic evaluation multiplied by a constant, one obtains

$$A \frac{u_o}{u_\infty} \left(\frac{\delta}{\delta_h} \right)^2 + B \left(1 - \frac{u_o}{u_\infty} \right) \left(\frac{\delta}{\delta_h} \right)^3 = \frac{D}{v} \frac{74 + 115(u_o/u_\infty)}{630} \quad (58)$$

The two constants A and B can be determined from the solutions available in the limiting cases of $u_o = 0$ and $u_o = u_\infty$. For the extreme case of $u_o = 0$, the boundary behaves like a solid surface and the mass transfer coefficient k_{x1} , is given by the expression valid for the laminar flow along a solid surface [2]:

$$k_{x1} = 0.33D \left(\frac{u_\infty}{vx} \right)^{1/2} \left(\frac{y}{D} \right)^{1/3} \quad (59)$$

In the other extreme case, $u_0 = u_\infty$ and the transport equation simplifies to

$$u_\infty \frac{\partial c}{\partial x} = D \frac{\partial^2 c}{\partial y^2}$$

which has, for the boundary conditions

$$\begin{aligned} c &= C & \text{for } x = 0 & \text{ and all } y \\ c &= C_i & \text{for } y = 0 & \text{ and all } x \end{aligned}$$

the solution

$$\frac{c - C_i}{C - C_i} = \frac{2}{\pi^{1/2}} \int_0^{2\left(\frac{y}{(4Dx/u_\infty)^{1/2}}\right)} e^{-\mu^2} d\mu$$

The mass transfer coefficient is in this case given by

$$k_{x,II} = (u_\infty D / \pi x)^{1/2} \quad (60)$$

For the constants A and B one thus obtains

$$A = 4/\pi \quad \text{and} \quad B = 0.9 \quad (61)$$

Equation (58) can also be obtained by integrating Eq. (55) with respect to y between zero and δ and by assuming that

$$(c - C)/(C_i - C) = F(y/\delta)$$

Integrating Eq. (55) with respect to y , one obtains

$$\frac{d}{dx} \int_0^\delta (c - C) u dy = -D \left(\frac{\partial c}{\partial y} \right)_{y=0} \quad (62)$$

Assuming in addition that

$$(c - C)/(C_i - C) = F(y/\delta) \quad (63)$$

and using Eq. (52) for u , there results

$$\frac{u_0}{u_\infty} A' \frac{d\delta}{dx} + \left(1 - \frac{u_0}{u_\infty} \right) B' \frac{d(\delta^2/\delta_h)}{dx} = \frac{DE}{u_\infty \delta} \quad (64)$$

where

$$A' = \int_0^1 F\left(\frac{y}{\delta}\right) d\frac{y}{\delta} = \text{const} \quad (65a)$$

$$B' = 2 \int_0^1 \frac{y}{\delta} F\left(\frac{y}{\delta}\right) d\frac{y}{\delta} = \text{const} \quad (65b)$$

and

$$E = - \left(\frac{dF(y/\delta)}{dy/\delta} \right)_{y/\delta=0} = \text{const} \quad (65c)$$

If one assumes that δ/δ_h is independent of x , one arrives again at Eq. (58). If a particular form is chosen for the function F , as one proceeds in the method of polynomials, the calculation of the constants A' , B' , and E becomes possible. While in this particular problem one can follow a parallelism between the algebraic method and the method of polynomials, the same parallelism can no longer be identified in the other examples examined. It is worth emphasizing that the use of the boundary layer thickness concept in the algebraic method does not imply the existence of a similarity solution. In general, the algebraic method interpolates between the two similarity solutions which are valid in the two asymptotic cases.

E. COMBINED FORCED AND FREE LAMINAR CONVECTION FROM VERTICAL SURFACES WHEN BOTH ARE IN THE SAME DIRECTION (ASSISTING FLOWS)

Equations 39–41 are again employed and the boundary conditions assume the form

$$u = v = 0, \quad T = T_w \quad \text{at } y = 0 \quad \text{and all } x \quad (66a)$$

$$u = u_\infty, \quad T = T_\infty \quad \text{at } y \rightarrow \infty \quad \text{and all } x \quad (66b)$$

and

$$u = u_\infty, \quad T = T_\infty \quad \text{at } x = 0 \quad \text{and all } y \quad (66c)$$

It is difficult to solve the system of Eqs. (39)–(41) for these boundary conditions. However, certain simplifying assumptions can be made, if the Prandtl number approaches large values. In this case, the thermal boundary layer becomes very thin and, therefore, only the fluid layer near the plate contributes significantly to the heat transfer resistance. The velocity components in Eq. (41) can then be approximated by the first term of their Taylor series expansions in terms of y . In addition, because the nonlinear inertial terms are negligible near the wall, one can further assume that the combined forced and free convection velocity is approximately equal to the sum of the velocities that would exist when these effects act independently. Therefore, for assisting flows at large Prandtl numbers (theoretically for $\text{Pr} \rightarrow \infty$), Eq. (41) can be rewritten in the form:

$$(u_F + u_N) \frac{\partial T}{\partial x} + (v_F + v_N) \frac{\partial T}{\partial y} = a \frac{\partial^2 T}{\partial y^2} \quad (67)$$

where the subscripts F and N refer to forced and natural convection, respectively. The velocity components of Eq. (67) are given by [20,5]

$$u_F = 0.332 u_\infty^{3/2} \nu^{-1/2} x^{-1/2} y, \quad v_F = 0.083 u_\infty^{3/2} \nu^{-1/2} x^{-3/2} y^2 \quad (68a)$$

and by [5]

$$u_N = 0.679 \text{Pr}^{-1/4} (g\beta \Delta T / \nu^2)^{3/4} \nu x^{1/4} y \quad \text{for } \text{Pr} \rightarrow \infty \quad (68b)$$

and

$$v_N = -0.084 \text{Pr}^{-1/4} (g\beta \Delta T / \nu^2)^{3/4} \nu x^{-3/4} y^2 \quad \text{for } \text{Pr} \rightarrow \infty \quad (68c)$$

It is important to emphasize that the forms of Eqs. (68) are obtainable from scaling considerations. Indeed, near the wall, one can write $u_F/u_\infty \propto y/\delta_h$, where δ_h is given by Eq. (26), and $u_N/u_{N0} \propto y/\delta$, where u_{N0} is given by Eq. (44) and δ by Eq. (45) [in which $A \ll B(v/a)$]. These expressions together with the continuity equation provide the forms of v_F and v_N .

The order-of-magnitude analysis leads to

$$A \text{Re}_x^{3/2} \text{Pr} + B \text{Ra}_x^{3/4} = \text{Nu}_x^3 \quad (69)$$

where

$$\text{Re}_x \equiv u_\infty x / \nu$$

The constants A and B can be calculated from the limiting expressions for free or forced convection. For isothermal plates [2,5],

$$\text{Nu}_{x,F} = 0.33 \text{Re}_x^{1/2} \text{Pr}^{1/3} \quad (70a)$$

and [17]

$$\text{Nu}_{x,N} = 0.50 \text{Ra}_x^{1/4} \quad (70b)$$

For constant wall heat flux [2],

$$\text{Nu}_{x,F} = 0.46 \text{Re}_x^{1/2} \text{Pr}^{1/3} \quad (71a)$$

and [17]

$$\text{Nu}_{x,N} = 0.56 \text{Ra}_x^{1/4} \quad (71b)$$

The constants in Eq. (69) can be calculated from the limiting cases provided by Eqs. (70) and (71). However, it is of more interest to rewrite Eq. (69) in terms of $\text{Nu}_{x,F}$ and $\text{Nu}_{x,N}$ [19]

$$\text{Nu}_x^3 = \text{Nu}_{x,F}^3 + \text{Nu}_{x,N}^3 \quad (72)$$

This result can be obtained without knowing the values of the proportionality constants in Eqs. (68), but only the forms of the velocity distributions. As noted

earlier, scaling arguments can provide these forms. Equation (72) constitutes a derivation of Churchill's suggestion [21]. Similar expressions can be derived for spheres or cylinders, by replacing the coordinate x by the diameter [19]. These approximate results complement the rigorous treatment of mixed convection given by Acrivos [22] and Sparrow and Gregg [23].

Let us compare the result obtained on the basis of the algebraic method with those obtained from an exact solution of Eq. (67). The solution of the latter equation for the boundary conditions (66) can be obtained through a similarity transformation. Indeed,

$$u = u_N + u_F = f_1(x)y \quad (73a)$$

and, because of the continuity equation,

$$v = v_N + v_F = -\frac{1}{2} \frac{df_1(x)}{dx} y^2 \quad (73b)$$

where

$$f_1(x) = 4x^{-1/2}(A_1 + 2A_2x^{3/4}) \equiv 4x^{-1/2}f_2(x) \quad (74)$$

$$A_1 = 0.083u_\infty^{3/2}v^{-1/2} \quad \text{and} \quad A_2 = 0.085v \text{Pr}^{-1/4}(g\beta \Delta T/v^2)^{3/4} \quad (75)$$

Now let us introduce the similarity variable

$$\eta = y/p(x) \quad (76)$$

Performing the calculations, one obtains

$$p(x) = \left\{ \frac{\alpha x^{3/4}}{A_2} - \frac{\alpha A_1^{3/2}}{A_2} \left[\frac{x^{3/4}}{(A_1 + 2A_2x^{3/4})^{3/2}} \right] \right\}^{1/3} \quad (77)$$

and

$$\frac{d^2T}{d\eta^2} + 3\eta^2 \frac{dT}{d\eta} = 0 \quad (78)$$

where α is a constant.

The solution of Eq. (78) for the boundary conditions (66) is

$$\frac{T - T_w}{T_\infty - T_w} = \frac{1}{\Gamma(4/3)} \int_0^\eta e^{-\mu^3} d\mu \quad (79)$$

where $\Gamma(4/3)$ is the gamma function $\Gamma(\xi)$ for $\xi = 4/3$. Defining the local heat transfer coefficient h_x by

$$h_x(T_w - T_\infty) = -k' \left(\frac{\partial T}{\partial y} \right)_{y=0} \quad (80)$$

one obtains

$$h_x = \frac{k'}{\Gamma(4/3)} \left(\frac{\partial \eta}{\partial y} \right)_{y=0} = \frac{k'}{\Gamma(4/3)} \frac{1}{p(x)} \quad (81)$$

Substituting for $p(x)$ from Eq. (77), Eq. (81) yields

$$\text{Nu}_x \equiv \frac{h_x x}{k'} = \frac{1}{\Gamma(4/3)} \left(\frac{A_2}{\alpha} \right)^{1/3} x^{3/4} [f_2(x)]^{1/2} \{ [f_2(x)]^{3/2} - A_1^{3/2} \}^{-1/3} \quad (82)$$

The expressions for $f_2(x)$, A_1 , and A_2 can be substituted in Eq. (82) to obtain the following representation for Nu_x :

$$\left(\frac{\text{Nu}_x}{\text{Nu}_{x,N}} \right)^3 = \frac{\{ 1 + \frac{2}{3}(\text{Nu}_{x,N}/\text{Nu}_{x,F})^3 \}^{3/2}}{\{ 1 + \frac{2}{3}(\text{Nu}_{x,N}/\text{Nu}_{x,F})^3 \}^{3/2} - 1} \quad (83)$$

For small values of $(\text{Nu}_{x,N}/\text{Nu}_{x,F})^3$, Eq. (83) reduces to Eq. (72). The two equations differ at most by 8% over the entire range.

We introduce the buoyancy factor as the relative influence of the natural convection over forced convection

$$B_x = \text{Gr}_x / \text{Re}_x^2 \quad (84)$$

It is instructive to compare the predictions of Eqs. (83) and (72) with the numerical solution obtained by Lloyd and Sparrow [24]. Table III shows that for large Prandtl numbers the difference is within 10%. The approximate equation is, unexpectedly, satisfactory even for low values of the Prandtl number if the buoyancy factor B_x is sufficiently small. Even though the error increases for larger values of B_x , this can be corrected by using the appropriate limiting values for $\text{Nu}_{x,N}$ and $\text{Nu}_{x,F}$. The first column in Table III for $\text{Pr} = 0.72$ is based on $\text{Nu}_{x,N}$ and $\text{Nu}_{x,F}$ for $\text{Pr} \rightarrow \infty$. The appropriate expressions for Prandtl numbers around unity are, however,

$$\text{Nu}_{x,N} = 0.387 \text{Ra}_x^{1/4} \quad (85)$$

and

$$\text{Nu}_{x,F} = 0.316 \text{Re}_x^{1/2} \text{Pr}^{1/3} \quad (86)$$

When these expressions are employed in Eq. (83), the predictions are in excellent agreement with the calculations of Lloyd and Sparrow (see third column of Table III under $\text{Pr} = 0.72$).

In Fig. 1, the experimental results of Gryzagoridis [25] are compared with the algebraic equation (72) and with the series solution of Szewczyk [26], which is accurate only for $B_x < 0.5$. It is of interest to note that while the interpolation equation (72) is expected to be valid at large Prandtl numbers only, it remains valid even for $\text{Pr} \approx 1$ if the appropriate expressions are employed for the two asymptotic expressions.

TABLE III
ASSISTING CONVECTION OVER ISOTHERMAL VERTICAL PLATES:
COMPARISON WITH THE NUMERICAL SOLUTION OF LLOYD AND SPARROW [24] ($Nu_x/Re_x^{1/2}$)

B_x	Pr = 100		Pr = 10		Pr = 0.72		
	This work	Lloyd and Sparrow	This work	Lloyd and Sparrow	This work ^a	Lloyd and Sparrow	This work ^b
0	1.5735	1.572	0.730	0.7281	0.3038	0.2956	0.283
0.01	1.587	1.575	0.741	0.7313	0.3125	0.2979	0.288
0.04	1.611	1.585	0.761	0.7404	0.327	0.3044	0.297
0.1	1.646	1.605	0.789	0.7574	0.348	0.3158	0.309
0.4	1.766	1.691	0.880	0.8259	0.411	0.3561	0.349
1.0	1.928	1.826	0.994	0.9212	0.483	0.4058	0.398
2.0	2.117	1.994	1.121	1.029	0.558	0.4584	0.451

^a $Nu_{x,N} = 0.492 Ra_x^{1/4}$ (expression for $Pr \rightarrow \infty$).

^b $Nu_{x,N} = 0.387 Ra_x^{1/4}$ and $Nu_{x,F} = 0.316 Re_x^{1/2} Pr^{1/3}$ (correct expression for $Pr = 0.72$).

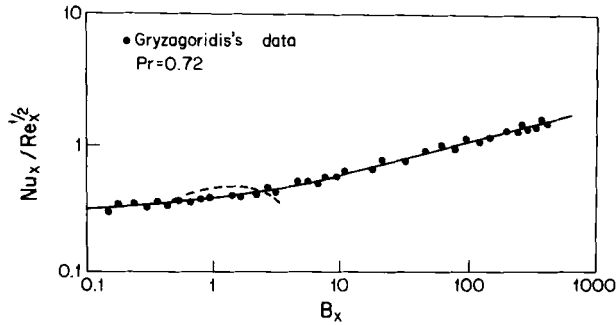


FIG. 1. Comparison of the predictions of the algebraic method (solid line) with the experimental data of Gryzagoridis and with the series solution of Szewczyk (broken line).

F. COMBINED CONVECTION IN INTERNAL FLOWS

In electrochemical reactors, the externally imposed velocity is often low. Therefore, natural convection can exert a substantial influence. As an example, let us consider a vertical parallel plate reactor in which the electrodes are separated by a distance d and let us assume that the electrodes are sufficiently distant from the reactor inlet for the forced laminar flow to be fully developed. Since the reaction occurs only at the electrodes, the concentration profile begins to develop at the leading edges of the electrodes. The thickness of the concentration boundary layer along the length of the electrode is assumed to be much smaller than the distance d between the plates, a condition that is usually satisfied in practice.

The velocity profile of the fully developed forced flow is given by

$$u_F = 6u_{av}[(y/d) - (y^2/d^2)] \quad (87)$$

where u_{av} is the average forced flow velocity through the reactor. Close to the electrode, the velocity components can be approximated by

$$u_F = (6u_{av}/d)y; \quad v_F = 0 \quad (88)$$

The natural convection velocity is given by Eq. (68b). The order-of-magnitude analysis provides the following algebraic equation:

$$(k_x x/D)^3 \equiv \text{Sh}_x^3 = A \text{Re}_x \text{Sc}(x/d) \pm B \text{Ra}_x^{3/4} \quad (89)$$

where $\text{Ra}_x \equiv g\Delta\rho x^3/\rho\nu a$ is the Rayleigh number for mass transfer, ρ is the density of the fluid, $\Delta\rho$ is the density difference between the fluid at the wall and at a large distance from the wall, k_x is the local mass transfer coefficient, and $\text{Re}_x \equiv u_{av}x/\nu$. The negative sign in Eq. (89) applies when the external flow and the buoyancy-induced flow oppose each other. When pure natural

convection is dominant, Eq. (89) must take the form of Eq. (48b) and one obtains

$$B = 0.127$$

The first part of Eq. (89) is just the cube of the Leveque [27] solution given by

$$\text{Sh}_{x,F} = 0.98 \left[\text{Re}_x \text{Sc} \frac{x}{d} \right]^{1/3} \quad (90)$$

Consequently, $A = (0.98)^3$, and Eq. (89) becomes

$$\text{Sh}_x = 0.98 \left[\text{Re}_x \text{Sc} \frac{x}{d} \right]^{1/3} \left\{ 1 \pm 0.136 \frac{\text{Ra}_x^{3/4}}{\text{Re}_x \text{Sc}(x/d)} \right\}^{1/3} \quad (91)$$

Experimentally one often measures the average value of the mass transfer coefficient, which is defined as

$$k_{av} = \int_0^A k_x dA / A = \int_0^L k_x W dx / WL$$

where $A = WL$, W is the width, and L is the length of the plates. Integrating Eq. (91) by parts, one can derive an expression for $\text{Sh}_{av} \equiv k_{av}d/D$. The integration leads to a power series in terms of x , from which, retaining the first two terms, one obtains [19]

$$\text{Sh}_{av} = 1.47 \text{Gz}^{1/3} \left[1 \pm 0.1 \frac{[\text{Ra}(d/L)]^{3/4}}{\text{Gz}} \right]^{1/3} \quad (92)$$

where $\text{Gz} = \text{Re} \text{Sc}(d/L)$ is the Graetz number, $\text{Re} = u_{av}d/\nu$, and $\text{Ra} \equiv g\Delta\rho d^3/\rho\nu\alpha$.

G. PENETRATION THEORY FOR THE RATE OF DIFFUSION ACCOMPANIED BY A CHEMICAL REACTION

The problem of absorption accompanied by a chemical reaction in a liquid film flowing along a vertical wall was often treated by using the framework of the penetration theory [28–32]. This theory also constitutes the starting point of the renewal models of turbulence [31,33,34].

In the penetration theory, the mass transport equation takes the form

$$\frac{\partial c}{\partial t} = D \frac{\partial^2 c}{\partial y^2} - K_1 c \quad (93)$$

where c is the concentration, t is the time, and K_1 is the reaction rate constant.

This equation is solved for the initial and boundary conditions

$$\begin{aligned} c &= 0 & \text{for } t = 0 & \text{ and all } y \\ c &= c^* & \text{for } y = 0 & \text{ and all } t \\ c &= 0 & \text{for } y \rightarrow \infty & \text{ and all } t \end{aligned} \quad (94)$$

The terms of Eq. (93) are evaluated as follows:

$$\frac{\partial c}{\partial t} \sim \frac{\Delta c}{t} \quad (95a)$$

$$D \frac{\partial^2 c}{\partial y^2} \sim \frac{D \Delta c}{\delta^2} \quad (95b)$$

and

$$K_1 c \sim K_1 \Delta c \quad (95c)$$

Introducing these expressions multiplied by constants in Eq. (93) yields

$$(A/t) + BK_1 = D/\delta^2 \quad (96)$$

where A and B are constants. The rate N of absorption per unit area of the interface and unit time is therefore given by

$$N = \frac{c^* D}{\delta} \equiv c^* \left[\frac{D(A + BK_1 t)}{t} \right]^{1/2} \quad (97)$$

The constants A and B can be obtained from the simple solutions available for the cases in which either $K_1 = 0$ or $\partial c / \partial t = 0$. In the first case,

$$\frac{\partial c}{\partial t} = D \frac{\partial^2 c}{\partial y^2} \quad (98)$$

and the rate is

$$N_I = \left(\frac{D}{\pi t} \right)^{1/2} c^* \equiv k_I c^* \quad (99)$$

where k_I is a mass transfer coefficient in the absence of reaction. In the second case,

$$D \frac{d^2 c}{dy^2} = K_1 c \quad (100)$$

and the rate of mass transfer is given by

$$N_{II} = c^* (K_1 D)^{1/2} \equiv k_{II} c^* \quad (101)$$

where k_{II} is the mass transfer coefficient for steady diffusion and reaction.

Eq. (97) must reduce to Eq. (99) for $K_1 = 0$ and to Eq. (101) for $t \rightarrow \infty$; therefore

$$N = c^* \left[\frac{D}{\pi t} (1 + \pi K_1 t) \right]^{1/2} \equiv kc^* \quad (102)$$

and

$$k^2 = k_I^2 + k_{II}^2 \quad (103)$$

or

$$\text{Sh}^2 = \text{Sh}_I^2 + \text{Sh}_{II}^2 \quad (104)$$

The Sherwood numbers have been obtained by multiplying Eq. (103) by x/D , where x is a length scale. The maximum difference between the simple equation (102) and the more complicated exact solution [28,29] is about 10% (see Table IV).

H. STEADY LAMINAR FLOW ALONG A PLATE WITH HOMOGENEOUS REACTION

In this case, the convective diffusion equation can be written as

$$u \frac{\partial c}{\partial x} + v \frac{\partial c}{\partial y} = D \frac{\partial^2 c}{\partial y^2} - K_1 c \quad (105)$$

and the boundary conditions are

$$\begin{aligned} c &= c_s & \text{at } y = 0 & \text{ and for all } x \\ c &= 0 & \text{for } y \rightarrow \infty & \text{ and for all } x \\ c &= 0 & \text{for } x = 0 & \text{ and for all } y \end{aligned} \quad (106)$$

TABLE IV
RATE OF DIFFUSION WITH FIRST-ORDER CHEMICAL REACTION

$K_1 t$	$N/[c^*(DK_1)^{1/2}]$ (interpolation)	$N/[c^*(DK_1)^{1/2}]$ (exact)	$K_1^{1/2} \int_0^t N dt / (c^* D^{1/2})$ (interpolation)	$K_1^{1/2} \int_0^t N dt / (c^* D^{1/2})$ (exact)
0.1	2.05	1.96		
0.2	1.61	1.51	0.55	0.54
0.4	1.34	1.23	0.89	0.82
0.6	1.24	1.12	1.09	1.04
0.8	1.18	1.07	1.34	1.27
1	1.15	1.05	1.57	1.50

Since for large Schmidt numbers, the depth of penetration by diffusion is very small, only the region near the wall affects the mass or heat transfer rate. Consequently, in such cases, one can retain only the first term in the Blasius expansions for the velocity components, to obtain

$$u \propto u_{\infty}^{3/2} y / \nu^{1/2} x^{1/2}, \quad v \propto u_{\infty}^{3/2} y^2 / \nu^{1/2} x^{3/2} \quad (107)$$

Let us note that Eqs. (107) can be obtained from scaling arguments alone, since near the wall $u/u_{\infty} \propto y/\delta_h$, where δ_h is given by $\delta_h \propto (\nu x/u_{\infty})^{1/2}$ [see Eq. (26)]. The algebraic method leads in this case to

$$A \operatorname{Re}_x^{3/2} \operatorname{Sc} + B(K_1 x^2/D)(x/\delta) = (x/\delta)^3 \quad (108)$$

Introducing the local mass transfer coefficient k_x and the local Sherwood number by the expressions

$$k_x = D/\delta \quad \text{and} \quad \operatorname{Sh}_x = k_x x/D = x/\delta \quad (109)$$

Eq. (108) becomes

$$A \operatorname{Re}_x^{3/2} \operatorname{Sc} + B(K_1 x^2/D) \operatorname{Sh}_x = \operatorname{Sh}_x^3 \quad (110)$$

The constants A and B can be determined from the solutions available for the simple cases in which either $K_1 = 0$ or $u_{\infty} = 0$. The first limiting case corresponds to the dissolution of a planar wall in a semiinfinite liquid in steady flow (Blasius flow), while the second limit corresponds to steady-state diffusion with chemical reaction in a stagnant fluid. For Blasius flow at large Schmidt numbers [2],

$$\operatorname{Sh}_{x,I} = 0.33 \operatorname{Re}_x^{1/2} \operatorname{Sc}^{1/3} \quad (111)$$

whereas for $u_{\infty} = 0$, one obtains (as in the previous example),

$$\operatorname{Sh}_{x,II} = (K_1 x^2/D)^{1/2} \equiv \operatorname{Da}_x^{1/2} \quad (112)$$

where Da_x is the Damköhler number. Eq. (110) can therefore be rewritten as

$$\operatorname{Sh}_{x,I}^3 + (\operatorname{Sh}_{x,II})^2 \operatorname{Sh}_x = \operatorname{Sh}_x^3 \quad (113)$$

This result can be obtained directly from Eq. (110) without first determining the constants A and B .

Chambré and Young [35] have solved the above problem, for $\operatorname{Sc} = 1$, by a perturbation expansion procedure. However, this method breaks down when $\operatorname{Sh}_{x,II}/\operatorname{Sh}_{x,I}$ exceeds roughly 4. Equation (113) is compared to the Chambré-Young solution in Table V to show that the interpolation procedure provides almost the same values as those resulting from the more exact solution. The maximum deviation from the exact results occurs when the convective and reaction effects are roughly equal (i.e., $\operatorname{Sh}_{x,II}/\operatorname{Sh}_{x,I} \approx 1$), and the error is generally within about 5–10%.

TABLE V
MASS TRANSFER IN FLOW ALONG A FLAT PLATE WITH
HOMOGENEOUS FIRST-ORDER REACTION

$X = (Sh_{x,\infty}/Sh_{x,1})$	$Y = (Sh_x/Sh_{x,1})$	
	This work	Chambré and Young
10^{-2}	1.00003	1.0002
10^{-1}	1.0033	1.0031
2×10^{-1}	1.0133	1.0118
4×10^{-1}	1.0533	1.0464
8×10^{-1}	1.2108	1.1815
1	1.3247	1.2796
2	2.1149	2.0036
$X \geq 5$	$Y \simeq X$	^a

^a The perturbation solution breaks down.

I. TRANSPORT PHENOMENA IN WEDGE FLOWS WITH SUCTION AT THE SURFACE

Suction (or injection) of fluids through confining surfaces is often used to control the boundary layer development over such surfaces. The rate of suction affects the transfer coefficients as well as the stability of the laminar flow. The group of problems called wedge flows or Falkner-Skan flows is characterized by free-stream velocities $U(x)$ that vary as a power of the distance x along the wedge measured from the leading edge [i.e., $U(x) = U_0 x^m$]. This class of problems has similarity solutions both for the flow field and for the temperature or concentration field [4] if the suction rate at the surface is of the form

$$v(x, y)_{y=0} = v_0(x) = K \left(\frac{m+1}{2} \frac{vU(x)}{x} \right)^{1/2} \quad (114)$$

where K is a constant. Near the wall, the velocity components are given by the following leading terms of the power series:

$$u = A(m)U(x)^{3/2}v^{-1/2}x^{-1/2}y \quad (115)$$

and

$$v = B_0(m)U(x)^{1/2}v^{1/2}x^{-1/2} + B_1(m)U(x)^{3/2}v^{-1/2}x^{-3/2}y^2 \quad (116)$$

where $A(m)$, $B_0(m)$, and $B_1(m)$ are known coefficients which depend on the exponent m of the free-stream velocity.

For sufficiently large values of the Prandtl or Schmidt number the rate of transfer is controlled by the region of thickness δ near the wall. The terms of the convective-thermal diffusivity equation

$$u \frac{\partial T}{\partial x} + v \frac{\partial T}{\partial y} = a \frac{\partial^2 T}{\partial y^2} \quad (117)$$

can be evaluated as follows:

$$u \frac{\partial T}{\partial x} \sim \frac{U(x)^{3/2} \delta}{v^{1/2} x^{3/2}} \Delta T \quad (118a)$$

$$v \frac{\partial T}{\partial y} \sim \frac{U(x)^{1/2} v^{1/2}}{x^{1/2} \delta} \Delta T + C_1 \frac{U(x)^{3/2} \delta}{v^{1/2} x^{3/2}} \Delta T \quad (118b)$$

and

$$a \frac{\partial^2 T}{\partial y^2} \sim a \frac{\Delta T}{\delta^2} \quad (118c)$$

Substitution of the preceding estimates in Eq. (117) and some rearrangements lead to

$$C_2 \text{Re}_x^{3/2} \text{Pr} + C_3 \text{Re}_x^{1/2} \text{Pr} \text{Nu}_x^2 = \text{Nu}_x^3 \quad (119)$$

where

$$\text{Re}_x = U(x)x/v \quad (120)$$

and

$$\text{Nu}_x = h_x x / k' \quad (121)$$

The constants C_2 and C_3 are determined from the solutions easily obtainable for the limiting cases of zero suction and no free-stream flow.

Expressions for the Nusselt number for zero suction are available for various values of m [4]. For the Blasius flow ($m = 0$), the expression has the form

$$\text{Nu}_{x,1} = 0.34 \text{Re}_x^{1/2} \text{Pr}^{1/3} \quad (122)$$

which leads to

$$C_2 = (0.34)^3 \quad (123)$$

For the zero free-stream flow, Eq. (117) becomes

$$v_0(x) \frac{dT}{dy} = a \frac{d^2 T}{dy^2} \quad (124)$$

The solution of Eq. (124) which satisfies the boundary condition

$$T = T_w \quad \text{at} \quad y = 0 \quad \text{and} \quad T = T_\infty \quad \text{as} \quad y \rightarrow \infty \quad (125)$$

is then

$$T = \exp(v_o y/a) \{ T_\infty [\exp(-v_o y/a) - 1] + T_w \} \quad (126)$$

One may note that Eq. (126) satisfies the boundary condition for $y \rightarrow \infty$ only if $v_o < 0$, that is, for suction only. The expression for the Nusselt number that follows from the definition of h_x ,

$$h_x = -k'(\partial T/\partial y)_{y=0}/(T_w - T_\infty) \quad (127)$$

is given in the zero free-stream flow case by

$$\text{Nu}_{x,\text{II}} = -v_o x/a \quad (128)$$

The particular form of $v_o(x)$ for which similarity solutions exist [Eq. (114)] can be substituted in Eq. (128) to obtain

$$\text{Nu}_{x,\text{II}} = -\left(\frac{m+1}{2}\right)^{1/2} K \text{Re}_x^{1/2} \text{Pr} \quad (129)$$

where K is a negative quantity. As a result, the second constant C_3 in Eq. (119) is related to K via the expression

$$C_3 = -[(m+1)/2]^{1/2} K \quad (130)$$

The Nusselt number Nu_x for the combined case can be written, regardless of the value of m , as [36]

$$\text{Nu}_{x,\text{I}}^3 + \text{Nu}_{x,\text{II}} \text{Nu}_x^2 = \text{Nu}_x^3 \quad (131)$$

One may note again that Eq. (131) follows immediately from Eq. (119), without it being necessary to know the values of the constants C_2 and C_3 .

A comparison between the values of Nu_x calculated from Eq. (131) and the exact numerical results of Stewart and Prober [37] is presented in Table VI for $m = 0$. The comparison shows that, even though the algebraic approach is strictly valid for large Prandtl numbers, it is sufficiently accurate even for $\text{Pr} \rightarrow 0(1)$, particularly when the suction rate is large ($|K| \geq 1$). It may also be noted that Stewart and Prober have provided some rather accurate analytic approximations for the transfer coefficient.

It is important to note that the algebraic equation (131) probably holds even when the velocity of suction at the wall $v_o(x)$ assumes a form different from Eq. (114). The latter equation involves the existence of a similarity solution, but this is not required for applying the algebraic method of interpolation.

TABLE VI

HEAT TRANSFER IN FLOW ALONG A FLAT PLATE WITH SUCTION AT THE PLATE

Re _x	Nu _x					
	Pr = 10; K = -5		Pr = 10; K = -0.5		Pr = 1; K = -5	
	This work	Stewart and Prober	This work	Stewart and Prober	This work	Stewart and Prober
1 × 10 ²	353.55	353.69	35.50	37.00	35.37	36.02
2 × 10 ²	500.00	500.19	50.18	52.33	50.02	50.94
4 × 10 ²	707.11	707.37	70.94	74.00	70.73	72.04
8 × 10 ²	1000.00	1000.38	100.29	104.66	100.03	101.89
1 × 10 ³	1118.04	1118.46	112.11	117.01	111.83	113.91
2 × 10 ³	1581.14	1581.74	158.50	165.48	158.15	161.10
4 × 10 ³	2236.07	2236.91	224.10	234.02	223.66	227.82
8 × 10 ³	3162.28	3163.47	316.85	330.96	316.29	322.19
1 × 10 ⁴	3535.54	3536.87	354.22	370.02	353.62	360.22
2 × 10 ⁴	5000.01	5001.89	500.84	523.29	500.08	509.43
4 × 10 ⁴	7071.07	7073.74	708.17	740.04	707.21	720.44
8 × 10 ⁴	10000.01	10003.77	1001.34	1046.58	1000.13	1018.86
1 × 10 ⁵	11180.34	11181.56	1119.48	1170.11	1118.18	1139.12

For arbitrary forms of $v_o(x)$, one simply has

$$\text{Nu}_{x,II} = -v_o x/a$$

which can be used together with Eq. (122) for predicting Nu_x . This re-emphasizes that the algebraic approximation method can be used even when the complex problem has no similarity solution.

J. MASS TRANSFER TO A CONTINUOUS PHASE FROM A SINGLE SPHERICAL DROP

For sufficiently large Schmidt numbers, the depth of penetration by diffusion is small compared to the droplet radius R . Therefore, the convective diffusion equation can be approximated by

$$v_r \frac{\partial c}{\partial y} + \frac{v_\theta}{R} \frac{\partial c}{\partial \theta} = D \frac{\partial^2 c}{\partial y^2} \quad (132)$$

where y is the distance from the surface of the bubble, θ is the polar angle, and v_r and v_θ are the radial and tangential velocity components, respectively.

For low Reynolds numbers and large Schmidt numbers, the components of the velocity can be approximated by retaining the first two terms in the series

expansions of the equations derived by Hadamard and Rybczynski [38,39]

$$v_r = -2 \left[u_o \frac{y}{R} + \frac{1}{2} \left(\frac{y}{R} \right)^2 \left(\frac{3}{2} U - 2u_o \right) \right] \cos \theta \quad (133)$$

and

$$v_\theta = \left[u_o + \frac{y}{R} \left(\frac{3}{2} U - 2u_o \right) \right] \sin \theta \quad (134)$$

Here U is the velocity of the drop and u_o is the velocity at the interface with respect to the center of the drop for $\theta = \pi/2$. For solidlike behavior, which occurs in the presence of surface active agents, u_o becomes zero, while $u_o \neq 0$ in systems in which the surface active agents are either absent or present in extremely small amounts [5,40]. When the interface has a solidlike behavior [5,40]

$$\text{Sh}_{\text{II}} \equiv \frac{2 \text{Rk}_{\text{II}}}{D} = 0.998 \left(\frac{2UR}{D} \right)^{1/3} \equiv 0.998 \text{Pe}^{1/3} \quad (135)$$

while for a liquidlike behavior [5,40]

$$\text{Sh}_{\text{I}} \equiv \frac{2 \text{Rk}_{\text{I}}}{D} = 0.923 \left(\frac{u_o}{U} \right)^{1/2} \text{Pe}^{1/2} \quad (136)$$

where Pe is the Peclet number.

The order-of-magnitude evaluation leads to [40]

$$0.849 \frac{u_o}{U} \text{Pe} \text{Sh} + 0.662 \left(\frac{3}{2} - 2 \frac{u_o}{U} \right) \text{Pe} = \text{Sh}^3 \quad (137)$$

which can be rewritten as

$$\text{Sh}_{\text{I}}^2 \text{Sh} + \text{Sh}_{\text{II}}^3 \left(1 - \frac{4}{3} \frac{u_o}{U} \right) = \text{Sh}^3 \quad (138)$$

For large Reynolds numbers, the interpolation equation has the form [40]

$$0.849 \frac{u_o}{U} \text{Sh}^{-2} \text{Re} + 0.278 \left(\frac{3}{2} - \frac{u_o}{U} \right) \left(\frac{3}{2} + \frac{u_o}{U} \right)^{1/2} \text{Re}^{3/2} \text{Sh}^{-3} = \text{Sc}^{-1} \quad (139)$$

where $\text{Re} \equiv 2RU/\nu$. Equation (139) can be rearranged as

$$\frac{2}{3} \frac{u_o}{U} \text{Sh} \text{Sh}_{\text{I}}^2 + \left(1 - \frac{2}{3} \frac{u_o}{U} \right) \left(1 + \frac{2}{3} \frac{u_o}{U} \right)^{1/2} \text{Sh}_{\text{II}}^3 = \text{Sh}^3 \quad (140)$$

where

$$\text{Sh}_{\text{I}} = 1.13 \text{Pe}^{1/2} \quad (141)$$

is valid for potential flow ($u_0/U = \frac{3}{2}$) [41], whereas

$$\text{Sh}_{II} = 0.8 \text{Re}^{1/2} \text{Sc}^{1/3} \quad (142)$$

is valid when the interface behaves like a solid boundary ($u_0 = 0$) [42–44]. Comparisons between the algebraic equations and those obtained by using the integral method are given in Figs. 2 and 3.

K. UNSTEADY-STATE MASS TRANSFER TO A ROTATING DISK

This problem has received special attention from electrochemists. If the rate of mass transfer is controlled by liquid diffusion, the governing unsteady-state transport equation

$$\frac{\partial c}{\partial t} + v \frac{\partial c}{\partial y} = D \frac{\partial^2 c}{\partial y^2} \quad (143)$$

must be solved for the boundary conditions

$$\begin{aligned} c &= c_\infty & \text{at } t &= 0 & \text{for all } y \\ c &= 0 & \text{at } y &= 0 & \text{for all } t \\ c &= c_\infty & \text{as } y &\rightarrow \infty & \text{for all } t \end{aligned} \quad (144)$$

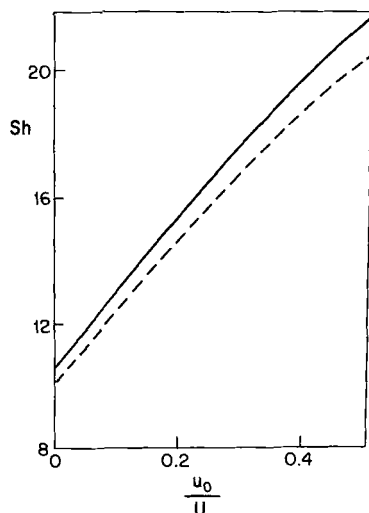


FIG. 2. Comparison for $\text{Pe} = 10^3$ between Eq. (137) (broken line) and the results of the integral method (solid line).

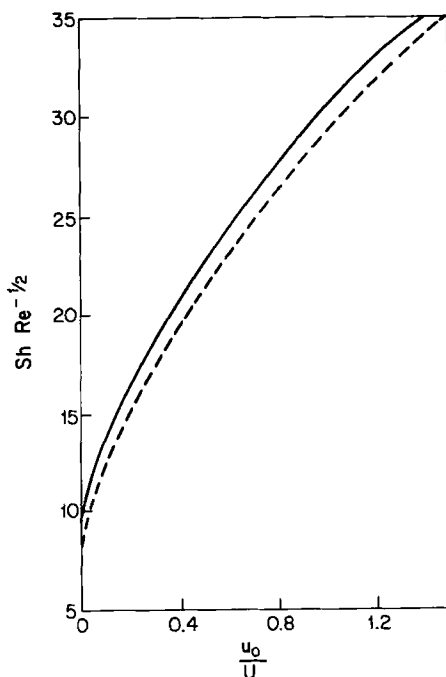


FIG. 3. Comparison for $Sc = 10^3$ between Eq. (139) (broken line) and the results of the integral method (solid line).

Here y is the distance to the disk and v is the velocity in that direction. Since the Schmidt number in this case is much larger than unity, only the velocity close to the disk is important in predicting the rate of mass transfer. This is given by [5]

$$v = -0.51 \omega^{3/2} y^2 / \nu^{1/2} \quad (145)$$

where ω is the rate of rotation of the disk in radians per second.

The application of the order-of-magnitude evaluation leads to

$$\frac{\partial c}{\partial t} \sim \frac{\Delta c}{t} \quad (146a)$$

$$v \frac{\partial c}{\partial y} \sim \frac{\omega^{3/2} \delta \Delta c}{\nu^{1/2}} \quad (146b)$$

and

$$D \frac{\partial^2 c}{\partial y^2} \sim D \frac{\Delta c}{\delta^2} \quad (146c)$$

Equation (143) can therefore be replaced by the algebraic equation

$$A \text{Fo}^{-1} \text{Sh} + B \text{Re}^{3/2} \text{Sc} = \text{Sh}^3 \quad (147)$$

where

$$\text{Fo} = \frac{Dt}{d^2}, \quad \text{Re} = \frac{\omega d^2}{\nu}, \quad \text{and} \quad \text{Sh} = \frac{kd}{D} \quad (148)$$

Fo being the Fourier number and d the diameter of the disk. The mass transfer coefficient k can be considered as interpolating between the steady-state convective diffusion at large times ($t \rightarrow \infty$) and unsteady-state diffusion at short times ($t \rightarrow 0$ and $\nu = 0$). The constants A and B of Eq. (147) follow from the solutions for these two limiting cases. For these two limiting cases

$$\text{Sh}_I = 0.62 \text{Re}^{1/2} \text{Sc}^{1/3} \quad (149)$$

and

$$\text{Sh}_{II} = \pi^{-1/2} \text{Fo}^{-1/2} \quad (150)$$

One thus obtains

$$A = 1/\pi \quad \text{and} \quad B = (0.62)^3 \quad (151)$$

Equation (147) can be also rearranged in the form

$$\text{Sh}_{II}^2 \text{Sh} + \text{Sh}_I^3 = \text{Sh}^3 \quad (152)$$

Of course, this result can be obtained directly from Eq. (147) without determining the constants A and B .

A comparison of the predictions of Eq. (152) with an approximate solution of Pleskov and Filinovski [45] is given in Table VII. Since the expression of

TABLE VII
UNSTEADY-STATE MASS TRANSFER TO A ROTATING DISK

$(1/1.212)(\text{Sh}_{II}/\text{Sh}_I)^{-2}$	$Y = \text{Sh}/\text{Sh}_I$	
	This work	Pleskov and Filinovski ^a
10^{-2}	9.09	8.93
5×10^{-3}	4.09	3.79
10^{-1}	2.93	2.57
5×10^{-1}	1.5	1.26
1	1.26	1.06
2	1.14	0.95
> 5	$Y \rightarrow 1$	$Y \rightarrow 0.94$

^a The equation given in Pleskov and Filinovski (45) is an approximation that is about 6% below the exact numerical results.

Pleskov and Filinovski is about 6% below the exact results, the comparison indicates that the algebraic method is accurate within 5 to 10%.

L. UNSTEADY HEAT TRANSFER TO A LIQUID IN STEADY LAMINAR FLOW ALONG A PLATE

Let us consider a semiinfinite fluid in steady laminar flow along a plate. Initially, the plate and fluid are at the temperature T_∞ , but for times $t > 0$ the temperature of the wall becomes equal to T_w . In this case, the temperature field satisfies the equation

$$\frac{\partial T}{\partial t} + u \frac{\partial T}{\partial x} + v \frac{\partial T}{\partial y} = a \frac{\partial^2 T}{\partial y^2} \quad (153)$$

and the appropriate initial and boundary conditions are

$$\begin{aligned} T &= T_0 & \text{for } t = 0 & \text{ and for all } x \text{ and } y \\ T &= T_w & \text{for } y = 0, \quad t > 0, & \text{ and all } x \\ T &= T_0 & \text{for } y \rightarrow \infty & \text{ and all } t \text{ and } x \end{aligned} \quad (154)$$

Assuming large Prandtl numbers, one can substitute only the first terms of Blasius series [Eqs. (68a)] for the velocity components u and v , and the algebraic evaluation leads to the expression:

$$\frac{A}{t} + B \frac{u_\infty^{3/2} \delta}{v^{1/2} x^{3/2}} = \frac{a}{\delta^2} \quad (155)$$

which can be rewritten in the form

$$A \frac{x^2}{at} \frac{x}{\delta} + B \text{Re}_x^{3/2} \text{Pr} = \left(\frac{x}{\delta} \right)^3 \quad (156)$$

The values of the constants A and B are calculated from the solutions available for (I) the steady-state heating of the flowing liquid and (II) the unsteady heating of the stagnant liquid. In the former case,

$$\text{Nu}_{x,I} \equiv \frac{k_{x,I} x}{k'} = 0.339 \text{Re}_x^{1/2} \text{Pr}^{1/3} \quad (157)$$

whereas in the latter,

$$\text{Nu}_{x,II} \equiv \frac{h_{x,II} x}{k'} = \left(\frac{x^2}{\pi a t} \right)^{1/2} \quad (158)$$

One thus obtains

$$\left(\frac{x^2}{\pi a t} \right) \text{Nu}_x + (0.339 \text{Re}_x^{1/2} \text{Pr}^{1/3})^3 = \text{Nu}_x^3 \quad (159)$$

It is convenient to rewrite Eq. (159) in the form [13]

$$\frac{1}{\pi} \frac{M}{\tau} + \frac{1}{27} = \frac{M^3}{\text{Pr}} \quad (160)$$

where $M \equiv (hx/k')\text{Re}_x^{-1/2}$ and $\tau = tu_\infty/x$.

As shown in Fig. 4 this expression compares well with the more exact solution of Cess [46].

In terms of the Nusselt numbers in the two extreme cases, Eq. (159) becomes

$$(\text{Nu}_{x,I})^3 + (\text{Nu}_{x,II})^2 \text{Nu}_x = \text{Nu}_x^3 \quad (161)$$

M. LAMINAR FREE CONVECTION ALONG A VERTICAL PLATE WITH HOMOGENEOUS REACTION

Equations (105) and (106) describe the concentration field. The fluid velocity components are approximated by Eqs. (68b) and (68c). The evaluation procedure leads in this case to the expression

$$(\text{Sh}_x/\text{Gr}_x^{1/4})^3 = (\text{Sh}_x/\text{Gr}_x^{1/4})(\text{Da}_{n,x}/\text{Gr}_x^{1/2}) + (0.503 \text{Sc}^{1/4})^3 \quad (162)$$

This equation leads in the case of convection without reaction to

$$\text{Sh}_{x,I} = 0.503 \text{Gr}_x^{1/4} \text{Sc}^{1/4} \quad (163)$$

and in the case of reaction without convection to

$$\text{Sh}_{x,II} = \text{Da}_{n,x}^{1/2} \quad (164)$$

where $\text{Gr}_x = g\beta c_s x^3/\nu^2$ and $\text{Da}_{n,x}$ (the Damkhöler number) = $[2/(n+1)] \times k_n c_s^{n-1} x^2/D$, n being the order of the reaction.

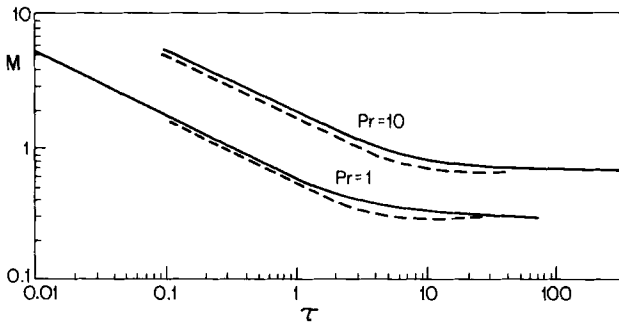


FIG. 4. Comparison between Eq. (160) (solid curve) and the more exact solution of Cess (broken curve).

Perturbation solutions for two special cases, namely, for $n = 1$ and $n = 2$, have been presented by Meadley and Rahman [47]. Results based on Eq. (162) and the "exact" values computed from the perturbation expansion are shown in Tables VIII and IX (for $n = 1$ and 2, respectively). The agreement is again within 5 to 10%. The expressions of Meadley and Rahman are not accurate for large values of the ratio $Da_{n,x}/Gr_x^{1/2}$. However, Eq. (162) can be used without any such restriction.

N. TURBULENT MASS TRANSFER WITH FIRST-ORDER CHEMICAL REACTION

Consider the turbulent flow of a liquid through a tube whose wall is dissolving in the liquid and that the diffusion of the solute is accompanied by a first-order chemical reaction. The turbulent diffusivity is employed to represent the turbulent transport. Since the dissolving species is consumed by reaction, only the region near the wall (whose thickness is small compared to

TABLE VIII
LAMINAR NATURAL CONVECTION TO A VERTICAL PLATE WITH FIRST-ORDER
HOMOGENEOUS REACTION

$X = (Da_{1,x}/Gr_x^{1/2})$	$Y = (Sh_x/Gr_x^{1/4})$			
	$Sc = 100$		$Sc = 10,000$	
	This work	Meadley and Rahman	This work	Meadley and Rahman
1×10^{-2}	1.59	1.54	5.03	4.98
1×10^{-1}	1.61	1.56	5.04	4.99
2×10^{-1}	1.63	1.58	5.04	5.00
4×10^{-1}	1.67	1.62	5.06	5.01
8×10^{-1}	1.76	1.70	5.08	5.03
1	1.80	1.74	5.10	5.04
2	2.00	1.94	5.16	5.11
4	2.38	2.34	5.29	5.23
8	3.05	3.12	5.56	5.48
1×10	3.35	3.53	5.69	5.60
2×10	$Y \rightarrow X^{1/2}$	^a	6.33	6.22
4×10			7.54	7.46
8×10			9.65	9.94
1×10^2			10.58	11.18
2×10^2			$Y \rightarrow X^{1/2}$	^a

^a The perturbation solution of Meadley and Rahman is not accurate for larger values of X .

TABLE IX
LAMINAR NATURAL CONVECTION FOR A VERTICAL PLATE WITH SECOND-ORDER
HOMOGENEOUS REACTION

$X = (\text{Da}_{2,x}/\text{Gr}_x^{1/2})$	$Y = (\text{Sh}_x/\text{Gr}_x^{1/4})$			
	$\text{Sc} = 100$		$\text{Sc} = 10,000$	
	This work	Meadley and Rahman	This work	Meadley and Rahman
1×10^{-2}	1.59	1.54	5.03	4.98
2×10^{-2}	1.59	1.55	5.03	4.98
4×10^{-2}	1.60	1.55	5.03	4.98
8×10^{-2}	1.61	1.56	5.04	4.99
1×10^{-1}	1.61	1.56	5.04	4.99
2×10^{-1}	1.63	1.59	5.04	5.00
4×10^{-1}	1.67	1.63	5.06	5.01
8×10^{-1}	1.76	1.72	5.08	5.04
1	1.80	1.76	5.10	5.05
2	2.00	1.99	5.16	5.12
4	2.38	2.43	5.29	5.26
8	3.05	3.32	5.56	5.53
1×10	3.35	3.77	5.69	5.67
2×10	4.57	5.99	6.33	6.36
4×10	$Y \rightarrow X^{1/2}$	^a	7.54	7.73
8×10			9.65	10.48
1×10^2			10.58	11.85
2×10^2			$Y \rightarrow X^{1/2}$	^a

^a The perturbation solution of Meadley and Rahman is not accurate for large values of X .

the radius of the tube) is relevant. The effect of curvature can therefore be neglected and the transport equation becomes

$$\frac{d}{dy} \left[(D + \varepsilon) \frac{dc}{dy} \right] - K_1 c = 0 \quad (165)$$

where ε is the turbulent diffusivity and y the distance to the wall. Equation (165) must be solved for the boundary conditions

$$c = c_s \quad \text{for } y = 0$$

and

$$c = 0 \quad \text{for } y \rightarrow \infty \quad (166)$$

Since, in this case, only a narrow region near the wall is relevant, one can use

for the turbulent diffusivity the expression [48,49]

$$\varepsilon = \gamma_o(y(\tau_o/\rho)^{1/2}/\nu)^3 \equiv \gamma y^3 \quad (167)$$

where τ_o is the shear stress at the wall, ρ is the density of the liquid, and γ_o is a constant. The order-of-magnitude evaluation procedure leads to

$$\frac{d}{dy} D \frac{dc}{dy} \sim D \frac{c_s}{\delta^2} \quad (168a)$$

$$\frac{d}{dy} \varepsilon \frac{dc}{dy} \sim \gamma \delta c_s \quad (168b)$$

and

$$K_1 c \sim K_1 c_s \quad (168c)$$

Therefore,

$$A \frac{D}{\delta^2} + B \gamma \delta = K_1 \quad (169)$$

In the limiting case in which $\gamma = 0$, Eq. (165) becomes

$$D \frac{d^2 c}{dy^2} - kc = 0 \quad (170)$$

When multiplied by dc/dy , this equation can be integrated readily to obtain the concentration gradient at $y = 0$,

$$\left(\frac{dc}{dy} \right)_{y=0} = - \left(\frac{K_1}{D} \right)^{1/2} c_s \quad (171)$$

The corresponding mass transfer coefficient k_H is therefore given by the expression

$$k_H \equiv D/\delta_H = (K_1 D)^{1/2} \quad (172)$$

Consequently, $A = 1$. In the absence of a chemical reaction

$$D/\delta_1^2 + B \gamma \delta_1 = 0 \quad (173)$$

Eliminating B between Eqs. (169) and (173) one obtains

$$(\delta_1/\delta)^2 - (\delta/\delta_1) = K_1 \delta_1^2/D \quad (174)$$

which, introducing the mass transfer coefficient $k = D/\delta$, becomes

$$(k/k_1)^2 - (k_1/k) = K_1 D/k_1^2 \equiv M \quad (175)$$

In Fig. 5, Eq. (175) is compared with the exact numerical solution of Eq. (165), obtained by Vieth *et al.* [50]. There is excellent agreement between the two.

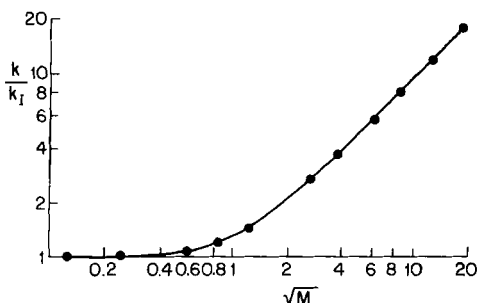


FIG. 5. Comparison between Eq. (175) (solid curve) and the results of the numerical solution of Vieth *et al.* (points).

In terms of the mass transfer coefficients k_I and k_{II} for the two extreme cases, Eq. (169) can be rewritten as

$$k^2 = k_{II}^2 + (k_I^3/k) \quad (176)$$

O. THE ALGEBRAIC METHOD AND THE RENEWAL MODELS

Turbulent mass transfer near a wall can be represented by various physical models. In one such model the turbulent flow is assumed to be composed of a succession of short, steady, laminar motions along a plate. The length scale of the laminar path is denoted by x_o and the velocity of the liquid element just arrived at the wall by u_o . Along each path of length x_o , the motion is approximated by the quasi-steady laminar flow of a semiinfinite fluid along a plate. This implies that the hydrodynamic and diffusion boundary layers which develop in each of the paths are assumed to be smaller than the thickness of the fluid elements brought to the wall by turbulent fluctuations. Since the diffusion coefficient is small in liquids, the depth of penetration by diffusion in the liquid element is also small. Therefore one can use the first terms in the Taylor expansion of the Blasius expressions for the velocity components. The rate of mass transfer in the laminar microstructure can be obtained by solving the equation

$$u \frac{\partial c}{\partial x} + v \frac{\partial c}{\partial y} = D \frac{\partial^2 c}{\partial y^2} - K_1 c \quad (177)$$

where

$$u \propto \frac{u_o y}{(xv/u_o)^{1/2}} \quad \text{and} \quad v \propto u_o \frac{y^2}{x(xv/u_o)^{1/2}} \quad (178)$$

There are now two length scales: the thickness δ of the diffusion boundary

layer and the length x_0 of the laminar path length. Hence,

$$u \frac{\partial c}{\partial x} \sim v \frac{\partial c}{\partial y} \sim \frac{u_0 \delta \Delta c}{x_0 (x_0 v / u_0)^{1/2}} \quad (179a)$$

$$D \frac{\partial^2 c}{\partial y^2} \sim D \frac{\Delta c}{\delta^2} \quad (179b)$$

and

$$K_1 c \sim K_1 \Delta c \quad (179c)$$

where δ is an average thickness of the diffusion boundary layer over the path length x_0 . Eq. (177) becomes

$$A \frac{D}{\delta^2} + B \frac{u_0 \delta}{x_0 (x_0 v / u_0)^{1/2}} = K_1 \quad (180)$$

From the solution available when convection is ignored, one obtains $A = 1$, while for the limiting case which is free of reaction, one can write

$$\frac{D}{\delta^2} + B \frac{u_0 \delta_1}{x_0 (x_0 v / u_0)^{1/2}} = 0 \quad (181)$$

Eliminating B between Eqs. (180) and (181), one again arrives at Eqs. (175) and (176).

P. RATES OF PARTICLE DEPOSITION UNDER COMBINED FLOW AND ASSISTING ELECTROSTATIC FIELD

Let us apply the interpolation procedure to a case involving an electric field. It is well known that the efficiency of the granular bed filters can be significantly increased by applying an external electrostatic field across the filter. In this case, fine ($< 0.5\text{-}\mu\text{m}$) particles deposit on the surface of the bed because of Brownian motion as well as because of the electrostatically generated dust particle drift [51]. The rate of deposition can be calculated easily for a laminar flow over a sphere in the absence of the electrostatic field [5]. The other limiting case, in which the motion of the particles is exclusively due to the electric field, could also be treated [52]. When, however, the two effects act simultaneously, only numerical solutions to the problem could be obtained [51].

The velocity components u_r and u_θ in the spherical polar coordinates r and θ are in this case given by the Stokes expressions

$$u_r = -U \left[1 - 1.5 \frac{R}{r} + 0.5 \left(\frac{R}{r} \right)^3 \right] \cos \theta \quad (182a)$$

and

$$u_\theta = \frac{U}{2} \left[2 - 1.5 \frac{R}{r} - 0.5 \left(\frac{R}{r} \right)^3 \right] \sin \theta \quad (182b)$$

where R is the radius of the spherical collector and U is the velocity of the undisturbed flow.

The electrostatic field E is due to the external field E_∞ and the field induced by the polarization of the collector. The components of the field in polar coordinates, when E_∞ and the flow are in the same direction, are [53]

$$E_r = -[2b(R/r)^3 + 1]E_\infty \cos \theta \quad (183a)$$

and

$$E_\theta = -[b(R/r)^3 - 1]E_\infty \sin \theta \quad (183b)$$

where

$$b = (\epsilon_C - \epsilon)/(\epsilon_C + 2\epsilon) \quad (184)$$

and ϵ_C and ϵ are the dielectric constants of the collector and of the free volume, respectively. The dust particles are assumed to be of uniform charge q . Therefore, the force acting on each of the particles is

$$\mathbf{F} = E\mathbf{q} \quad (185)$$

and the flux generated by the electric field can be calculated as

$$\mathbf{j}_e = B\mathbf{F}n \quad (186)$$

where B is the mobility coefficient and n is the concentration of the particles. The mobility coefficient B is related to the diffusion coefficient D via the expression

$$B = D/kT \quad (187)$$

where k is the Boltzmann constant and T is the absolute temperature.

Two additional electrostatic forces, the space charge effect and the image force, are also present. As shown by Shapiro *et al.* [54], their effect can, however, be neglected when q and the dust concentration are sufficiently small.

Since the diffusion coefficient of the dust particles is very small, the thickness of the diffusion boundary layer is small compared to the radius R of the collector. Therefore, the concentration distribution and the rate of deposition can be calculated by substituting for the velocity and electric fields the expressions valid for $y/R \ll 1$. In that region, Eqs. (182) and (183) become

$$u_r = -\frac{3}{2}U(y^2/R^2)\cos \theta \quad (188a)$$

$$u_\theta = \frac{3}{2}U(y/R)\sin \theta \quad (188b)$$

$$E_r = -(2b + 1)E_\infty \cos \theta \quad (189a)$$

and

$$E_\theta = (1 - b)E_\infty \sin \theta \quad (189b)$$

Since diffusion along the interface is negligible compared with that normal to the interface, the convective diffusion equation can be approximated by

$$\begin{aligned} & \left[\frac{3}{2} U \frac{y}{R} + (1 - b) Bq E_\infty \right] \sin \theta \frac{\partial n}{R \partial \theta} \\ & - \left[\frac{3}{2} U \frac{y^2}{R^2} + (2b + 1) Bq E_\infty \right] \cos \theta \frac{\partial n}{\partial y} = D \frac{\partial^2 n}{\partial y^2} \end{aligned} \quad (190)$$

The appropriate boundary conditions are

$$n = 0 \quad \text{for } y = 0 \quad (191a)$$

and

$$n = n_\infty \quad \text{for } y \rightarrow \infty \quad (191b)$$

The terms of Eq. (190) are evaluated by replacing y and dy by the thickness δ of the boundary layer and dn by n_∞ . One obtains

$$D \frac{\partial^2 n}{\partial y^2} \sim D \frac{n_\infty}{\delta^2} \quad (192a)$$

$$\frac{3}{2} U \frac{y}{R} \sin \theta \frac{\partial n}{R \partial \theta} \sim Un_\infty \frac{\delta}{R^2} \quad (192b)$$

$$(1 - b) Bq E_\infty \sin \theta \frac{\partial n}{R \partial \theta} \sim \frac{(1 - b) Bq E_\infty n_\infty}{R} \quad (192c)$$

$$\frac{3}{2} U \frac{y^2}{R^2} \cos \theta \frac{\partial n}{\partial y} \sim \frac{Un_\infty \delta}{R^2} \quad (192d)$$

and

$$(2b + 1) Bq E_\infty \cos \theta \frac{\partial n}{\partial y} \sim \frac{(2b + 1) Bq E_\infty n_\infty}{\delta} \quad (192e)$$

Replacing each of the terms of Eq. (190) by its evaluating expression from Eqs. (192) multiplied by a constant yields

$$A \frac{Un_\infty \delta}{R^2} + A'(2b + 1) \frac{Bq E_\infty n_\infty}{\delta} + A''(1 - b) \frac{Bq E_\infty n_\infty}{R} = \frac{Dn_\infty}{\delta^2} \quad (193)$$

Because $\delta \ll R$ and $2b + 1 > (1 - b)$,

$$\frac{(1 - b) Bq E_\infty n_\infty}{R} \ll \frac{(2b + 1) Bq E_\infty n_\infty}{\delta}$$

and Eq. (193) becomes

$$A \frac{U\delta}{R^2} + A' \frac{(2b+1)BqE_\infty}{\delta} = \frac{D}{\delta^2} \quad (194)$$

Introducing the mass transfer coefficient k , defined by

$$k = D/\delta \quad (195)$$

and the Sherwood and Peclet numbers

$$\text{Sh} \equiv \frac{2Rk}{D} = \frac{2R}{\delta}, \quad \text{Pe} = \frac{RU}{D}, \quad \text{and} \quad \tilde{\text{Pe}} = \frac{RBqE_\infty}{D} \quad (196)$$

Eq. (194) can be rewritten as

$$\frac{M \text{Pe}}{\text{Sh}^3} + \frac{M'(2b+1)\tilde{\text{Pe}}}{\text{Sh}} = 1 \quad (197)$$

The constants M and M' can be determined by using the expressions valid in the limiting cases in which $E_\infty = 0$ or $U = 0$.

When $E_\infty = 0$ [5],

$$\text{Sh} = 1.26 \text{Pe}^{1/3} \quad (198)$$

while when $U = 0$ [52],

$$\text{Sh} = \frac{2b+1}{2} \tilde{\text{Pe}} \quad (199)$$

Consequently,

$$\frac{\text{Sh}}{\text{Pe}^{1/3}} = \left\{ (1.26)^3 + \frac{2b+1}{2} \left(\frac{\text{Sh}}{\text{Pe}^{1/3}} \right)^2 \frac{\tilde{\text{Pe}}}{\text{Pe}^{1/3}} \right\}^{1/3} \quad (200)$$

The maximum deviation between Eq. (200) and the numerical solution of Shapiro and Laufer [51] is less than 10%.

Q. DISCUSSION

In the examples treated in Section II, expressions for the rate of transfer in coupled processes have been derived by using scaling arguments and by interpolating between two limiting cases. Although the method is very simple, its results are generally within 10% of the more exact (and more complicated) solutions. As expected, the form of the interpolation equation depends on the particular physical problem. Indeed, in terms of the Nusselt (Sherwood) numbers for the two extreme cases between which the interpolation is carried

out, the algebraic equation is quadratic in the case of penetration theory with chemical reaction and cubic for mixed (free plus forced) convection. This difference in form can be associated with different kinds of velocity profiles. The tangential velocity component is independent of the distance from the interface in the penetration model, but it varies linearly with the distance in the mixed convection case. In the other cases treated, convection with reaction, convection with suction, and steady convection with unsteady temperature field, the interpolation equation is also cubic, but one of the terms consists of mixed Sherwood (or Nusselt) numbers of the form $Sh_{x,\parallel}^2 Sh_x$ or $Sh_{x,\parallel} Sh_x^2$. When a chemical reaction or an unsteady concentration (or temperature) field is involved, the mixed term is of the form $Sh_{x,\parallel}^2 Sh_x$; when suction is involved, the mixed term has the form $Sh_{x,\parallel} Sh_x^2$.

IV. Turbulent Heat and Mass Transfer

A. INTRODUCTION

The transport equations for laminar motion can be formulated, in general, easily and difficulties may lie only in their solution. On the other hand, for turbulent motion the formulation of the basic equations for the time-averaged local quantities constitutes a major physical difficulty. In recent developments, one considers that turbulence (chaos) is predictable from the time-dependent transport equations. However, this point of view is beyond the scope of the present treatment. For the present, some simple procedures based on physical models and scaling will be employed to obtain useful results concerning turbulent heat or mass transfer.

First, a physical model is used to describe turbulence near a solid boundary, the motion being represented by a succession of short laminar paths. The turbulent fluctuations bring elements of liquid to the proximity of the wall. These elements of liquid proceed short distances along the wall in laminar motion, after which they dissolve into the bulk, being replaced by other elements, and so on. Thus, the problem of turbulence is reduced to the solution of a simple laminar motion. The path length of the laminar motion as well as the velocity of the element of liquid brought close to the wall by fluctuations are obtained on the basis of dimensional considerations. The physical scaling method is employed to obtain expressions for the mass or heat transfer coefficient in each of the laminar paths. When a quasi-steady state in each laminar path is assumed, the model is applied to the flow of Newtonian and non-Newtonian fluids through a tube; to turbulent heat or mass transfer in a stirred vessel; to heat transfer in separated flows; to heat transfer between a fluid flowing through a fixed or fluidized bed and the wall; to heat transfer

between a bubble bed and the wall; and to boiling heat transfer. A more complicated version of the model which includes transient contributions is also discussed.

Second, the mechanism of mass transfer near a liquid boundary is examined by means of a physical model that involves a roll cell structure near the interface. The elements of liquid have a translatory motion with the average local velocity and a circulatory one in the roll cell. Two limiting cases are examined: (1) the elements of liquid keep their identity without any change during the motion along the inside paths of the roll cell, and (2) the elements of liquid undergo complete exchange (acquire the bulk concentration) during their inside motion. In the first limiting case, the rate of mass transfer is increased in comparison to that predicted by the penetration theory since the time interval spent by the element of liquid at the interface is reduced. The second limiting case is similar to the Danckwerts [31] renewal model. This treatment is employed for turbulent flow and for the case of interfacial turbulence induced by the Marangoni effect.

B. TURBULENT FLOW NEAR A SOLID BOUNDARY

The turbulent transport equations are obtained in the traditional treatment of turbulence by time averaging the unsteady-state transport equations, after substituting the concentration and velocity components by the sum of their mean values and the corresponding time-dependent fluctuations. The following expression is thus obtained for the (time) average of the number of moles \bar{N} that are transferred per unit time through unit area, in the direction y normal to the wall:

$$\bar{N} = -D \frac{\partial \bar{c}}{\partial y} + \bar{v}\bar{c} + \overline{v'c'} \quad (201)$$

where \bar{c} is the (time) average concentration, \bar{v} is the time average of the y component of the velocity, v' is the fluctuating y component of the velocity, c' is the fluctuation of the concentration, D is the diffusion coefficient, and the bar denotes time averages. In what follows, \bar{v} will be taken as zero. In the classic theory of turbulence, the fluctuation c' is expressed as the product of a certain length l , called the mixing length, and $\partial \bar{c} / \partial y$. Hence

$$\bar{N} = -(D + \overline{v'l})(\partial \bar{c} / \partial y) \quad (202)$$

Assuming that the mixing length for the concentration field is equal to that of the velocity field, the turbulent diffusivity

$$\varepsilon = \overline{v'l} \quad (203)$$

becomes equal to the turbulent kinematic viscosity. This means that, at least in principle, information regarding ε could be obtained from the (time-average) velocity distribution near the wall. However, in liquids the diffusion coefficient is very small ($D \approx 10^{-5}$ cm²/sec) and the Schmidt number $\nu/D \approx 10^3$. As a result, the turbulent kinematic viscosity is negligible in comparison with the kinematic viscosity in the relevant region near the wall where the concentration has an appreciable variation. Therefore, it is difficult to measure the turbulent kinematic viscosity very near the wall. From the classic theory of turbulence it nevertheless follows that, in the immediate vicinity of the wall, ε is a function of y , ν , the shear stress τ_0 at the wall, and the density ρ of the fluid. Dimensional considerations lead therefore to

$$\varepsilon = \nu \phi \left(\frac{y(\tau_0/\rho)^{1/2}}{\nu} \right) \quad (204)$$

Does the turbulent diffusivity ε decay to zero at a certain distance from the wall or at the wall itself? At present, there is unanimous agreement that turbulence decays at the wall as [48,49,55]

$$\frac{\varepsilon}{\nu} \propto \left(\frac{y(\tau_0/\rho)^{1/2}}{\nu} \right)^n \quad (205)$$

where values between 2 and 4 have been suggested for the exponent n . Measurements of the mass transfer coefficient [56] from the dissolution of the wall of a tube into a turbulent liquid with very large Schmidt numbers (up to $Sc = 10^5$) indicate that $n = 3$. The arguments which have been adduced [49] on behalf of Eq. (205) will be examined in some detail because by stressing some of the contradictions which arise in the turbulent diffusivity concept, the plausibility of the suggested physical model will appear in a more natural manner. Equation (205) with $n = 3$ can be derived if one assumes that $l \propto y$ and that the tangential component of the fluctuation $u' \propto \bar{u} \propto y$, where \bar{u} is the average local velocity of the main flow. The continuity equation

$$\frac{\partial u'}{\partial x} + \frac{\partial v'}{\partial y} = 0 \quad (206)$$

leads to

$$v' \propto y^2 \quad (207)$$

and consequently to

$$\varepsilon \propto y^3 \quad (208)$$

The turbulent diffusivity concept involves a local (point) description of the transfer process, which is physically reasonable as long as the mixing length is

sufficiently small in comparison with the distance to the wall. However, near the wall (but not in its immediate vicinity) $l = 0.4y$ [4], and the preceding condition is not satisfied. In addition, because \bar{u} depends only on y , $\partial u'/\partial x$ differs from zero only if the proportionality constant relating u' and \bar{u} depends on x . Since the experimental values of ε are independent of x , the dependence on x is probably repeated quasi-periodically over small successive paths. Consequently, ε might be considered a result of both a temporal and a spatial averaging. The first comment suggests that a nonlocal description of turbulence near the wall might be more appropriate than a local one, whereas the second suggests that the hydrodynamic process repeats itself over short, successive paths. It is worth noting that Fage and Townsend [57], in following the motion of small suspended particles by means of an ultramicroscope, have observed large lateral displacements very near the wall and that the motions of the particles are almost rectilinear along the wall, in the interval between two such displacements. Both comments concerning turbulent diffusivity and the preceding experimental observations suggest that one should represent turbulence near a solid by a succession of short laminar motions, the quasi-local turbulent quantities being averages over the short path [58]. In other words, this model considers that elements of liquid, which have been brought at the wall by turbulent fluctuations, are moving through short laminar paths along the wall, after which they dissolve into the bulk of the fluid, being replaced by other elements of liquid, and so on (see Fig. 6a). This model, proposed by Ruckenstein in 1958 [58], borrows the renewal idea from Higbie [30] and Danckwerts [31], but accounts for the microhydrodynamic structure of the elements of liquid instead of considering them to be solidlike. Further, in contrast with the latter models, which provide only the dependence of the mass transfer coefficient on the diffusion coefficient, Ruckenstein [58] relates the mass transfer coefficient not only to the diffusion coefficient but also to hydrodynamics.

A more realistic description that avoids the countercurrent flow in the region between two successive paths is represented in Fig. 6b, but we will assume that the regions 2 have a much smaller extent than the regions 1. It is appropriate to cite here references [59,60] in which the Danckwerts renewal idea was used to describe the turbulent boundary layer near a wall, as well as the 1969 paper of Black [61] in which a model similar to that of Ruckenstein [58] is considered.

More recent experiments [62] concerning the viscous sublayer have shown a three-dimensional structure for turbulence near the wall. In a plane normal to the mean flow, counterrotating eddy pairs are involved (Fig. 6c), whereas in the direction of the mean flow, the motion is quasi-periodic (as described earlier). Since the wavelength along the mean flow is much larger than along the perimeter of the tube, a simplified bidimensional model may account only

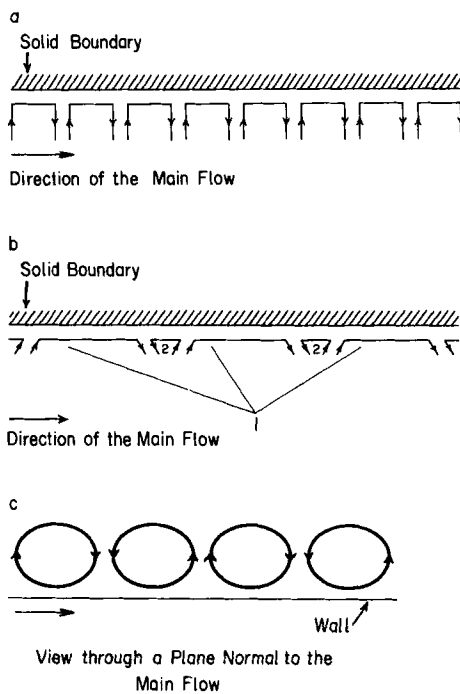


FIG. 6. (a) The flow pattern assumed in the physical model for the motion near the wall. (b) A more realistic flow pattern of the motion. (c) The roll cell pattern near the wall in a section normal to the main direction of flow.

for what happens in the plane normal to the mean flow. The steady laminar motion along a plate is used in the first model to represent the elementary phenomenon occurring along each path length, in the direction of the mean flow, whereas the steady stagnation flow pattern appears to be an adequate simplifying description for the motion in the plane normal to the mean flow and will be employed in the second model. As shown subsequently, the final expression for the turbulent mass transfer is the same in both models. For this reason, one expects the derived equation to constitute an adequate relationship between the parameters involved.

C. MODEL BASED ON STEADY LAMINAR MOTION ALONG A PLATE

In this model, the velocity and concentration fields are described by the equations valid for the steady laminar motion of a semiinfinite fluid along a plate. Therefore, the velocity components in each of the paths satisfy the

equations

$$u \frac{\partial u}{\partial x} + v \frac{\partial u}{\partial y} = v \frac{\partial^2 u}{\partial y^2} \quad (209)$$

and

$$\frac{\partial u}{\partial x} + \frac{\partial v}{\partial y} = 0 \quad (210)$$

and the concentration field satisfies the equation

$$u \frac{\partial c}{\partial x} + v \frac{\partial c}{\partial y} = D \frac{\partial^2 c}{\partial y^2} \quad (211)$$

The length x_0 of the laminar path is assumed to be so short that the thickness of the hydrodynamic boundary layer and the depth of penetration by diffusion remain smaller than the thickness of the liquid element that are brought and move along the wall. For additional complexities see Ruckenstein [58]. Let us denote by u_0 the uniform velocity of an element of fluid which has just arrived at the wall and by δ_h the thickness of the hydrodynamic boundary layer. Using a scaling procedure, one can evaluate the terms in Eqs. (209) and (210) by

$$u \frac{\partial u}{\partial x} \sim \frac{u_0^2}{x} \quad (212a)$$

$$v \frac{\partial u}{\partial y} \sim \frac{u_0 \delta_h}{x} \frac{u_0}{\delta_h} \sim \frac{u_0^2}{x} \quad (212b)$$

and

$$v \frac{\partial^2 u}{\partial y^2} \sim \frac{v u_0}{\delta_h^2} \quad (212c)$$

Consequently, Eq. (209) leads to

$$\delta_h^2 \propto vx/u_0 \quad (213)$$

At sufficiently large Schmidt numbers [as in liquids, where the diffusion coefficient is very small ($D \sim 10^{-5} \text{ cm}^2/\text{sec}$)], only the region very near the wall is affected by diffusion. Therefore, the velocity distribution can be approximated by the first term in the Taylor expansion

$$u/u_0 \propto y/\delta_h \equiv y(u_0/vx)^{1/2} \quad (214)$$

Combining Eq. (214) with the continuity equation, one obtains

$$v/u_0 \propto y^2 u_0^{1/2} / v^{1/2} x^{3/2} \quad (215)$$

The evaluation procedure leads to

$$u \frac{\partial c}{\partial x} \sim \frac{\delta u_o^{3/2}}{v^{1/2} x^{1/2}} \frac{\Delta c}{x} \quad (216a)$$

$$v \frac{\partial c}{\partial y} \sim \frac{\delta u_o^{3/2}}{v^{1/2} x^{1/2}} \frac{\Delta c}{x} \quad (216b)$$

and

$$D \frac{\partial^2 c}{\partial y^2} \sim D \frac{\Delta c}{\delta^2} \quad (216c)$$

where $\delta = \delta(x)$ is the thickness of the diffusion boundary layer. Consequently, Eq. (211) yields

$$\delta^3 \propto D v^{1/2} x^{3/2} / u_o^{3/2} \quad (217)$$

which, when rewritten in terms of the mass transfer coefficient $k_x = D/\delta$, becomes

$$k_x \propto (u_o v / x)^{1/2} (D/v)^{2/3} \quad (218)$$

Since the term “local” in the case of turbulent flow refers to a path of length x_o , the local turbulent mass transfer coefficient should be defined as the average

$$k = \frac{1}{x_o} \int_0^{x_o} k_x dx \quad (219)$$

where x_o is the length of the laminar path. Hence,

$$k \propto (u_o v / x_o)^{1/2} (D/v)^{2/3} \quad (220)$$

The path length x_o can be related to the shear stress at the wall and the velocity u_o . Indeed, the shear stress at the wall $\tau_{o,x}$ is given by

$$\frac{\tau_{o,x}}{\rho} = v \left(\frac{\partial u}{\partial y} \right)_{y=0} \propto \frac{v u_o}{\delta_h} \quad (221)$$

The average τ_o of $\tau_{o,x}$ over the path length x_o should be considered as the “local” turbulent shear stress at the wall. Hence

$$\tau_o = \frac{1}{x_o} \int_0^{x_o} \tau_{o,x} dx \propto \rho \frac{v^{1/2} u_o^{3/2}}{x_o^{1/2}} \quad (222)$$

from where one obtains

$$x_o \propto v u_o^3 (\tau_o / \rho)^{-2} \quad (223)$$

Eliminating x_o between Eqs. (220) and (223) yields

$$k = (D/v)^{2/3} (\tau_o / \rho) (1/u_o) \quad (224)$$

The proportionality constant is unity because the numerical coefficients in Eqs. (220) and (223), which can be obtained on the basis of exact solutions, lead to such a value. As for the velocity u_o , the following considerations can be used to relate this quantity to τ_o/ρ . The universal law of velocity distribution near the solid surface has the form

$$\frac{u}{(\tau_o/\rho)^{1/2}} = F\left(\frac{y(\tau_o/\rho)^{1/2}}{v}\right) \quad (225)$$

Since the region of origin of the eddies which penetrate up to the wall must be at a critical distance y_{crit} , corresponding to a critical Reynolds number

$$\frac{y_{crit}(\tau_o/\rho)^{1/2}}{v} = \text{const}$$

one finds

$$u_o \propto (\tau_o/\rho)^{1/2} \quad (226)$$

Eliminating u_o between Eqs. (224) and (226), one finally obtains

$$k \propto (\tau_o/\rho)^{1/2}(D/v)^{2/3} \quad (227)$$

D. MODEL BASED ON STEADY STAGNATION LAMINAR FLOW

As already noted in Section IV,B, turbulence can be described in the plane normal to the main flow by the stagnation flow pattern. For steady laminar stagnation flow, $u = \alpha_o x$ and $v = -\alpha_o y$ far from the solid surface and [2]

$$k \propto \left(\frac{v}{D}\right)^{1/3} \frac{D}{(v/\alpha_o)^{1/2}} \quad (228)$$

where α_o is a constant with the dimensions of seconds⁻¹. The state of turbulence near the wall can be characterized by τ_o , ρ , and η . Since the number of quantities is 4 while the number of dimensions involved is 3, a single dimensionless group can be formed, which must be a constant. Consequently,

$$\alpha_o \propto \tau_o/\rho v \quad (229)$$

Eliminating α_o between Eqs. (228) and (229), Eq. (227) is again obtained.

One may note that two kinds of considerations are involved in the two treatments of turbulent mass transfer near a solid boundary. First, the local turbulent behavior is described by microlaminar motions over short path lengths, and, second, the scales of the laminar microstructure are expressed in terms of the characteristics of the turbulent motion.

E. UNSTEADY LAMINAR MOTION USED TO DESCRIBE TURBULENT TRANSPORT

Pinczewski and Sideman [63] have introduced additional transient terms in the steady-state model of Ruckenstein. Eqs. (209) to (211) were therefore replaced by the unsteady equations

$$\frac{\partial u}{\partial t} + u \frac{\partial u}{\partial x} + v \frac{\partial u}{\partial y} = v \frac{\partial^2 u}{\partial y^2} \quad (230)$$

$$\frac{\partial u}{\partial x} + \frac{\partial v}{\partial y} = 0 \quad (231)$$

$$\frac{\partial c}{\partial t} + u \frac{\partial c}{\partial x} + v \frac{\partial c}{\partial y} = D \frac{\partial^2 c}{\partial y^2} \quad (232)$$

The new boundary conditions are

$$\begin{aligned} u &= u_0 & \text{for } t = 0 & \text{ and all } y \text{ and } x \\ u &= u_0 & \text{for } y \rightarrow \infty & \text{ and all } t \text{ and } x \\ u &= 0 & \text{for } y = 0 & \text{ and } t > 0 \text{ and all } x \\ c &= c_0 & \text{for } t = 0 & \text{ and all } y \text{ and } x \\ c &= c_0 & \text{for } y \rightarrow \infty & \text{ and all } t \text{ and } x \\ c &= c_i & \text{for } y = 0 & \text{ and } t > 0 \text{ and all } x \end{aligned} \quad (233)$$

These boundary conditions, and hence the model, involve the assumption that an element of liquid having a uniform velocity u_0 is brought at time $t = 0$ in a given small region of the surface and that fluid is flowing in this region along the wall during a time Δ . The approximate solution which has been used must be, however, replaced since it involves the quasi-steady approximation at short times and the transient approximation at long times, instead of the opposite. Since a simple analytical solution to this problem is not possible, the algebraic approximation is now employed to obtain an expression for the time-dependent thickness of the hydrodynamic boundary layer and further for the mass transfer coefficient. The terms of Eq. (230) are evaluated as follows:

$$\frac{\partial u}{\partial t} \sim \frac{u_0}{t}, \quad u \frac{\partial u}{\partial x} \sim \frac{u_0^2}{x}, \quad v \frac{\partial u}{\partial y} \sim u \frac{\partial u}{\partial x} \sim \frac{u_0^2}{x} \quad (234)$$

and

$$v \frac{\partial^2 u}{\partial y^2} \sim \frac{v u_0}{\delta_h^2}$$

Therefore,

$$(A/t) + (Bu_o/x) = v/\delta_h^2 \quad (235)$$

The solutions available for the asymptotic cases of negligible nonlinearities and steady state allow determination of the constants A and B . In the first case,

$$\frac{\partial u}{\partial t} = v \frac{\partial^2 u}{\partial y^2} \quad (236)$$

the solution of which, for the appropriate initial and boundary conditions, is

$$u = \frac{2}{\pi^{1/2}} u_o \int_0^{\frac{y}{(4vt)^{1/2}}} \exp(-\mu^2) d\mu \quad (237)$$

Since the velocity u becomes almost equal to u_o at a distance $y = \delta_h$, where

$$\delta_h/(4vt)^{1/2} \approx 1.5 \quad (238)$$

one obtains

$$A = \frac{1}{9}$$

In the steady-state case [2,4],

$$\delta_h = 5.2(vx/u_o)^{1/2} \quad (239)$$

Therefore,

$$B = 1/27$$

Equation (235) can be written as

$$\delta_h^2 = \frac{v}{1/9t + u_o/27x} \quad (240)$$

By using Eq. (68a) it is easy to show that the first term in the Taylor expansion of u for the steady-state case has the form

$$u/u_o = 1.7(y/\delta_h) \quad (241)$$

Note that, in the other extreme case, one also obtains, on the basis of Eqs. (237) and (238), $u/u_o = 1.7(y/\delta_h)$. [In fact, the value 1.5 of the constant in Eq. (238) was chosen in such a way as to obtain in both limiting cases the same value for the coefficient which multiplies the ratio y/δ_h .] Therefore, Eq. (241) will be used for the velocity u in the present context, with δ_h given by Eq. (240). The continuity equation, yields

$$\frac{v}{u_o} = \frac{1.7}{108} \frac{u_o y^2}{v^{1/2} x^2} \left(\frac{1}{9t} + \frac{u_o}{27x} \right)^{-1/2} \quad (242)$$

Since expressions for the velocity components are now available, the terms of the convective diffusion equation (232) can be evaluated as

$$\begin{aligned}\frac{\partial c}{\partial t} &\sim \frac{\Delta c}{t} \\ u \frac{\partial c}{\partial x} &\sim \frac{\delta u_o}{v^{1/2} x} \left(\frac{1}{9t} + \frac{u_o}{27x} \right)^{1/2} \Delta c \\ v \frac{\partial c}{\partial y} &\sim \frac{u_o^2 \delta}{v^{1/2} x^2} \left(\frac{1}{9t} + \frac{u_o}{27x} \right)^{-1/2} \Delta c \\ D \frac{\partial^2 c}{\partial y^2} &\sim \frac{D}{\delta^2} \Delta c\end{aligned}\tag{243}$$

Equation (232) can thus be replaced by the algebraic expression

$$\frac{A}{t} + B \frac{\delta u_o}{v^{1/2} x} \left(\frac{1}{9t} + \frac{u_o}{27x} \right)^{1/2} + C \frac{u_o^2 \delta}{v^{1/2} x^2} \left(\frac{1}{9t} + \frac{u_o}{27x} \right)^{-1/2} = \frac{D}{\delta^2} \tag{244}$$

where A , B , and C are constants. The constants B and C cannot be determined independently. However, since Eq. (244) is an interpolation equation, it is reasonable to consider that a similar interpolating expression could be employed for the average mass transfer coefficient. The following expression for the average mass transfer coefficient is obtained by replacing t by Δ , x by x_o , and δ by $\delta_m (= D/k)$ in expression (244):

$$\frac{A}{\Delta} + B \frac{\delta_m u_o}{v^{1/2} x_o} \left(\frac{1}{9\Delta} + \frac{u_o}{27x_o} \right)^{1/2} + C \frac{u_o^2 \delta_m}{v^{1/2} x_o^2} \left(\frac{1}{9\Delta} + \frac{u_o}{27x_o} \right)^{-1/2} = \frac{D}{\delta_m^2} \tag{245}$$

On the basis of Eqs. (252), which are derived later, one can write

$$\Delta \propto x_o/u_o \tag{246}$$

and, consequently, Eq. (245) becomes

$$\frac{A}{\Delta} + B' \frac{\delta_m}{v^{1/2}} \left(\frac{u_o}{x_o} \right)^{3/2} = \frac{D}{\delta_m^2} \tag{247}$$

where B' is a new constant. In terms of the average mass transfer coefficient $k = D/\delta_m$, Eq. (247) can be rewritten as

$$k^3 = Ak \frac{D}{\Delta} + B' \frac{u_o^{3/2} D^2}{v^{1/2} x_o^{3/2}} \tag{248}$$

In the case without convection, the mass transfer coefficient is given by the expression

$$k_1 = (4/\pi)^{1/2} (D/\Delta)^{1/2} \tag{249}$$

whereas in the steady-state case it is given by the expression

$$k_{II} = 0.68(u_o/x_o)^{1/2} D^{2/3} \nu^{-1/6} \quad (250)$$

Comparing Eq. (248) with Eqs. (249) and (250) yields $A = 1.27$ and $B' = 0.314$. Consequently,

$$k^3 = 1.27k \frac{D}{\Delta} + 0.314(u_o/x_o)^{3/2} (D^2/\nu^{1/2}) \quad (251)$$

The state of turbulence near the wall can be characterized by τ_o , ρ , and η . Hence Δ , x_o and u_o are functions of the preceding quantities. Since only single dimensionless groups can be formed, they must be constants. Hence,

$$\Delta \propto \frac{\nu}{\tau_o/\rho}, \quad u_o \propto (\tau_o/\rho)^{1/2}, \quad \text{and} \quad x_o \propto \frac{\nu}{(\tau_o/\rho)^{1/2}} \quad (252)$$

Replacing in Eq. (248) Δ , u_o , and x_o with their expressions from (252) yields

$$k^3 = \alpha k \text{Sc}^{-1} (\tau_o/\rho) + \beta \text{Sc}^{-2} (\tau_o/\rho)^{3/2} \quad (253)$$

α and β being constants.

The experimental data regarding the renewal time Δ have been expressed as [64]

$$\Delta = 243[\nu/(\tau_o/\rho)] \quad (254)$$

and the wall shear stress τ_o is given by

$$\tau_o/\rho = (f/2)u_m^2 \quad (255)$$

where f is the friction factor and u_m is the average velocity. For turbulent flow in a tube, the friction factor f can be calculated using the Blasius expression

$$f/2 = 0.023 \text{Re}^{-0.2} \quad (256)$$

where $\text{Re} \equiv u_m 2R/\nu$, u_m being the average velocity and R the radius of the tube. If one assumes that $x_o/u_o = \Delta$, one obtains

$$(k/u_m)^3 = 3 \times 10^{-7} \text{Re}^{-0.3} \text{Sc}^{-2} + 1.2 \times 10^{-4} (k/u_m) \text{Sc}^{-1} \text{Re}^{-0.2} \quad (257)$$

The first term on the right-hand side of Eq. (257) is provided by the quasi-steady model, whereas the second represents the contribution of the transient process. Measurements of the mass transfer coefficients from the dissolution of the wall of a tube into a turbulent liquid having Schmidt numbers as large as 10^5 could be correlated with the expression [56]

$$\text{Sh} \equiv 2kR/D = 0.0096 \text{Re}^{0.913} \text{Sc}^{0.346} \quad (258)$$

A comparison of the empirical correlation (258) with the theoretical result (257) shows that the quasi-steady term leads to the same dependence on the

Schmidt number, $Sh \propto Sc^{1/3}$, as the experiment does. The transient term leads to a too strong dependence, $Sh \propto Sc^{1/2}$. In addition, one can easily verify that, for sufficiently large values of the Schmidt number, the term in Eq. (257) due to the transient process has the dominant contribution to the value of the mass transfer coefficient and that the values predicted are much too large.

Using the quasi-steady model and writing

$$x_o/u_o = 243[v/(\tau_o/\rho)] \quad (254a)$$

one obtains

$$Sh = 0.0067 Re^{0.9} Sc^{1/3} \quad (259)$$

The exponent of the Schmidt number in Eq. (259) coincides with the experimental one, while the coefficient 0.0067 is somewhat low. However, one must not take very seriously the value of 243 for the coefficient in Eq. (254a). Accounting for the statistical distribution of the pathlength x_o and the associated average value of the mass transfer coefficient with respect to this distribution, one might avoid the slight discrepancy.

In reality, the turbulent process is more complex than described by any of the preceding models. The transient model exaggerates the importance of the transient process, while the quasi-steady model neglects the transient effects. It is easier to understand the shortcomings of the former model than the compensatory effects which cause the latter model to be in better agreement with experiment. Indeed, the boundary conditions (233) involve the assumption that, at time zero, an element of liquid, which has the velocity u_o , is brought in a given fixed region near the wall and that during a time Δ , the fluid is flowing in that region along the wall. However, an eddy which has arrived at the wall will move along the wall being entrained by the flow of liquid. The mentioned boundary conditions do not properly account for this propagating feature. Perhaps the quasi-steady model better approximates this propagation because the concentration c depends on t via the combination $x - Ut$, where U is a velocity. This may reduce Eq. (232) to an equation similar in form to the steady-state equation (211) but with velocity components which are quasi-periodical functions of time.

More complex models involving several length and velocity scales have been examined elsewhere [58].

F. TURBULENT MASS OR HEAT TRANSFER COEFFICIENT IN A TUBE FOR Sc OR $Pr > 1$

When the Schmidt (or Prandtl) number is sufficiently large, the transfer coefficient near the wall, as calculated in the preceding section, can approximate the overall transfer coefficient. For smaller values of the Schmidt

number, the resistance due to the core region also has to be taken into account. Reynolds analogy leads for the core region to:

$$\frac{c - c_o}{u - u_o} = \frac{N_o}{\tau_o/\rho} \quad (260)$$

where N_o is the wall mass flux and u_o and c_o are the values of u and c at the outer limit of the wall layer. The region near the wall is very thin compared to the fully turbulent one. Therefore, the average concentration can be calculated by using only Eq. (260) to obtain

$$c_m - c_o = \frac{N_o}{\tau_o/\rho} \left[\frac{(u'_m)^2}{u_m} - u_o \right] \quad (261)$$

where

$$c_m = \frac{1}{\pi R^2 u_m} \int_0^R 2\pi r u c \, dr \quad (262)$$

and

$$(u'_m)^2 = \frac{1}{\pi R^2} \int_0^R 2\pi r u^2 \, dr \quad (263)$$

r being the distance from the center of the tube. Since x_o is short, we assume that the thickness of the hydrodynamic boundary layer is much smaller than the thickness of the element of fluid. In addition, if the Schmidt number is not too small, we can still use the first terms in the expansion of the velocity components. For the wall region, one can therefore write

$$N_o = -\beta^{1/3} \text{Sc}^{-2/3} (\tau_o/\rho)^{1/2} (c_i - c_o) \quad (264)$$

where c_i is the concentration at the interface. For the overall mass transfer coefficient, defined by

$$N_o = -k(c_i - c_m) \quad (265)$$

one obtains [65]

$$\frac{k}{u_m} = \frac{f/2}{(u'_m/u_m)^2 + \beta'(f/2)^{1/2}[(v/D)^{2/3} - 1]} \quad (\beta' \equiv \beta^{-1/3}) \quad (266)$$

For heat transfer, good agreement with experiment is provided by the equation

$$\frac{h}{\rho c_p u_m} = \frac{f/2}{1.10 + 12.8(f/2)^{1/2}[(v/a)^{2/3} - 1]} \quad (267)$$

where c_p is the specific heat. A similar expression was proposed by Friend and Metzner [66].

The preceding expressions can easily be extended to non-Newtonian fluids by using, for the region near the wall, the quasi-steady model [67]. For a power law fluid

$$\tau = K(du/dy)^n \quad (268)$$

and one can still use Eqs. (266) and (267) by replacing the kinematic viscosity ν by the quantity ν' defined by

$$\nu' = \frac{\tau_o/\rho}{du/dy} = \left(\frac{\tau_o}{\rho}\right)^{(n-1)/n} \left(\frac{K}{\rho}\right)^{1/n} \quad (269)$$

G. TURBULENT HEAT OR MASS TRANSFER IN A STIRRED VESSEL

The motion which occurs in this case is generated by the dissipation of the mechanical energy supplied by stirring. Denoting by P the mechanical energy supplied per unit time and by V the volume of the vessel, the energy ξ_m dissipated, on the average, per unit volume is given by

$$P = V\xi_m \quad (270)$$

Of course, the energy dissipated per unit volume is not uniform and the nonuniformity depends on the details of the stirring device. Nonetheless, in what follows we will consider, for the sake of simplicity, that the energy dissipated per unit volume is uniform. The following problems are of interest:

- (a) heat transfer between liquid and either the wall of the vessel or the cooling or heating coil introduced into the vessel;
- (b) rate of dissolution of large unsuspended crystals in the liquid;
- (c) rate of dissolution of suspended crystallites in the liquid.

In case (a), turbulence can be described as in a pipe, with the difference that stirring ensures the uniformity of temperature in the core of the fluid vessel. Near the wall, the process is described by the quasi-steady model. This leads to

$$h/\rho c_p = \beta^{1/3} \text{Pr}^{-2/3} (\tau_o/\rho)^{1/2} \quad (271)$$

The shear stress τ_o at the wall can be expressed in terms of P . Indeed τ_o is given by the expression

$$\frac{\tau_o}{\rho} = \nu \left(\frac{du}{dy} \right)_{y=0} \quad (272)$$

and the energy dissipated per unit volume in a point located at the solid

boundary is

$$\frac{\xi_o}{\rho} = v \left(\frac{du}{dy} \right)_{y=0}^2 \quad (273)$$

By eliminating the velocity gradient between Eqs. (272) and (273), one obtains

$$\frac{\tau_o}{\rho} = (\xi_o v / \rho)^{1/2} \quad (274)$$

Consequently, Eq. (271) becomes [68]

$$h / \rho c_p = \beta^{1/3} \text{Pr}^{-2/3} (\xi_o v / \rho)^{1/4} \quad (275)$$

A similar expression was suggested later by Calderband and Moo-Young [69]. Concerning the value of the constant $\beta^{1/3}$, Eq. (267) suggests a value of 0.078. The mechanical energy consumed per unit time by a blade stirrer can be evaluated by using the expression [70a]

$$P = d^5 n^3 \rho F[(nd^2/v), (gd^3/v^2), \dots] \quad (276)$$

where d is the diameter of the circle described by the end points of the stirrer blades, n is the number of revolutions per unit time, and the friction coefficient F is a function of the Reynolds number nd^2/v , the Galileo number gd^3/v^2 , and various geometric ratios. Combining Eqs. (275) and (276), one obtains [68]

$$\text{Nu} \equiv \frac{d^{1/4} V^{1/4} h}{k'} = \beta^{1/3} F^{1/4} \text{Re}^{3/4} \text{Pr}^{1/3} \quad (277)$$

Expressing the friction coefficient F in terms of Reynolds number via [70a]

$$F \propto \text{Re}^{-m} \quad \text{with} \quad 0.20 < m < 0.40 \quad (278)$$

Eq. (277) becomes

$$\text{Nu} \propto \text{Re}^{0.7} \text{Pr}^{1/3} \quad \text{for} \quad m = 0.20 \quad (279a)$$

and

$$\text{Nu} \propto \text{Re}^{0.65} \text{Pr}^{1/3} \quad \text{for} \quad m = 0.40 \quad (279b)$$

For comparison, let us note that experiment shows that for the heat transfer between liquid and wall [70b],

$$hD/k' = 0.36 \text{Re}^{0.67} \text{Pr}^{1/3}$$

where D is the diameter of the vessel. Equations (279) are also in agreement with the correlations suggested for the dissolution of a fixed crystal in a stirred liquid [71] when the mass transfer constitutes the rate-determining step of the process.

For suspended particles, the relative velocity is zero and turbulence brings elements of liquid into contact with the particles, elements which are renewed after time intervals Δ . In this case, one can assume that the mass transfer between the solid and liquid is unsteady and that the concentration distribution in each element of liquid during the time Δ is provided by the solution of the equation

$$\frac{\partial c}{\partial t} = D \frac{\partial^2 c}{\partial y^2} \quad (280)$$

Since Δ is short, one can consider that the depth of penetration by diffusion is smaller than the thickness of the element of liquid. Consequently, the concentration distribution can be calculated by using the expression valid for a semiinfinite fluid:

$$\frac{c - C_i}{C_b - C_i} = \frac{2}{\pi^{1/2}} \int_0^{y/(4Dt)^{1/2}} \exp(-\mu^2) d\mu \quad (281)$$

where C_i is the concentration at the interface and C_b is that in the bulk of the liquid.

For the average mass transfer coefficient over the time interval Δ , one thus obtains

$$k = 1.13(D/\Delta)^{1/2} \quad (282)$$

The state of turbulence near the wall is characterized by ξ_o , ρ , and v . Dimensional analysis leads, therefore, to

$$\Delta \propto (\xi_o/\rho v)^{-1/2} \quad (283)$$

Combining Eqs. (282) and (283), one obtains

$$k \propto (D/v)^{1/2} (\xi_o v/\rho)^{1/4} \quad (284)$$

While of the same form, Eqs. (284) and (275) have different exponents of the Schmidt number. Now, Eq. (277) is replaced by [34]

$$\text{Sh} \equiv d^{1/4} V^{1/4} k/D \propto F^{1/4} \text{Re}^{3/4} \text{Sc}^{1/2} \quad (285)$$

H. HEAT TRANSFER BETWEEN A FLUID FLOWING THROUGH A FIXED OR FLUIDIZED BED AND A WALL

The quasi-steady laminar model is now employed to describe the heat transfer near the wall. Note that while the shear stress at the wall can be related easily to the pressure drop for the flow in a tube, it is more difficult to establish a relation between these two quantities for a packed or fluidized bed. However, while for the flow in a tube the dissipated energy is not uniform over the section

of the tube, such an assumption is more plausible for the flow through a packed bed. Indeed, a packed bed can be modeled as a bundle of tubes (having a diameter of the order of the size of the particles) in each of which the behavior of the fluid is similar. Therefore, the dissipated energy can be considered uniform over the section of the bed and is given by the expression

$$\xi = U \Delta p / h S \varepsilon \quad (286)$$

where U is the volumetric flow rate, Δp is the pressure drop, h is the height of the bed, S is the cross-sectional area of the tube, and ε is the free-volume fraction of the bed.

The pressure drop in a fixed bed can be related to the volumetric flow rate U via the expression [70a]

$$\Delta p = \lambda (h/D_e)(v^2/2)\rho\varepsilon \quad (287)$$

where h is the height of the bed, D_e is the equivalent diameter of the voids ($D_e = 4\varepsilon/\sigma$, σ being here the surface area of the particles per unit volume and ε the porosity of the bed), $v = U/S$, and λ is the friction coefficient. The friction coefficient can be related to the Reynolds number via [70a]

$$\lambda = 140(vD_e/\nu)^{-1} \quad \text{for } vD_e/\nu < 40 \quad (288a)$$

and

$$\lambda = 16(vD_e/\nu)^{-1/5} \quad \text{for } vD_e/\nu > 40 \quad (288b)$$

Eqs. (275), (286), (287), and (288) yield for a fixed bed the expressions

$$hD_e/k' \propto (vD_e/\nu)^{0.5} \text{Pr}^{1/3} \quad \text{for } vD_e/\nu < 40 \quad (289a)$$

and

$$hD_e/k' \propto (vD_e/\nu)^{0.7} \text{Pr}^{1/3} \quad \text{for } vD_e/\nu > 40 \quad (289b)$$

which are in reasonable agreement with those obtained empirically [72]:

$$hD_e/k' \propto (vD_e/\nu)^{0.5} \quad \text{for } vD_e/\nu < 40 \quad (290a)$$

and

$$hD_e/k' \propto (vD_e/\nu)^{0.8} \quad \text{for } vD_e/\nu > 40 \quad (290b)$$

Neglecting in the case of liquid fluidized beds the fraction of liquid which flows as "bubbles," the preceding approach can be extended to liquid fluidized beds. In this case,

$$\Delta p/h = (1 - \varepsilon)g(\rho_s - \rho) \quad (291)$$

where ρ_s is the density of the particles, ρ is the density of the fluid, and ε is the fluid volume fraction.

Consequently,

$$\frac{\xi}{\rho} = \frac{v(1 - \varepsilon)g(\rho_s - \rho)}{\rho\varepsilon} \quad (292)$$

and

$$\frac{h}{k'} = \beta^{1/3} \text{Pr}^{1/3} \left[\frac{v(1 - \varepsilon)g(\rho_s - \rho)}{\varepsilon v^3 \rho} \right]^{1/4} \quad (293)$$

The velocity v can be related to ε via the Richardson and Zaki expression [73]

$$v/v_d = \varepsilon^{4.6} \quad (294)$$

where v_d is the sedimentation velocity of the particle. It is interesting to note that the heat transfer coefficient h has a maximum for a value of ε of about 0.8. This happens because the dissipated energy increases with v but decreases as ε increases [see Eq. (292)].

Equation (293) cannot be applied to gas fluidized beds because in the latter case, the fluidized bed contains a large number of bubbles. The rate of heat transfer between the bed and wall is determined in the latter case by the heat transfer in the packets (clusters) of solid particles (through which the gas flows at the minimum fluidization velocity) which are exchanged, because of bubbling, between the wall and the bulk of the fluidized bed [74]. The heat transfer coefficient is given in the latter case by an expression similar to Eq. (282):

$$h = \{[(4/\pi)\rho'c'k']/\Delta\}^{1/2} \quad (295)$$

where ρ' , c' , and k' are the density, specific heat, and thermal conductivity in the packets, respectively. In the packets, the void fraction is considered to be equal to that at the minimum fluidization velocity and the thermal conductivity as that of the corresponding fixed bed. The specific heat c' is taken to be the heat capacity of the solid particles which constitute the packet.

Two approaches have been used to calculate Δ . One of them is based on the two-phase model of fluidized beds and the other is based on the stability theory. In the two-phase model [75], the flow of gas in excess to that corresponding to the minimum fluidization velocity traverses the fluidized bed as bubbles. On this basis, one can write the following equation for the volume fraction ψ occupied by the bubbles:

$$(1 - \psi)(1 - \varepsilon_{\min}) = 1 - \varepsilon \quad (296)$$

where ε is the volume fraction occupied by the gas and ε_{\min} is its value for the minimum fluidization velocity. For the velocity of the bubbles one can use the

equation of Davis and Taylor [75]:

$$v_b = 0.711g^{1/2}D_b^{1/2} \quad (297)$$

where D_b is the bubble diameter. Employing the two-phase model, one can relate v_b to ε and v via the expression, derived by Teoreanu [76],

$$v_b - v_{\min} = [(1 - \varepsilon_{\min})/(\varepsilon - \varepsilon_{\min})](v - v_{\min}) \quad (298)$$

where v is the superficial gas velocity.

Let us consider that the bubbles are uniformly distributed into the bed and that they are arranged in a simple cubical lattice. The following expression is thus obtained for the distance L between bubbles:

$$L = (\pi/6)^{1/3}\psi^{-1/3}D_b \quad (299)$$

Considering that the renewal frequency Δ^{-1} is given by the renewal frequency of the bubbles in a given point in the vicinity of the wall, one can write

$$\Delta = L/v_b \quad (300)$$

Combining Eqs. (297) through (300) yields [77]

$$\frac{1}{\Delta} = 0.64g \frac{\varepsilon - \varepsilon_{\min}}{(1 - \varepsilon_{\min})^{1/3} \{v_{\min} + [(1 - \varepsilon_{\min})/(\varepsilon - \varepsilon_{\min})](v - v_{\min})\}} \quad (301)$$

For the experimental conditions used by Mickley and Fairbanks, this equation predicts a value of about 6 sec^{-1} for Δ^{-1} , in satisfactory agreement with the experimental values.

The second approach for the prediction of Δ is based on the linear stability theory. It is well known that the homogeneous structure of a fluidized bed, in which the solid particles are arranged in the knots of an imaginary lattice, is not stable to perturbations [78–80]. One can consider that the bubbles which form in a fluidized bed constitute the final stage of the growth of small-density perturbations applied to the homogeneous structure [81]. Unfortunately, the growth of the perturbation can be computed with ease only as long as the perturbation is small, since as soon as the perturbation becomes too large, the linear approximation is no longer valid. However, the dynamics of a fluidized bed near a wall can be described by a renewal model. Furthermore, among the small perturbations the one increasing most rapidly (the dominant perturbation, i.e., the perturbation for which the real part of the factor multiplying the time has the maximum value) is expected to be felt in the final stage of the growth of the perturbation. Consequently, on the one hand, the renewal model can represent the quasi-periodic unsteady exchange between the region near the wall and the bulk, and, on the other hand, the consequences of the dominant perturbation are likely to be felt in the final stage of growth of the

perturbation. Therefore, one could identify the renewal frequency $1/\Delta$ with the imaginary part of the factor multiplying the time in the expression of the perturbation, calculated for the dominant wavelength. Such calculations have been carried out [81], and the results provide values for Δ between 5 and 10 s^{-1} , in the same range as the experimental results of Mickley and Fairbanks [74].

I. HEAT TRANSFER BETWEEN A BUBBLE BED AND A VERTICAL WALL

The bubbling through a liquid generates two kinds of motions: (a) a general motion of circulation caused by the ensemble of bubbles and (b) local micromotions generated by individual bubbles. The presence of the wall decreases the number density of bubbles located there, in comparison to their density in the central region. This density gradient will probably determine an ascending motion in the central region and a descending motion near the wall. The rate of heat transfer is determined by the process which takes place near the wall. It is likely that the descending motion in this region is turbulent. Therefore, one can use the quasi-steady laminar model to obtain

$$h \propto k'(u_0/\nu x_0)^{1/2} \text{Pr}^{1/3} \quad (302)$$

The velocity u_0 and the laminar path length x_0 can be related to measurable physical quantities by using dimensional analysis. Indeed, the circulatory motion is induced by the buoyancy force $g\Delta\rho$, where $\Delta\rho$ is the difference between the density near the wall (assumed to be equal to that of the liquid) and the density of the bubble bed

$$\Delta\rho = \rho - [\rho(1 - \varepsilon) + \rho'\varepsilon] \approx \varepsilon\rho \quad (303)$$

where ρ and ρ' are the densities of the liquid and gas, respectively, and ε is the volume fraction of the bubbling gas. Intuition suggests that u_0 and x_0 depend on the buoyant force $g\rho\varepsilon$ and on the viscosity ν and density ρ of the liquid. Therefore,

$$x_0 \propto \nu^{2/3}(g\varepsilon)^{-1/3} \quad (304)$$

and

$$u_0 \propto \nu^{1/3}(g\varepsilon)^{1/3} \quad (305)$$

Combining Eqs. (302), (304), and (305) yields [82]

$$h = Ck'(g\varepsilon/\nu^2)^{1/3}(\nu/a)^{1/3} \quad (306)$$

where from the comparison with experiment [82], $C = 0.28$. Equation (306) is in good agreement with the results of the experiments reported in the literature [83–85].

J. BOILING HEAT TRANSFER FROM A HORIZONTAL SURFACE IN THE REGIME OF ISOLATED BUBBLES

Experiment [86,87] has shown that in the neighborhood of a bubble growing at an active site and detaching from it, strong forward and backward motions of the liquid take place. As the number of active centers and the frequency of bubble generation increase, the bubble columns entrain the liquid almost continuously. This ascending motion of the liquid is compensated by a descending motion in the space between the bubble columns, which is continued in the neighborhood of the heating surface with a movement quasi-parallel to the latter. Around every active center, one can ascribe a domain having a square form of area L^2 , L being the distance between two such active centers [88]. Obviously, the rate of heat transfer is affected by the hydrodynamic process which takes place in the vicinity of the heating surface. Let us first consider that the motion along the surface is laminar. Though the motion of the liquid is more complex, it will be assumed, for the sake of simplicity, that it can be approximated by the motion of a liquid along a plate, the distance covered by the liquid being $\frac{1}{2}(L - R_0)$, where $R_0/2$ represents the average between the zero-size bubble and the size R_0 of the detaching bubble. The heat transfer coefficient, evaluated as that along a plate, is given by

$$h \propto k' [u_o/v(L - R_0)]^{1/2} (v/a)^{1/3} \quad (307)$$

where u_o is the velocity of the descending liquid arrived at the plate. The factor $1 - (\pi/4)(R_0/L)^2$ should be included to account for the average surface area covered by bubbles through which the rate of heat transfer is negligible.

The circulatory motion described is due to the buoyant force $g\Delta\rho$, where $\Delta\rho = \rho - [\rho(1 - \varepsilon) + \rho'\varepsilon] = (\rho - \rho')\varepsilon$, ρ being the density of the liquid, ρ' that of the vapor, and ε the volume fraction of the vapor in the neighborhood of the surface. The velocity u_o of the liquid should depend on $g\Delta\rho$, the kinematic viscosity ν , and density ρ . Since the number of physical quantities is four, while that of the independent dimensions involved is three, it follows that a single dimensionless group can be formed, which must be a constant. Consequently,

$$u_o \propto \left(\frac{\rho - \rho'}{\rho} g \varepsilon \nu \right)^{1/3} \quad (308)$$

Assuming that the motion of the liquid is turbulent and using the quasi-steady laminar model to describe turbulence, the heat transfer coefficient is given by the expression

$$h \propto k' (u_o/\nu x_o)^{1/2} \text{Pr}^{1/3} \quad (309)$$

where x_0 is the length of the laminar path and u_0 is the velocity of the liquid at the start of the path. One may note that the same equation is used for both the laminar and turbulent cases. The difference lies in the fact that the length of the laminar flow path is determined in the laminar case by the bubble spacing and in the turbulent case by the quantities which characterize the state of turbulence of the liquid. In the latter case, both u_0 and x_0 depend on $g(\rho - \rho')\varepsilon$, ρ , and η . Dimensional considerations lead to

$$u_0 \propto \left(\frac{\rho - \rho'}{\rho} g \nu \varepsilon \right)^{1/3} \quad (310)$$

and

$$x_0 \propto \left(\frac{\rho - \rho'}{\rho} g \varepsilon \right)^{-1/3} \nu^{2/3} \quad (311)$$

Combining Eqs. (309) through (311) yields

$$h \propto k' \left(\frac{\rho - \rho'}{\rho} \frac{g \varepsilon}{\nu^2} \right)^{1/3} \left(\frac{\nu}{a} \right)^{1/3} \quad (312)$$

A factor accounting for the negligible contribution to the heat transfer of the heating surface occupied by the bubbles should be included in Eq. (312). Equation (312) was previously proposed by Zuber [89], on the basis of an analogy with turbulent free convection. The present derivation is based on a relatively general physical model of turbulence near a wall. The latter author has also shown that Eq. (312) is in good agreement with experiment. The preceding discussion of boiling heat transfer emphasizes only the features of the problem related to turbulence and its treatment by scaling.

K. MASS TRANSFER TO SEPARATED FLOWS

For the turbulent motion in a tube, the mass transfer coefficient k is proportional to the diffusion coefficient at the power of $2/3$. It is easy to realize by inspection that this value of the exponent is a result of the linear dependence of the tangential velocity component on the distance y from the wall. For the turbulent motion in a tube, the shear stress $\tau \approx \tau_0 = \text{const}$ near the wall, whereas for turbulent separated flows, the shear stress is small at the wall near the separation point (becoming zero at this point) and depends on the distance to the wall. Thus, the tangential velocity component has, in the latter case, no longer a linear dependence on y and a different exponent for the diffusion coefficient is expected. For separated flows, it is possible to write under certain conditions that [90]

$$\tau = \tau_0 + y\alpha \quad (313)$$

where α can be assumed to be approximately equal to the pressure gradient $\partial p / \partial x$. For the sake of simplicity, let us consider only the region very close to the separation point where

$$\tau = \alpha y \quad (314)$$

with $\alpha = \text{const.}$

Introducing the latter expression in

$$\tau = \eta \frac{du}{dy} \quad (315)$$

one obtains

$$u = (\alpha/2\eta)y^2 \quad (316)$$

The convective diffusion equation becomes

$$\frac{\alpha}{2\eta} y^2 \frac{\partial c}{\partial x} = D \frac{\partial^2 c}{\partial y^2} \quad (317)$$

This equation can be easily integrated exactly by using a similarity transformation. The scaling approach is, however, much simpler and leads to the same result. Physical scaling replaces each of the terms of Eq. (317) by the expressions

$$\frac{\alpha}{2\eta} y^2 \frac{\partial c}{\partial x} \sim \frac{\alpha}{2\eta} \delta^2 \frac{\Delta c}{x} \quad (318a)$$

$$D \frac{\partial^2 c}{\partial y^2} \sim D \frac{\Delta c}{\delta^2} \quad (318b)$$

and provides the following algebraic equation for the thickness δ of the diffusion boundary layer:

$$\delta^4 \propto \eta x / \alpha \quad (319)$$

The mass transfer coefficient is therefore given by the expression

$$k \propto D^{3/4} (\alpha/\eta)^{1/4} x_0^{-1/4} \quad (320)$$

Since the path length x_0 is expected to be a function of α , η , and ρ , dimensional analysis leads to

$$x_0 \propto \nu^{1/3} (\alpha/\eta)^{-1/3} \quad (321)$$

and, consequently,

$$k \propto D^{3/4} \nu^{-5/12} (\alpha/\rho)^{1/3} \quad (322)$$

Since in the vicinity of the separation point

$$\alpha \approx \partial p / \partial x \propto U^2 \quad (323)$$

Eq. (322) becomes

$$k \propto D^{3/4} v^{-5/12} U^{2/3} \quad (324)$$

It is of interest to note that the exponent of the diffusion coefficient is indeed $3/4$ (hence different from that in a tube) and that Richardson [91] has obtained a value of $2/3$ for the exponent of the velocity while studying experimentally the heat and mass transfer in turbulent separated flows.

L. SIMPLE GENERALIZATION OF THE TUBE AND SEPARATED FLOW CASES

The scope of this section is not so much to treat these two cases together as to emphasize the fact that careful scaling can provide additional information. Let us consider that

$$\tau = \alpha y^n \quad (325)$$

This expression applies to the case of a tube with $n = 0$ and to the case of separated flow with $n = 1$. For the sake of simplicity, α is considered to be independent of x . Of course, the value of the constant α is different in the two cases. Because $\tau = \eta(du/dy)$, one obtains

$$u = \frac{\alpha}{\eta(1+n)} y^{n+1} \quad (326)$$

and the convective diffusion equation along each of the paths becomes

$$\frac{\alpha}{(1+n)\eta} y^{n+1} \frac{\partial c}{\partial x} = D \frac{\partial^2 c}{\partial y^2} \quad (327)$$

Since the diffusion coefficient is small, the depth of penetration by diffusion is also small. Consequently, it is likely that the depth of penetration by diffusion is smaller than the thickness of the fluid element flowing along the wall for all values of $x \leq x_0$. Therefore, the distribution of concentration can be approximated by that valid in a semiinfinite fluid. The similarity variable

$$\mu = y/\delta(x) \quad (328)$$

allows us to transform Eq. (327) into

$$D \frac{d^2 c}{d\mu^2} + \frac{\alpha}{(1+n)\eta} \left(\frac{y}{\delta}\right)^{n+2} \delta^{n+2} \frac{d\delta}{dx} \frac{dc}{d\mu} = 0 \quad (329)$$

Here $c = c(\mu)$ is compatible with Eq. (329) only if

$$\frac{\alpha}{(1+n)\eta} \delta^{n+2} \frac{d\delta}{dx} = \beta D \quad (330)$$

where β is a constant.

It is convenient to chose $\beta = n + 3$. One thus obtains

$$\delta = \left[\frac{(n+3)^2(n+1)\eta}{\alpha} \right]^{1/(n+3)} (Dx)^{1/(n+3)} \quad (331)$$

and

$$\frac{d^2c}{d\mu^2} + (n+3)\mu^{n+2} \frac{dc}{d\mu} = 0 \quad (332)$$

The solution of Eq. (332) for the appropriate boundary conditions is

$$\frac{c - c_i}{c_o - c_i} = \frac{\int_0^\mu \exp(-s^{n+3}) ds}{\Gamma[(n+4)/(n+3)]} \quad (333)$$

where c_i is the concentration at the solid interface and c_o is the concentration in the bulk. Therefore, the mass flux N is given by

$$N = -D \left(\frac{\partial c}{\partial y} \right)_{y=0} = \frac{D(c_i - c_o)}{\Gamma[(n+4)/(n+3)]} \left[\frac{\alpha}{(n+3)^2(n+1)\eta} \right]^{1/(n+3)} (Dx)^{-1/(n+3)} \quad (334)$$

and for the average mass transfer coefficient k over the path of length x_o , one obtains

$$k = \frac{n+3}{n+2} \frac{D^{(n+2)/(n+3)}}{\Gamma[(n+4)/(n+3)]} \left[\frac{\alpha}{(n+3)^2(n+1)\eta} \right]^{1/(n+3)} x_o^{-1/(n+3)} \quad (335)$$

An expression for the length x_o of the laminar path can be obtained from dimensional considerations by noting that the state of turbulence near the wall can be characterized by α , ρ , and η . Dimensional analysis leads to

$$x_o \propto (\alpha/\eta)^{-1/(n+2)} \nu^{1/(n+2)} \quad (336)$$

and consequently,

$$k \propto D^{(n+2)/(n+3)} (\alpha/\rho)^{1/(n+2)} \nu^{-(n+4)/(n+2)(n+3)} \quad (337)$$

For $n = 0$, Eq. (337) leads to the expression valid for the flow in a pipe, while for $n = 1$ one obtains the equation valid for the separated flow.

Since the number of quantities involved is four (x_o , α , ρ , η) and the number of independent dimensions is three, a single dimensionless group can be formed which must be a constant. However, the proportionality constant in

Eq. (336) is not a universal constant, but a function of n , the form of which cannot be predicted by the preceding considerations. An analysis of the problem in terms of more fundamental (primary) quantities may be useful in this respect.

The eddies which give rise to short laminar motions along the wall are generated in the vicinity of the boundary in a region, located at the distance y_0 from the interface, dominated by turbulence. The intensity of these eddies can be characterized by their kinetic energy E_0 at that distance. The path length x_0 is expected to depend on E_0 and on the physical constants η and ρ . Consequently, dimensional analysis leads to

$$x_0 = e_1(v/E_0^{1/2}) \quad (338)$$

where e_1 is a universal constant.

Even though Eq. (338) was derived by dimensional scaling, it is more general than Eq. (336) since the former is not restricted to a specific case. The constant e_1 is a universal constant, while the proportionality constant in expression (336) involves a particular value of n . It is, however, necessary for each specific situation to relate E_0 to the corresponding quantities. The method which is used in what follows to relate E_0 to specific quantities was suggested by Prandtl [92] and Spalding [93]. For the sake of simplicity, a unidimensional equation will be employed to describe turbulence in the fully developed turbulent region. An equation for the kinetic energy E of the eddies is written by equating the rate of dissipation per unit volume of the turbulent energy to the sum of the variation of the diffusion flux of turbulent energy and the rate of generation per unit volume of turbulent energy. The rate of dissipation per unit volume is written, on the basis of dimensional analysis, as $A\rho E^{3/2}/y$, y being the distance to the surface and A being a universal constant. The turbulent diffusivity ε is expressed, again on dimensional grounds, as $\varepsilon = eE^{1/2}y$, where e is a universal constant. Because the rate of generation is given by $\tau(du/dy)$ and the variation of the flux of the turbulent energy by $B\rho(d/dy)[E^{1/2}y(dE/dy)]$ with B a new constant, one obtains

$$\frac{AE^{3/2}}{y} - B\frac{d}{dy}\left(yE^{1/2}\frac{dE}{dy}\right) - \frac{\tau}{\rho}\frac{du}{dy} = 0 \quad (339)$$

Eliminating du/dy by means of the equation

$$\frac{\tau}{\rho} = eE^{1/2}y\frac{du}{dy} \quad (340)$$

and Eq. (325), Eq. (339) becomes

$$\frac{AE^{3/2}}{y} - B\frac{d}{dy}\left(yE^{1/2}\frac{dE}{dy}\right) - \frac{\alpha^2 y^{2n}}{e\rho^2 E^{1/2} y} = 0 \quad (341)$$

The solution of this equation that satisfies the boundary condition

$$E \rightarrow 0 \quad \text{for} \quad y = 0$$

is

$$E = \frac{\alpha/\rho}{[e(A - \frac{3}{2}Bn^2)]^{1/2}} y^n \quad (342)$$

The distance y_0 can be related, again on dimensional grounds, to E_0 and v by the expression

$$y_0 = e_2 v/E_0^{1/2} \quad (343)$$

where e_2 is a constant.

Combining Eqs. (342) and (343) yields

$$E_0 = \left\{ \frac{e_2^n}{[e(A - \frac{3}{2}Bn^2)]^{1/2}} \right\}^{2/(2+n)} v^{2n/(2+n)} \left(\frac{\alpha}{\rho} \right)^{2/(2+n)} \quad (344)$$

and, consequently,

$$x_0 = e_1 \frac{[e(A - \frac{3}{2}Bn^2)]^{1/[2(2+n)]}}{e_2^{n/(2+n)}} v^{2/(2+n)} \left(\frac{\alpha}{\rho} \right)^{-1/(2+n)} \quad (345)$$

For the mass transfer coefficient k one thus obtains

$$k = \frac{n+3}{n+2} \frac{e_1^{-1/(n+3)} [e(A - \frac{3}{2}Bn^2)]^{-1/[2(n+2)(n+3)]}}{[(n+1)(n+3)^2]^{1/(n+3)} e_2^{-n/[(n+3)(n+2)]} \Gamma\left(\frac{n+4}{n+3}\right)} \\ \times D^{(n+2)/(n+3)} \left(\frac{\alpha}{\rho} \right)^{1/(n+2)} v^{-(n+4)/[(n+2)(n+3)]} \quad (346)$$

Compared with Eq. (337), Eq. (346) provides the dependence of the proportionality constant in Eq. (337) on n .

The procedure used in this section, which could be called successive scaling, does indeed provide additional information. A simpler example of successive scaling will be presented in the next section.

M. TURBULENT MASS TRANSFER NEAR A LIQUID-FLUID INTERFACE BASED ON THE TURBULENT DIFFUSIVITY CONCEPT: TURBULENT FLOW OF A LIQUID FILM ON A VERTICAL WALL

Two approaches can be used for the analysis of turbulent mass transfer near a liquid-fluid interface. One has the time-averaged convective diffusion equation as the starting point. For obtaining in that procedure an equation for

the local time-averaged concentration, the concept of turbulent diffusivity is employed and some assumptions are made concerning its dependence on the distance to the interface and other parameters. The second approach, initiated by Higbie [30] and Danckwerts [31], has as the starting point a physical model for the turbulence near the fluid–liquid interface. While the emphasis in the present contribution is on the latter approach, it is instructive, for comparison, to present also results which are obtained on the basis of the first approach. Let us consider, in this respect, the turbulent flow of a liquid film on a vertical wall. An expression for the turbulent diffusivity ε can be obtained by starting from

$$\varepsilon = \overline{lv'} \quad (347)$$

where l is the mixing length and v' is the normal component of the fluctuating part of the velocity. Assuming that $u' \propto u$, where u (the x component of the average velocity) is independent of the distance y to the interface, the continuity equation

$$\frac{\partial u'}{\partial x} + \frac{\partial v'}{\partial y} = 0 \quad (348)$$

leads to

$$v' \propto y \quad (349)$$

Considering that the mixing length $l \propto y$, one obtains

$$\varepsilon \propto y^2 \quad (350)$$

In contrast to a solid boundary, the damping of the turbulence at the liquid–fluid interface can also be affected by the surface tension σ of the liquid. In other words, the state of turbulence near that interface is dependent not only on a characteristic velocity u_o , on the viscosity η of the liquid and its density ρ , but also on the surface tension σ of the liquid. The reciprocal time constant τ^{-1} , which must be included for dimensional reasons in Eq. (350), is therefore expected to be a function of the four physical quantities:

$$\tau = F(u_o, \eta, \sigma, \rho)$$

Since the number of quantities is five and the number of dimensions involved is three, two dimensionless groups can be formed and dimensional analysis leads to

$$\phi(\tau u_o^2/\nu, u_o^3 \tau \rho / \sigma) = 0 \quad (351)$$

In contrast to the case of a solid boundary, dimensional considerations do not provide an expression for τ in the case of a liquid boundary. In order to obtain explicit expressions for τ , two extreme cases can be considered. In one, τ is assumed to be independent of σ , whereas in the other, τ is assumed to be

independent of ν . In the first case, one obtains

$$\tau \propto \nu/u_0^2 \quad (352a)$$

and therefore

$$\varepsilon \propto (u_0^2/\nu)y^2 \quad (352b)$$

whereas in the second, one obtains

$$\tau \propto \sigma/\rho u_0^3 \quad (353a)$$

and as a result

$$\varepsilon \propto (\rho u_0^3/\sigma)y^2 \quad (353b)$$

Integrating Eq. (202), one obtains, for large Schmidt numbers, for the mass transfer coefficient k , the expressions

$$k \propto u_0(D/\nu)^{1/2} \quad (354)$$

if Eq. (352b) is used for ε , and the Levich equation [5]

$$k \propto D^{1/2}\rho^{1/2}u_0^{3/2}/\sigma^{1/2} \quad (355)$$

if Eq. (353b) is employed. For a liquid film in turbulent flow along a vertical wall, one can consider that $u_0 = (g\delta_f)^{1/2}$, where g is the gravitational acceleration and δ_f is the thickness of the film. On the other hand, for turbulent flow and at least for a sufficiently large Reynolds number the thickness δ should depend on Q (the liquid flow rate in cubic centimeters per centimeter second) and on g and should be independent of viscosity. Dimensional analysis leads in this case to the expression

$$\delta_f \propto Q^{2/3}g^{-1/3} \quad (356)$$

and Eqs. (354) and (355) become

$$k \propto Q^{1/3}g^{1/3}(D/\nu)^{1/2} \quad (357)$$

and

$$k \propto Q^{1/2}g^{1/2}(D\rho/\sigma)^{1/2} \quad (358)$$

As noted in the next section, experiment appears to indicate that the influence of viscosity is more important than that of the surface tension.

N. TURBULENT MASS TRANSFER IN A STIRRED VESSEL: RATE OF ABSORPTION THROUGH THE FREE SURFACE OF THE LIQUID

The motion of the liquid is in this case a result of the dissipation of the mechanical energy supplied by the stirring. The energy dissipated per unit volume ξ is assumed to be uniform and related to the mechanical energy P

supplied per unit time via the expressions given in Section IV,G. The state of turbulence in the neighborhood of the interface can be characterized by ξ , ρ , σ , and ν . Ignoring the effect of ν , one obtains

$$\varepsilon \propto (\xi/\rho)^{3/5}(\sigma/\rho)^{-2/5}y^2 \quad (359)$$

and

$$k \propto D^{1/2}(\xi/\rho)^{3/10}(\sigma/\rho)^{-2/10} \quad (360)$$

while ignoring the effect of σ , one gets

$$\varepsilon \propto (\xi/\rho\nu)^{1/2}y^2 \quad (361)$$

and

$$k \propto (D/\nu)^{1/2}(\xi\nu/\rho)^{1/4} \quad (362)$$

When the expressions of Section IV,G are used, Eqs. (360) and (362) become

$$k \propto D^{1/2}n^{9/10}F^{3/10}d^{3/2}V^{-3/10}(\sigma/\rho)^{-1/5} \quad (362a)$$

and

$$k \propto D^{1/2}\nu^{-1/4}n^{3/4}F^{1/4}d^{5/4}V^{-1/4} \quad (362b)$$

The experimental results obtained by Davies *et al.* [94] show that

$$k \propto n^{0.62} \quad (363)$$

and therefore suggest that viscosity plays a more important role than the surface tension. However, this conclusion is not necessarily true because Eqs. (360) and (362) involve the unrealistic assumption that the dissipated energy ξ is uniform over the volume of the liquid.

O. PHYSICAL MODEL APPROACH FOR TURBULENT MASS TRANSFER NEAR A LIQUID-FLUID INTERFACE

The point of view based on a physical model started with the 1935 paper of Higbie [30]. While the main problem treated by Higbie was that of the mass transfer from a bubble to a liquid, it appears that he had recognized the utility of his representation for both packed beds and turbulent motion. The basic idea is that an element of liquid remains in contact with the other phase for a time Δ and during this time, absorption takes place in that element as in the unsteady diffusion in a semiinfinite solid. The mass transfer coefficient k should therefore depend on the diffusion coefficient D and on the time Δ . Dimensional analysis leads in this case to the expression

$$k \propto (D/\Delta)^{1/2} \quad (364)$$

In the case of the mass transfer from a bubble of radius R and velocity U , Δ should be a function of the latter two quantities and dimensional considerations provide the equation

$$\Delta \propto R/U \quad (365)$$

One thus obtains

$$k \propto (DU/R)^{1/2} \quad (366)$$

One may note that the preceding two-step dimensional analysis provides an equation for the mass transfer coefficient, whereas the conventional dimensional analysis, which involves the quantities k , D , U , and R , can tell us only that

$$k/U = F(UR/D)$$

Of course, the two-step dimensional analysis involves, in addition, the physical argument that the element of liquid remains in contact with the bubble for the length of time Δ .

Danckwerts [31], in one of the most original contributions to the chemical engineering literature, has further developed Higbie's treatment, particularly for the treatment of turbulent mass transfer. The main assumptions of his treatment are that (1) the elements of liquid at the interface are continuously renewed, as a consequence of turbulent fluctuations, with fresh ones from the bulk of the liquid and (2) the absorption process in each liquid element can be described during its stay at the interface by the unsteady diffusion equation in a semiinfinite solid. A statistical distribution is obtained for the ages of the elements at the interface by considering that the mean rate of production of fresh surfaces is constant and equal to s and that the chance of an element to be replaced is independent of its age. The average mass transfer coefficient over the ensemble defined by the preceding statistical distribution will therefore depend on D and s , and on dimensional grounds, one can write

$$k \propto (Ds)^{1/2} \quad (367)$$

The main result obtained by Danckwerts, especially when absorption is accompanied by a chemical reaction, was a clear separation of the physicochemical parameters from the hydrodynamic ones. No explicit expressions have been, however, proposed for the renewal frequency s . While this problem will be examined later, for the moment various questions that can be raised concerning the two basic assumptions will be emphasized.

First, the renewed elements of liquid are considered solidlike, without a microhydrodynamic structure, even though it is difficult to visualize how solid bodies can replace one another. It is clear that these elements of liquid should be able to deform for such a replacement to occur.

Second, the renewal is actually a consequence of the hydrodynamics of turbulence. The question is whether one can improve the model by using a more complete hydrodynamic description so that the renewal can arise as a consequence of the model rather than being a supplementary assumption. An answer to the first question is given in Section IV,P and to the second in Section IV,T.

P. A MODIFIED DANCKWERTS THEORY

The main theoretical tool in the Danckwerts model is Higbie's penetration theory, which is used to predict the rate of absorption in the elements of liquid exchanged between the bulk and the interface. As already noted, the simple penetration theory involves a rigid structure of the elements of liquid. One can improve the model by considering that they have a microhydrodynamic structure. The representation of turbulence that follows implies a Lagrangian description for the elements of liquid brought at the interface and an Eulerian description of their microstructure. The velocity components in the microstructure are taken with respect to a frame of reference moving with the average velocity. Near a liquid interface it is reasonable to assume that the microstructure velocity component along the interface is almost independent of the distance y to the interface. Therefore, the convective diffusion equation valid for the microstructure has the form

$$\frac{\partial c}{\partial t} + u(x, t) \frac{\partial c}{\partial x} + v(x, t, y) \frac{\partial c}{\partial y} = D \frac{\partial^2 c}{\partial y^2} \quad (368)$$

The diffusion coefficient being very small, the depth of penetration by diffusion can be considered small compared with the thickness of the element of liquid. Therefore, the distribution of concentration in the element of liquid can be obtained from the solution of Eq. (368) for a semiinfinite liquid; hence for the initial and boundary conditions,

$$c = c_0 \quad \text{for } t = 0 \quad \text{and all } x \quad \text{and } y \quad (369a)$$

$$c = c_i \quad \text{for } y = 0 \quad \text{and all } x \quad \text{and } t \quad (369b)$$

$$c = c_0 \quad \text{for } y \rightarrow \infty \quad \text{and all } x \quad \text{and } t \quad (369c)$$

and

$$c = c_0 \quad \text{for } x = 0 \quad \text{and all } y \quad \text{and } t \quad (369d)$$

The similarity variable

$$\eta = y/\delta(x, t) \quad (370)$$

transforms Eq. (368) into

$$\frac{d^2c}{d\eta^2} + \alpha_1 \eta \frac{dc}{d\eta} = 0 \quad (371)$$

and

$$\frac{\partial \varepsilon}{\partial t} + u \frac{\partial \varepsilon}{\partial x} + 2 \frac{\partial u}{\partial x} \varepsilon = 2\alpha_1 D \quad (372)$$

where $\varepsilon \equiv \delta^2$ (not to be confused with the turbulent diffusivity) and α_1 ($\alpha_1 > 0$) is an arbitrary constant which is set equal to 2. The solution of Eq. (371) for the boundary conditions (369) has the form

$$\frac{c - c_o}{c_i - c_o} = 1 - \frac{2}{\pi^{1/2}} \int_0^{y/\delta} \exp(-\mu^2) d\mu \quad (373)$$

The rate of mass transfer is given by

$$N = -D \left(\frac{\partial c}{\partial y} \right)_{y=0} = \frac{2}{\pi^{1/2}} \frac{D}{\delta} (c_i - c_o) \quad (374)$$

and the mass transfer coefficient is

$$k = \frac{N}{(c_i - c_o)} = \frac{2}{\pi^{1/2}} \frac{D}{\delta} \quad (375)$$

Equations for the thickness δ of the diffusion boundary layer can be obtained by solving Eq. (372). Equations (369a) and (369b) are compatible with Eq. (373) only if

$$\delta = 0 \quad \text{for } t = 0 \quad \text{and all } x \quad (376a)$$

and

$$\delta = 0 \quad \text{for } x = 0 \quad \text{and all } t \quad (376b)$$

Two cases are examined in what follows. In the first, $u = u(t)$, and in the second, $u = u(x)$.

Let us first consider $u = u(t)$. The method of characteristics leads in this case to

$$\varepsilon - 4Dt = \phi \left[\int_0^t u(t) dt - x \right] \quad (377)$$

In order to satisfy both conditions (376), two cases must be considered. For

$$\int_0^t u(t) dt - x < 0, \quad \phi = 0 \quad (378)$$

and thus condition (376a) is satisfied, while for

$$\int_0^t u(t) dt - x > 0, \quad \phi \left[\int_0^t u(t) dt \right] = -4Dt \quad (379)$$

and condition (376b) is satisfied.

By defining a quantity τ by the expression

$$\int_0^\tau u(t) dt = \int_0^t u(t) dt - x \equiv x_1(t) - x \quad (380)$$

Equation (377) becomes

$$\varepsilon = 4Dt \quad \text{for } x > x_1 \quad (381a)$$

and

$$\varepsilon = 4D(t - \tau) \quad \text{for } x < x_1 \quad (381b)$$

and the mass transfer coefficient is therefore given by

$$k = \begin{cases} \left(\frac{D}{\pi(t - \tau)} \right)^{1/2} & \text{for } x < x_1 \end{cases} \quad (382a)$$

$$k = \begin{cases} \left(\frac{D}{\pi t} \right)^{1/2} & \text{for } x > x_1 \end{cases} \quad (382b)$$

Compared with the Higbie penetration theory, the main difference consists in the fact that both the spatial and temporal dependence of the concentration are taken into account. In other words, the elements of liquid are characterized not only by their time of contact Δ with the interface, but also by their dimension x_0 along the main flow direction. The average mass transfer coefficient should be, therefore, defined as

$$\bar{k} = \frac{1}{x_0 \Delta} \int_0^{x_0} \int_0^\Delta k dx dt \quad (383)$$

which, combined with Eqs. (382), leads to

$$\bar{k} = \frac{1}{x_0 \Delta} \left(\frac{D}{\pi} \right)^{1/2} \int_0^\Delta \left[\int_0^{x_0 + \gamma(x_1 - x_0)} \frac{dx}{(t - \tau)^{1/2}} + \gamma \int_{x_1}^{x_0} \frac{dx}{t^{1/2}} \right] dt \quad (384)$$

where

$$\gamma = \begin{cases} 1 & \text{for } x_1 < x_0 \\ 0 & \text{for } x_1 > x_0 \end{cases}$$

A statistical distribution can be employed with respect to x_0 and Δ . Denoting by $\psi(\Delta, x_0) d\Delta dx_0$ the number of states in $d\Delta$ and dx_0 , the average mass

transfer coefficient will be given by

$$\bar{k} = \frac{\int_0^\infty \int_0^\infty \bar{k}(\Delta, x_0) \psi(\Delta, x_0) d\Delta dx_0}{\int_0^\infty \int_0^\infty \psi(\Delta, x_0) d\Delta dx_0} \quad (385)$$

This provides an equation which has the same form as that obtained on the basis of the Higbie penetration theory:

$$\bar{k} = (Ds)^{1/2} \quad (386)$$

As in the Danckwerts equation, the frequency s does not depend on the diffusion coefficient. Unlike the Danckwerts equation, however, it results from both a spatial and temporal averaging.

Let us now assume that $u = u(x)$. The method of characteristics leads in this case to

$$\varepsilon u^2(x) - 4D \int_0^x u(x) dx = \phi \left[t - \int_0^x \frac{dx}{u(x)} \right] \quad (387)$$

In order to satisfy Eqs. (376b) and (376a), one must have

$$\phi = 0 \quad \text{for} \quad t - \int_0^x \frac{dx}{u(x)} > 0 \quad (388)$$

and

$$\phi \left[- \int_0^x \frac{dx}{u(x)} \right] = -4D \int_0^x u(x) dx \quad \text{for} \quad t - \int_0^x \frac{dx}{u(x)} < 0 \quad (389)$$

For obtaining the form of function ϕ in the latter equation, let us introduce the function

$$z = \int_0^x \frac{dx}{u(x)} \quad (390)$$

and consider that it is possible to express the integral $\int_0^x u(x) dx$ in the form

$$\int_0^x u(x) dx = F(z) \quad (391)$$

As a result, Eq. (389) can be written as

$$\phi(-z) = -4DF(z) \quad \text{for} \quad t - z < 0 \quad (392)$$

Consequently,

$$\delta^2 u^2(x) = 4D \{ F(z) - F(z - t) \} \quad \text{for} \quad z - t > 0 \quad (393a)$$

and

$$\delta^2 u^2(x) = 4D \int_0^x u(x) dx \quad \text{for} \quad z - t < 0 \quad (393b)$$

The mass transfer coefficient k is therefore given by

$$k = \begin{cases} \left(\frac{D}{\pi}\right)^{1/2} \frac{u(x)}{\{F(z) - F(z-t)\}^{1/2}} & \text{for } z-t > 0 \end{cases} \quad (394a)$$

$$k = \begin{cases} \left(\frac{D}{\pi}\right)^{1/2} \frac{u(x)}{\{\int_0^x u(x) dx\}^{1/2}} & \text{for } z-t < 0 \end{cases} \quad (394b)$$

and the average mass transfer coefficient can be written in the form

$$\begin{aligned} \bar{k} = & \frac{1}{x_0 \Delta} \left(\frac{D}{\pi}\right)^{1/2} \int_0^\Delta \left[\int_0^{x_0 + \gamma(x_1 - x_0)} \frac{u(x) dx}{\{\int_0^x u(x) dx\}^{1/2}} \right. \\ & \left. + \gamma \int_{x_1(t)}^{x_0} \frac{u(x) dx}{\{F(z) - F(z-t)\}^{1/2}} \right] dt \end{aligned} \quad (395)$$

where x_1 is defined by

$$\int_0^{x_1(t)} \frac{dx}{u(x)} = t \quad (396)$$

For the average with respect to an ensemble characterized by a statistical distribution of Δ and x_0 , one can use Eq. (385). An expression of the same form as Eq. (386) is thus obtained again. More complicated statistical distributions with respect to some parameters which characterize the velocity distribution are of particular interest for the following physical reasons. It is impossible to visualize in the Danckwerts model the manner in which the elements of liquid at the interface are replaced with elements from the bulk. In contrast, in the present model, one can explain the replacement by considering near the interface a succession of arriving and departing regions. Elements of liquid that arrive in one of the regions leave the interface in the two neighboring departing regions. This means that $u(x)$ is positive in one of the regions and negative in the neighboring two regions. Denoting by β a parameter in the expression of the velocity $u(x)$ which makes the latter positive or negative and by $\phi(\beta) d\beta$ the number of states in β , the average mass transfer coefficient can be defined as

$$\bar{k} = \int_{-\infty}^{+\infty} k\phi(\beta) d\beta / \int_{-\infty}^{+\infty} \phi(\beta) d\beta \quad (397)$$

However, the final information is again that resulting from the Danckwerts model:

$$\bar{k} = (Ds)^{1/2} \quad (398)$$

The conclusion is that, whatever model is used to represent the microhydrodynamic structure of the liquid elements, the assumption that $u = u(x, t)$ still

leads to the same result [Eq. (398)] for the mass transfer coefficient. While the present model constitutes a more realistic picture than that of Danckwerts, the information obtained is the same, namely, that the mass transfer coefficient is proportional to $D^{1/2}$. This general property of an entire class of models can be understood directly from Eq. (372). This equation clearly shows that whatever form is adopted for $u(x, t)$, including $u = 0$ as in the Higbie–Danckwerts approach,

$$\varepsilon \equiv \delta^2 \propto D \quad (399)$$

and hence

$$k \propto D^{1/2} \quad (400)$$

Denoting, for the simplicity of writing, the multiple average mass transfer coefficient also by k , dimensional considerations lead to

$$k \propto (Ds)^{1/2} \quad (401)$$

where s has the dimensions of a frequency.

Q. MASS TRANSFER IN A LIQUID FILM IN TURBULENT MOTION ALONG A VERTICAL WALL

In contrast to Section IV,M, where the turbulent diffusivity was employed to derive an expression for the mass transfer coefficient, in this section expression (401), which is based on a physical model, constitutes the starting point. Concerning the renewal frequency s , the following dimensional considerations can lead to useful expressions. The state of turbulence near the interface can be characterized by a characteristic velocity $u_o = (g\delta_f)^{1/2}$, the dynamic viscosity η , the surface tension σ , and the density ρ . Therefore

$$s = F_1(u_o, \eta, \sigma, \rho)$$

Dimensional analysis rearranges these physical quantities in the form of related dimensionless groups:

$$F_2(sv/u_o^2, s\sigma/u_o^3\rho) = 0 \quad (402)$$

Considering the effect of viscosity more important than that of surface tension, one obtains

$$s \propto u_o^2/\nu \quad (403)$$

while the opposite assumption leads to

$$s \propto u_o^3\rho/\sigma \quad (404)$$

Eliminating s between Eq. (401) and either Eq. (403) or Eq. (404), one obtains

$$k \propto u_o(D/\nu)^{1/2} \quad (405)$$

and

$$k \propto (D\rho/\sigma)^{1/2} u_o^{3/2} \quad (406)$$

Equations (405) and (406) coincide with Eqs. (354) and (355), derived on the basis of the turbulent diffusivity concept, and, of course, the expressions used in Section IV,M for u_o lead again to Eqs. (357) and (358).

R. MASS TRANSFER THROUGH THE FREE SURFACE OF A STIRRED LIQUID

As in Section IV,N, the state of motion near the interface can be characterized by the energy ξ dissipated per unit volume, the viscosity η , the surface tension σ , and the density ρ . Therefore

$$s = F_3(\xi, \nu, \sigma, \rho)$$

and dimensional analysis provides the dimensionless groups

$$F_4\left(\frac{s\sigma^{2/5}}{\rho^{1/5}\xi^{3/5}}, \frac{s\rho^{1/2}\nu^{1/2}}{\xi^{1/2}}\right) = 0 \quad (407)$$

When one considers the effect of surface tension more important,

$$s \propto (\xi/\rho)^{3/5}(\sigma/\rho)^{-2/5} \quad (408)$$

whereas when viscosity is assumed to play the main role,

$$s \propto (\xi/\rho\nu)^{1/2} \quad (409)$$

The expressions which are obtained by combining Eq. (401) with either Eq. (408) or Eq. (409), namely,

$$k \propto D^{1/2}(\xi/\rho)^{3/10}(\sigma/\rho)^{-2/10} \quad (410)$$

and [34]

$$k \propto D^{1/2}(\xi/\rho\nu)^{1/4} \quad (411)$$

coincide again with those derived on the basis of the turbulent diffusivity approach.

Compared with the more traditional theories based on turbulent diffusivity, the use of physical models enables a clearer understanding of the mechanism of turbulent transfer. A comparison of both theories shows that they are not contradictory and provide the same final results. Both start with transport equations that are valid in laminar flow. The more traditional theory involves

a time averaging of these equations. A number of average quantities are thus introduced upon which bears the entire difficulty of the problem. Expressions are obtained for these average quantities by using analogies with the kinetic theory of gases as well as dimensional considerations. In the other kind of theory, a model is used and the averaging is performed later on expressions obtained for the mass flux on the basis of the model. Dimensional considerations provide information about the hydrodynamic parameters, such as the renewal frequency s .

S. ROLL CELL MODELS FOR TURBULENT MASS TRANSFER

In the renewal models one assumes that elements of liquid are continuously renewed between the bulk and the interface, but no details concerning the hydrodynamics of renewal are provided. A possible explanation of the renewal process by means of some hydrodynamic rotating structures superposed on the main translatory motion was suggested by Fortescue and Pearson [95] for turbulent flow and by Ruckenstein [96] for interfacial turbulence and turbulent flow. Fortescue and Pearson [95] use a numerical procedure to solve the convective diffusion equation and the results are represented in terms of an equation which coincides with that provided by the renewal models. Ruckenstein [96] identifies two extreme cases and derives analytical expressions for these extreme cases. The physical justification of such a model is as follows: the velocity fluctuations impinge elements of liquid upon the interface. This generates motions in both directions along the interface. If the frequency at which the turbulent pulses impinge upon the interface is sufficiently large, a roll cell structure, as shown in Fig. 7, will form. As a result, an element of liquid has a translatory motion with the local average velocity of the liquid and a circulatory motion in the roll cell. That trains of pulses impinging on the interface lead to rotating structures could be

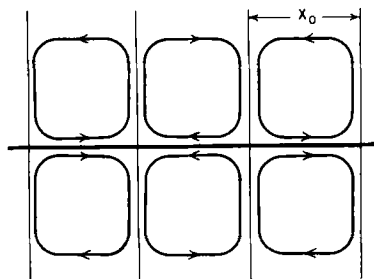


FIG. 7. The roll cell model.

visualized in a very simple experiment [97]. Into an open, transparent, prismatic cell filled with ethylene glycol, artificial pulses of ethylene glycol containing 5% water were injected near the liquid–air interface by means of a tube connected to a pump. A Schlieren arrangement allows one to see the rotating structures.

Before attempting a quantitative approach to the problem, it is instructive to examine the problem qualitatively [96]. An element of liquid which just reaches the interface covers along the interface a distance x_0 and then leaves the interface and moves along the inside paths of the roll cell. Two extreme situations can be considered: (1) the liquid elements maintain their identity without significant change of concentration during their motion along the inside paths of the roll cell, and (2) the elements of liquid are completely refreshed (acquire the concentration of the bulk) during their inside motion. In the first case, the mass transfer coefficient can be obtained from the Higbie equation by replacing the time t of contact between the phases by $t(\theta'/\theta)$, θ'/θ being the fraction of time which an element of liquid spends at the interface and exchanges mass with the other phase (θ is the circulation time and θ' is the time in which the elements of liquid cover the distance x_0 along the interface). Consequently, in this extreme case, the average mass transfer coefficient k is given by [96]

$$k = \left(\frac{4}{\pi}\right)^{1/2} \left(\frac{D}{t(\theta'/\theta)}\right)^{1/2} \equiv \left(\frac{4}{\pi}\right)^{1/2} \left(\frac{D_a}{t}\right)^{1/2} \quad (412)$$

where the apparent diffusion coefficient D_a is greater than D . In the second extreme case, the liquid elements that reach the interface are always fresh. In this case, which is similar to the renewal models, the average mass transfer coefficient depends on θ' and is independent of t . Consequently, the average mass transfer coefficient can be obtained from the Higbie expression by replacing the time t by θ' [96]:

$$k = (4/\pi)^{1/2} (D/\theta')^{1/2} \quad (413)$$

T. QUANTITATIVE FORMULATIONS OF THE ROLL CELL MODEL

The preceding qualitative considerations can be somewhat improved by choosing for the velocity distribution some expressions which are compatible with a cell model [98] even though they are not obtained as solutions to the equations of motion. Such expressions are, for instance,

$$u = u_0[1 + A \sin K(x - u_0 t) \cos(K_1 y)] \quad (414)$$

and

$$v = -(AKu_0/K_1) \cos K(x - u_0 t) \sin(K_1 y) \quad (415)$$

where u , the x component of the velocity, and v , the y component of the velocity, satisfy the continuity equation. These velocity components describe a two-dimensional roll cell structure propagating with the velocity u_0 in the direction of the main motion of the fluid (Fig. 8).

The convective diffusion equation which must be solved therefore has the form

$$\begin{aligned} \frac{\partial c}{\partial t} + u_0[1 + A \cos(K_1 y) \sin K(x - u_0 t)] \frac{\partial c}{\partial x} \\ - \frac{AKu_0}{K_1} \cos K(x - u_0 t) \sin(K_1 y) \frac{\partial c}{\partial y} = D \frac{\partial^2 c}{\partial y^2} \end{aligned} \quad (416)$$

Considering $A \ll 1$ and using the change of variables

$$X = Kx, \quad Y = K_1 y, \quad \text{and} \quad Z = K(x - u_0 t) \quad (417)$$

transforms Eq. (416) into

$$\frac{\partial c}{\partial X} - A \cos Z \sin Y \frac{\partial c}{\partial Y} = \frac{DK_1^2}{Ku_0} \frac{\partial^2 c}{\partial Y^2} \quad (418)$$

Introducing the dimensionless quantities:

$$\alpha = (AKu_0/DK_1^2) \cos Z \quad \text{and} \quad \beta = Ku_0/DK_1^2 \quad (419)$$

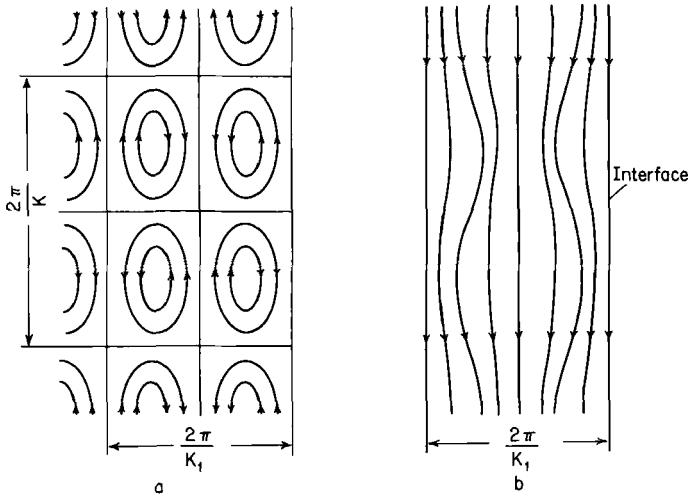


FIG. 8. Roll cell model: (a) stream lines in a frame of reference moving with the average liquid velocity; (b) stream lines in a fixed frame of reference.

Equation (418) can be rewritten as

$$\beta \frac{\partial c}{\partial X} - \alpha \frac{\partial c}{\partial Y} \sin Y = \frac{\partial^2 c}{\partial Y^2} \quad (420)$$

Equation (420) must be solved for the boundary conditions

$$\begin{aligned} c &= c_o & \text{for } X = 0 & \text{ and all } Y \\ c &= c_i & \text{for } Y = 0 & \text{ and all } X \\ c &= c_o & \text{for } Y \rightarrow \infty & \text{ and all } X \end{aligned} \quad (421)$$

The Carson transformation is used for the solution of Eq. (420):

$$V = p \int_0^\infty e^{-p\xi} \frac{c - c_o}{c_i - c_o} d\xi \quad (422)$$

Equation (420) becomes

$$V'' + \alpha V' \sin Y - \beta p V = 0 \quad (423)$$

and must be solved for the boundary conditions

$$V = 1 \quad \text{for } Y = 0 \quad (424a)$$

and

$$V = 0 \quad \text{for } Y = \infty \quad (424b)$$

Without the second term, Eq. (423) has a solution of the form $e^{-\mu Y}$. In order to take into account the second term, a solution of the form

$$V = e^{-\mu Y} \sum_{-\infty}^{\infty} V_n e^{inY} = \sum_{-\infty}^{+\infty} V_n e^{Y(in - \mu)} \quad (425)$$

is sought. Introducing this expansion in (423), there results

$$-\gamma_n V_{n-1} + V_n + \delta_n V_{n+1} = 0 \quad (n = 0, \pm 1, \pm 2, \dots) \quad (426)$$

where

$$\gamma_n = \frac{\alpha (n + i\mu) - 1}{2(n + i\mu)^2 + \beta p} \quad (427a)$$

and

$$\delta_n = \frac{\alpha (n + i\mu) + 1}{2(n + i\mu)^2 + \beta p} \quad (427b)$$

The constant μ is determined from the compatibility condition of the

homogeneous infinite system of Eqs. (426). Neglecting all the terms with $|n| > 2$, one obtains

$$\begin{aligned}
 V_{-2} + \delta_{-2}V_{-1} &= 0 \\
 -\gamma_{-1}V_{-2} + V_{-1} + \delta_{-1}V_0 &= 0 \\
 -\gamma_0V_{-1} + V_0 + \delta_0V_1 &= 0 \\
 -\gamma_1V_0 + V_1 + \delta_1V_2 &= 0 \\
 -\gamma_2V_1 + V_2 &= 0
 \end{aligned} \tag{428}$$

Equating to zero the determinant of this homogeneous system of equations, one obtains the following equation for μ :

$$\begin{aligned}
 (\beta p - \mu^2)[(\beta p - \mu^2 + 1)^2 + 4\mu^2][(\beta p - \mu^2 + 4)^2 + 16\mu^2] + \frac{\alpha^2}{2}\{(\beta p - \mu^2) \\
 [(2 - \mu^2)(\beta p - \mu^2 + 1)(\beta p - \mu^2 + 4) + 2\mu^2(9\beta p - 5\mu^2 + 10)] \\
 + \mu^2(1 + \mu^2 - \beta p)[(\beta p - \mu^2 + 4)^2 + 16\mu^2]\} \\
 + \frac{\alpha^4}{16}[(1 + \mu^2)(4 + \mu^2)(\beta p - \mu^2) + 2\mu^2(1 + \mu^2)(\beta p - \mu^2 - 4)] = 0
 \end{aligned} \tag{429}$$

For small values of p , Eq. (429) leads to

$$\mu = \pm \frac{(8 + \alpha^2)(\beta p)^{1/2}}{(64 - 16\alpha^2 + 3\alpha^4)^{1/2}} \tag{430}$$

Only the positive root is retained, since the negative one does not satisfy the boundary condition (424b).

For large values of p , an expansion of the form

$$\mu = a_1(\beta p)^{1/2} + a_0 + \frac{a_{-1}}{(\beta p)^{1/2}} + \dots \tag{431}$$

is sought to obtain

$$a_1 = 1, \quad a_0 = 0, \quad a_{-1} = \frac{4\alpha^2(16 - \alpha^2)}{3\alpha^4 - 64\alpha^2 + 1024} \tag{432}$$

Since only the mass flux at the free interface is of interest, only an expression for this quantity is established. For $V'_{Y=0}$, Eq. (425) gives

$$V'_{Y=0} = \sum_{-\infty}^{+\infty} (in - \mu)V_n = i \sum_{-\infty}^{+\infty} nV_n - \mu \sum_{-\infty}^{+\infty} V_n \tag{433}$$

The boundary condition (424a) leads to

$$\sum_{-\infty}^{+\infty} V_n = 1 \quad (434)$$

and, consequently,

$$V'_{Y=0} = i \sum_{-\infty}^{+\infty} n V_n - \mu \quad (435)$$

Solving the system of Eqs. (428) and (434), one obtains

$$V_0 \left[1 + \frac{\delta_{-1}(\delta_{-2} - 1)}{1 + \gamma_{-1}\delta_{-2}} + \frac{\gamma_1(\gamma_2 + 1)}{1 + \delta_1\gamma_2} \right] = 1 \quad (436a)$$

$$V_1 = \frac{\gamma_1 V_0}{1 + \delta_1\gamma_2} \quad (436b)$$

$$V_2 = \gamma_2 V_1 \quad (436c)$$

$$V_{-1} = V_1^* \quad (436d)$$

$$V_{-2} = V_2^* \quad (436e)$$

where the quantities marked by asterisks are the corresponding complex conjugate ones. For $p \rightarrow 0$,

$$V'_{Y=0} = - \frac{(8 + 8\alpha + 3\alpha^2)(\beta p)^{1/2}}{(64 - 16\alpha^2 + 3\alpha^4)^{1/2}} \quad (437)$$

and for $p \rightarrow \infty$,

$$V'_{Y=0} = - \left[(\beta p)^{1/2} + \frac{B}{(\beta p)^{1/2}} \right] \quad (438)$$

where

$$B = \frac{4\alpha[(1024 - 64\alpha^2 + 3\alpha^4)(64 + 32\alpha + 8\alpha^2 + \alpha^3) + 24\alpha^4(16 - \alpha^2)]}{(32 + \alpha^2)(32 + 16\alpha + 3\alpha^2)(1024 - 64\alpha^2 - 3\alpha^4)} \quad (439)$$

For the mass flux, defined by

$$N = -D \left(\frac{\partial c}{\partial y} \right)_{y=0} \quad (440)$$

one thus obtains

$$N = \left(\frac{Du_0}{\pi x} \right)^{1/2} \frac{(8 + 8\alpha + 3\alpha^2)(c_i - c_0)}{(64 - 16\alpha^2 + 3\alpha^4)^{1/2}} \equiv \left(\frac{Du_0}{\pi x} \right)^{1/2} \psi(x)(c_i - c_0) \quad (441)$$

for large values of x by using the expression of V valid for small values of p and

$$N = \left(\frac{Du_o}{\pi x} \right)^{1/2} \left(1 + \frac{2B}{\beta} Kx \right) (c_i - c_o) \quad (442)$$

for small values of x by using the expression of V valid for large values of p .

One can show that the preceding calculations, in which only five terms of the expansion (425) were retained, are valid for $|\alpha| \leq 2$. In order to increase the range of validity, additional calculations have been carried out in which nine terms were retained. In this case, one obtains for $|\alpha| \leq 4$ and for large values of x

$$\begin{aligned} N &= \left(\frac{Du_o}{\pi x} \right)^{1/2} \frac{[1 + \alpha + (7\alpha^2/16) + (5\alpha^3/48) + (5\alpha^4/384)](c_i - c_o)}{[1 - (\alpha^2/8) + \frac{7}{3}(\alpha/4)^4 - \frac{29}{9}(\alpha/4)^6(1 - (\alpha^2/16))]^{1/2}} \\ &\equiv \left(\frac{Du_o}{\pi x} \right)^{1/2} \psi(x)(c_i - c_o) \end{aligned} \quad (443)$$

The quantity ψ represents the amplification of the flux at large distances ($x \rightarrow \infty$) with respect to the one provided by the traditional penetration theory. The average amplification factor for large values of x , defined by

$$\bar{\psi} = \frac{1}{2\pi} \int_0^{2\pi} \psi dZ \quad (444)$$

is plotted in Fig. 9 as a function of the parameter

$$\alpha_o = AKu_o/DK_1^2 \quad (445)$$

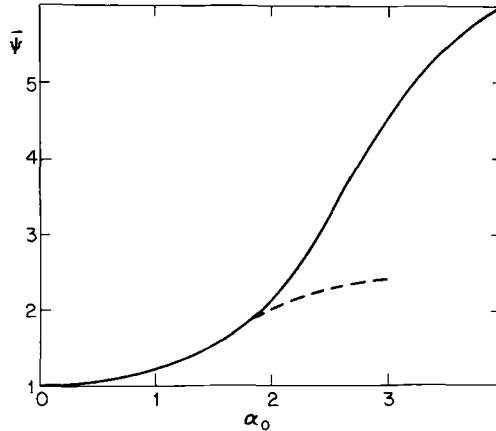


FIG. 9. Amplification factor $\bar{\psi}$ versus α_o . The solid line represents the results of calculations carried out with nine terms in the series expansion; the broken line with five terms in the series expansion.

Consequently, a roll cell structure superposed over an average motion can lead to a large increase in the rate of mass transfer compared to the one predicted by the penetration theory. The mass transfer takes place in this case as if an apparent constant (independent of time and position) diffusion coefficient, larger than the molecular one, is acting. The average amplification factor $\bar{\psi}$ depends only on α_0 and increases with this parameter. One can consider α_0 as the product of a Peclet number u_0/DK_1 multiplied by a cell number AK/K_1 , which contains the geometrical characteristics of the roll cell and its circulation intensity. The average amplification factor increases with the wave number of the cell in the x direction and decreases when the molecular diffusion coefficient and the wave number of the cell in the y direction become larger.

The preceding calculations are, however, valid only if $\alpha_0 < 4$. It is instructive, for reasons which will soon become clear, to consider the case in which α_0 is very large. For the sake of simplicity let us consider that α_0 is large because K_1 is very small and hence that $K_1 y$ is also small. In this case, one can write that $\sin K_1 y \approx K_1 y$ and Eq. (420) becomes

$$\beta \frac{\partial c}{\partial X} - \alpha Y \frac{\partial c}{\partial Y} = \frac{\partial^2 c}{\partial Y^2} \quad (446)$$

Equation (446) can be solved by means of the similarity transformation

$$c = c(\eta), \quad \eta = Y/\Delta(X) \quad (447)$$

Introducing in Eq. (446), one obtains

$$-2 \frac{dc}{d\eta} \left[\frac{\beta}{4} \frac{\partial \Delta^2}{\partial X} + \frac{\alpha \Delta^2}{2} \right] = \frac{d^2 c}{d\eta^2} \quad (448)$$

and since the concentration c is a function only of η ,

$$\frac{\beta}{4} \frac{\partial \Delta^2}{\partial X} + \frac{\alpha \Delta^2}{2} = \text{const} \quad (449)$$

Selecting the constant equal to unity, we have to solve equation

$$\frac{d^2 c}{d\eta^2} + 2\eta \frac{dc}{d\eta} = 0 \quad (450)$$

for the boundary conditions (421). One obtains

$$\frac{c - c_0}{c_i - c_0} = 1 - \frac{2}{\pi^{1/2}} \int_0^{\eta/\Delta} e^{-\mu^2} d\mu \quad (451)$$

and

$$\Delta^2 = \frac{2}{\alpha} \left[1 - \exp\left(-\frac{2\alpha}{\beta} Kx\right) \right] \quad (452)$$

Therefore

$$N = \frac{2DK_1}{\Delta\pi^{1/2}}(c_i - c_o) \equiv k(c_i - c_o) \quad (453)$$

which, for sufficiently large values of Kx , leads to

$$k = \begin{cases} \left(\frac{2ADu_o K}{\pi} \cos Z \right)^{1/2} (c_i - c_o) & \text{if } \alpha > 0 (\cos Z > 0) \\ 0 & \text{if } \alpha < 0 \end{cases} \quad (454)$$

Consequently, the average value of k with respect to time is given by the expression

$$\bar{k} = 0.293(DAKu_o)^{1/2}(c_i - c_o) \quad (455)$$

which shows that \bar{k} is proportional to $D^{1/2}$. Since the factor AKu_o is independent of x and has the dimensions of a frequency, Eq. (455) has the same structure as the expression derived on the basis of the renewal models. In the present treatment, the renewal is, however, a result of the velocity distribution and not a supplementary assumption as in the renewal models. In the case of turbulent flow, Eq. (455) can be completed by means of dimensional considerations similar to those already employed in the previous sections. The final results are, of course, the same: Eqs. (405) and (406). Equation (412) and its somewhat improved counterpart Eq. (443) are, however, new; some of their applications are discussed in the next section in connection with interfacial turbulence. For different derivations of expressions similar to (455) see references [96,99].

U. INFLUENCE OF THE MARANGONI EFFECT ON THE MASS TRANSFER BETWEEN TWO PHASES

The Marangoni effect is a result of the tendency of an interface to relax into a state of minimum free energy through the expansion of the regions of low interfacial tension and the contraction of those with a high one. The surface tension gradient generates a shear stress which affects the motions in the vicinity of the interface and therefore the mass transfer between phases. In the laminar case, the velocity generated by the Marangoni effect is important only for small values of the Reynolds number, as demonstrated concerning either the effect of the surface active agents on the mass transfer [5] or the effect of a surface tension gradient (caused by the mass transfer between phases) in rectification and extraction [100]. While interfacial turbulence constitutes the main concern of this section, it is instructive to examine first the effect of the surface tension gradient on the mass transfer between a bubble and a liquid at low Reynolds numbers, since this simpler problem sheds light on some of the

relevant physicochemical parameters [100]. Consider therefore a bubble of radius R rising with a velocity U . Internal circulation is set up as shown in Fig. 10. As a result of mass transfer between bubbles and liquid, a surface tension gradient will be set up. This surface tension gradient produces displacements in the interface in the direction of increasing surface tension. Depending on the direction of the mass transfer or, in distillation, on the type of system studied, we have either (a) $\sigma_1 > \sigma_2$ or (b) $\sigma_1 < \sigma_2$. In case (a), where $\partial\sigma/\partial z > 0$, the Marangoni effect reduces the internal circulation and the velocity of bubble rise and hence reduces the mass transfer coefficient. In case (b), where $\partial\sigma/\partial z < 0$, the Marangoni effect increases the internal circulation and the velocity of bubble rise and therefore increases the mass transfer coefficient. Consequently, the direction of the mass transfer affects the value of the mass transfer coefficient. This problem differs from those treated by Hadamard [38] and Levich [5] only with respect to one boundary condition, namely, that involving the shear stress generated by the Marangoni effect:

$$\eta \left(\frac{1}{R} \frac{\partial v_r}{\partial \theta} + \frac{\partial v_\theta}{\partial r} - \frac{v_\theta}{R} \right) + \frac{1}{R} \frac{\partial \sigma}{\partial \theta} = \eta' \left(\frac{1}{R} \frac{\partial v'_r}{\partial \theta} + \frac{\partial v'_\theta}{\partial r} - \frac{v'_\theta}{R} \right) \quad \text{for } r = R \quad (456)$$

Here the superscript prime symbol refers to the dispersed phase, η is the viscosity, v_r and v_θ the radial and tangential velocity components, θ and r are the polar coordinates, and σ is the surface tension. In the case under consideration,

$$-\frac{1}{R} \frac{\partial \sigma}{\partial \theta} = \frac{d\sigma}{dz} \sin \theta \quad (457)$$

The calculations lead to

$$U = \frac{2}{3} \frac{R^2 g}{\eta} (\rho - \rho') \frac{\eta + \eta'}{2\eta + 3\eta'} - \frac{2}{3} \frac{R}{2\eta + 3\eta'} \frac{d\sigma}{dz} \quad (458)$$

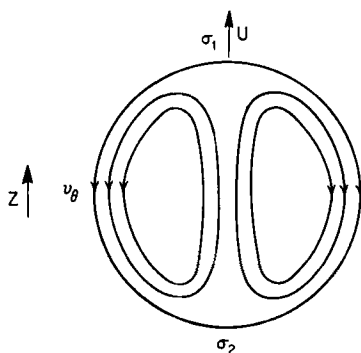


FIG. 10. Circulation patterns in a bubble for flows with low Reynolds numbers.

and

$$u_o = \frac{1}{3} \frac{R^2 g}{2\eta + 3\eta'} (\rho - \rho') - \frac{R}{2\eta + 3\eta'} \frac{d\sigma}{dz} \quad (459)$$

u_o being the value of v_θ for $r = R$ and $\theta = \pi/2$, ρ the density, and g the gravitational acceleration.

For the mass transfer coefficient, one can use the expression obtained on the basis of the algebraic method [Eq. (137)]:

$$0.849 \frac{u_o}{U} \text{Sh}^{-2} + 0.662 \left(\frac{3}{2} - 2 \frac{u_o}{U} \right) \text{Sh}^{-3} = \text{Pe}^{-1} \quad (460)$$

Equations (460), (458), and (459) show that the sign of $d\sigma/dz$, hence the direction of the mass transfer or in distillation the type of the system, influences the value of the transfer coefficient, which is larger if the transfer leads to a decrease of the surface tension at the interface with z .

The effect of the surface tension gradient on mass transfer is particularly important when it induces a spontaneous agitation near the interface known as interfacial turbulence. The occurrence of turbulence in the vicinity of the interface between two phases has been explained by Sternling and Scriven [101] as a result of a hydrodynamic instability. They have determined the conditions under which small perturbations are amplified or damped by the Marangoni effect. Any perturbation generates convection currents which in turn cause concentration changes along the interface and, hence, local changes in the interfacial tension gradient. Depending on the manner in which the interfacial tension is affected by concentration, the motions generated by the Marangoni effect can amplify or damp those caused by the perturbations. In the first situation, a spontaneous agitation will be generated in the vicinity of the interface, whereas in the second, no spontaneous agitation will occur. For this reason, some systems can be stable with the solute transfer in one direction and unstable with the transfer in the opposite direction. This suggests that there exists a directional dependence of the mass transfer coefficient. Such a directional dependence was observed experimentally by Grassman and Anderes [102], who introduced into a boiling binary liquid vapor bubbles of one or another of the components, and by Olander and Reddy [103], who have studied the nitric acid transfer from an aqueous medium to an organic one and vice versa in a stirred tank. A dependence of the mass transfer on the driving force was also obtained by Sawistowski and Goltz [104], by Maroudas and Sawistowski [105], and by Bakker *et al.* [106].

In the experiments mentioned only physical phenomena occur. Sherwood and Wei [107], investigating the mechanism of the extraction process of acetic acid from an organic solvent in a basic aqueous solution, found that the

transfer rate is several times higher than the value resulting from the conventional theories of mass transfer accompanied by a chemical reaction. Visual observations have revealed a certain interfacial activity to which the disagreement between the traditional theories and experiment has been attributed. They also noted that the presence of a chemical reaction greatly increases the surface activity and the rate of the process.

In many of these experiments, interfacial turbulence was the obvious visible cause of the unusual features of the rate of mass transfer. There are, however, experimental results in which no interfacial activity was observed. Brian *et al.* [108] have drawn attention to the severe disagreement existing between the penetration theory and data for the absorption of carbon dioxide in monoethanolamine. They have performed experiments on the absorption of CO_2 with simultaneous desorption of propylene in a short, wetted wall column. The desorption of propylene without absorption of CO_2 agrees closely with the predictions of the penetration theory. If, however, both processes take place simultaneously, the rate of desorption is greatly increased. This enhancement must be linked to a hydrodynamic effect induced by the absorption of CO_2 and the only one which can occur appears to be the interfacial turbulence caused by the Marangoni effect. No interfacial activity was observed because of the small scale and small intensity of the induced turbulence.

Ruckenstein and Berbente [109] have extended the approach of Sternling and Scriven to the case in which a chemical reaction occurs to demonstrate that the criteria of instability in this case differ essentially from those valid for the case of diffusion without chemical reaction. Even small values of the reaction rate constant essentially change the conditions under which instability occurs.

Interfacial turbulence leads to the formation of cellular (or other type) structures of the interface. They have been studied by optical methods, using a Schlieren technique, by Kroepelin and Newmann [110], by Linde [111], and by Orell and Westwater [112, 113]. A recent book contains contributions largely dedicated to theoretical studies regarding the instability caused by the Marangoni effect [114]. The roll cells can also be simulated experimentally by continuous feeding through a capillary of a liquid which has a lower surface tension over the interface of two liquids into which it dissolves. When several sources of Marangoni effect of this type are used, it is possible to simulate the present physical model, since a roll cell structure organizes. In Fig. 11 one photograph obtained through a Schlieren technique by Suciu and Smighelschi [96] is given. The upper layer is paraffin oil and the lower layer is ethylene glycol. At the interface, ethylacetate is fed continuously through two glass capillaries. This photograph shows that in this particular case the thickness of the roll cell is approximately equal to x_0 . If one assumes that the

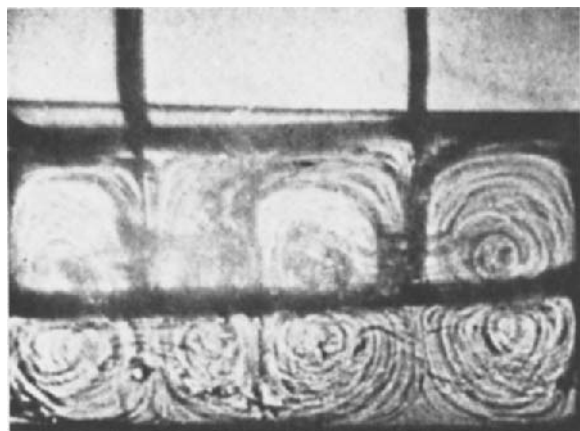


FIG. 11. Simulation of the physical model by means of two sources of Marangoni effect generation. The upper phase is paraffin oil and the lower phase is ethylene glycol. Through the two capillaries (the two vertical black streaks) ethyl acetate is fed.

circulation velocity is the same along the contour of the roll cell, the ratio θ'/θ [see Eq. (412)] can be evaluated as being of the order of $\frac{1}{4}$.

Some of these experiments can be interpreted by means of Eq. (412) or equivalently by its more theoretical version (443). Indeed, Bakker *et al.* [106] have investigated the transfer of acetic acid or acetone between cocurrent streams of water and an organic phase or between carbon tetrachloride and water. The penetration theory could be used to represent the data if the diffusion coefficient were replaced by an apparent diffusion coefficient about four times larger. This means that in their case, the ratio θ'/θ was $\frac{1}{4}$. The experiments of Brian *et al.* [108] could also be represented by a similar expression but with a lower value of θ'/θ .

Now some expressions for the quantities involved in the mass transfer coefficient will be obtained [96]. The velocity at the interface is evaluated by using the following two approximations: (1) The x velocity component, although dependent on x , is replaced by its average U over the path of length x_0 . (2) The velocity distribution in the vicinity of the interface is approximated for each path of length x_0 by that valid for the motion of a plate moving with the velocity U over a semiinfinite liquid whose velocity is U_1 .

The Marangoni effect generates a stress along the interface. Therefore the equilibrium of forces in the x direction leads to

$$\tau_1 - \tau_2 = -d\sigma/dx \quad (461)$$

where τ_1 and τ_2 are the shear stresses on the two sides of the interface. Since we replace the x velocity component at the interface by its average value over the

path length x_0 , it is appropriate to replace Eq. (461) also by its average over x_0 :

$$\int_0^{x_0} \tau_1 dx - \int_0^{x_0} \tau_2 dx = -\Delta\sigma \quad (462)$$

Here $\Delta\sigma$ represents the difference between the interfacial tension at the end and at the beginning of the path. When the refreshing of the elements of liquid is complete, $\Delta\sigma$ is equal to the difference between the interfacial tension at the equilibrium concentration at the interface and the interfacial tension between the liquid phases at their bulk concentrations. The problem of the boundary layer that develops when a solid planar surface moves continuously was treated by several authors. Tsou *et al.* [115] have derived the following expression for the local wall shear stress τ :

$$\tau = c_f \frac{1}{2} \rho U^2 \quad (463)$$

where if the liquid at infinite distance has zero velocity,

$$c_f \text{Re}^{1/2} = 0.88 \quad (\text{Re} = Ux/\nu) \quad (464)$$

One may note that the constant for the Blasius flow is 0.664 instead of 0.88. If the velocity at infinity $U_i \neq 0$, then

$$c_f \text{Re}^{1/2} = 2 \left(\frac{d(u/U)}{d[y(U/\nu x)^{1/2}]} \right)_{y=0} \equiv 2F \left(\frac{U_i}{U} \right) \quad (465)$$

A few values of F as a function of U_i/U are given in Table X. On the basis of the preceding equations, Eq. (462) can be rearranged as

$$2\rho_1 \nu_1^{1/2} U^{3/2} F_1 x_0^{1/2} + 2\rho_2 \nu_2^{1/2} U^{3/2} F_2 x_0^{1/2} = -\Delta\sigma \quad (466)$$

When the velocity at large distance is zero or sufficiently small compared to U , one obtains the equation

$$0.88(\rho_1 \nu_1^{1/2} + \rho_2 \nu_2^{1/2}) x_0^{1/2} U^{3/2} = -\Delta\sigma \quad (467)$$

which relates U to $\Delta\sigma$ and x_0 .

Some numerical calculations of the mass transfer coefficient are given in Table XI. They were performed for several values of x_0 on the basis of Eq. (413). The time θ' in that expression is given by $\theta' = x_0/U$. The values of $\Delta\sigma$ have been taken in the range considered in the experiments of Sawistvoski and Goltz [104]. The calculated values of the mass transfer coefficient are

TABLE X

U_i/U	0	0.62	1	1.78	∞
F	-0.44	-0.20	0	0.50	0.33

TABLE XI

$$v_1 = v_2 = 10^{-2} \text{ cm}^2/\text{sec}; \rho_1 = \rho_2 = 1 \text{ g/cm}^3; D = 10^{-5} \text{ cm}^2/\text{sec}$$

$\Delta\sigma$ (dynes/cm)	k (cm/sec)		
	$x_0 = 10^{-1} \text{ cm}$	$x_0 = 10^{-2} \text{ cm}$	$x_0 = 10^{-3} \text{ cm}$
1	3×10^{-2}	1.4×10^{-1}	0.64
5	5×10^{-2}	2.4×10^{-1}	1.1
10	6.4×10^{-2}	3×10^{-1}	1.4
20	8×10^{-2}	3.7×10^{-1}	1.7

of the same order as the experimental one if $x_0 = 10^{-1}$ to 10^{-2} cm. One may note that the dimensions of the cells observed experimentally [113] are in the same range.

In the cases in which a single liquid phase is involved, an additional expression relating x_0 to $\Delta\sigma$ can be obtained, on dimensional grounds. Let us consider a single liquid phase and rewrite Eq. (467) as

$$0.88\rho v^{1/2}x_0^{1/2}U^{3/2} = |\Delta\sigma| \quad (468)$$

Further, let us consider that x_0 depends on $\Delta\sigma$, ρ , and v and is independent of σ . Dimensional analysis leads therefore to the expression

$$x_0 \propto v^2/(|\Delta\sigma|/\rho) \quad (469)$$

Eliminating x_0 between Eqs. (468) and (469), one obtains

$$U \propto |\Delta\sigma|/\rho v \quad (470)$$

Consequently,

$$\theta' \propto v^3/(|\Delta\sigma|/\rho)^2 \quad (471)$$

and

$$k \propto (D/v)^{1/2}(|\Delta\sigma|/\rho v) \quad (472)$$

When the velocity at large distances is not negligible, Eq. (466) should constitute the starting point, and it is necessary to express F_1 and F_2 in terms of U_i/U for the two phases.

V. DETERMINISTIC APPROACH TO TURBULENT MASS TRANSFER

In this section we emphasize a parallelism between the Danckwerts statistical model and a deterministic representation of the turbulent mass transfer [116]. The starting point was the observation that an almost

periodical function can simulate turbulence. Let us consider, for instance, the function

$$u = B_1 \sin w_1 t + B_2 \sin w_2 t$$

in which the frequencies w_1 and w_2 are not commensurate with one another. In this case, the time dependence of u has some of the "disordered" features of the turbulent fluctuations. The preceding function, represented in its most simple form in Fig. 12, constitutes the most simple version of an almost periodical function, and, of course, other almost periodical functions might be more appropriate simulators of the turbulent process. A possible representation of the turbulent mass transfer may therefore be based on an almost periodical time and/or spatial dependence of the velocity. Let us consider, for instance, that in the roll cell model we have, instead of the periodical function $A \sin(Kx - u_0 t)$, an almost periodical function. The preceding established equations remain valid if α is replaced by an almost periodical function. The main difference arises when the average value is calculated, since in the almost periodical case there is no period for the time dependency of the velocity components. For this reason, the average must be defined in a different way, namely,

$$\bar{k} = \frac{1}{T} \int_0^T k dt \quad (T \rightarrow \infty)$$

Let us divide T in a large number of intervals; denote by $\psi(\theta) d\theta$ the number of intervals in $d\theta$; and consider that for each interval, there is a corresponding value $k(\theta)$. The preceding expression can therefore be written as

$$\bar{k} = \int_0^\infty k(\theta) \psi(\theta) d\theta / \int_0^\infty \psi(\theta) d\theta$$

thus acquiring the form of the equations used in the renewal models when residence time distributions are taken into account.

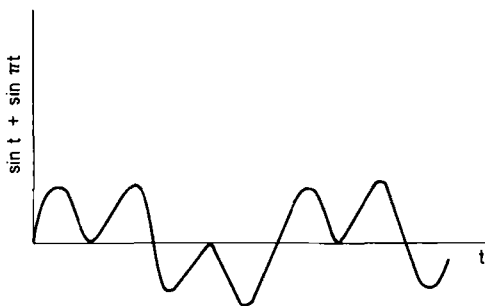


FIG. 12. $\sin t + \sin \pi t$ versus t .

V. Closing Remarks

The main message of this chapter is that simple procedures which avoid exact solutions of the transport equations as well as simple models based on the solutions of some simple transport equations are useful in obtaining information even in some relatively complex cases. The algebraic method, which was illustrated here with a large number of examples, replaces the convective diffusion equation by an algebraic expression. The constants which are thus introduced are determined from solutions available for simple asymptotic cases. The fact that the microstructure of the elements of liquid is characterized in the models used to represent turbulence by a length scale which is small in comparison with any characteristic dimension of the system ensures some universality to the model. Indeed, the same equation, borrowed from the laminar flow along a plate, can be applied to numerous situations. Finally, the new dimensional analysis proposed, which involves two kinds of time and length scales, also provides some meaning to the exponent of the Reynolds number in the expression of the Sherwood or Nusselt number.

Let us close by noting that starting with the papers of Saltzman [117] and Lorentz [118], the problem of turbulent transport has been amenable to analysis on the basis of the unsteady-state transport equations without any additional assumptions. While this extremely meaningful procedure is outside the scope of the present contribution, at least a few [117–125] from a very large number of references need mention.

References

1. Landau, L. D., and Lifshitz, E. M., "Fluid Mechanics." Pergamon, Oxford, 1959.
2. Kays, W. M., and Crawford, M. E., "Convective Heat and Mass Transfer," 2nd Ed. McGraw-Hill, New York, 1980.
3. Prandtl, L., *Verhand. Int. Math. Kongr., 3rd Heidelberg, 1904* p. 494 (1905).
4. Schlichting, H., "Boundary Layer Theory," 6th Ed. McGraw-Hill, New York, 1968.
5. Levich, V. G., "Physicochemical Hydrodynamics." Prentice Hall, New York, 1962.
6. Beard, D. W., and Walters, K., *Proc. Cambridge Philos. Soc.* **60**, 667 (1964).
7. White, J. L., and Metzner, A. B., *AIChE J.* **11**, 324 (1965).
8. Denn, M. M., *Chem. Eng. Sci.* **22**, 395 (1967).
9. Schowalter, W. R., "Mechanics of Non-Newtonian Fluids." Pergamon, Oxford, 1978.
10. Metzner, A. B., White, J. L., and Denn, M. M., *AIChE J.* **12**, 863 (1966).
11. James, D. F., and Acosta, A., *J. Fluid Mech.* **42**, 269 (1970).
12. Piret, E. L., James, W., and Stacey, W., *Ind. Eng. Chem.* **39**, 1098 (1947).
13. Ruckenstein, E., *Rev. Roum. Phys.* **7**, 153 (1962).
- 14a. Ruckenstein, E., *Chem. Eng. Sci.* **37**, 1505 (1982).
- 14b. Ruckenstein, E., in "Handbook of Heat and Mass Transfer" (N. P. Cheremisinoff, ed.), Vol. 1, p. 83. Gulf Publishing, Houston, 1986.

15. Ruckenstein, E., *AIChE J.* **26**, 830 (1980).
16. LeFevre, E. J., *Proc. Int. Congr. Appl. Mech.*, 9th **4**, 168 (1957).
17. Churchill, S. W., and Ozoe, H., *J. Heat Transfer, Trans. ASME Ser. C* **95**, 540 (1973).
18. Potter, O. E., *Chem. Eng. Sci.* **6**, 170 (1957).
19. Ruckenstein, E., and Rajagopalan, R., *Chem. Eng. Commun.* **4**, 15, (1980).
20. Blasius, H., *Z. Math. Phys.* **56**, 1 (1908).
21. Churchill, S. W., *AIChE J.* **23**, 10 (1977).
22. Acrivos, A., *Chem. Eng. Sci.* **21**, 343 (1966).
23. Sparrow, E. M., and Gregg, J. L., *J. Appl. Mech.* **26**, 133 (1959).
24. Lloyd, J. R., and Sparrow, E. M., *Int. J. Heat Mass Transfer* **13**, 434 (1970).
25. Gryzagoridis, J., *Int. J. Heat Mass Transfer* **18**, 911 (1975).
26. Szweczyk, A. A., *J. Heat Transfer* **86**, 501 (1964).
27. Leveque, M. A., *Ann. Mines* **13**, 201, 305, 381 (1928).
28. Astarita, G., "Mass Transfer with Chemical Reaction." Elsevier, Amsterdam, 1967.
29. Danckwerts, P. V., "Gas-Liquid Reactions." McGraw-Hill, New York, 1970.
30. Higbie, R., *Trans. AIChE* **31**, 365 (1935).
31. Danckwerts, P. V., *Ind. Eng. Chem.* **43**, 1468 (1951).
32. Kramers, H., and Beek, W. J., *Accad. Naz. Lincei, Fasci. Alta Technol. Chim V° Corso Estivo Chim., Varese* p. 25 (1960).
33. Toor, H. L., and Marchello, J. M., *AIChE J.* **4**, 97 (1958).
34. Ruckenstein, E., *Rev. Chim. (Bucharest)* **8**, 749 (1957); **9**, 689 (1958).
35. Chambré, P. L., and Young, J. D., *Phys. Fluids* **1**, 48 (1958).
36. Ruckenstein, E., and Rajagopalan, R., in "Recent Advances in the Engineering Analysis of Chemically Reacting Systems" (L. K. Doraiswamy, ed.), p. 1. Wiley, New Delhi, 1984.
37. Stewart, W. E., and Prober, R., *Int. J. Heat Mass Transfer* **5**, 1149 (1962).
38. Hadamard, J., *C. R. Acad. Sci. Paris* **152**, 1735 (1911).
39. Rybczynsky, W., *Bull. Acad. Sci. Cracow A-40* (1911).
40. Ruckenstein, E., *Chem. Eng. Sci.* **19**, 131 (1964).
41. Boussinesq, J., *Ann. Chim. Phys.* **29**, 364 (1913).
42. Frössling, N., *Lunds Univ. Arrsskr. F. F. AVD* **36**, 4 (1940).
43. Akselrud, G. A., *Zh. Fiz. Khim. SSSR* **24**, 1446 (1953).
44. Garney, F. H., and Keey, R. B., *Chem. Eng. Sci.* **9**, 119 (1958).
45. Pleskov, Y. V., and Filinovski, V. Y., "The Rotating Disc Electrode." Consultants Bureau, New York, 1976.
46. Cess, R. D., *J. Heat Transfer, Trans. ASME Ser. C* **83**, 274 (1961).
47. Meadley, C. K., and Rahman, M., *Can. J. Chem. Eng.* **52**, 552 (1974).
48. Murphree, E. V., *Ind. Eng. Chem.* **24**, 726 (1932).
49. Reichardt, H., *Z.A.M.M.* **31**, 208 (1951); Lin, C. S., Moulton, R. W., and Putnam, G. L., *Ind. Eng. Chem.* **45**, 636 (1953).
50. Vieth, W. R., Porter, J. H., and Sherwood, T. K., *Ind. Eng. Chem. Fundam.* **3**, 1 (1963).
51. Shapiro, M., and Laufer, G., *J. Colloid Interface Sci.* **99**, 256 (1984).
52. Zebel, G., *J. Colloid Interface Sci.* **27**, 294 (1968).
53. Jackson, J. D., "Classical Electrodynamics." Wiley, New York, 1975.
54. Shapiro, M., Laufer, G., and Gutfinger, C., *Atmos. Environ.* **17**, 447 (1983).
55. Frank-Kamenetsky, D. A., "Diffusion and Heat Transfer in Chemical Kinetics." Plenum, New York, 1969.
56. Harriot, P., and Hamilton, R. M., *Chem. Eng. Sci.* **20**, 1073 (1965).
57. Fage, A., and Townsend, H. C. H., *Proc. R. Soc. London Ser. A* **135**, 656 (1932).
58. Ruckenstein, E., *Chem. Eng. Sci.* **7**, 265 (1958); **18**, 233 (1963).
59. Hanrathy, T. J., *AIChE J.* **2**, 359 (1956).

60. Einstein, H. A., and Li, H., *Proc. ASCE, J. Eng. Mech. Div.* **82**, 1 (1956).
61. Black, Th. J., "Viscous Drag Reduction" (C. S. Wells, ed.), p. 383. Plenum, New York, 1969.
62. Kline, S. J., and Rundstadler, P. W., *J. Appl. Mech.* **26**, 166 (1959); Blakewell, Jr., H. P., and Lumley, J. L., *Phys. Fluids* **10**, 1880 (1967); Kline, S. J., Reynolds, W. D., Schraub, F. A., and Rundstadler, P. W., *J. Fluid Mech.* **30**, 741 (1967).
63. Pinczewski, W. V., and Sideman, S., *Chem. Eng. Sci.* **29**, 1969 (1974).
64. Corino, E. R., and Brodkey, R. S., *J. Fluid Mech.* **37**, 1 (1969).
65. Ruckenstein, E., *Stud. Cercetari Fiz. (Bucharest)* **9**, 190 (1958).
66. Friend, W. L., and Metzner, A. B., *AIChE J.* **4**, 393 (1958).
67. Ruckenstein, E., *Chem. Eng. Sci.* **27**, 947 (1972).
68. Ruckenstein, E., *Bul. Sci. Ser. Mat-Fiz., Acad R.P.R.* **6**, 449 (1954).
69. Calderbank, P. H., and Moo-Young, M. B., *Chem. Eng. Sci.* **16**, 39 (1961).
- 70a. Bratu, E. A., "Operations and Equipments in Chemical Engineering," Vol. I, 2nd Ed. Ed. Technica, Bucharest, 1969.
- 70b. Bratu, E. A., "Operations and Equipments in Chemical Engineering," Vol. II, 1st Ed. Ed. Technica, Bucharest, 1961.
71. Hickson, A. W., and Baum, I. S., *Ind. Eng. Chem.* **33**, 1433 (1941); **33**, 1478 (1941).
72. Yagi, S., and Wakao, N., *AIChE J.* **5**, 79 (1959).
73. Richardson, J. F., and Zaki, W. N., *Trans. Inst. Chem. Eng. (London)* **32**, 35 (1954).
74. Mickley, H. S., and Fairbanks, D. F., *AIChE J.* **1**, 374 (1955).
75. Davidson, J. F., and Harrison, D., "Fluidized Particles," Cambridge Univ. Press, London, 1963.
76. Teoreanu, I., *Rev. Chim. (Bucharest)* **11**, 691 (1960).
77. Ruckenstein, E., *Ind. Eng. Chem. Fundam.* **5**, 139 (1966).
78. Ruckenstein, E., *Rev. Phys.* **7**, 138 (1962).
79. Jackson, R., *Trans. Inst. Chem. Eng. (London)* **41**, 13 (1963).
80. Pigford, R. L., and Baron, Th., *Ind. Eng. Chem. Fundam.* **4**, 81 (1965).
81. Ruckenstein, E., *Chem. Eng. Sci.* **21**, 113 (1966).
82. Ruckenstein, E., and Smigelschi, O., *Trans. Inst. Chem. Eng. (London)* **43**, 334 (1965).
83. Kast, W., *Int. J. Heat Mass Transfer* **5**, 329 (1962); *Chem. Ing. Tech.* **35**, 785 (1963).
84. Sokolov, V. N., and Salamanin, A. D., *Zh. Prikl. Khim.* **35**, 1022 (1962).
85. Sokolov, V. N., and Bushkov, M. D., *Zh. Prikl. Khim.* **37**, 639 (1964).
86. Jakob, M., and Linke, W., *Phys. Z.* **36**, 367 (1935).
87. Jakob, M., and Fritz, W., *Forsch. Ver. Dtsch. Ing.* **2**, 435 (1931).
88. Ruckenstein, E., *Int. J. Heat Mass Transfer* **7**, 191 (1964).
89. Zuber, N., *Int. J. Heat Mass Transfer* **6**, 53 (1963).
90. Townsend, A. A., *J. Fluid Mech.* **11**, 97 (1961).
91. Richardson, P. D., *Chem. Eng. Sci.* **18**, 149 (1963).
92. Prandtl, L., *Nachr. Akad. Wiss. Göttingen* p. 6 (1945).
93. Spalding, D. B., *J. Fluid Mech.* **27**, 97 (1967).
94. Davies, J. T., Kilner, A. A., and Ratcliff, G. A., *Chem. Eng. Sci.* **19**, 583 (1964).
95. Fortescue, G. E., and Pearson, J. R. A., *Chem. Eng. Sci.* **22**, 1163 (1967).
96. Ruckenstein, E., *Int. J. Heat Mass Transfer* **11**, 1753 (1968).
97. Ruckenstein, E., and Suciu, D. G., *Chem. Eng. Sci.* **24**, 2395 (1969).
98. Ruckenstein, E., and Berbente, C., *Chem. Eng. Sci.* **25**, 475 (1970).
99. Stewart, W. E., Angelo, J. B., and Lightfoot, E. N., *AIChE J.* **16**, 771 (1970).
100. Ruckenstein, E., *Chem. Eng. Sci.* **19**, 505 (1964).
101. Sterling, C. V., and Scriven, L. E., *AIChE J.* **5**, 514 (1959).
102. Grassman, P., and Anderes, G., *Chem. Ing. Tech.* **31**, 154 (1959); Anderes, G., *Chem. Ing. Tech.* **34**, 597 (1962).

103. Olander, D. R., and Reddy, L. B., *Chem. Eng. Sci.* **19**, 63 (1964).
104. Sawistovski, H., and Goltz, G. E., *Trans. Inst. Chem. Eng. (London)* **41**, 174 (1963).
105. Maroudas, N. G., and Sawistovski, H., *Chem. Eng. Sci.* **19**, 919 (1964).
106. Bakker, C. A. P., Fentener van Vlissingen, F. H., and Beek, W. J., *Chem. Eng. Sci.* **22**, 1349 (1967).
107. Sherwood, T. K., and Wei, J. C., *Ind. Eng. Chem.* **49**, 1030 (1957).
108. Brian, P. L. T., Vivian, J. E., and Matiatos, D. C., *AIChE J.* **13**, 28 (1967).
109. Ruckenstein, E., and Berbente, C., *Chem. Eng. Sci.* **19**, 329 (1964).
110. Kroepelin, H., and Neumann, H. J., *Naturwissenschaften* **44**, 304 (1957).
111. Linde, H., *Colloid Zh.* **22**, 333 (1960).
112. Orell, A., and Westwater, J. W., *Chem. Eng. Sci.* **16**, 127 (1961).
113. Orell, A., and Westwater, J. W., *AIChE J.* **8**, 350 (1962).
114. Sorensen, J. S. (ed.), "Dynamics and Instability of Fluid Interfaces," Lecture Notes in Physics No. 105. Springer-Verlag, Berlin, 1979.
115. Tsou, F. K., Sparrow, E. M., and Goldstein, R. J., *Int. J. Heat Mass Transfer* **10**, 219 (1967).
116. Ruckenstein, E., *Chem. Eng. Sci.* **23**, 363 (1968); *Chem. Eng. J.* **2**, 1 (1971).
117. Saltzman, B., *J. Atmos. Sci.* **19**, 329 (1962).
118. Lorenz, E. N., *J. Atmos. Sci.* **20**, 130 (1963).
119. Reulle, D., and Takens, F., *Commun. Math. Phys.* **20**, 167 (1971).
120. Feigenbaum, M. J., *J. Stat. Phys.* **9**, 25 (1978); **21**, 669 (1979).
121. Feigenbaum, M. J., *Phys. Lett. A* **74**, 375 (1979).
122. Feigenbaum, M. J., *Commun. Math. Phys.* **77**, 65 (1980).
123. Eckmann, J. P., *Rev. Mod. Phys.* **53**, 643 (1981).
124. Lanford, O. E., *Annu. Rev. Fluid Mech.* **14**, 347 (1982).
125. Sparrow, C., "The Lorenz Equations: Bifurcation, Chaos, and Strange Attractions" (*Appl. Math. Sci.* **41**). Springer-Verlag, New York, 1982.

MATHEMATICAL MODELING OF PACKED BED REACTORS: NUMERICAL SOLUTIONS AND CONTROL MODEL DEVELOPMENT

Rohit Khanna and John H. Seinfeld

**Department of Chemical Engineering
California Institute of Technology
Pasadena, California 91125**

I. Introduction

Mathematical models of packed bed reactors are needed for the description of steady-state and dynamic behavior for process design, optimization, and control. Although insufficient detail can lead to a model incapable of accurately representing the reactor's response to changes in operating variables, excessive detail can lead to a model that is computationally impractical and/or contains parameters the values of which cannot accurately be determined from operating data. Clearly, the type of model and its level of complexity in representing the physical system depend on the use for which the model is being developed.

One approach to developing mathematical models is to begin with one that contains a relatively detailed description of the physical system and then to derive simpler models by identifying those elements that can be approximated while still retaining the essential behavior of the system (see, for example, Aris, 1978). This is the approach that we will follow here. Our particular interest will be in deriving mathematical models of packed bed reactors that are appropriate for use in designing control systems. Thus, we will be interested in models capable of simulating dynamic behavior.

This chapter presents an analysis of the development of dynamic models for packed bed reactors, with particular emphasis on models that can be used in control system design. Our method of attack will be first to formulate a comprehensive, relatively detailed packed bed reactor model; next to consider the techniques available for numerical solution of the model; then, utilizing

one such numerical solution, to examine simplifications of the model based on its underlying physics; and finally to study how the model may be reduced mathematically to one useful for control system design.

We have chosen to concentrate on a specific system throughout the chapter, the methanation reaction system. Thus, although our development is intended to be generally applicable to packed bed reactor modeling, all numerical results will be obtained for the methanation system. As a result, some approximations that we will find to apply in the methanation system may not in other reaction systems, and, where possible, we will point this out. The methanation system was chosen in part due to its industrial importance, to the existence of multiple reactions, and to its high exothermicity.

In Section II we offer some general introductory remarks on packed bed reactor models. The methanation system is given in Section III. The detailed reactor model is presented in Section IV. We then discuss approaches to numerical solution of the model in Section V, with a detailed exposition of one approach, orthogonal collocation. Solutions obtained using orthogonal collocation are presented in Section VI, and an additional numerical technique, orthogonal collocation on finite elements, is introduced in Section VII. Common physical assumptions made in packed bed reactor modeling are evaluated in Section VIII. Finally, the development of a simplified model appropriate for control system design is the subject of Sections IX and X.

II. Packed Bed Reactor Models

Mathematical models for packed bed reactors have over the years received a great deal of attention (see, for example, Smith, 1970; Hlavacek, 1970; Paris and Stevens, 1970; Froment, 1972; Karanth and Hughes, 1974; Carberry, 1976; Froment and Bischoff, 1979). By and large, detailed models of packed bed reactors were formulated at an early stage, but much of the early work focused on simplified models owing largely to the computational limitations associated with the comprehensive models. Recently, the problem of numerical solution of the models has received considerable attention, with a number of key studies having been carried out in this area. Advances over the past decade in computational techniques for the solution of partial differential equations such as those describing a packed bed catalytic reactor now allow one to explore the question of model complexity in detail.

Mathematical models of packed bed reactors can be classified into two broad categories: (1) one-phase, or *pseudohomogeneous*, models in which the reactor bed is approximated as a quasi-homogeneous medium and (2) two-phase, or *heterogeneous*, models in which the catalyst and fluid phases and the heat and mass transfer between phases are treated explicitly. Although the

heterogeneous models are more physically realistic, they have not been used as widely as pseudohomogeneous models for two reasons. First, the numerical solution of the heterogeneous model is considerably more difficult than for the pseudohomogeneous model, and, second, there are many situations for which the pseudohomogeneous model is a perfectly acceptable model. One object of this chapter will be to examine the validity of the pseudohomogeneous approach within the context of the methanation system considered.

A significant step in the numerical solution of packed bed reactor models was taken with the introduction of the method of orthogonal collocation to this class of problems (Finlayson, 1971). Although Finlayson showed the method to be much faster and more accurate than that based on finite differences and to be easily applicable to two-dimensional models with both radial temperature and concentration gradients, the finite difference technique remained the generally accepted procedure for packed bed reactor model solution until about 1977, when the analysis by Jutan *et al.* (1977) of a complex butane hydrogenolysis reactor demonstrated the real potential of the collocation procedure.

Since that time several studies have been published in which orthogonal collocation has been used as the core algorithm in numerically implementing a packed bed reactor model. Although we will not attempt to survey all the prior work done on numerical solution of packed bed reactor models, we will focus on orthogonal collocation and its variations. An object of this chapter is to present the basic techniques of orthogonal collocation and orthogonal collocation on finite elements as applied to packed bed reactor models, to discuss when each of the available approaches within this class might be useful, and to illustrate the methods with a detailed application to the methanation packed bed system.

III. Reaction System

To retain consistency throughout this presentation, we will consider a general nonadiabatic, packed bed reactor, as shown in Fig. 1, with a central axial thermal well and countercurrent flow of cooling fluid in an exterior jacket.¹ We focus on the methanation reaction since methanation is a reaction of industrial importance and since methanation exhibits many common difficulties such as high exothermicity and undesirable side reactions.

¹ Although this modeling description refers to a general, nonadiabatic packed bed reactor with an axial thermal well, the analysis easily extends to the consideration of adiabatic reactors and those without thermal wells. These are merely subsets of the more general case.

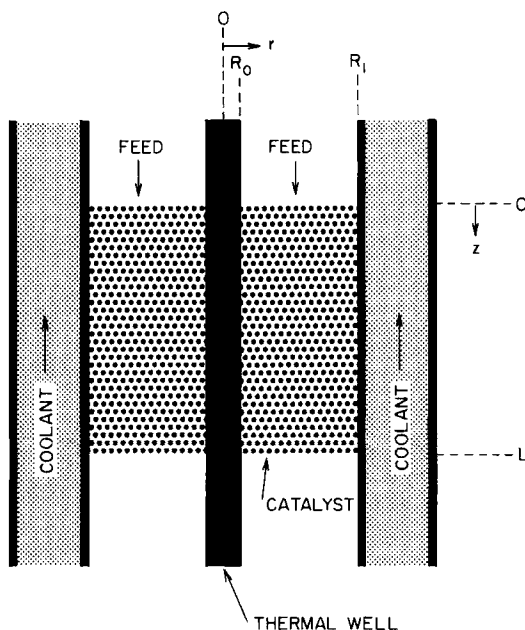


FIG. 1. Packed bed reactor configuration.

Moreover, we feel that it is instructive to use a concrete example for our development, but one that is easily extendable to other systems.

Methanation is one of a more general class of Fischer–Tropsch processes in which carbon monoxide and carbon dioxide are hydrogenated to form various light hydrocarbons and water. Although the primary reaction using a nickel on alumina catalyst is the methanation of carbon monoxide, appreciable side reactions can occur in the methanation system. The reactions in the methanation system are shown in Table I and include carbon dioxide

TABLE I
REACTIONS IN METHANATION SYSTEMS

System	Reaction
CO methanation	$\text{CO} + 3\text{H}_2 \rightleftharpoons \text{CH}_4 + \text{H}_2\text{O}$
CO ₂ methanation	$\text{CO}_2 + 4\text{H}_2 \rightleftharpoons \text{CH}_4 + 2\text{H}_2\text{O}$
Steam shift	$\text{CO} + \text{H}_2\text{O} \rightleftharpoons \text{CO}_2 + \text{H}_2$
Carbon deposition	$2\text{CO} \rightarrow \text{CO}_2 + \text{C}$
Nickel carbonyl formation	$\text{Ni} + 4\text{CO} \rightarrow \text{Ni}(\text{CO})_4$
Fischer–Tropsch	$n\text{CO} + 2n\text{H}_2 = (\text{CH}_2)_n + n\text{H}_2\text{O}$

methanation, steam shift, carbon deposition, nickel carbonyl formation, and other Fischer–Tropsch processes. By operating at $H_2:CO$ ratios of about 3:1 and temperatures above $200^\circ C$, most side reactions can be suppressed and only the CO methanation, CO_2 methanation, and steam-shift reactions should be significant. Of these three reactions, only two are independent, the CO methanation and steam-shift reactions.

A global rate expression for CO methanation over a nickel catalyst is given by Lee (1973) and Vatcha (1976). They report that a Langmuir–Hinshelwood rate law of the form

$$R_M = \frac{k_{0M} \exp(-E_{aM}/R_g T) P_{CO} (P_{H_2})^{0.5} (1 - v)}{1 + K_1 P_{H_2} + K_2 P_{CH_4}} \quad (1)$$

where

$$v = \frac{P_{CH_4} P_{H_2O}}{P_{CO} (P_{H_2})^3} \frac{1}{K_{pM}} \quad (2)$$

is superior to simple power law relationships. These reaction kinetics [Eqs. (1) and (2)] are based on the experimental data of Lee (1973) from a catalytic CSTR under conditions of ideal mixing with a Harshaw Ni–0104T nickel–Kieselguhr catalyst and extensions by Vatcha (1976) to include the factor $(1 - v)$ to reduce the rate to zero at equilibrium.

A complete analysis of the steam-shift reaction is provided by Moe (1962), who reports a rate expression of the form

$$R_S = k_{0S} \exp(-E_{aS}/R_g T) \left[x_{CO_2} x_{H_2} - \frac{x_{CO} x_{H_2O}}{K_{ps}} \right] \quad (3)$$

which should be appropriate over a wide range of operating conditions. The pressure dependence of the steam-shift reaction rate

$$R_{S(p)} = R_{S(1atm)} (f_1 + f_2 P) \quad (4)$$

is also derived from empirical results (Moe, 1962).

The equilibrium constants K_{pM} and K_{ps} are taken as functions of temperature as given by

$$\ln K_{pM} = K_{pM1} + K_{pM2}/T, \quad \ln K_{ps} = K_{ps1} + K_{ps2}/T \quad (5)$$

Vatcha reports that the rate expression given by Eq. (1) describes the global rate, thus allowing gas phase concentrations to be used in the reaction analysis. Global reaction kinetics will be used in the analysis to follow. Consequently, these kinetics must account for microscopic processes such as adsorption/desorption on the catalyst surface and intraparticle diffusion. Since most available kinetic information is based on steady-state data, a major

concern is the extent to which transient adsorption/desorption processes and intraparticle diffusion are accounted for in the rate expression. Although intraparticle diffusion can be shown to be generally insignificant in the reactor dynamics,² experimental efforts are needed to gain further information on the dynamics of adsorption/desorption processes.

IV. Formulation of the Mathematical Model

A two-dimensional, two-phase model of a packed bed reactor will now be developed. The heterogeneous packed bed reactor consisting of solid, generally nonspherical, catalyst particles and reacting gas is represented as two phases, with the assumption that each phase may be treated as a continuum insofar as changes occur smoothly and continuously throughout the bed. This continuum assumption for each phase is generally valid for most industrial reactors and should be valid under the conditions of this analysis (Carberry and Wendel, 1963; Hlavacek, 1970; Stewart, 1967), as long as the ratio of bed diameter to particle diameter and the axial aspect ratio are sufficiently large. The energy and mass fluxes can then be treated in a form based on continuum transport theory.

Many investigations have assumed that the difference between the catalyst and gas temperatures is negligible in tubular reactors for fast-flowing gas–solid systems. Industrial experience and experimental studies (Gould, 1969; Hoiberg *et al.*, 1971; Froment, 1974; Jutan *et al.*, 1977) have verified that there is often very little temperature difference (< 5 K) between the catalyst and gas at steady state. However, the two-phase representation may be necessary for simulating *dynamic situations* since considerable (> 10 K) differences can exist between gas and solid temperatures during transient conditions. The problems of measuring gas and solid temperatures separately can and often are in practice circumvented by using an internal thermocouple well, and for that reason we have included the possibility of a central thermal well in the general reactor configuration in Fig. 1.

Our analysis begins by incorporating all axial and radial dispersion processes, including axial conduction within the thermal well. Axial conduction in the outer wall is neglected on the basis of the first assumption presented later and on Bonvin's (1980) results showing that the conduction in the outer wall is most likely insignificant and can be neglected if axial dispersion in the bed is retained. Although radial gradients within the bed

² The time constants for the temperature and concentration profiles in the pellet to change are at least an order of magnitude faster than the time constants for the temperature and concentration profiles in the reactor bed.

must be included if there is cooling at the reactor wall, radial temperature gradients within the thermal well are neglected due to its comparatively small radius and high thermal conductivity.

We also account for density, heat capacity, and molecular weight variations due to temperature, pressure, and mole changes, along with temperature-induced variations in equilibrium constants, reaction rate constants, and heats of reaction. Axial variations of the fluid velocity arising from axial temperature changes and the change in the number of moles due to the reaction are accounted for by using the overall mass conservation or continuity equation.

The major assumptions underlying the original model are the following.

(1) The reactor wall temperature is equal to the cooling fluid temperature and is independent of length along the reactor (Carberry and Wendel, 1963; Jutan *et al.*, 1977; Smith, 1970). The validity of this assumption is generally based on the high thermal conductivity of the reactor wall and on the use of boiling fluids or high convection in the outer cooling shell.

(2) Gas properties are functions of temperature, pressure, and total moles as dictated by the ideal gas law. The assumption of ideal gas behavior will be accurate as long as the operating temperatures of the reactor are much higher than the critical temperatures of the component species and the pressures are relatively low and is in general valid for most gaseous reaction systems.

(3) There is no radial velocity, and the axial velocity across the radius of the packed bed is uniform. Schwartz and Smith (1953) found that the velocity across the diameter of a packed bed is not uniform for radial aspect ratios (tube-to-particle diameter) less than about 30, due to the significant effect of the increased void space near the wall where the particles are locally ordered. This result has been verified by Hoiberg *et al.* (1971) for a packed bed reactor with radial aspect ratio about 50. They considered a radial velocity variation suggested by experimental observations with a sharp peak about 15% greater than the mean fluid velocity situated close to the wall. Simulations using their model showed results virtually identical to those obtained with a uniform velocity profile.³

(4) The physical properties of the solid catalyst and thermal well are taken as constant, since the conditions within the reactor introduce only minor

³ Preliminary residence time distribution studies should be conducted on the reactor to test this assumption. Although in many cases it may be desirable to increase the radial aspect ratio (possibly by crushing the catalyst), this may be difficult with highly exothermic solid-catalyzed reactions that can lead to excessive temperature excursions near the center of the bed. Carberry (1976) recommends reducing the radial aspect ratio to minimize these temperature gradients. If the velocity profile in the reactor is significantly nonuniform, the mathematical model developed here allows predictive equations such as those by Fahien and Stankovic (1979) to be easily incorporated.

variations in these parameters, and the heats of reaction and gas heat capacities are taken as linear functions of temperature.

(5) Hlavacek (1970) has shown that radiation between the solid catalyst and gas can significantly affect the temperature dynamics in packed bed systems operating in excess of 673 K. Since most packed bed systems usually operate well below these conditions, radiation terms are not explicitly included in the model. However, their effect can to some degree be accounted for in the overall heat transfer coefficients.⁴

A complete description of the reactor bed involves the six differential equations that describe the catalyst, gas, and thermal well temperatures, CO and CO₂ concentrations, and gas velocity. These are the continuity equation, three energy balances, and two component mass balances. The following equations are written in dimensional quantities and are general for packed bed analyses. Systems without a thermal well can be treated simply by letting h_{ts} , h_{tg} , and R_0 equal zero and by eliminating the thermal well energy equation. Adiabatic conditions are simulated by setting h_{ws} and h_{wg} equal to zero.

Total Mass Conservation (Continuity)

$$\frac{\partial \rho_g}{\partial t} + \frac{\partial(\rho_g u_g)}{\partial z} = 0 \quad (z = 0, \quad \rho_g u_g = \rho_{g0} u_{g0}) \quad (6)$$

Energy Balance for the Gas

The energy equation for an ideal gas neglecting viscous heating is (Bird *et al.*, 1960)

$$\rho_g c_{p_g} \frac{DT}{Dt} = -\nabla \cdot q + \frac{DP}{Dt} + Q \quad (7)$$

Using $DP/Dt = v_z \partial P / \partial z$ and Fourier's law, we obtain

$$\rho_g c_{p_g} \frac{DT}{Dt} = \nabla \cdot k \nabla T + v_z \frac{\partial P}{\partial z} + Q \quad (8)$$

Let us estimate the relative importance of the term $v_z \partial P / \partial z$ as compared with its counterpart $\rho_g c_{p_g} v_z \partial T / \partial z$:

$$\frac{v_z (\partial p / \partial z)}{\rho_g c_{p_g} v_z (\partial T / \partial z)} \approx \frac{\Delta P}{\rho_g c_{p_g} \Delta T} \quad (9)$$

where ΔP is the pressure drop across the bed and ΔT is a typical temperature rise. Here ΔP can be estimated from the Ergun equation (Bird *et al.*, 1960)

⁴ But not entirely since radiation effects are nonlinearly related to temperature.

for the conditions we will study subsequently as 0.023 atm for a bed of length 30 cm, void fraction of 0.57, axial gas velocity of 75 cm/sec, inlet temperature of 573 K, and inlet pressure of 10 atm. The ratio defined by Eq. (9) is then about 0.02 for temperature gradients of 50 K. Under such conditions, the convective derivative of the pressure [in Eq. (8)] can be neglected and we do so henceforth:

$$\rho_g c_{p_g} \frac{DT}{Dt} = \nabla \cdot k \nabla T + Q \quad (10)$$

Then for the reactor bed after assuming k_{zg} and k_{rg} constant,

$$\varepsilon \rho_g c_{p_g} \frac{\partial T_g}{\partial t} = -\varepsilon \rho_g u_g c_{p_g} \frac{\partial T_g}{\partial z} + k_{zg} \frac{\partial^2 T_g}{\partial z^2} - \frac{U_{sg}(T_g - T_s)}{V_b} + \frac{k_{rg}}{r} \frac{\partial}{\partial r} \left[r \frac{\partial T_g}{\partial r} \right] \quad (11)$$

with

$$r = R_0, \quad k_{rg} \frac{\partial T_g}{\partial r} = h_{tg}(T_g - T_l)$$

$$r = R_1, \quad -k_{rg} \frac{\partial T_g}{\partial r} = h_{wg}(T_g - T_w)$$

$$z = 0, \quad k_{zg} \frac{\partial T_g}{\partial z} = h_{sg}(T_g - T_s) - u_g c_{p_g} \rho_g \varepsilon (T_0 - T_g)$$

$$z = L, \quad -k_{zg} \frac{\partial T_g}{\partial z} = h_{sg}(T_g - T_s)$$

Note that the convective term in the outlet boundary condition is generally assumed negligible (Hoiberg *et al.*, 1971). This assumption is used throughout the ensuing analysis. Also note that the gas heat capacity c_{p_g} , gas density ρ_g , and gas velocity u_g are functions of position and time due to their dependence on concentration, pressure, and temperature.

Energy Balance for the Catalyst

Using an analysis similar to that for the energy balance of the gas and after assuming constant physical properties of the solid phase,

$$(1 - \varepsilon) \rho_s c_{p_s} \frac{\partial T_s}{\partial t} = k_{zs} \frac{\partial^2 T_s}{\partial z^2} + (-\Delta H_M) R_M + (-\Delta H_S) R_S - \frac{U_{sg}(T_s - T_g)}{V_b} + \frac{k_{rs}}{r} \frac{\partial}{\partial r} \left[r \frac{\partial T_s}{\partial r} \right] \quad (12)$$

with

$$\begin{aligned}
 r = R_0, \quad k_{rs} \frac{\partial T_s}{\partial r} &= h_{ts}(T_s - T_t) \\
 r = R_1, \quad -k_{rs} \frac{\partial T_s}{\partial r} &= h_{ws}(T_s - T_w) \\
 z = 0, \quad k_{zs} \frac{\partial T_s}{\partial z} &= h_{sg}(T_s - T_g) \\
 z = L, \quad -k_{zs} \frac{\partial T_s}{\partial z} &= h_{sg}(T_s - T_g)
 \end{aligned}$$

The heats of reaction for the methanation and steam-shift reactions are taken as linear functions of temperature:

$$\Delta H_i = \Delta H_{i1} T + \Delta H_{i2} \quad (13)$$

based on literature data and standard temperature dependence of the heat capacities of the gas components.

Energy Balance for the Thermal Well

Assuming constant physical properties in the thermal well,

$$\rho_t c_{pt} \frac{\partial T_t}{\partial t} = k_{zt} \frac{\partial^2 T_t}{\partial z^2} + \frac{U_{ts}}{V_t} (T_{sr=R_0} - T_t) + \frac{U_{tg}}{V_t} (T_{gr=R_0} - T_t) \quad (14)$$

with

$$\begin{aligned}
 z = 0, \quad T_t &= T_{t_0} \\
 z = L, \quad \frac{\partial T_t}{\partial z} &= 0
 \end{aligned}$$

De Wasch and Froment (1971) discuss the calculation of the wall heat transfer coefficients for the fluid and gas phases based on a lumped wall heat transfer coefficient. Furthermore, radial heat conduction in the thermal well is neglected since it should be of minor importance for a thin solid well.

Mass Balance in the Reactor Section

Since two independent reactions exist, a mass balance must be written for each of two independent species. We select these as CO and CO₂. Note that $i = 1$ refers to CO and $i = 2$ refers to CO₂ in the following.

The equation of continuity in cylindrical coordinates is (Bird *et al.*, 1960)

$$\frac{\partial c_i}{\partial t} + \left[\frac{1}{r} \frac{\partial(rN_{ir})}{\partial r} + \frac{1}{r} \frac{\partial N_{i\theta}}{\partial \theta} + \frac{\partial N_{iz}}{\partial z} \right] = R_i \quad (15)$$

It is customary in representing the axial and radial mass fluxes in a packed bed to define axial and radial mass diffusivities D_z and D_r by

$$N_{iz} = c_i u_g - c D_z \frac{\partial x_i}{\partial z}, \quad N_{ir} = -c D_r \frac{\partial x_i}{\partial r}$$

where there is no bulk flow in the radial direction. If we then incorporate the void fraction and apply the continuity equation for species i assuming angular symmetry, we obtain

$$\frac{\partial c_i}{\partial t} = -\frac{\partial(c_i u_g)}{\partial z} + D_z \frac{\partial}{\partial z} \left(c \frac{\partial x_i}{\partial z} \right) + \frac{D_r}{r} \frac{\partial}{\partial r} \left(r c \frac{\partial x_i}{\partial r} \right) - \frac{\bar{R}_i}{\varepsilon} \quad (16)$$

where $\bar{R}_1 = R_M - R_S$, $\bar{R}_2 = R_S$, and with

$$\begin{aligned} r &= R_0, R_1, & \frac{\partial x_i}{\partial r} &= 0 \\ z &= 0, & u_g(c_{i0} - c_i) &= -c D_z \frac{\partial x_i}{\partial z} \\ z &= L, & \frac{\partial x_i}{\partial z} &= 0 \end{aligned}$$

Since the rate terms R_M and R_S are taken to be global rates, incorporating all mass transfer limitations, bulk phase concentrations can be used throughout the analysis. Although species concentration is proportional to mole fraction, $c_i = c x_i$, complications arise since the total number of moles decreases as the methanation reaction progresses. Therefore to simplify the analysis technique, the mass balances are written using molecular weights and mole fractions based on inlet conditions. Letting δ be the moles of CO reacted in the methanation reaction per total inlet moles,

$$\delta = \frac{x_{10} + x_{20} - x_1 - x_2}{1 + 2x_1 + 2x_2} \quad (17)$$

the following relations hold

$$\hat{M}_g = M_g(1 - 2\delta), \quad \hat{x}_i = x_i(1 - 2\delta) \quad (18)$$

The advantage of this formulation is that the molecular weight based on inlet

conditions \hat{M}_g is constant. Thus

$$c_i = \frac{x_i \rho_g}{M_g} = \frac{\hat{x}_i \rho_g}{\hat{M}_g}, \quad c = \frac{\rho_g}{M_g} = \frac{\rho_g(1-2\delta)}{\hat{M}_g} \quad (19)$$

Then after application of the overall continuity, Eq. (16) becomes

$$\begin{aligned} \rho_g \frac{\partial \hat{x}_i}{\partial t} = & -u_g \rho_g \frac{\partial \hat{x}_i}{\partial z} + D_z \frac{\partial}{\partial z} \left[\rho_g \frac{\partial \hat{x}_i}{\partial z} + \frac{2\rho_g \hat{x}_i}{1-2\delta} \frac{\partial \delta}{\partial z} \right] \\ & + \frac{D_r}{r} \frac{\partial}{\partial r} \left[r \rho_g \frac{\partial \hat{x}_i}{\partial r} + \frac{2\rho_g \hat{x}_i r}{1-2\delta} \frac{\partial \delta}{\partial r} \right] - \frac{\bar{R}_i M_g}{\varepsilon} \end{aligned} \quad (20)$$

with

$$\begin{aligned} r = R_0, R_1, \quad & \frac{\partial \hat{x}_i}{\partial r} + \frac{2\hat{x}_i}{1-2\delta} \frac{\partial \delta}{\partial r} = 0 \\ z = 0, \quad & u_g(\hat{x}_{i0} - \hat{x}_i) = -D_z \left[\frac{\partial \hat{x}_i}{\partial z} + \frac{2\hat{x}_i}{1-2\delta} \frac{\partial \delta}{\partial z} \right] \\ z = L, \quad & \frac{\partial \hat{x}_i}{\partial z} + \frac{2\hat{x}_i}{1-2\delta} \frac{\partial \delta}{\partial z} = 0 \end{aligned}$$

Furthermore, algebraic manipulation of the boundary conditions using the reaction relationship $\delta = \hat{x}_{10} + \hat{x}_{20} - \hat{x}_1 - \hat{x}_2$ leads to⁵

$$\begin{aligned} r = R_0, R_1, \quad & \frac{\partial \hat{x}_i}{\partial r} = 0 \\ z = 0, \quad & u_g(\hat{x}_{i0} - \hat{x}_i) = -D_z \frac{\partial \hat{x}_i}{\partial z} \\ z = L, \quad & \frac{\partial \hat{x}_i}{\partial z} = 0 \end{aligned}$$

Additional Relations

Finally, relationships for density and pressure changes are necessary. The ideal gas law leads to

$$\rho_g = \frac{M_g P}{R_g T} \quad (21)$$

The changes in the pressure along the bed are taken as linear by assuming

⁵ The stipulation $\hat{x}_{10} + \hat{x}_{20} \neq \frac{1}{2}$ is needed for derivation of the reduced boundary conditions.

uniform packing and negligible wall effects. The overall pressure drop across the bed is defined by the Ergun equation (Perry and Chilton, 1973)

$$\Delta P = L \left[\frac{150(1 - \varepsilon)\mu_g}{D_p} + 1.75\rho_{g0}u_{g0} \right] \frac{1 - \varepsilon}{\varepsilon^3} \frac{u_{g0}}{D_p} \quad (22)$$

where

$$D_p = \frac{6(\text{volume of particle})}{\text{external surface area of particle}}$$

It should be noted that the importance of the continuity equation is in evaluating actual velocities within the reactor bed as influenced by the mole, temperature, and pressure changes. Because of the use of mass velocities ($\rho_g u_g$), the importance of the actual velocities is really restricted to cases where pressure relationships such as the Blake-Kozeny equation or velocity effects on heat transfer parameters are considered. As will be shown later, very little increased computational effort is introduced by retaining the continuity equation, since it is solved as a set of algebraic equations.

The nondimensionalization of the packed bed reactor model is based on

$$\begin{aligned} \zeta &= z/L, & \Theta &= T/T_0, & \rho_g^* &= \rho_g/\bar{\rho}_{g0} \\ \eta &= r/R_1, & y_i &= \hat{x}_i/\bar{x}_{CO}^0, & c_{pg}^* &= c_{pg}/\bar{c}_{pg} \\ \vartheta &= t\bar{u}_{g0}/L, & v_g &= u_g/\bar{u}_{g0}, & \hat{M}_g^* &= \hat{M}_g/\bar{M}_{g0} \end{aligned}$$

Note that in the following dimensionless equations the asterisk is dropped from ρ_g^* , c_{pg}^* and \hat{M}_g^* and that

$$\begin{aligned} \varphi_0 &= R_0/R_1 \\ \rho_g &= M_g P/R_g T_g = \hat{M}_g \hat{P}/R_g T_g \rightarrow \rho_g^* = \hat{M}_g^* \hat{P}^*/\Theta_g \\ \hat{P}^* &= \hat{P}/P_{\zeta=0}, \quad \tau = \hat{P}_{\zeta=1}/\hat{P}_{\zeta=0} - 1 \\ c_{pg} &= c_{pg1} T_0 + c_{pg2} \end{aligned}$$

Total Mass Conservation (Continuity)

$$\frac{\partial \rho_g}{\partial \vartheta} + \frac{\partial (\rho_g v_g)}{\partial \zeta} = 0 \quad (\zeta = 0, \quad \rho_g v_g = \rho_{g0} v_{g0}) \quad (23)$$

Energy Balance for the Gas

$$\rho_g c_{pg} \frac{\partial \Theta_g}{\partial \vartheta} = -\rho_g v_g c_{pg} \frac{\partial \Theta_g}{\partial \zeta} + \alpha_g \frac{\partial^2 \Theta_g}{\partial \zeta^2} - \gamma_g (\Theta_g - \Theta_s) + \frac{\beta_g}{\eta} \frac{\partial}{\partial \tau} \left[\eta \frac{\partial \Theta_g}{\partial \eta} \right] \quad (24)$$

with

$$\begin{aligned}
 \eta = \varphi_0, \quad & \frac{\partial \Theta_g}{\partial \eta} = \lambda_{\text{irg}}(\Theta_g - \Theta_t) \\
 \eta = 1.0, \quad & -\frac{\partial \Theta_g}{\partial \eta} = \lambda_{\text{wrg}}(\Theta_g - \Theta_w) \\
 \zeta = 0, \quad & \frac{\partial \Theta_g}{\partial \zeta} = \lambda_{\text{szg}}(\Theta_g - \Theta_s) - \frac{v_{g0} c_{pg} \rho_g}{\alpha_g}(\Theta_0 - \Theta_g) \\
 \zeta = 1.0, \quad & -\frac{\partial \Theta_g}{\partial \zeta} = \lambda_{\text{szg}}(\Theta_g - \Theta_s)
 \end{aligned}$$

Energy Balance for the Catalyst

$$\begin{aligned}
 \frac{\partial \Theta_s}{\partial \vartheta} = \alpha_s \frac{\partial^2 \Theta_s}{\partial \zeta^2} + \frac{\beta_s}{\eta} \frac{\partial}{\partial \eta} \left[\eta \frac{\partial \Theta_s}{\partial \eta} \right] + \gamma_s(\Theta_g - \Theta_s) \\
 + \kappa_1(1 + \varphi_1 \Theta_{s_i}) R'_M + \kappa_2(1 + \varphi_2 \Theta_{s_i}) R'_s
 \end{aligned} \quad (25)$$

with

$$\begin{aligned}
 \eta = \varphi_0, \quad & \frac{\partial \Theta_s}{\partial \eta} = \lambda_{\text{irs}}(\Theta_s - \Theta_t) \\
 \eta = 1.0, \quad & -\frac{\partial \Theta_s}{\partial \eta} = \lambda_{\text{wrs}}(\Theta_s - \Theta_w) \\
 \zeta = 0, \quad & \frac{\partial \Theta_s}{\partial \zeta} = \lambda_{\text{szg}}(\Theta_s - \Theta_g) \\
 \zeta = 1.0, \quad & -\frac{\partial \Theta_s}{\partial \zeta} = \lambda_{\text{szg}}(\Theta_s - \Theta_g)
 \end{aligned}$$

Energy Balance for the Thermal Well

$$\frac{\partial \Theta_t}{\partial \vartheta} = \alpha_t \frac{\partial^2 \Theta_t}{\partial \zeta^2} + \gamma_{\text{ts}}(\Theta_{s_r = \varphi_0} - \Theta_t) + \gamma_{\text{tg}}(\Theta_{g_r = \varphi_0} - \Theta_t) \quad (26)$$

with

$$\begin{aligned}
 \zeta = 0, \quad & \Theta_t = \Theta_{t_0} \\
 \zeta = 1.0, \quad & \frac{\partial \Theta_t}{\partial \zeta} = 0
 \end{aligned}$$

Mass Balance in the Reactor Section

$$\begin{aligned} \frac{\partial y_i}{\partial \vartheta} = & -v_g \frac{\partial y_i}{\partial \zeta} + \frac{\alpha_m}{\rho_g} \frac{\partial}{\partial \zeta} \left[\rho_g \frac{\partial y_i}{\partial \zeta} + \frac{2\rho_g y_i}{1-2\delta} \frac{\partial \delta}{\partial \zeta} \right] + \frac{\beta_m}{\rho_g \eta} \frac{\partial}{\partial \eta} \left[\eta \rho_g \frac{\partial y_i}{\partial \eta} + \frac{2\rho_g y_i \eta}{1-2\delta} \frac{\partial \delta}{\partial \eta} \right] \\ & + \begin{cases} -\sigma_1 \frac{\Theta_{gi}}{\bar{P}} R'_M + \sigma_2 \frac{\Theta_{gi}}{\bar{P}} R'_s & (k=1) \\ -\sigma_3 \frac{\Theta_{gi}}{\bar{P}} R'_s & (k=2) \end{cases} \end{aligned} \quad (27)$$

where

$$\begin{aligned} \frac{\partial^2 \delta}{\partial \zeta^2} &= -\bar{x}_1^0 \frac{\partial^2 y_1}{\partial \zeta^2} - \bar{x}_2^0 \frac{\partial^2 y_2}{\partial \zeta^2} \\ \frac{\partial \delta}{\partial \zeta} &= -\bar{x}_1^0 \frac{\partial y_1}{\partial \zeta} - \bar{x}_2^0 \frac{\partial y_2}{\partial \zeta} \\ \eta = \varphi_0, \quad & \frac{\partial y_i}{\partial \eta} = 0 \\ \eta = 1.0, \quad & \frac{\partial y_i}{\partial \eta} = 0 \\ \zeta = 0, \quad & \frac{\partial y_1}{\partial \zeta} = \frac{v_g}{\alpha_m} (y_1 - y_1^0) \\ \zeta = 1.0, \quad & \frac{\partial y_1}{\partial \zeta} = 0 \end{aligned}$$

In these equations, the dimensionless quantities are defined as follows.

Aspect Ratios

$$\text{axial} \quad n = L/d_p, \quad \text{radial} \quad m = R_1/d_p, \quad \text{overall} \quad a = L/R_1$$

Axial Dispersion

$$\begin{aligned} \alpha_g &= \frac{k_{zg}}{\bar{\rho}_{g0} \varepsilon \bar{C}_{pg} L \bar{u}_{g0}} = (\text{Pe}_{zh} \varepsilon n)^{-1} \\ \alpha_s &= \frac{k_{zs}}{\bar{u}_{g0} c_{ps} \rho_s (1-\varepsilon) L}, \quad \alpha_t = \frac{k_t}{\rho_t c_{pt} \bar{u}_{g0} L} \\ \alpha_m &= \frac{D_z}{L \bar{u}_{g0}} = (\text{Pe}_{zm} n)^{-1} \end{aligned}$$

Radial Dispersion

$$\beta_s = \frac{k_s}{\rho_s c_{p_s}(1-\varepsilon)R_1^2 \bar{u}_{g0}}, \quad \beta_g = \frac{k_{rg}L}{\bar{\rho}_{g0} \bar{c}_{p_g} \varepsilon R_1^2 \bar{u}_{g0}} = \frac{a}{\text{Pe}_{rg} \varepsilon m}$$

$$\beta_m = \frac{D_r L}{R_1^2 \bar{u}_{g0}} = \frac{a}{\text{Pe}_{rm} m}$$

Heat Transfer

$$\gamma_s = \frac{U_{sg}L}{\bar{u}_{g0} V_b \rho_s c_{p_s}(1-\varepsilon)}, \quad \gamma_{ts} = \frac{U_{ts}L}{V_t \rho_t c_{p_t} \bar{u}_{g0}}$$

$$\gamma_g = \frac{U_{sg}L}{\bar{u}_{g0} V_b \bar{\rho}_{g0} \bar{c}_{p_g} \varepsilon}, \quad \gamma_{tg} = \frac{U_{tg}L}{V_t \rho_t c_{p_t} \bar{u}_{g0}}$$

Heats of Reaction

$$\kappa_1 = \frac{L(-\Delta H_{M_2})P_{T_0}^{1.5}(\bar{x}_{H_2}^0)^{0.5}\bar{x}_{CO}k_{0M}}{\bar{u}_{g0}c_{p_s}\bar{T}_0}, \quad \kappa_2 = \frac{L(-\Delta H_{S_2})\bar{x}_{CO_2}^0\bar{x}_{H_2}^0k_{0S}}{\bar{u}_{g0}c_{p_s}\bar{T}_0}$$

$$\varphi_1 = \frac{\bar{T}_0(\Delta H_{M_1})}{\Delta H_{M_g}}, \quad \varphi_2 = \frac{\bar{T}_0(\Delta H_{S_1})}{\Delta H_{S_2}}$$

Reaction Coefficients

$$\sigma_1 = \frac{\bar{M}_{g0}L\rho_s(1-\varepsilon)P_{T_0}^{1.5}(\bar{x}_{H_2}^0)^{0.5}k_{0M}}{\varepsilon\bar{\rho}_{g0}\bar{u}_{g0}}$$

$$\sigma_2 = \frac{\bar{M}_{g0}L\rho_s(1-\varepsilon)\bar{x}_{H_2}^0\bar{x}_{CO_2}^0k_{0S}}{\varepsilon\bar{\rho}_{g0}\bar{u}_{g0}\bar{x}_{CO}^0}, \quad \sigma_3 = \frac{\bar{M}_{g0}L\rho_s(1-\varepsilon)\bar{x}_{H_2}^0k_{0S}}{\varepsilon\bar{\rho}_{g0}\bar{u}_{g0}}$$

Biot Numbers

$$\lambda_{gzs} = h_{sg}L/k_{zs}, \quad \lambda_{szg} = \frac{h_{sg}L}{k_{zg}}$$

$$\lambda_{wrs} = \frac{h_{ws}R_1}{k_{rs}}, \quad \lambda_{wrg} = \frac{h_{wg}R_1}{k_{rg}}$$

$$\lambda_{trs} = \frac{h_{ts}R_1}{k_{rs}}, \quad \lambda_{trg} = \frac{h_{tg}R_1}{k_{rg}}$$

Reaction Rates

$$R_M = \rho_s(1-\varepsilon)P_{T_0}^{1.5}(\hat{x}_{H_2}^0)^{0.5}\hat{x}_{CO}^0k_{0M}R'_M$$

$$R_S = \rho_s(1-\varepsilon)\hat{x}_{CO}^0\hat{x}_{H_2}^0k_{0S}R'_S$$

V. Numerical Solution

The mathematical model developed in the preceding section consists of six coupled, three-dimensional, nonlinear partial differential equations along with nonlinear algebraic boundary conditions, which must be solved to obtain the temperature profiles in the gas, catalyst, and thermal well; the concentration profiles; and the velocity profile. Numerical solution of these equations is required.

A. SOLUTION TECHNIQUES

A comparison of the benefits and drawbacks of common numerical solution techniques for complex, nonlinear partial differential equation models is given in Table II. Note that it is common and in some cases necessary to use a combination of the techniques in the different dimensions of the model.

TABLE II
NUMERICAL SOLUTION TECHNIQUES FOR PARTIAL DIFFERENTIAL EQUATIONS
ARISING IN PACKED BED REACTOR MODELING

Method	Benefits	Drawbacks
Finite difference	Has simple construction Is easily extended to multiple dimensions Solution is stable for sharp gradients or in response to a concentration or temperature front Leads directly to state-space representation	Is often computationally prohibitive since accurate solutions may require a large number of grid points
Methods of weighted residuals Galerkin's method Orthogonal collocation	Generally needs few grid points resulting in a low-order model Leads directly to state-space representation	Can have difficulties with sharp gradients or fronts since a smooth function is specified over the domain May lead to control modeling difficulties since inputs affect all states immediately.
Orthogonal collocation on finite elements	Can account for sharp gradients if elements are picked well Leads directly to state-space representation	Can have problems with placement of elements, especially if location of steep gradients moves or is unknown

The finite difference method involves dividing the domain into intervals with the boundary points between intervals being called the grid or mesh points. Then for a continuous function across the interval, a Taylor series expansion can be used to deduce difference formulas for first and second derivatives. If the differential equations are written at each grid point using the difference formulas and the values at the first and last grid point include the boundary conditions, enough equations are available to solve for the value of the function at each grid point.

Although the finite difference technique is generally easily implemented and is quite robust, the procedure often becomes numerically prohibitive for packed bed reactor models since a large number of grid points may be required to accurately define the solution. Thus, since the early 1970s most packed bed studies have used one of the methods of weighted residuals rather than finite differences.

The method of weighted residuals comprises several basic techniques, all of which have proved to be quite powerful and have been shown by Finlayson (1972, 1980) to be accurate numerical techniques frequently superior to finite difference schemes for the solution of complex differential equation systems. In the method of weighted residuals, the unknown exact solutions are expanded in a series of specified trial functions that are chosen to satisfy the boundary conditions, with unknown coefficients that are chosen to give the "best" solution to the differential equations:

$$y(x) = \varphi_0(x) + \sum_{k=0}^N c_k \varphi_k(x) \quad (28)$$

These trial functions are substituted into the differential equations, and the result is the residual R . This residual is weighted by functions characteristic of the particular method, and the weighted residuals are minimized over the domain of the independent variable V . In particular, the weighted integrals of the residuals are set to zero.

The two most common of the methods of weighted residuals are the Galerkin method and collocation. In the Galerkin method, the weighting functions are chosen to be the trial functions, which must be selected as members of a complete set of functions. (A set of functions is complete if any function of a given class can be expanded in terms of the set.) Also according to Finlayson (1972),

A continuous function is zero if it is orthogonal to every member of a complete set. Thus the Galerkin method forces the residual to be zero by making it orthogonal to each member of a complete set of functions (in the limit as $N \rightarrow \infty$).

In the collocation method, the weighting functions are chosen to be the Dirac delta function

$$w_j = \delta(x - x_j) \quad (29)$$

Thus

$$\int_V w_j R dV = R \Big|_{x_j} \quad (30)$$

This technique then forces the residual to be zero at N specified collocation points. As N increases, the residual is zero at more and more points and presumably approaches zero everywhere.

These methods of weighted residuals are generally recommended for packed bed reactor modeling since solution computing time is usually low since the solution can usually be accurately defined with only a few grid points.

A compromise between the high dimensionality of the finite difference approach and the method of weighted residuals' inability to accurately define profiles with sharp gradients often leads to numerical procedures using a combination of the techniques. One such example is orthogonal collocation on finite elements (OCFE) (Carey and Finlayson, 1975). The method of weighted residuals uses a series of polynomials, each of which is defined over the entire range $0 \leq \zeta \leq 1$, as a trial function for the axial collocation. Complications with this global procedure arise in the presence of steep gradients or abrupt changes in the solution profile. In such situations, it may be advantageous to use trial functions that are defined over only part of the region and piece together adjacent functions to provide an approximation over the entire domain. Using such a procedure, smaller regions can be used near the location of the steep gradient. The OCFE technique involves using orthogonal collocation within each of these elements. A similar analysis can be performed using the Galerkin method within each element.

The major problem with this technique is that it is only effective if the elements are picked optimally. This selection is by no means trivial and may render the technique ineffectual in situations where the location of steep gradients is unknown or does not remain fixed.

Another potential solution technique appropriate for the packed bed reactor model is the method of characteristics. This procedure is suitable for hyperbolic partial differential equations of the form obtained from the energy balance for the gas and catalyst and the mass balances if axial dispersion is neglected and if the radial dimension is first discretized by a technique such as orthogonal collocation. The thermal well energy balance would still require a numerical technique that is not limited to hyperbolic systems since axial conduction in the well is expected to be significant.

It should be noted that since the mathematical description of the packed bed reactor consists of three dimensions, one does not need to select a single technique suitable for the entire solution but can choose the best technique for reduction of the model in each of the separate dimensions. Thus, for example, orthogonal collocation could be used in the radial dimension where the

profiles are generally smooth and symmetric, finite differences could be used axially to account for sharp gradients near the hot spot, and the resulting equations could be numerically integrated in time. Another possibility is that presented by Yu *et al.* (1982) for a moving-bed coal gasifier in which computation is done using orthogonal collocation in the radial variable, exponential collocation in time, and numerical integration in the axial direction. Because of our interest in generating a low-order control model that consists of ordinary differential equations in time, we have chosen to employ orthogonal collocation in both the radial and axial dimensions.

B. ORTHOGONAL COLLOCATION

Of the various methods of weighted residuals, the collocation method and, in particular, the orthogonal collocation technique have proved to be quite effective in the solution of complex, nonlinear problems of the type typically encountered in chemical reactors. The basic procedure was used by Stewart and Villadsen (1969) for the prediction of multiple steady states in catalyst particles, by Ferguson and Finlayson (1970) for the study of the transient heat and mass transfer in a catalyst pellet, and by McGowin and Perlmutter (1971) for local stability analysis of a nonadiabatic tubular reactor with axial mixing. Finlayson (1971, 1972, 1974) showed the importance of the orthogonal collocation technique for packed bed reactors.

The orthogonal collocation method has several important differences from other reduction procedures. In collocation, it is only necessary to evaluate the residual at the collocation points. The orthogonal collocation scheme developed by Villadsen and Stewart (1967) for boundary value problems has the further advantage that the collocation points are picked optimally and automatically so that the error decreases quickly as the number of terms increases. The trial functions are taken as a series of orthogonal polynomials which satisfy the boundary conditions and the roots of the polynomials are taken as the collocation points. A major simplification that arises with this method is that the solution can be derived in terms of its value at the collocation points instead of in terms of the coefficients in the trial functions and that at these points the solution is exact.

A description of the technique requires appropriate definitions of the orthogonal polynomials $P_m(x)$ as

$$P_m(x) = \sum_{j=0}^m c_j x^j \quad (31)$$

with degree m and order $m + 1$. The coefficients are defined so as to require the orthogonality condition

$$\int_a^b w(x) P_n(x) P_m(x) dx \quad (n = 0, 1, 2, \dots, m - 1) \quad (32)$$

to be satisfied for weighting functions $w(x) \geq 0$. For boundary value problems, the solution is expanded in terms of orthogonal polynomials with the first term satisfying the given boundary conditions, followed by a series that has unknown coefficients, with each term satisfying homogeneous boundary conditions. Various expansions are then possible. The most common and useful are

$$\begin{aligned} y_N(x) &= \sum_{i=1}^{N+1} a_i x^{i-1}, & y_N(x) &= \sum_{i=1}^{N+1} b_i P_{i-1}(x) \\ y_N(x) &= \sum_{i=1}^{N+1} y(x_i) L_i(x) \end{aligned} \quad (33)$$

C. RADIAL COLLOCATION

The first step in the solution procedure is discretization in the radial dimension, which involves writing the three-dimensional differential equations as an enlarged set of two-dimensional equations at the radial collocation points with the assumed profile identically satisfying the radial boundary conditions. An examination of experimental measurements (Valstar *et al.*, 1975) and typical radial profiles in packed beds (Finlayson, 1971) indicates that radial temperature profiles can be represented adequately by a quadratic function of radial position. The quadratic representation is preferable to one of higher order since only one interior collocation point is then necessary,⁶ thus not increasing the dimensionality of the system. The assumed radial temperature profile for either the gas or solid is of the form

$$\Theta^{(n)}(\vartheta, \zeta, \eta) = \sum_{i=1}^{n+2} d_i(\vartheta, \zeta) \eta^{i-1} \quad (34)$$

with the number n of interior radial collocation points taken as one. This profile must satisfy the boundary conditions and must be exact at the collocation points $\eta = \varphi_0$, r_c , and 1.0, where the interior collocation point r_c is selected as the zero of the appropriate orthogonal polynomial. This formulation is equivalent to using the trial function

$$y(x) = b + cx + x(1-x) \sum_{i=1}^N a_i P_{i-1}(x) \quad (35)$$

given by Villadsen and Stewart (1967) for nonsymmetric profiles.⁷

Application of the procedure, presented subsequently, of satisfying the boundary conditions with the assumed profile leads to the coefficients $d_i(\vartheta, \zeta)$ for the profiles in terms of the temperatures at the collocation point, within the

⁶ Along with two boundary points, there are three collocation points.

⁷ Due to the presence of the thermal well, a nonsymmetric function is necessary to describe the profile between $\eta = \varphi_0$ and $\eta = 1.0$.

well, and at the outer wall. Since the objective of radial collocation is to eliminate the radial derivatives, Eq. (34) is then substituted into the partial differential equations.

For example, consider the radial temperature profile in the gas. At the three radial collocation points $\eta = \varphi_0$, r_c , and 1.0, let the gas temperatures be Θ_{g0} , Θ_{gr} , and Θ_{g1} and assume that the radial profile is quadratic:

$$\Theta_g(\vartheta, \zeta, \eta) = d_0(\vartheta, \zeta) + d_1(\vartheta, \zeta)\eta + d_2(\vartheta, \zeta)\eta^2 \quad (36)$$

This profile must satisfy the boundary conditions

$$\left. \frac{\partial \Theta_g}{\partial \eta} \right|_{\eta=\varphi_0} = \lambda_{\text{trg}}(\Theta_{g\eta=\varphi_0} - \Theta_t), \quad \left. \frac{\partial \Theta_g}{\partial \eta} \right|_{\eta=1} = -\lambda_{\text{wrg}}(\Theta_{g\eta=1} - \Theta_w) \quad (37)$$

where λ_{trg} and λ_{wrg} are the dimensionless radial Biot numbers at the thermal well and cooling wall, respectively. The profile must also be exact at the three collocation points:

$$\begin{aligned} \Theta_{g0} &= d_0 + d_1 \varphi_0 + d_2 \varphi_0^2 \\ \Theta_{gr} &= d_0 + d_1 r_c + d_2 r_c^2 \\ \Theta_{g1} &= d_0 + d_1 + d_2 \end{aligned} \quad (38)$$

After rearranging and eliminating Θ_{g0} and Θ_{g1} ,

$$\begin{bmatrix} 1 & r_c & r_c^2 \\ \lambda_{\text{trg}} & \varphi_0 \lambda_{\text{trg}} - 1 & \varphi_0^2 \lambda_{\text{trg}} - 2\varphi_0 \\ \lambda_{\text{wrg}} & \lambda_{\text{wrg}} + 1 & \lambda_{\text{wrg}} + 2 \end{bmatrix} \begin{bmatrix} d_0 \\ d_1 \\ d_2 \end{bmatrix} = \begin{bmatrix} \Theta_{gr} \\ \lambda_{\text{trg}} \Theta_t \\ \lambda_{\text{wrg}} \Theta_w \end{bmatrix} \quad (39)$$

Since

$$\partial \Theta_g / \partial \eta = d_1 + 2d_2 \eta, \quad \partial^2 \Theta_g / \partial \eta^2 = 2d_2 \quad (40)$$

the dimensionless form of Eq. (24) becomes

$$\rho_g c_{pg} \frac{\partial \Theta_g}{\partial \vartheta} = -\rho_g v_g c_{pg} \frac{\partial \Theta_g}{\partial \zeta} + \alpha_g \frac{\partial^2 \Theta_g}{\partial \zeta^2} + \beta_g \left[4d_2 + \frac{d_1}{r_c} \right] + \gamma_g(\Theta_s - \Theta_g) \quad (41)$$

where Θ_g and Θ_s are now the temperatures at the radial collocation point r_c and ρ_g and c_{pg} are now dimensionless parameters, normalized with respect to the inlet steady-state values. Similar results are obtained for the energy balance on the catalyst. Although the solutions of the differential equations are then obtained for the temperatures at the radial collocation point, the temperature at any radial point can easily be determined using the radial profile given by Eq. (36) along with the solutions for $d_i(\vartheta, \zeta)$ given by Eq. (39).

For radial concentration profiles, a quadratic representation may not be adequate since application of the zero flux boundary conditions at $\eta = \varphi_0$ and $\eta = 1.0$ leads to $d_2 = d_3 = 0$. Thus a quadratic representation for the concentration profiles reduces to the assumption of uniform radial concentrations, which for a highly exothermic system may be significantly inaccurate.

Although additional radial collocation points increase the dimensionality of the resulting model, they may be necessary to accurately express the radial concentration profiles. Preliminary analysis in this section considers only one interior radial concentration collocation point, although a detailed analysis of this assumption is presented in Section VI.E.

Thus, at this point the original differential equations have been reduced from three-dimensional in variables ζ , η , and ϑ to two-dimensional in variables ζ and ϑ by orthogonal collocation in the radial variable η . The reduced temperature equations are a function of the dependent variables at the radial collocation point r_c , but incorporate radial information via the well and wall temperatures. Radial profiles can be generated from the collocation equation by using the expressions for the coefficients $d_i(\vartheta, \zeta)$. Similarly, the continuity equations are functions of the concentrations at each collocation point for multipoint radial collocation. With one interior collocation point for the concentration, the system consists of six differential equations describing the overall continuity, energy balance for the thermal well, energy balance for the gas and catalyst in terms of conditions at r_c , and mass balances for CO and CO₂. The incentive for using only one radial collocation point is clear, since the number of two-dimensional partial differential equations is the same as the original number of three-dimensional equations.

D. AXIAL COLLOCATION

Since the resulting system after radial collocation is still too complex for direct mathematical solution, the next step in the solution process is discretization of the two-dimensional system by orthogonal collocation in the axial direction. Although elimination of the spatial derivatives by axial collocation increases the number of equations,⁸ they become ordinary differential equations and are easily solved using traditional techniques. Since the position and number of points are the only factors affecting the solution obtained by collocation, any set of linearly independent polynomials may be used as trial functions. The Lagrangian polynomials of degree N based on the collocation points ζ_j

$$L_i(\zeta) = \prod_{j=0, j \neq i}^{N+1} \left(\frac{\zeta - \zeta_j}{\zeta_i - \zeta_j} \right) \quad (i = 0, 1, \dots, N + 1) \quad (42)$$

are used here. The differential equations are then collocated at the N zeros, ζ_k , $k = 1, 2, \dots, N$, of a Legendre polynomial. Since only one Lagrangian is nonzero at a collocation point and since the residual is set equal to zero at this point, the coefficient of the Lagrangian term is equal to the solution at that point.

⁸ Since more than one axial collocation point is generally necessary.

Following the development of Villadsen and Michelsen (1978), the assumed axial profiles are

$$\begin{aligned}
 \Theta_s(\zeta, \vartheta) &= \sum_{i=0}^{N+1} \Theta_{s,i}(\vartheta) L_i(\zeta) \\
 \Theta_g(\zeta, \vartheta) &= \sum_{i=0}^{N+1} \Theta_{g,i}(\vartheta) L_i(\zeta) \\
 \Theta_t(\zeta, \vartheta) &= \sum_{i=0}^{N+1} \Theta_{t,i}(\vartheta) L_i(\zeta) \\
 y_j(\zeta, \vartheta) &= \sum_{i=0}^{N+1} y_{j,i}(\vartheta) L_i(\zeta) \quad (j = 1, 2) \\
 v_g(\zeta, \vartheta) &= \sum_{i=0}^{N+1} v_{g,i}(\vartheta) L_i(\zeta)
 \end{aligned} \tag{43}$$

Since the $L_i(\zeta)$ are known functions based solely on the collocation points, the differential operators can be applied *a priori*:

$$A_{ji} = \left. \frac{dL_i(\zeta)}{d\zeta} \right|_{\zeta_j}, \quad B_{ji} = \left. \frac{d^2 L_i(\zeta)}{d\zeta^2} \right|_{\zeta_j} \tag{44}$$

Then after operating on the assumed solutions with the differential operators and substituting into the partial differential equations, the residuals are set equal to zero at the collocation points.

The collocation points are calculated using programs given by Villadsen and Michelsen (1978) for calculating the zeros of an arbitrary Jacobi polynomial $P_N^{(\alpha, \beta)}(x)$ that satisfies the orthogonality relationship

$$\int_0^1 u^\beta (1-u)^\alpha P_i(u) P_j(u) du = C_i \delta_{ij} \tag{45}$$

where C_i is a constant, δ_{ij} is the delta function, and α and β are chosen on the basis of the geometry of the system. For the packed bed reactor, zeros of $P_N^{(0,0)}(z)$ are used as collocation points.

The resulting equations in terms of conditions at the collocation points z_i are the following.

Catalyst Energy Balance

$$\begin{aligned}
 \frac{d\Theta_{s_i}}{d\vartheta} &= \alpha_s \sum_{j=0}^{N+1} B_{ij} \Theta_{s_j} + \omega_1 \Theta_{s_i} + \omega_2 \Theta_{t_i} + \gamma_s \Theta_{g_i} \\
 &\quad + \kappa_1 (1 + \varphi_1 \Theta_{s_i}) R'_M + \kappa_2 (1 + \varphi_2 \Theta_{s_i}) R'_S + \omega_3 \\
 \sum_{j=0}^{N+1} A_{0,j} \Theta_{s_j} &= \lambda_{gzs} (\Theta_{s_0} - \Theta_{g_0}), \quad \sum_{j=0}^{N+1} A_{N+1,j} \Theta_{s_j} = \lambda_{gzs} (\Theta_{g_{N+1}} - \Theta_{s_{N+1}})
 \end{aligned} \tag{46}$$

Gas Energy Balance

$$\frac{(\tau\zeta_i + 1)\hat{M}_g c_{p_g}}{\Theta_{g_i}} \frac{d\Theta_{g_i}}{d\vartheta} = \frac{-(\tau\zeta_i + 1)v_{g_i}\hat{M}_g c_{p_g}}{\Theta_{g_i}} \sum_{j=0}^{N+1} A_{ij}\Theta_{g_j} + \alpha_g \sum_{j=0}^{N+1} B_{ij}\Theta_{g_j} + \omega_4\Theta_{g_i} + \omega_5\Theta_{t_i} + \gamma_g\Theta_{s_i} + \omega_6 \quad (47)$$

$$\sum_{j=0}^{N+1} A_{0,j}\Theta_{g_j} = -\lambda_{szg}(\Theta_{s_0} - \Theta_{g_0}) + \frac{v_{g_0}M_{g_0}c_{p_{g_0}}}{\alpha_g\Theta_{g_j}}(\Theta_{g_0} - \Theta_0)$$

$$\sum_{j=0}^{N+1} A_{N+1,j}\Theta_{g_j} = \lambda_{szg}(\Theta_{s_{N+1}} - \Theta_{g_{N+1}})$$

Mass Balances

$$\begin{aligned} \frac{dy_{k_i}}{d\vartheta} = & -v_{g_i} \sum_{j=0}^{N+1} A_{ij}y_{k_j} + \alpha_m \left\{ \sum_{j=0}^{N+1} B_{ij}y_{k_j} + \left[\sum_{j=0}^{N+1} A_{ij}y_{k_j} \right] \right. \\ & \times \left[\frac{\tau}{\tau\zeta_i + 1} - \frac{1}{\Theta_{g_i}} \sum_{j=0}^{N+1} A_{ij}\Theta_{g_j} \right] - \frac{2y_{k_i}}{1 - 2\delta} \frac{\partial^2 \delta}{\partial \zeta^2} - \frac{2}{1 - 2\delta} \left[\sum_{j=0}^{N+1} A_{ij}y_{k_j} \right] \frac{\partial \delta}{\partial \zeta} \\ & \left. - \frac{2y_{k_i}}{1 - 2\delta} \left[\frac{\tau}{\tau\zeta_i + 1} - \frac{1}{\Theta_{g_i}} \sum_{j=0}^{N+1} A_{ij}\Theta_{g_j} \right] \frac{\partial \delta}{\partial \zeta} + \frac{4y_{k_i}}{(1 - 2\delta)^2} \left[\frac{\partial \delta}{\partial \zeta} \right]^2 \right\} \\ & + \begin{cases} -\sigma_1 \frac{\Theta_{g_i}}{\bar{P}} R'_M + \sigma_2 \frac{\Theta_{g_i}}{\bar{P}} R'_S & (k = 1) \\ -\sigma_3 \frac{\Theta_{g_i}}{\bar{P}} R'_S & (k = 2) \end{cases} \end{aligned} \quad (48)$$

where

$$\begin{aligned} \frac{\partial^2 \delta}{\partial \zeta^2} &= - \left[\bar{x}_1^0 \sum_{j=0}^{N+1} B_{ij}y_{1_j} + \bar{x}_2^0 \sum_{j=0}^{N+1} B_{ij}y_{2_j} \right] \\ \frac{\partial \delta}{\partial \zeta} &= - \left[\bar{x}_1^0 \sum_{j=0}^{N+1} A_{ij}y_{1_j} + \bar{x}_2^0 \sum_{j=0}^{N+1} A_{ij}y_{2_j} \right] \\ \sum_{j=0}^{N+1} A_{0,j}y_{k_j} &= \frac{v_{g_0}}{\alpha_m}(y_{k_0} - y_k^0), \quad \sum_{j=0}^{N+1} A_{N+1,j}y_{k_j} = 0 \end{aligned}$$

Thermal Well Energy Balance

$$\frac{d\Theta_{t_i}}{d\vartheta} = \alpha_t \sum_{j=0}^{N+1} B_{ij}\Theta_{t_j} + \omega_7\Theta_{s_i} + \omega_8\Theta_{g_i} + \omega_9\Theta_{t_i} + \omega_{10} \quad (49)$$

$$\sum_{j=0}^{N+1} A_{N+1,j}\Theta_{t_j} = 0$$

Overall Continuity

$$\Theta_{g_i} \sum_{j=0}^{N+1} A_{ij} v_{g_i} - \frac{d\Theta_{g_i}}{d\vartheta} + \frac{v_{g_i} \Theta_{g_i} \tau}{\tau \zeta_i + 1} - v_{g_i} \sum_{j=0}^{N+1} A_{ij} \Theta_{g_j} = 0 \quad (50)$$

Note that $i = 1, 2, \dots, N$ for all of the equations except the last, where $i = 1, 2, \dots, N + 1$; that the ω_i coefficients are the result of radial collocation; and that all other dimensionless parameters are defined as shown previously. Furthermore, the reaction terms R'_M and R'_S are calculated at the conditions at the collocation points.

The resulting equations are a set of $6N + 1$ ordinary differential equations along with algebraic boundary conditions. The solution procedure is further simplified by solving the last equation for v_{g_i} as a set of algebraic equations, using the gas temperatures and derivatives of the gas temperatures from the solutions of the remaining differential equations.⁹ Additionally, simple algebraic manipulation allows for explicit solution of v_{g_0} , Θ_{t_0} , $\Theta_{t_{N+1}}$, y_{i_0} and $y_{i_{N+1}}$, while solution for Θ_{s_0} , $\Theta_{s_{N+1}}$, Θ_{g_0} , and $\Theta_{g_{N+1}}$ requires the simultaneous solution of four coupled algebraic equations. The resulting dynamic model is then a set of $5N$ coupled, nonlinear ordinary differential equations and $N + 5$ coupled, nonlinear algebraic equations, where N is the number of interior axial collocation points.

Typical steady-state profiles along a reactor obtained by other authors (Jutan *et al.*, 1977; Hoiberg *et al.*, 1971) indicate that these profiles can be represented by relatively low-order polynomials. However, temperature profiles with steep gradients, as may be likely in a highly exothermic system such as methanation, may require higher-order polynomials. Although approximation error is reduced by increasing the number of collocation points, numerical problems with fitting higher-order polynomials to process curves may result. Section X addresses the model dimensionality in detail. Presently, let it suffice to say that 6–8 axial collocation points are generally sufficient, leading to a system of 30–40 coupled, nonlinear ordinary differential equations and 11–13 coupled, nonlinear algebraic equations.

E. NUMERICAL SIMULATION

Steady-state solutions can be obtained by carrying a dynamic simulation to steady state or by setting the time derivatives equal to zero in the ordinary differential equations and then solving the resulting system of $6N + 5$ algebraic equations. In the latter technique, solutions for very steep axial profiles often show numerical convergence problems. These problems can be reduced by using better initial guesses or by varying the actual solution algorithm. In extreme cases, it may be necessary to carry the dynamic solution

⁹ That is, effectively substituting Eq. (47) into Eq. (50) for $d\Theta_{g_i}/d\vartheta$.

part way to steady state and then use its results as an initial guess of the steady-state solution.

Owing to the large size of the problem and the complexity of the nonlinear equations, both dynamic and steady-state solutions require powerful algorithms for the solution of nonlinear algebraic equations and for the solution of initial value problems in ordinary differential equations. Considerable analysis of various solution algorithms led to the final selection of the techniques described in this section due to their robustness under a great variety of conditions and their relative speed of solution in comparison to other techniques. Most other procedures exhibited convergence problems. Even the selected techniques fail to converge under certain conditions, but in general are flexible enough to allow solution with the adjustment of several convergence parameters.

Although the solution of the algebraic equations is relatively simple for the dynamic simulations, it is extremely difficult for steady-state solutions with poor initial estimates of the solution profiles. Two methods are used in the computer simulation programs developed in this work for the solution of the systems of nonlinear algebraic equations. These are based on algorithms by Powell (Rabinowitz, 1970) and Brown (1967). Although Brown's algorithm is in most cases more powerful than that of Powell, it is in general significantly slower. Thus although the computer programs use either technique, Brown's algorithm is only used in those cases where Powell's algorithm fails to converge to an appropriate solution.

Dynamic solutions of the mathematical model for the packed bed reactor also require a powerful method for initial value problems in ordinary differential equations. Although several effective techniques are available, the system of ordinary differential equations describing the reactor is solved in this work by using an Adams–Moulton predictor–corrector technique with the method of Runge–Kutta–Gill being used to start the integration process, and the nonlinear system of algebraic equations is solved by using Powell's hybrid algorithm (Rabinowitz, 1970) or Brown's (1967) algorithm. Combining these techniques with a variable time-step analysis, based on increasing the time steps as the derivatives decrease during the approach to steady state, leads to an efficient solution procedure for obtaining dynamic reactor responses.

VI. Analysis of Model Behavior

Our objective in this section is to study the steady-state and transient effects of various parameters, operating conditions, and modeling assumptions on the predicted behavior of the reactor. These studies will allow us to form

conclusions concerning the importance of various physical and chemical phenomena and the importance of a generalized overall model structure. We reiterate that our overall goal is not simply to simulate the methanation system, but rather to deduce important conclusions of general applicability to packed bed reactor modeling.

A. SYSTEM PARAMETERS

The numerical values of the parameters used for this analysis are based on published results of packed bed analyses. Typical values of the major parameters are shown in Table III.¹⁰

Two sets of typical operating conditions are used for the simulations presented. These are shown in Table IV and will be referred to as standard type I or II conditions. Type I corresponds to operation at moderate to high temperatures, pressures, and flow rates with relatively low inlet CO and H₂ concentrations and small amounts of inlet CH₄, CO₂, and H₂O either from recycle or from the upstream process. Type II is based on conditions for the industrial use of methanation in synthetic natural gas production. Note that the inlet methane concentration is much higher than in type I.

TABLE III
TYPICAL REACTOR PARAMETERS

Catalyst parameters		Thermal well parameters	
c_{p_s}	0.23 cal/g K	c_{p_t}	0.12 cal/g K
ρ_g	1.04 g/cm ³	ρ_t	8.02 g/cm ³
k_{zs}, k_{rs}	0.0005 cal/sec cm K	k_{zt}	0.039 cal/sec cm K
Heat transfer parameters		Reactor parameters	
U_{sg}	17.02 cal/sec K	L	30.00 cm
U_{ts}	0.02 cal/sec K	R_0	0.159 cm
U_{tg}	0.14 cal/sec K	R_1	1.194 cm
λ_{gzs}	600.00	Pe_{mz}	10.00
λ_{szg}	13.00	Pe_{mr}	2.00
$\lambda_{trs} = \lambda_{wrs}$	7.16	Pe_{hz}	2.00
$\lambda_{trg} = \lambda_{wrg}$	1.25	Pe_{br}	8.00

¹⁰ Effective thermal conductivities and heat transfer coefficients are given by De Wasch and Froment (1971) for the solid and gas phases in a heterogeneous packed bed model. Representative values for Peclet numbers in a packed bed reactor are given by Carberry (1976) and Mears (1976). Values for Peclet numbers from 0.5 to 200 were used throughout the simulations.

TABLE IV
TYPICAL OPERATING CONDITIONS

Type I conditions			
Parameters	$\varepsilon = 0.40$ $u_{g0} = 75 \text{ cm/sec}$	$T_0 = 573 \text{ K}$ $P = 20 \text{ atm}$	$T_w = 573 \text{ K}$
Inlet mole fractions	$x_{\text{CH}_4} = 0.02$ $x_{\text{CO}} = 0.03$	$x_{\text{CO}_2} = 0.03$ $x_{\text{H}_2} = 0.20$	$x_{\text{H}_2\text{O}} = 0.024$
Type II conditions			
Parameters	$\varepsilon = 0.57$ $u_{g0} = 75 \text{ cm/sec}$	$T_0 = 573 \text{ K}$ $P = 10 \text{ atm}$	$T_w = 573 \text{ K}$
Inlet mole fractions	$x_{\text{CH}_4} = 0.60$ $x_{\text{CO}} = 0.06$	$x_{\text{CO}_2} = 0.015$ $x_{\text{H}_2} = 0.19$	$x_{\text{H}_2\text{O}} = 0.02$

B. STEADY-STATE BEHAVIOR

Steady-state axial concentration and gas and solid temperature profiles at various radial positions and for type I conditions are displayed in Fig. 2 and the corresponding radial temperature profiles are displayed in Fig. 3. The concentration profiles show the mole fractions of CO and CO₂ based on the total inlet moles to keep the results from being obscured by the decrease in total moles due to reaction. At the conditions chosen for type I operation, the methanation reaction is quite rapid and approaches completion. The steam-shift reaction, which is much slower, leads to a slight formation of CO₂. Note that the overall conversion of the CO₂ is actually quite small (less than 1%) at these conditions. At higher temperatures, the conversion of CO₂ is much more significant. The steady-state temperature profiles (Figs. 2b and 3) show that a "hot spot" is present about halfway through the reactor bed and is predominant near the center of the bed. The presence of such a hot spot is a result of the cooling jacket and is common in nonadiabatic packed bed reactors. The steady-state temperature profiles show a difference of up to 10 K between the solid and gas temperatures, and later transient results show differences up to 20 K (leading to differences of over 20% in the reaction rates). In the small region near the cooling wall, even the steady-state temperature differences between the solid and gas are significant due to the higher heat transfer between the solid and cooling wall than that between the gas and the cooling wall. The radial temperature profiles (Fig. 3) also verify the necessity for the radial temperature collocation analysis, since the radial gradients are significant throughout the bed. Notice that except near the cooling wall the catalyst temperature is greater than the gas temperature due to the exothermic reaction occurring on the catalyst surface.

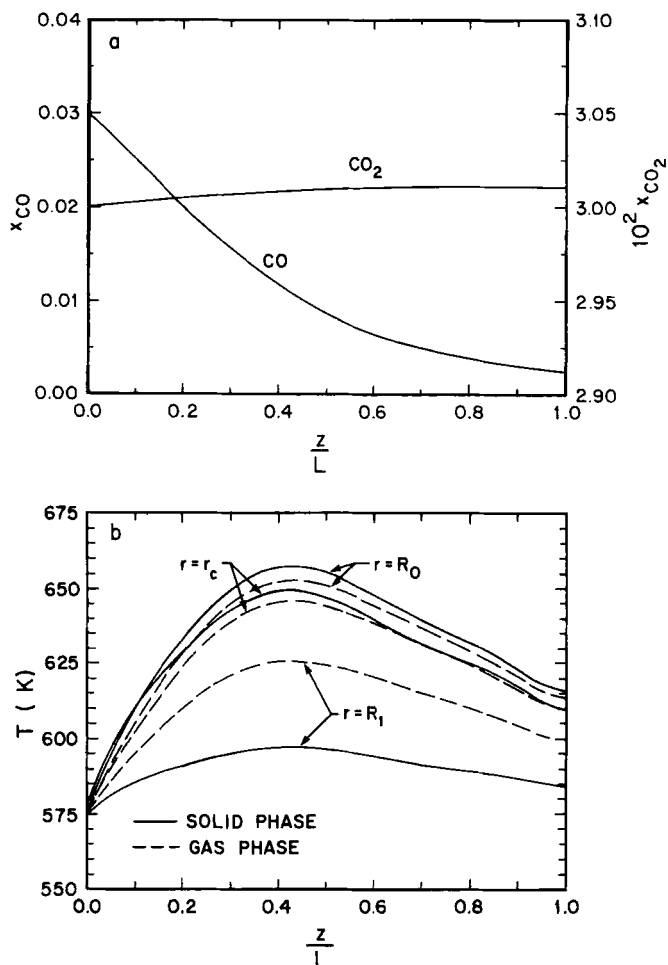


FIG. 2. (a) Steady-state axial profiles, type I conditions. (b) Concentration profiles based on inlet moles.

C. DYNAMIC BEHAVIOR

The real power of the model developed in this work lies in the transient or dynamic simulations such as those necessary for control system design. The model we have developed can be used to simulate the effects on the reactor of various process disturbances and input changes. Under normal reactor operating conditions, step or pulse changes in inlet gas temperatures, concentrations, or velocity or changes in cooling rates can significantly affect

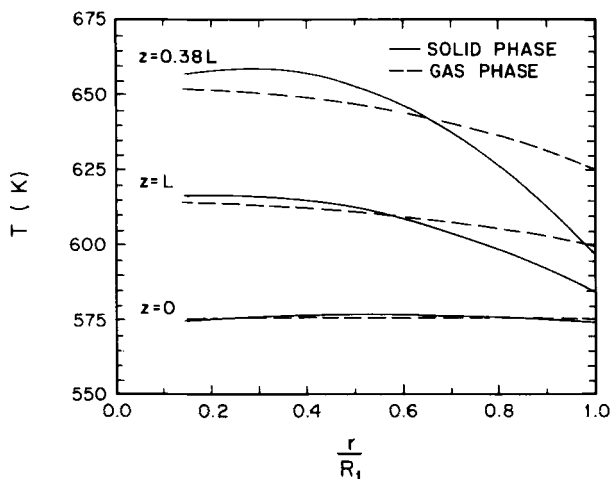


FIG. 3. Steady-state radial temperature profiles, type I conditions.

the behavior of the process. The effect of disturbances on the behavior of the reactor must be understood for optimal system operation and control.

Figure 4 shows the effect of a 10% drop in the inlet gas temperature (from 573 to 515.7 K) on the axial temperature profiles within the reactor for standard type I operating conditions. Although the inlet gas temperature is reduced, the cooling jacket temperature remains unchanged ($T_w = 573$ K),

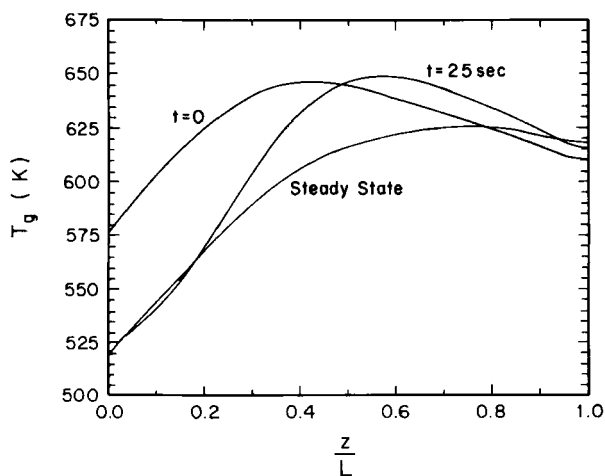


FIG. 4. Response of gas temperature to a 10% drop in inlet gas temperature, type I conditions.

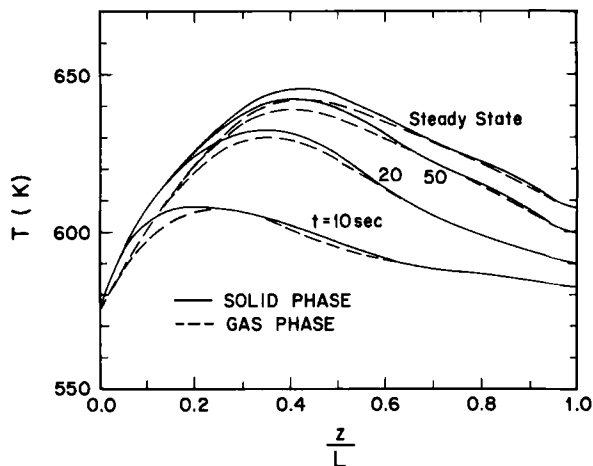


FIG. 5. Gas and catalyst temperature profiles during start-up, type I conditions.

and the cooling jacket acts as a heating system in the early part of the reactor and as a cooling system in the later part, in effect transferring heat from the later stage to the early stage of the reactor. Figure 4 also shows that although the inlet gas temperature is reduced, the steady-state outlet temperature actually increases by about 8 K, since the hot spot shifts further down the reactor, effectively reducing the cooling region. As expected, the responses of the concentration profiles (not shown) are much faster than those of the thermal profiles, indicating the possible applicability of the quasi-steady-state approximation for the concentrations (this will be discussed in detail in Section VIII,B).

Figure 5 shows the axial gas and solid temperature profiles during start-up operation. Notice that the hot spot in the reactor moves down the bed as the heat of reaction increases the temperature of the catalyst particles. Also note the significant temperature difference between the catalyst and gas in the early part of the reactor, where conversion is rapid due to the heat of reaction being generated on the catalyst surface. These differences are even more pronounced (over 20 K) near the center of the bed and near the outer wall.¹¹

D. EFFECTS OF REACTOR OPERATING CONDITIONS ON REACTOR BEHAVIOR

One of the major purposes of accurate mathematical modeling of the reactor bed is to study the effects of various operating conditions on the

¹¹ The profiles shown in Fig. 5 are at the radial collocation point r_c .

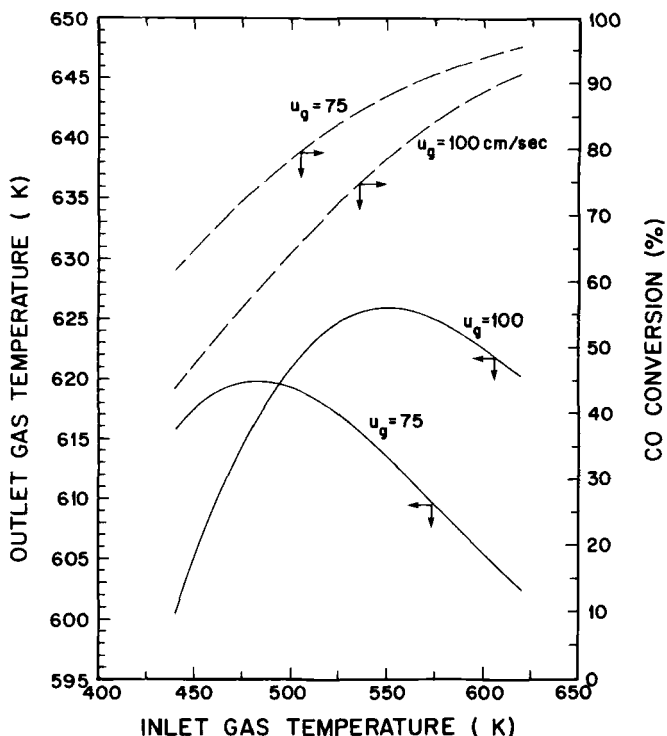


FIG. 6. Effect of inlet gas temperature on outlet gas temperature, type I conditions.

behavior of the reactor, thus allowing process optimization and insight into the performance of the system under changes in various input parameters. This enables careful design of control structures for the experimental system without significant *a priori* experimentation.

Figure 6 shows the effect of the inlet gas temperature on both the outlet gas temperature and CO conversion. As expected, the conversion and the hot spot temperature increase with increasing inlet gas temperature. However, under many conditions, the outlet gas temperature is inversely related to inlet gas temperature. An increase in the inlet gas temperature produces a decrease in the outlet gas temperature¹² as a result of the shifting of the hot spot down the bed (see Fig. 4 also). However, as shown in Fig. 6, this is not true throughout the possible operating regimes. Obviously, this behavior can lead to significant control difficulties if the control design is based on the outlet gas temperature, as is often the case. Figure 6 also shows the significant effect that the inlet

¹² The so-called wrong-way behavior.

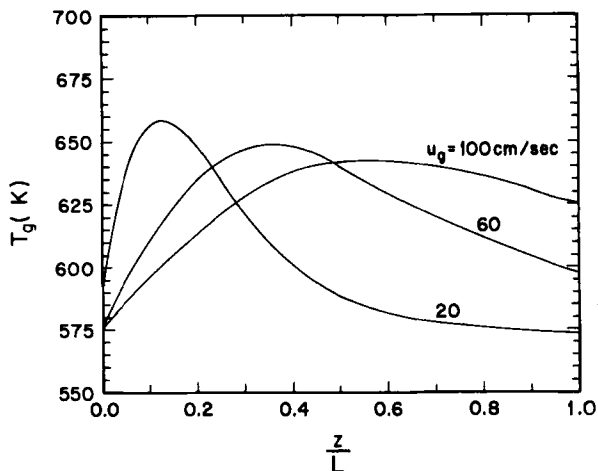


FIG. 7. Effect of inlet gas velocity on steady-state gas temperature profile, type I conditions.

velocity has on conversion and temperatures. Figure 7 shows the steady-state axial gas temperature profiles at various inlet gas velocities. A sudden drop in the inlet flow rate would cause the hot spot to become much more pronounced and to shift towards the entrance of the bed. Major problems could result from the substantial increase in hot spot temperature. The lower flow rates also lead to higher conversions (not shown).

E. ANALYSIS OF RADIAL CONCENTRATION PROFILES

Radial gradients are generally ignored in dynamic modeling of packed bed reactors. As pointed out by Jutan *et al.* (1977), in one of the only other major dynamic packed bed reactor studies that incorporates radial profiles, radial gradients are important in industrial processes where wall cooling is required for safety or control. The original mathematical model developed in this chapter includes complete radial analysis of both the temperature and concentration profiles. In the radial discretization of the model using orthogonal collocation, one interior radial collocation point was used. This along with the two radial boundary values at the thermal well and cooling wall resulted in an inherent assumption of quadratic radial gradients. An examination of experimental measurements (Valstar *et al.*, 1975) and typical radial profiles (Finlayson, 1971) for similar reactors indicates that radial temperature profiles can adequately be represented by a quadratic function of radial position. This quadratic representation is preferable to one of higher

order since the dimensionality of the system is minimized through the use of only one interior collocation point.

However, a quadratic representation of the radial concentration profile may not be adequate since application of zero flux conditions at the inner thermal well and outer cooling wall with a quadratic profile reduces to an assumption of uniform radial concentrations. Although additional radial

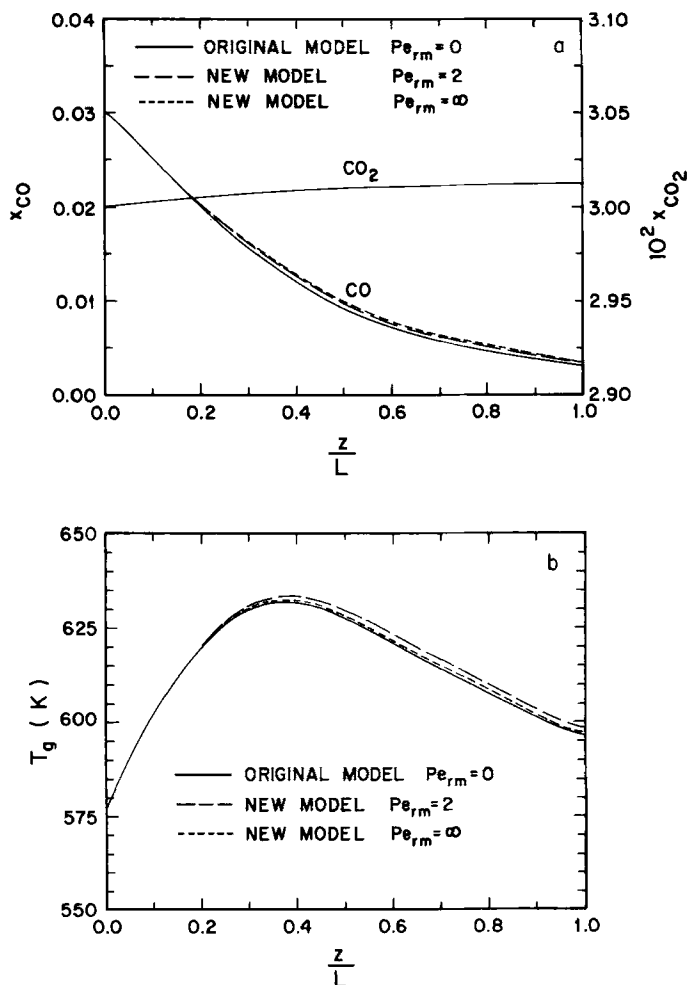


FIG. 8. Gas temperature and CO and CO₂ mole fractions: (a) multipoint radial concentration collocation, type I conditions; (b) gas temperatures at the radial temperature collocation point.

collocation points greatly increase the dimensionality of the resulting model, they may be necessary to accurately express the radial concentration profiles.

Simulations can be performed using additional radial collocation points for the concentration profiles and compared to those using the earlier model. In the simulations, the bulk concentration can then be obtained by integrating the radial profiles:

$$\text{Bulk concentration} = \frac{\int_{R_0}^{R_1} 2\pi r y_i(r) dr}{\int_{R_0}^{R_1} 2\pi r dr} \quad (51)$$

allowing direct comparison with previous simulations. Figure 8 shows a comparison of the axial gas temperature and bulk concentration profiles for the reactor with standard type I operating conditions by using the original model with no radial concentration gradient (i.e., infinite radial diffusion) and by using the new model with a representative radial mass Peclet number of 2.0 and with a radial mass Peclet number of infinity (i.e., no radial diffusion).

Simulations show that the radial and axial temperature and bulk concentration profiles are effectively not influenced by these modeling differences. Figure 9 shows the radial concentration profiles at $\zeta = 0.38$ and at the reactor outlet. Even with very high Peclet numbers, the differences between the radial concentration profile across the relatively small bed and the assumed uniform profile are minimal. Under typical operating conditions with small Peclet numbers, there is no benefit to increasing the number of radial collocation points, especially in light of the increased dimensionality of the resulting system.

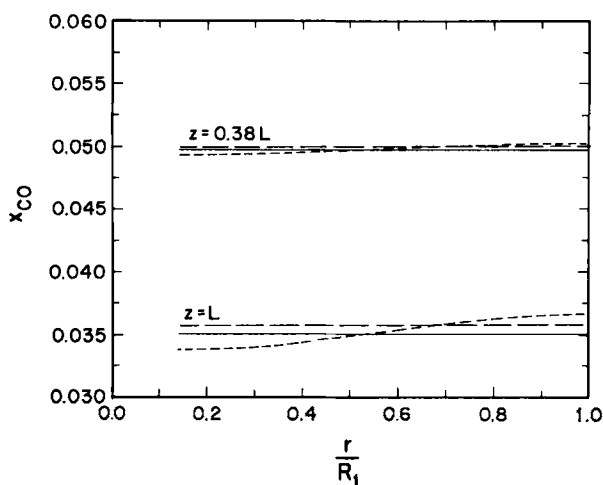


FIG. 9. Radial mole fraction profiles, multipoint radial collocating, type I conditions: —, original model-infinite radial diffusion; —, new model $Pe_{rm} = 2$; ---, new model $Pe_{rm} = \infty$.

F. ADIABATIC CONDITIONS

Modeling of the packed bed catalytic reactor under adiabatic operation simply involves a slight modification of the boundary conditions for the catalyst and gas energy balances. A zero flux condition is needed at the outer reactor wall and can be obtained by setting the outer wall heat transfer coefficients h_{ws} and h_{wg} (or corresponding Biot numbers) equal to zero. Simulations under adiabatic operation do not significantly alter any of the conclusions presented throughout this work and are often used for verification

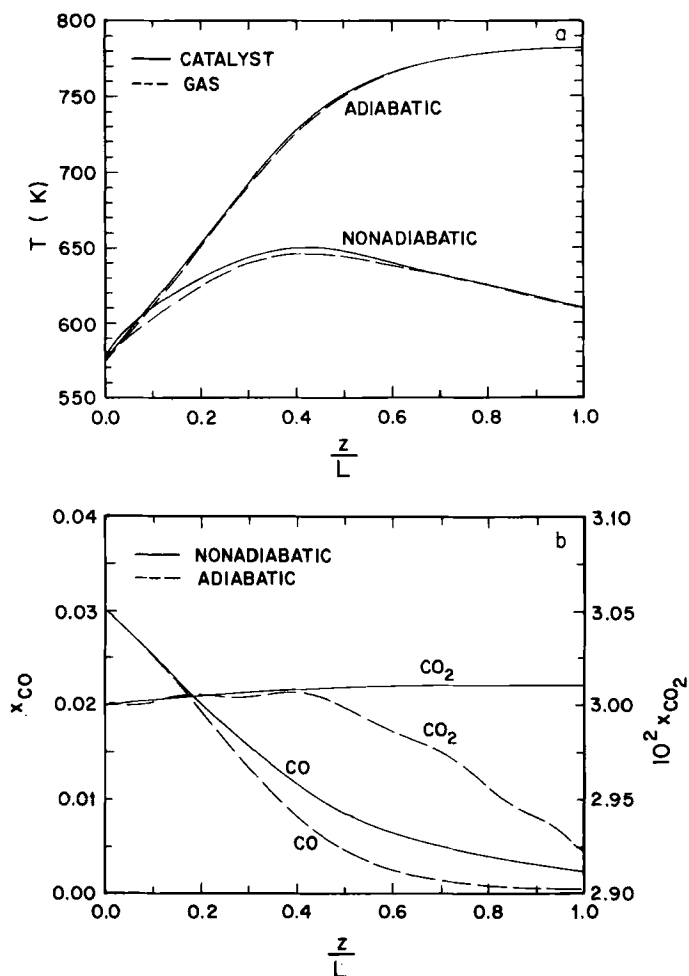


FIG. 10. Adiabatic and nonadiabatic steady-state Profiles, type I conditions.

of worst-case nonadiabatic operation. Figure 10 shows the adiabatic steady-state temperature and concentration profiles for standard type I operating conditions. As expected, the temperature rise through the bed is more dramatic than in the nonadiabatic case, leading to much higher conversions through the bed. Owing to the lack of any cooling, no hot spot develops and all heat generated by the reaction is removed from the bed by the product gas, resulting in a very high temperature rise (200 K) within the bed. Also note that in the adiabatic analysis the temperature difference between the gas and catalyst is negligible. Although the heat transfer coefficient between the gas and solid is as large as in the nonadiabatic case, major differences exist during nonadiabatic operation between the radial heat transfer through each phase.¹³ The results shown in Fig. 10a along with other simulations indicate that a homogeneous analysis of the bed may be adequate for adiabatic operation.

Figure 10b shows that CO conversion is much higher under adiabatic operation due to the higher bed temperatures. Note that the conversion of the CO₂ becomes important as soon as the CO is nearly depleted. The "rippling" in the CO₂ curve is a result of the axial orthogonal collocation.¹⁴ Numerical solution problems such as this will be discussed in Section VII.

G. EFFECT OF THERMAL WELL

The mathematical model developed in this work allows for an analysis of the effects of a central axial thermal well. Although the presence of the well was found to have little effect on the concentration profiles, it significantly alters the transient temperature response of the reactor bed, since its large thermal capacitance increases the thermal time constant of the bed. Figure 11 shows the progression of the radial temperature profiles in the catalyst at the reactor exit ($z = L$) during reactor start-up. As shown, the steady-state profiles are similar, although conduction along the thermal well slightly alters the surrounding gas temperature. The transient behavior exemplifies the slow response of the thermal well. It can be seen that the response of the exit temperature profile is rapid without the well, with steady state being approached in under 1 min; whereas the presence of the well introduces a finite heat sink into the reactor center that slowly absorbs some of the heat produced. More than 5 min are necessary to approach steady state with a ($\frac{1}{8}$)-in.-diameter well. This is further seen in Fig. 12, where the temporal

¹³ The heat transfer coefficient from the solid to the outer wall and the radial conduction in the solid is greater than the corresponding parameters in the gas phase.

¹⁴ Although only 6 axial collocation points are used in most simulations, 12 points were necessary here and even then the results are less than optimum.

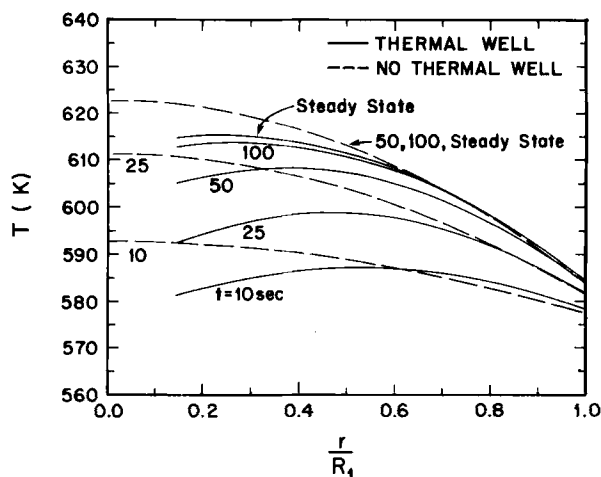


FIG. 11. Effect of thermal well on transient radial temperature profiles, type II conditions.

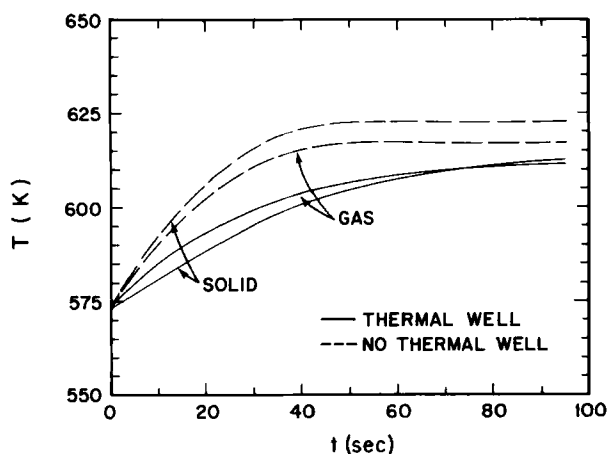


FIG. 12. Dynamic behavior of temperatures at outlet of bed, type II conditions.

behavior of the catalyst and gas temperatures at the reactor exit are compared with and without the presence of the thermal well. Figure 11 also shows that the temperatures in the reactor center are higher without the thermal well, as would be expected. However, the simulations show that the well has very little effect on the axial concentration profiles, and overall conversion is only slightly affected.

Although the thermal well increases the thermal capacitance of the reactor bed and reduces the reaction volume, these effects alone cannot account for the dramatic increase in the thermal time constants of the bed with a thermal well.¹⁵ Whereas the dynamics of the catalyst particle temperatures are very fast due to the heat generation on the particles from the exothermic reactions, the dynamics of the thermal well temperatures are much slower since the heat is generated on the surrounding particles. Much of this energy is transferred to the outer cooling jacket or out of the bed with the gas phase. Only a small portion is transferred to the thermal well and even this through relatively slow mechanisms, thus resulting in the slow dynamic behavior of the well. Since a thermal well is sometimes used in industry to obtain temperature measurements for process monitoring or control, we note the importance of incorporating even a relatively small well into the modeling and control analysis.

Simple modifications to the model development presented in this work allow for simulating systems that do not include a central thermal well. For these cases, the heat transfer coefficients h_{ig} and h_{is} and the inner radius R_0 are set equal to zero and the energy balance for the thermal well is neglected. In such cases, the dimensionality of the mathematical system is reduced by N , since one partial differential equation is eliminated.

VII. Orthogonal Collocation on Finite Elements

Due to the reversibility of the reactions and the equilibrium constraints included in the rate expressions, severe temperature and concentration profiles are generally not observed in this system. As a result, the orthogonal collocation procedure used for the numerical solution of the resulting model shows little numerical instability and allows for rapid solution of most profiles simply by increasing the number of collocation points. However, in many chemical systems, the interesting features of the solution are confined to a small region where the solution profile changes rapidly. The orthogonal collocation method may become unwieldy in such a case because a large number of collocation points may be needed so that enough are placed within this region to provide an accurate representation of the solution.

A drawback of the orthogonal collocation technique is its inability to accurately define profiles with sharp gradients or abrupt changes, since the

¹⁵ Due to the relatively small radius of the well, the thermal capacitance $V\rho c_p$ of the bed with the thermal well (16 cal/K) is only slightly higher than that without (14 cal/K) and the loss in reaction volume is only about 2%.

technique requires fitting a single polynomial to the entire profile. Under such cases, although the solution will be exact at the collocation points, significant oscillations in the profile can be observed. An obvious alternative would be to resort to a finite difference procedure in which accurate representation of the solution is then possible even under extremely steep gradients simply by increasing the number of grid points. However, this technique can easily become computationally prohibitive due to the extremely high dimensionality of the resulting system. A compromise between the orthogonal collocation (OC) and finite difference techniques has been proposed by Carey and Finlayson (1975). This procedure is called orthogonal collocation on finite elements (OCFE).

A. FORMULATION OF THE OCFE TECHNIQUE

Finlayson (1980) used the OCFE procedure for several examples with sharp gradients, including diffusion and reaction in a porous catalyst pellet and transient convective diffusion. His analysis of the orthogonal collocation method, the finite difference method, and the orthogonal collocation on finite elements scheme for these and other chemical systems shows that the "orthogonal collocation method is by far and away the best method" except for systems with sharp profiles, in which case, the OCFE technique is then preferred. Finlayson points out that detailed, comparative studies of even simple two-dimensional problems using OCFE are rare due to the complexity of the procedure. This section provides the first OCFE analysis of a heterogeneous packed bed reactor model along with comparisons to simple orthogonal collocation results. This OCFE analysis is performed on the two-dimensional system resulting after the radial orthogonal collocation presented in Section V,C.

Two major forms of the OCFE procedure are common and differ only in the trial functions used. One uses the Lagrangian functions and adds conditions to make the first derivatives continuous across the element boundaries, and the other uses Hermite polynomials, which automatically have continuous first derivatives between elements. Difficulties in the numerical integration of the resulting system of equations occur with the use of both types of trial functions, and personal preference must then dictate which is to be used. The final equations that need to be integrated after application of the OCFE method in the axial dimension to the reactor equations (radial collocation is performed using simple orthogonal collocation) can be expressed in the form

$$\mathbf{K} \frac{d\mathbf{a}}{dt} = \mathbf{A}\mathbf{a} - \mathbf{f}(\mathbf{a}) \quad (52)$$

Using Hermite interpolation within the elements, the \mathbf{K} matrix is not diagonal. Explicit solution methods cannot be applied to this system of equations easily because of this nondiagonal matrix, and most integration packages are also not suitable for such a system. However, using Lagrangian functions within the elements, the continuity and boundary conditions have no time derivatives, and the \mathbf{K} matrix in the preceding equation is diagonal with nonzero elements representing a residual and zero diagonal elements for the algebraic conditions. Most standard integration packages are also not suitable for mixed systems of algebraic and differential equations.

The OCFE discretization analysis and computer programs that we will describe allow general specification of the number of finite elements and the degree of the collocation functions within each element. This is again an advancement over prior analyses where the same degree of collocation was often used within each element. The entire domain is divided as shown in Fig. 13. Within each of N_E elements, we apply orthogonal collocation as usual by using Lagrangian functions. The residual is evaluated at the internal collocation points. Using the Lagrangian polynomials, we need to guarantee continuity of the first derivatives or fluxes between elements. In our analysis, we use the continuity of the first derivative. We thus append $N_E - 1$ conditions at the element boundaries. Then the solution has continuous derivatives throughout the domain. With the additional two boundary conditions at $\zeta = 0$ and $\zeta = 1$, there are a sufficient number of conditions to solve for the profile at all of the collocation points and at the element boundaries.

For the k th element, we define the transformation

$$u = (z - z_{(k)})/h_k \quad (h_k = z_{(k+1)} - z_{(k)}) \quad (53)$$

so that the variable u is between zero and one in the element.¹⁶ Redefining the differential equations in terms of the variable u allows the application of standard orthogonal collocation within each element. Figure 14 illustrates the local numbering system within each element. If we then define N_E as the number of elements, N_k as the number of interior collocation points in element k , and M_k as $N_k + 2$, the relation between the global numbering i, j and the local numbering I, J is given by

$$i = \left[\sum_{j=1}^{k-1} (N_j + 1) \right] + I, \quad z_i = z_{(k)} + u_I h_k \quad (54)$$

Then starting from the most general form of the dimensionless equations after the one-point radial collocation, we can apply the OCFE procedure. As

¹⁶ Note that z in this expression is the normalized axial coordinate (equivalent to ζ).

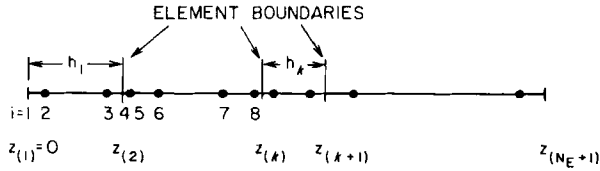


FIG. 13. Orthogonal collocation on finite elements global indexing system.

an example, let us consider the energy equation for the solid:

$$\begin{aligned} \frac{\partial \Theta_s}{\partial \eta} &= \alpha_s \frac{\partial^2 \Theta_s}{\partial \zeta^2} + \omega_1 \Theta_s + \omega_2 \Theta_t + \gamma_s \Theta_g + \kappa_1 (1 + \varphi_1 \Theta_s) R'_M \\ &\quad + \kappa_2 (1 + \varphi_2 \Theta_s) R'_s + \omega_3 \end{aligned} \quad (55)$$

$$\begin{aligned} z = 0 \quad \frac{\partial \Theta_s}{\partial \zeta} &= \lambda_{gzs} (\Theta_s - \Theta_g) \\ z = 1 \quad \frac{\partial \Theta_s}{\partial \zeta} &= \lambda_{gzs} (\Theta_g - \Theta_s) \end{aligned}$$

All temperatures in this equation are in terms of the conditions at the radial collocation point.

Then for $k = 1$ to N_E

$$z = z_{(k)} + u h_k \quad (56)$$

Thus within each element

$$\begin{aligned} \frac{\partial \Theta_s}{\partial \eta} &= \frac{\alpha_s}{h_k^2} \frac{\partial^2 \Theta_s}{\partial u^2} + \omega_1 \Theta_s + \omega_2 \Theta_t + \gamma_s \Theta_g + \kappa_1 (1 + \varphi_1 \Theta_s) R'_M \\ &\quad + \kappa_2 (1 + \varphi_2 \Theta_s) R'_s + \omega_3 \end{aligned} \quad (57)$$

with the overall boundary conditions

$$\left. \frac{1}{h_1} \frac{\partial \Theta_s}{\partial u} \right|_{u=0} = \lambda_{gzs} (\Theta_s - \Theta_g), \quad \left. \frac{1}{h_{N_E}} \frac{\partial \Theta_s}{\partial u} \right|_{u=1} = \lambda_{gzs} (\Theta_g - \Theta_s)$$

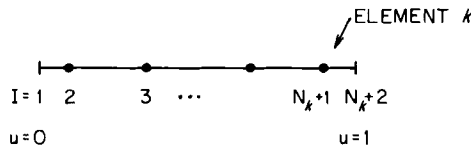


FIG. 14. Orthogonal collocation on finite elements local indexing system.

If we assume axial profiles within each element $k = 1, \dots, N_E$ of the form

$$\Theta_s(u, t) = \sum_{I=1}^{M_k} \Theta_{sII}(t) L_{II}(u) \quad (58)$$

where as before L_{II} are Lagrangian interpolation polynomials, then as usual

$$A_{I,J} = \frac{dL_J(u)}{du} \Big|_{z_{II}}, \quad B_{I,J} = \frac{d^2 L_J(u)}{du^2} \Big|_{z_{II}} \quad (59)$$

After applying orthogonal collocation,

$$\begin{aligned} \frac{d\Theta_{sII}}{d\vartheta} = & \frac{\alpha_s}{h_k^2} \sum_{J=1}^{M_k} B_{I,J} \Theta_{sJ} + \omega_1 \Theta_{sII} + \omega_2 \Theta_{tII} + \gamma_s \Theta_{gII} + \kappa_1 (1 + \varphi_1 \Theta_{sII}) R'_M \\ & + \kappa_2 (1 + \varphi_2 \Theta_{sII}) R'_S + \omega_3 \end{aligned} \quad (60)$$

within element k for the interior collocation points $II = 2, \dots, N_k + 1$.

Then if we require the continuity of the first derivatives between the elements so that the first derivative of the solution is continuous in the entire domain $0 \leq \zeta \leq 1$,

$$\left[\frac{1}{h_{k-1}} \sum_{J=1}^{M_{k-1}} A_{M_{k-1},J} \Theta_{sJ} \right]_{\text{element } k-1} = \left[\frac{1}{h_k} \sum_{J=1}^{M_k} A_{I,J} \Theta_{sJ} \right]_{\text{element } k} \quad (61)$$

The system boundary conditions then only affect the first and last elements:

$$\begin{aligned} \frac{1}{h_1} \sum_{J=1}^{M_1} A_{I,J} \Theta_{sJ} &= \lambda_{gzs} (\Theta_{s_1} - \Theta_{g_1}) \\ \frac{1}{h_{N_E}} \sum_{J=1}^{M_{N_E}} A_{N_E,J} \Theta_{sJ} &= \lambda_{gzs} (\Theta_{g_{M_{N_E}}} - \Theta_{s_{M_{N_E}}}) \end{aligned} \quad (62)$$

This same analysis is then performed for the energy balance for the gas, the energy balance for the thermal well, the two mass balances, and the continuity equation. The final coupled system of algebraic and differential equations consists of $5N$ ordinary differential equations and $N + 6(N_E + 1)$ algebraic equations, where

$$N = \sum_{k=1}^{N_E} N_k \quad (63)$$

It should be pointed out that this approach using Lagrangian polynomials gives identical results to those that would be obtained using Hermite polynomials since on each element we use orthogonal polynomials of the same order, since the boundary conditions are satisfied by both solutions, since the residuals are evaluated at the same points, and since the first derivatives are continuous across the element boundaries. The only preference for one over

the other is for convenience. The Lagrangian formulation, however, has the added advantage of being applicable in situations where the flux is continuous across the element boundaries but the first derivative is discontinuous. This can occur if there is some type of physical change at the boundary.

A major advantage of the orthogonal collocation solution schemes is that the optimal location of the collocation points is automatically determined as the zeros of the orthogonal polynomial after specification of the number of collocation points. This point carries through to the OCFE technique; however, in this procedure, one must also specify the number and position of the elements. Several means for this are available. The simplest involves preliminary solutions using orthogonal collocation to provide reasonable estimates since, even though the OC solution may be numerically unsatisfactory due to oscillations in the profiles, it can give accurate indications of break points in the profiles.

If the OCFE solution procedure is to be used regularly for system analysis, a careful study of the problem of locating elements is necessary. Finlayson (1980) gives a basis for this study in a cursory examination of variable grid spacing and elements sizes, or "adaptive meshes" as he calls them. The simplest procedure is based on physical information about the solution profile such as in the present case the point where CO is depleted within the reactor bed.

B. MODEL COMPARISONS

A large number of steady-state simulations were performed using this OCFE procedure. Using the reversible rate expressions considered throughout this chapter, the importance of the OCFE procedure is not fully perceived since even for conditions with very steep profiles, an accurate, non-oscillating solution can usually be obtained simply by increasing the number of collocation points in the orthogonal collocation analysis.¹⁷ Due to the reversibility of the kinetics and the relatively low activation energy, the profiles remain relatively smooth without any abrupt changes or sharp transitions.

Figure 15 shows the axial gas temperature and concentration profiles for type 1 conditions with the velocity reduced to $u_{g0} = 15$ cm/sec, which leads to steep profiles with nearly complete conversion of the CO early in the reactor bed. This figure shows a comparison of the steady-state profiles using both orthogonal collocation with eight collocation points and orthogonal collocation on finite elements. As shown, the numerical problems (oscillatory solution) exhibited in the orthogonal collocation solution with eight collocation points are completely eliminated by using OCFE with appropriate selection of the

¹⁷ Figures 10b shows simulations using orthogonal collocation with possible numerical difficulties.

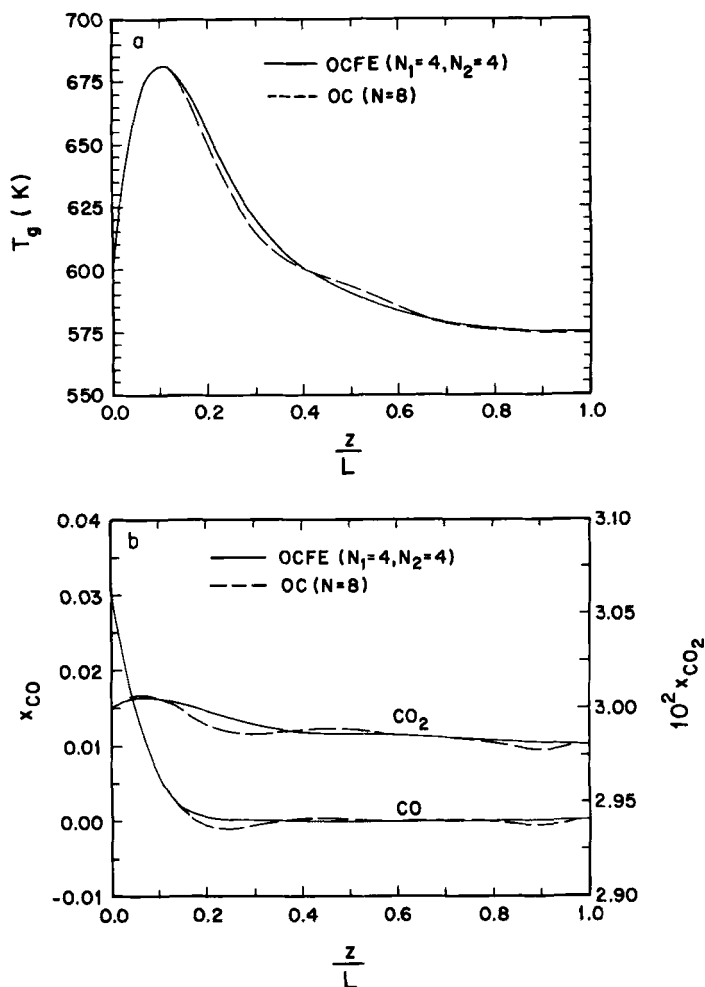


FIG. 15. Comparison of profiles computed by orthogonal collocation and orthogonal collocation on finite elements.

elements and order of collocation within the elements. Based on an expected abrupt change in the concentration profile at about $\zeta \approx 0.20$ (from the preliminary orthogonal collocation results), an OCFE solution was obtained using two elements of length 0.2 and 0.8 with $N_1 = 4$ and $N_2 = 4$ or a total of eight interior collocation points and one interior boundary point.

As shown in Figure 15, the OCFE procedure is capable of handling the abrupt concentration profile change where the reaction reaches completion

while the orthogonal collocation procedure shows significant error in the profiles. Increasing the number of collocation points in either element for the OCFE solution has no significant beneficial effect on the axial profiles and can introduce oscillations in the elements. Increasing the number of elements without using sufficient interior collocation points or misplacing the elements can lead to anomalous results owing to the individual polynomial representations and continuity conditions at the element boundaries.

VIII. Evaluation of Common Physical Simplifications in Packed Bed Modeling

Due to the complexities of the full mathematical description of a packed bed reactor and the complications with numerical solution, the extensive use of physical modeling simplifications is common. Assumptions that reduce the complexity of the resulting mathematical model such as neglecting dispersion effects and radial gradients have been discussed earlier. Basically, the common assumptions of neglecting radial temperature gradients, neglecting thermal dispersion, and neglecting the variation of physical properties may reduce the accuracy of the resulting model without reducing the dimensionality of the resulting representation.

To this point, all of the mechanisms necessary for the accurate description of the physical and chemical phenomena occurring in the packed bed reactor have been included and the effects of various modeling simplifications have been studied. We continue this analysis by considering several major simplifications that do not simply reduce the structure of the partial differential equations but actually significantly reduce the number of necessary equations or the dimensionality of the model. These simplifications include the extensive use of pseudohomogeneous models—those that do not distinguish between the conditions within the fluid and those on the solid catalyst—and the assumptions of quasi steady state for concentrations and negligible energy accumulation in the gas phase.

Table V shows some typical criteria used for evaluating the potential approximations for packed bed reactor modeling. Many other criteria are also used and some of these are referenced in this chapter.

A. DISPERSION EFFECTS

Much work has been focused on the significance of dispersion terms in the transient material and energy equations for packed bed reactors. In general, axial diffusion of mass and energy and radial diffusion of mass have been

TABLE V
APPROXIMATIONS IN PACKED BED REACTOR MODELING^a

Approximation	Criteria
Neglect axial dispersion	$L/d_p > 50$ for $Re > 20$ (Carberry, 1976)
Quasi steady state for concentration	$(1 - \epsilon)\rho_s c_{p_s} / \epsilon \rho_g c_{p_g} \gg 1$
Pseudohomogeneous analysis	$T_s - T_g \approx \gamma \lambda \Delta A / \beta$ small (Wei <i>et al.</i> , 1984)
Negligible energy accumulation in gas	$(1 - \epsilon)\rho_s c_{p_s} / \epsilon \rho_g c_{p_g} \gg 1$

^a For the pseudohomogeneous analysis criterion, a predictive expression for the temperature difference between the gas- and solid-phase temperatures for a fixed bed reactor is given by Wei *et al.* (1984). In this expression, β is the dimensionless heat transfer coefficient, ΔA is the total heat generation in the reactor, and γ is the fraction of the heat effect going to the solid phase. For the example packed bed reactor used throughout this chapter, the temperature difference between the gas and solid phases is in many cases up to 10 K.

neglected in comparison with convective terms in most packed bed reactor studies (Carberry and Wendel, 1963; De Wasch and Froment, 1971; Hlavacek, 1970; Hoiberg *et al.*, 1971; Jutan *et al.*, 1977; Valstar *et al.*, 1975).

For packed bed reactors, Carberry and Wendel (1963), Hlavacek and Marek (1966), and Carberry and Butt (1975) report that axial dispersion effects are negligible if the reactor length is sufficient. These and other researchers (Young and Finlayson, 1973; Mears, 1976) have developed criteria based on the reactor length for conditions where axial dispersion can safely be neglected. The criterion shown in Table V is a classic criterion for neglecting axial mass dispersion. The works by Young and Finlayson (1973) and Mears (1976) provide more detailed criteria to predict when axial dispersion is unimportant in nonisothermal packed bed reactors.

Since the tube length/pellet diameter for the conditions we are examining is about 150, just at the limit of most of the published criteria for neglecting axial dispersion of energy, careful analysis of these dispersion effects is needed.¹⁸ However, neglecting axial mass dispersion should be a safe assumption since the tube length/pellet diameter is well above the value of 50 generally recommended. Radial mass dispersion can also be neglected and is inherently eliminated from our model since the one-point radial collocation results in a uniform radial concentration profile. However, radial diffusion of energy must be retained since it is one of the most important physical processes influencing the dynamic and steady-state behavior of the system.

Simulations using the full model were used to study the influence of these dispersion effects and to verify some of the common assumptions. A wide

¹⁸ Yu *et al.* (1982, 1983) give an example of a moving-bed coal gasifier in which axial thermal dispersion must be included in the model.

range of Peclet numbers were used in the simulations. On the basis of extensive previous studies, the radial gas Peclet number should range from 5 to 10 and the axial gas Peclet numbers from 0.5 to 2.0 (Carberry, 1976). For completeness, our simulations used Peclet numbers over a wider range.

Comparison of steady-state profiles shows that neglecting axial mass diffusion has very little effect on the temperature and concentration profiles even though the axial gradients are significant. However, Figure 16 shows that neglecting the axial thermal dispersion in the gas does affect the solution

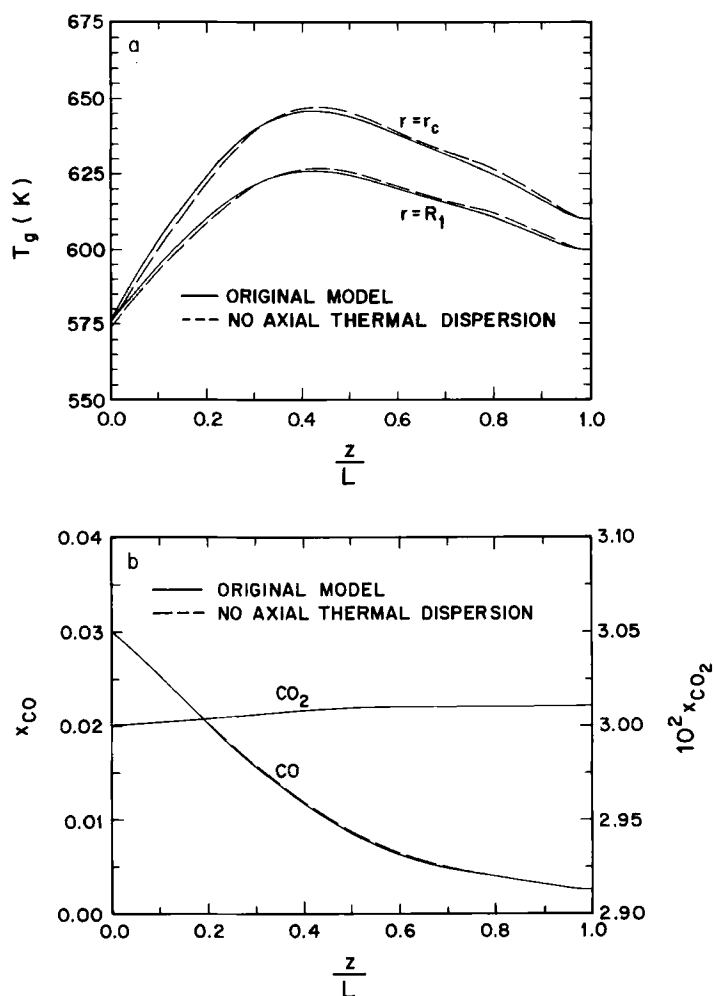


FIG. 16. Steady-state profiles neglecting axial thermal dispersion, type I conditions.

profiles somewhat. The axial temperature profiles are offset and the concentration profiles are shifted slightly. Further simulations show minimal effect of neglecting the axial conduction of energy in the solid.

The figure also shows that neglecting the axial thermal dispersion leads to slight instabilities ("rippling") in the orthogonal collocation solution of the axial temperature profile with six collocation points. This rippling, which is even more pronounced under type II conditions, is a result of the axial orthogonal collocation and in this case can be reduced by increasing the number of collocation points. However, this leads to a substantial increase in model dimensionality and thus solution time. Obviously, the axial thermal diffusion has a stabilizing effect on the numerical solution using orthogonal collocation and actually damps the behavior of the solution polynomial.

The reduction in solution time for these simulations is minimal and in some cases the elimination of the axial diffusion terms actually increases the solution time. Simulations show that neglecting the axial dispersion of mass has little effect on numerical computation time, whereas eliminating axial dispersion of energy may significantly increase computation time and only rarely decreases it substantially.

In summary, our analysis of the effects of dispersion on the simulated behavior of the reactor, along with the work by Bonvin (1980), shows the necessity of including the thermal dispersion terms. Simulations here verify that the numerical stability of the model is greatly enhanced by retaining these dispersive effects and that, although minor additional effort may be necessary in the model development, the numerical solution time may actually be reduced by retaining some of these terms. Furthermore, simulations verify that the axial dispersion of mass can usually be neglected, although the inclusion of these terms in the model introduces little complication in the collocation solution; whereas other solution procedures are often significantly hindered by these second derivative terms. The radial dispersion of mass seemingly has little effect on either the simulated results using a detailed radial concentration analysis as presented in Section VI,E or solution times and can safely be neglected.

B. HOMOGENEOUS VERSUS HETEROGENEOUS MODEL

De Wasch and Froment (1971) and Hoiberg *et al.* (1971) published the first two-dimensional packed bed reactor models that distinguished between conditions in the fluid and on the solid. The basic emphasis of the work by De Wasch and Froment (1971) was the comparison of simple homogeneous and heterogeneous models and the relationships between "lumped" heat transfer parameters (wall heat transfer coefficient and thermal conductivity) and the "effective" parameters in the gas and solid phases. Hoiberg *et al.* (1971)

presented the first detailed, two-dimensional, heterogeneous dynamic modeling analysis (a homogeneous analysis was used for the steady-state calculations). This work considered the amount of detail necessary in dynamic models through a comparison of experimental and calculated results for a packed bed reactor in which the highly exothermic reaction between hydrogen and oxygen occurred on a platinum catalyst. A limitation of this work was the amount of detail possible for numerical solution using the finite difference solution scheme.

In our original system of partial differential equations, to obtain a pseudohomogeneous model the two energy balances can be combined by eliminating the term $(U_{sg}/V_b)(T_s - T_g)$, that describes the heat transfer between the solid and the gas. If the gas and solid temperatures are assumed to be equal ($T_s = T_g$)¹⁹ and the homogeneous gas/solid temperature is defined as T , the combined energy balance for the gas and solid becomes

$$[\rho_s c_{ps}(1 - \varepsilon) + \rho_g c_{pg} \varepsilon] \frac{\partial T}{\partial t} = -\rho_g c_{pg} u_g \varepsilon \frac{\partial T}{\partial z} + k_z \frac{\partial^2 T}{\partial z^2} + k_r \left[\frac{\partial^2 T}{\partial r^2} + \frac{1}{r} \frac{\partial T}{\partial r} \right] + (-\Delta H_M) R_M + (-\Delta H_S) R_S \quad (64)$$

where k_z and k_r are effective conductivities for the combined gas–solid system. Additionally, since

$$\frac{\rho_g c_{pg} \varepsilon}{\rho_s c_{ps}(1 - \varepsilon)} \approx 0.004 \quad (65)$$

the coefficient of the time derivative reduces to

$$[\rho_s c_{ps}(1 - \varepsilon) + \rho_g c_{pg} \varepsilon] \approx \rho_s c_{ps}(1 - \varepsilon) \quad (66)$$

The boundary conditions are

$$\begin{aligned} z = 0, \quad k_z \frac{\partial T}{\partial z} &= u_g c_{pg} \rho_g \varepsilon (T - T_0) \\ z = L, \quad \frac{\partial T}{\partial z} &= 0 \\ r = R_0, \quad k_r \frac{\partial T}{\partial r} &= h_i (T - T_i) \\ r = R_1, \quad -k_r \frac{\partial T}{\partial r} &= h_w (T - T_w) \end{aligned} \quad (67)$$

¹⁹ Wei *et al.* (1984) show that the average temperature difference between the solid and gas phase is $\gamma \lambda \Delta A / \beta$ for fixed bed reactors. This then defines one possible criterion for the applicability of the pseudohomogeneous model as given in Table V. Another possible criterion is that given by Vortmeyer and Schaefer (1974), discussed later in this section.

where h_i and h_w are effective heat transfer coefficients between the gas–solid medium and the thermal well and cooling wall, respectively.

Equation (64) is solved with the continuity equation, the energy balance for the thermal well,²⁰ and the concentration equations by using the same procedure as for the full system. The dimensionality of the model has now been reduced by N (i.e., the model now has order $4N$). Although standard mixing rules can be used to develop relationships between the effective and overall heat transfer coefficients of the homogeneous model (k_z, k_r, h_i, h_w, U_i) and the individual gas and solid coefficients of the two-phase model ($k_{zs}, k_{zg}, k_{rs}, k_{rg}, h_{is}, h_{ws}, h_{ig}, h_{wg}, U_{is}, U_{ig}$), the significance of direct comparisons between the simulations with the two-phase analysis and the homogeneous analysis is questionable due to the limited accuracy of these mixing rules. Some attempts (Vortmeyer and Schaefer, 1974) have been made to improve these mixing rules, but are not accurate enough for direct comparison of the simulations of the two models.

Solution times using the homogeneous model are 15 to 25% less than that for the full two-phase analysis, although the accuracy of the results may be somewhat in question. Figure 17 shows the axial temperature and concentration profiles under type I operating conditions. Although these simulations appear similar to those obtained with the heterogeneous analysis, no direct comparison is possible, as was explained earlier.

However, simulations using the heterogeneous analysis even with high inlet velocities lead to steady-state temperature profiles with differences of up to 10 K between the solid and gas phases and transient results with differences up to 20 K due to the high exothermicity of the methanation reaction on the catalyst surface. These temperature differences can lead to significant errors in the predicted reaction rates. Therefore, although a homogeneous analysis may be adequate for reactions that are only slightly exothermic or simulations of steady-state phenomena, a heterogeneous analysis is necessary for dynamic simulations of highly exothermic reaction processes.²¹

The increased dimensionality of the heterogeneous system can be reduced using other techniques that require much milder assumptions. For example, the assumption of negligible energy accumulation in the gas phase based on

²⁰ With an overall heat transfer coefficient being used rather than U_{is} and U_{ig} .

²¹ Measurement difficulties that arise in model verification or parameter estimation using a heterogeneous analysis are also often cited as reasons for a homogeneous analysis. Although theoretically it is possible to measure separately the gas and solid temperatures, in practice it is difficult without seriously affecting flow patterns within the reactor bed. These difficulties can be minimized by using an internal thermal well, as is common in industrial systems, and including this thermal well in the model development. This eliminates the concern over whether temperature measurements within the reactor bed are actually measuring gas or solid temperatures or a combination of both.

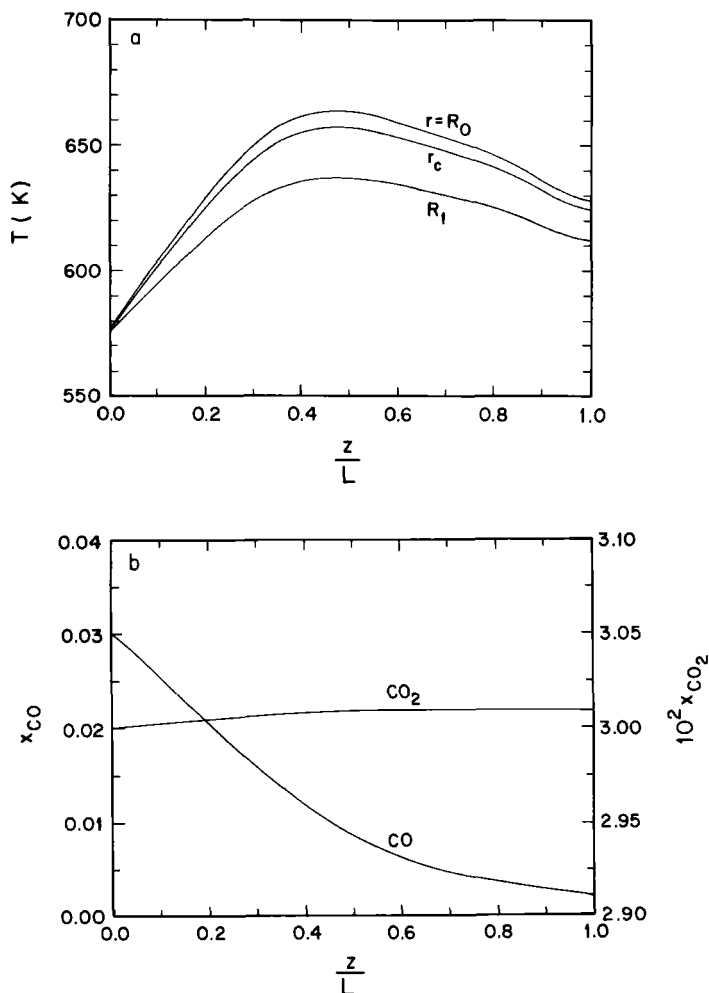


FIG. 17. Steady-state profiles, homogeneous model, type I conditions.

the approximation [Eq. (66)] provides the same reduction in system dimensionality as the homogeneous analysis.

Another procedure often used with less stringent assumptions than the equality of the gas and solid temperatures is the pseudohomogeneous analysis proposed by Vortmeyer and Schaefer (1974). This procedure has proved to be quite effective for simple adiabatic packed bed analyses and involves reducing the energy balances for the gas and catalyst to a single equation using the

assumption

$$\frac{\partial^2 \Theta_g}{\partial z^2} = \frac{\partial^2 \Theta_s}{\partial z^2} \quad (68)$$

Justification for this assumption is strictly empirically based.

Although this assumption is often not too restrictive, additional assumptions must be introduced to reduce the mathematical model to the pseudohomogeneous form for reactors that are nonadiabatic or require radial temperature considerations. For the full mathematical model, the following assumptions would be necessary in addition to Eq. (68): first negligible energy accumulation in the gas phase; second, no axial diffusion in the gas phase or

$$\frac{\partial}{\partial z} \left[\frac{\partial^2 T_g}{\partial z^2} \right] = 0$$

third,

$$\frac{\partial}{\partial r} \left[\frac{1}{r} \frac{\partial T_s}{\partial r} \right] = \frac{\partial}{\partial r} \left[\frac{1}{r} \frac{\partial T_g}{\partial r} \right]$$

and fourth,

$$\frac{\partial(\rho_g u_g)}{\partial z} = 0$$

These assumptions are often too restrictive for standard nonadiabatic packed bed analyses and should be tested carefully before being used.

C. QUASI-STEADY-STATE APPROXIMATION FOR CONCENTRATION

Transient simulations using the full, nonlinear model show that under the conditions studied concentration profiles reach a quasi steady state quite rapidly (often within 3 to 5 sec), whereas the thermal response of the reactor bed is much slower²² due to the large heat capacity of the reactor bed and thermal well. An example of this phenomenon is shown in Fig. 18, where the transient responses of the solid temperatures, thermal well temperatures, and concentrations are shown for a major step change in the inlet gas temperature and inlet CO concentration. In this example, the effect of the step change is nearly immediate on the concentration profiles, with the major effect being within the first 10 sec. However, Fig. 18a shows that the thermal well temperatures and the catalyst temperatures take up to 10 times as long as the

²² Thermal time constants are about two orders of magnitude greater than the concentration time constants.

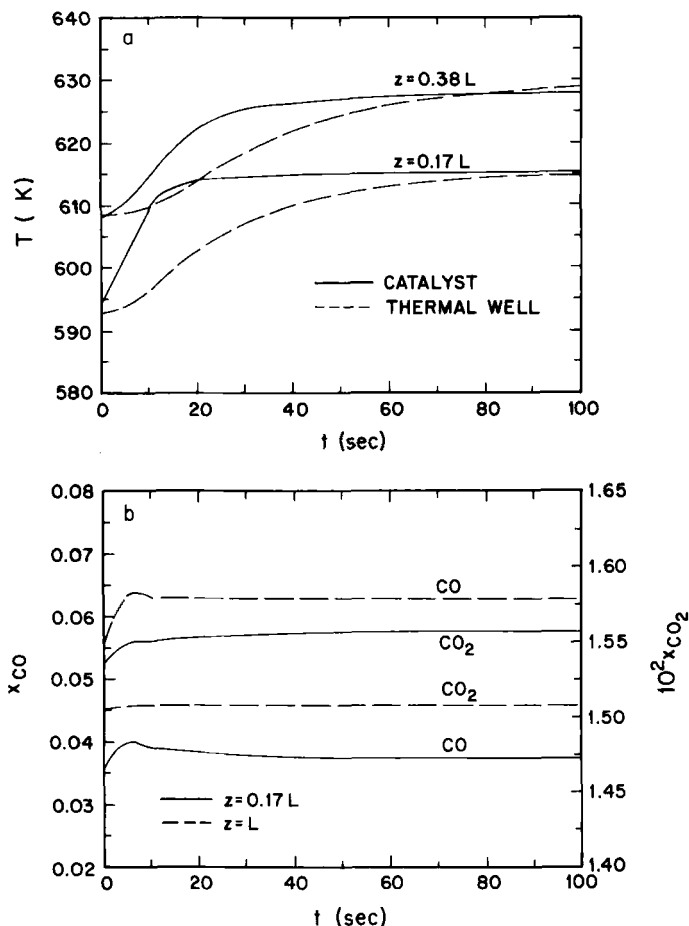


FIG. 18. Transient response to step-input change of T_0 from 573 to 593 K and x_{CO}^0 from 0.06 to 0.07, type II conditions.

concentrations to approach the new steady state after the input step change. Note that the catalyst temperatures shown in the figure are at the radial collocation point $r = r_c$ and that the response of the catalyst temperatures near the center of the reactor (not shown) is very similar to that of the thermal well.

Furthermore, comparison of the thermal v_T and the concentration v_C wave velocities as defined by Gould (1969)

$$v_T = \frac{\rho_g c_{p_g} u_g \varepsilon}{\rho_s c_{p_s} (1 - \varepsilon)}, \quad v_C = u_g \quad (69)$$

verifies this quasi steady state for the concentration profiles. As in many solid-catalyzed gas reactions, the ratio²³ of the concentration wave velocity to the thermal wave velocity is quite large.²⁴ This implies that the concentration profiles reach a quasi steady state rapidly and that this quasi steady state then follows the slowly changing temperature profile. Jutan *et al.* (1977) have also shown that the concentration dynamics can be ignored in packed bed modeling.

The quasi-steady-state approximation then allows the concentration time derivatives to be set equal to zero,

$$\frac{\partial \hat{x}_{\text{CO}}}{\partial t} \approx 0, \quad \frac{\partial \hat{x}_{\text{CO}_2}}{\partial t} \approx 0 \quad (70)$$

in the original partial differential equations or in the linearized model, thus reducing $2N$ of the discretized ordinary differential equations to algebraic equations. In the linear system, these algebraic equations can be solved directly for the concentrations and substituted into the differential equations.

Simulations show negligible differences in the transient temperature and concentration profiles as a result of this quasi-steady-state approximation. The major advantage of this assumption should be apparent in control system design, where a reduction in the size of the state vector is computationally beneficial or in the time-consuming simulations of the full nonlinear model.

However, the quasi-steady-state approximation is by no means applicable to all reactor beds, but rather its applicability depends on the reactor configuration and conditions. For example, for a moving-bed coal gasifier, Yoon *et al.* (1979) and Yu *et al.* (1982) show that the quasi-steady-state approximation is only good for small changes and seems to give response times that are in error by a factor of two for large changes.

D. NEGLIGIBLE ENERGY ACCUMULATION IN THE GAS PHASE

Another potential model simplification involves assuming negligible energy accumulation in the gas phase as compared to that in the solid, which is equivalent to the earlier approximation [Eq. (66)] based on the relative magnitude of the energy accumulation in the gas and solid. For our system, the accumulation of energy in the solid is approximately 250 to 300 times that in the gas phase due to the relative thermal capacitance of the gas [Eq. (65)] and the similarity of the temporal behavior of the gas and catalyst temperatures (e.g., Fig. 19). Thus the accumulation term in the energy balance

²³ This ratio provides the criterion for the applicability of the quasi-steady-state approximation for the concentration as shown in Table V.

²⁴ About 250 for this reactor.

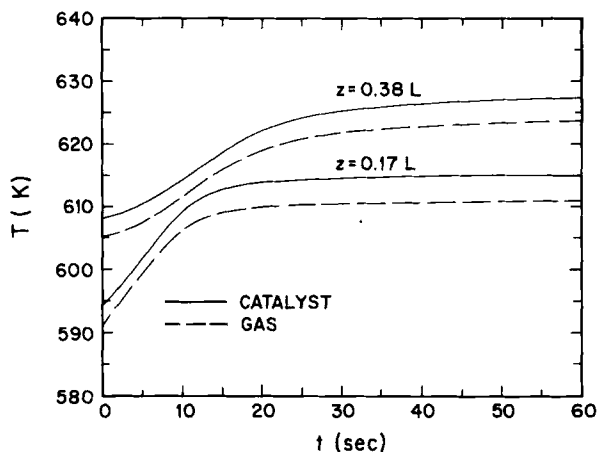


FIG. 19. Transient temperature response to step-input change of T_0 from 573 to 593 K and x_{CO}^0 from 0.06 to 0.07, type II conditions.

for the gas phase can be neglected:

$$\rho_g c_{p_g} \varepsilon \frac{\partial \Theta_g}{\partial t} \approx 0 \quad (71)$$

in comparison to the energy accumulation in the catalyst and thermal well. This reduces N of the original ordinary differential equations (after orthogonal collocation) to algebraic equations.

Although the mathematical criterion for the assumption of negligible energy accumulation in the gas phase given in Table V is identical to that for the quasi-steady-state approximation for concentration, this assumption should not be confused with the quasi-steady-state approximation. In the assumption of negligible energy accumulation, the temporal behavior of the gas-phase temperature is very similar to that of the solid phase and the reduction of the gas energy balance is accomplished due to the relative magnitudes of energy accumulation in the gas and solid. In the quasi-steady-state approximation for the concentration, the reduction of the concentration equations is a result of the concentration profiles reaching their steady state relatively fast in comparison to the temperature profiles. The criteria for the approximations are identical since the relative slowness of the thermal wave velocity in comparison to the concentration wave velocity (which defines the criterion for the application of the quasi-steady-state approximation) results from the relatively high thermal capacitance of the solid phase relative to the gas phase (this defines the criterion for the assumption of negligible energy accumulation in the gas phase).

IX. Control Model Development

In designing a control system for a packed bed reactor, to make the most effective use of modern control theory it is necessary to reduce the size of the model from that we have been using. In this section, we consider how this reduction is carried out.

A. STATE-SPACE REPRESENTATION

In simplifying the packed bed reactor model, it is advantageous for control system design if the equations can be reduced to fit into the framework of modern multivariable control theory, which usually requires a model expressed as a set of linear first-order ordinary differential equations in the so-called state-space form:

$$\dot{\mathbf{x}}(t) = \mathbf{Ax}(t) + \mathbf{Bu}(t) + \mathbf{Dd}(t), \quad \mathbf{y}(t) = \mathbf{Hx}(t) + \mathbf{Fu}(t) \quad (72)$$

where $\mathbf{x}(t)$, $\mathbf{u}(t)$, $\mathbf{d}(t)$, and $\mathbf{y}(t)$ are the state, control, disturbance, and measurement vectors, respectively. The state vector consists of process variables which together define the condition of the system. The control and measurement vectors consist of the manipulated inputs to the process and the process measurements, respectively.

Since the orthogonal collocation or OCFE procedure reduces the original model to a first-order nonlinear ordinary differential equation system, linearization techniques can then be applied to obtain the linear form (72). Once the dynamic equations have been transformed to the standard state-space form and the model parameters estimated, various procedures can be used to design one or more multivariable control schemes.

In the development of a general state-space representation of the reactor, all possible control and expected disturbance variables need to be identified. In the following analysis, we will treat the control and disturbance variables identically to develop a model of the form

$$\dot{\mathbf{x}}(t) = \mathbf{Ax}(t) + \mathbf{Ww}(t), \quad \mathbf{y}(t) = \mathbf{Hx}(t) + \mathbf{Fw}(t) \quad (73)$$

where $\mathbf{w}(t)$ now contains all control and disturbance terms, $\mathbf{Ww}(t) = \mathbf{Bu}(t) + \mathbf{Dd}(t)$. When specific control studies are desired, the $\mathbf{Ww}(t)$ term can simply be separated into the appropriate control term $\mathbf{Bu}(t)$ and disturbance term $\mathbf{Dd}(t)$, depending on the selected control configuration.

Consider the simplified flow diagram of a reactor system shown in Fig. 20. In this example, we have included the possibility of several input streams, a product recycle loop, and a feed-effluent heat exchanger so as to again represent a very general reactor system. The possible control variables or disturbances to the process are the flow rates of the input gases, the recycle

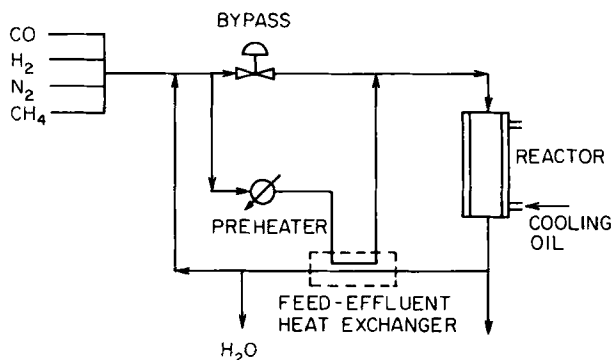


FIG. 20. Packed bed reactor system including feed-effluent heat exchanger.

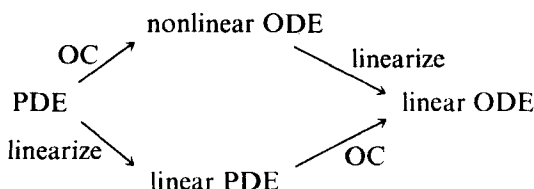
ratio, the cooling jacket temperature, the heat load of the preheater, and the feed-effluent heat exchanger bypass. From the reactor's point of view (and thus the reactor model's), the inlet gas temperature, the cooling wall temperature, the gas velocity, and the inlet gas concentration can be affected. We will thus consider the control and disturbance vector of the form

$$\mathbf{w} = [\Theta_w, v_{g0}, \Theta_0, y_1^0, y_2^0, y_{H_2O}^0, y_{H_2}^0, y_{CH_4}^0]^T \quad (74)$$

where these variables are nondimensional and the superscript and subscript zeros indicate inlet conditions.

B. MODEL LINEARIZATION

Although in this chapter we have chosen to linearize the mathematical system after reduction to a system of ordinary differential equations, the linearization can be performed prior to or after the reduction of the partial differential equations to ordinary differential equations. The numerical problem is identical in either case. For example, linearization of the nonlinear partial differential equations to linear partial differential equations followed by application of orthogonal collocation results in the same linear ordinary differential equation system as application of orthogonal collocation to the nonlinear partial differential equations followed by linearization of the resulting nonlinear ordinary differential equations. The two processes are shown:



The normalized reaction rate expressions are first linearized about the steady-state operating conditions (ss) using a first-order Taylor series,

$$R(\Theta_s, y_1, y_2, y_{\text{CH}_4}^0, y_{\text{H}_2}^0, y_{\text{H}_2\text{O}}^0, y_1^0, y_2^0) \approx R_s + \sum_z \left(\frac{\partial R}{\partial z} \right)_s (z - \bar{z}) \quad (75)$$

where $z = \Theta_s, y_1, y_2, y_{\text{CH}_4}^0, y_{\text{H}_2}^0, y_{\text{H}_2\text{O}}^0, y_1^0, y_2^0$.

The algebraic equations for the orthogonal collocation model consist of the axial boundary conditions along with the continuity equation solved at the interior collocation points and at the end of the bed. This latter equation is algebraic since the time derivative for the gas temperature can be replaced with the algebraic expression obtained from the energy balance for the gas. Of these, the boundary conditions for the mass balances and for the energy equation for the thermal well can be solved explicitly for the concentrations and thermal well temperatures at the axial boundary points as linear expressions of the conditions at the interior collocation points. The set of four boundary conditions for the gas and catalyst temperatures are coupled and are nonlinear due to the convective term in the inlet boundary condition for the gas phase. After a Taylor series expansion of this term around the steady-state inlet gas temperature, gas velocity, and inlet concentrations, the system of four equations is solved for the gas and catalyst temperatures at the boundary points.

The continuity equations for the velocities at the interior collocation points and at the end of the reactor are then linearized using the following relationship:

$$\begin{aligned} v_{g,i} \Theta_{g,j} &\approx \bar{v}_i \bar{\Theta}_{g,j} + \bar{v}_{g,i} (\bar{\Theta}_{g,i} - \bar{\Theta}_{g,j}) + \bar{\Theta}_{g,j} (v_{g,i} - \bar{v}_{g,i}) \\ &= \bar{v}_{g,i} \bar{\Theta}_{g,j} + \bar{\Theta}_{g,j} v_{g,i} - \bar{v}_{g,i} \bar{\Theta}_{g,j} \end{aligned} \quad (76)$$

The algebraic equations for the end-point gas temperatures are then substituted into the linearized continuity equations, which are then solved for the velocities. The linearized reaction rate expressions and the linearized expressions for the velocities and for the concentrations and temperatures at the axial boundary points are substituted into the ordinary differential equations.

The final linearized model is of the form

$$\dot{\mathbf{x}} = \mathbf{Ax} + \mathbf{Ww} + \mathbf{C} \quad (77)$$

where the state vector

$$\mathbf{x} = [\Theta_{s_1}, \dots, \Theta_{s_N}, \Theta_{g_1}, \dots, \Theta_{g_N}, \Theta_{t_1}, \dots, \Theta_{t_N}, y_{1_1}, \dots, y_{1_N}, y_{2_1}, \dots, y_{2_N}]^T \quad (78)$$

consists of the catalyst temperatures, the gas temperatures, the thermal well temperatures, the CO concentrations, and the CO₂ concentrations at the interior collocation points. The control and disturbance variables are

$$\mathbf{w} = [T_w, v_{g0}, \Theta_0, y_1^0, y_2^0, y_{H_2O}^0, y_{H_2}^0, y_{CH_4}^0]^T \quad (79)$$

This linear system is then of order $5N$, where N is the number of interior collocation points. The constants \mathbf{C} in the equations can be easily eliminated by using deviation variables about the steady-state values. At steady state, $\dot{\mathbf{x}} = 0$ and thus

$$0 = \mathbf{A}\bar{\mathbf{x}} + \mathbf{W}\bar{\mathbf{w}} + \mathbf{C} \quad (80)$$

Subtracting this from the original equation,

$$\dot{\mathbf{x}} = \mathbf{A}(\mathbf{x} - \bar{\mathbf{x}}) + \mathbf{W}(\mathbf{w} - \bar{\mathbf{w}}) \quad (81)$$

Letting

$$\mathbf{x}' = \mathbf{x} - \bar{\mathbf{x}} \quad \text{and} \quad \mathbf{w}' = \mathbf{w} - \bar{\mathbf{w}} \quad (82)$$

the resulting equation is of the desired state-space form

$$\dot{\mathbf{x}}' = \mathbf{A}\mathbf{x}' + \mathbf{W}\mathbf{w}' \quad (83)$$

Note that in the following analyses, we will drop the prime symbol. It should still be clear that deviation variables are being used. Then this linear representation can easily be separated into the standard state-space form of Eq. (72) for any particular control configuration. Numerical simulation of the behavior of the reactor using this linearized model is significantly simpler than using the full nonlinear model. The first step in the solution is to solve the full, nonlinear model for the steady-state profiles. The steady-state profiles are then used to calculate the matrices \mathbf{A} and \mathbf{W} . Due to the linearity of the system, an analytical solution of the differential equations is possible:

$$\mathbf{x}'(t) = e^{[(t-t_0)\mathbf{A}]} \mathbf{x}'(t_0) + \int_{t_0}^t e^{[(t-s)\mathbf{A}]} \mathbf{W}\mathbf{w}'(s) ds \quad (84)$$

Then if we consider a time interval ($t \rightarrow t + dt$) over which \mathbf{w} is constant,²⁵ this solution simplifies to

$$\mathbf{x}'(t + dt) = e^{\mathbf{A}dt} \mathbf{x}'(t) + \mathbf{A}^{-1}(e^{\mathbf{A}dt} - \mathbf{I})\mathbf{W}\mathbf{w}'(t) \quad (85)$$

The major complications in this analytical solution are obviously the matrix exponential and matrix inverse. If we let

$$\mathbf{A} = \mathbf{S}\mathbf{A}\mathbf{S}^{-1} \quad (86)$$

²⁵ We can take very small time steps dt if needed.

where Λ is a diagonal matrix of the eigenvalues of A and S is the corresponding matrix of eigenvectors, we then get

$$e^{\Lambda dt} = S e^{\Lambda dt} S^{-1} \quad \text{and} \quad A^{-1} = S \Lambda^{-1} S^{-1} \quad (87)$$

where $e^{\Lambda dt}$ and Λ^{-1} are easily calculated since Λ is diagonal. Thus after the steady state is determined and the time steps dt are selected, we can calculate the eigenvalues and eigenvectors of the matrix A and from these the values of A^{-1} and $e^{\Lambda dt}$. These lengthy calculations only need to be performed once for each steady state and selected time step. Of course, these time steps can be quite large with the only restriction being that the control and disturbance variables are nearly constant during this period. If these variables are constant over more than one selected time step, even the value of $A^{-1}(e^{\Lambda dt} - I)Ww'$ will be constant and will not have to be recalculated between time steps.

The determination of eigenvalues and eigenvectors of the matrix A is based on a routine by Grad and Brebner (1968). The matrix is first scaled by a sequence of similarity transformations and then normalized to have the Euclidian norm equal to one. The matrix is reduced to an upper Hessenberg form by Householder's method. Then the QR double-step iterative process is performed on the Hessenberg matrix to compute the eigenvalues. The eigenvectors are obtained by inverse iteration.

C. SIMULATIONS WITH THE LINEARIZED MODEL

Figure 21 shows the simulated dynamic behavior of the gas temperatures at various axial locations in the bed using both the linear and nonlinear models for a step change in the inlet CO concentration from a mole fraction of 0.06 to 0.07 and in the inlet gas temperature from 573 to 593 K. Figure 22 shows the corresponding dynamic behavior of the CO and CO₂ concentrations at the reactor exit and at a point early in the reactor bed. The axial concentration profiles at the initial conditions and at the final steady state using both the linear and nonlinear simulations are shown in Fig. 23. The temporal behavior of the profiles shows that the discrepancies between the linear and nonlinear results increase as the final steady state is approached. Even so, there are only slight differences (less than 2% in concentrations and less than 0.5% in temperatures) in the profiles throughout the dynamic responses and at the final steady state even for this relatively major step-input change.

Figure 24 shows dynamic linear and nonlinear simulations of the gas temperatures at $\zeta = 0.17$ and $\zeta = 0.38$, and Fig. 25 shows the exit CO and CO₂ concentrations for a 50-sec disturbance in the inlet gas temperature from 573 to 601.65 K (a 5% increase) and in the inlet CO concentration from a mole fraction of 0.06 to 0.072 (a 20% increase). Again we find that only minor

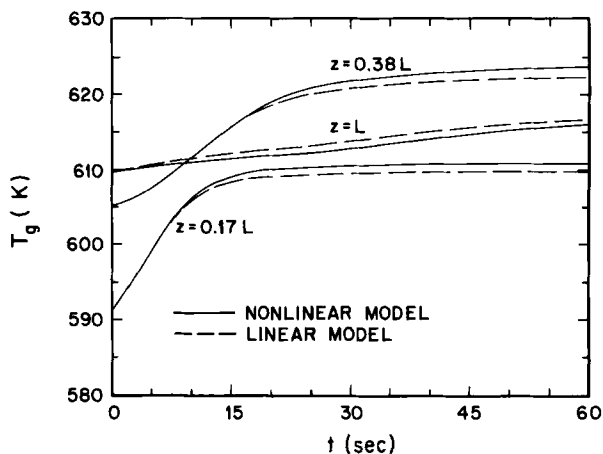


FIG. 21. Gas temperature dynamics resulting from a step change of T_0 from 573 to 593 K and of x_{CO}^0 from 0.06 to 0.07, type II conditions.

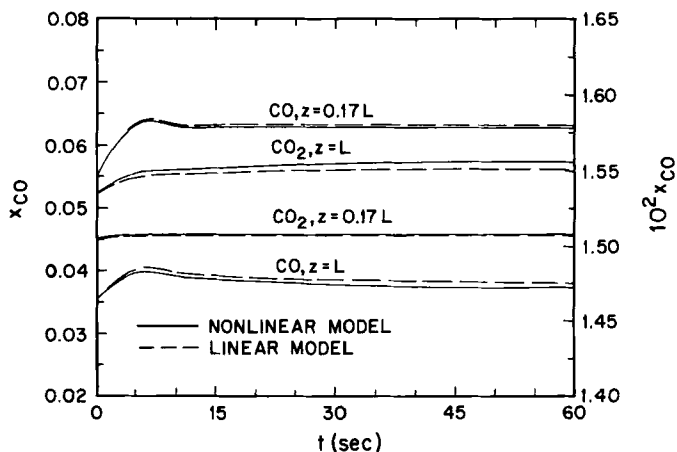


FIG. 22. Concentration dynamics resulting from a step change of T_0 from 573 to 593 K and of x_{CO}^0 from 0.06 to 0.07, type II conditions.

differences (less than 2%) are apparent between the two models and only then at conditions sufficiently far from the steady state. As expected, the models give identical results when the original steady state is reestablished after the disturbance.

Thus the simulations show that the linear model is quite accurate for conditions near the steady state. Of course, losses in accuracy are greater, the

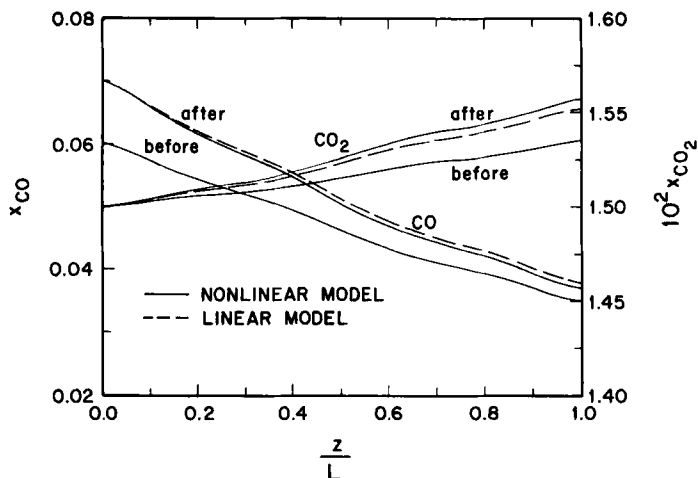


FIG. 23. Steady-state concentration profiles before and after step change of T_0 from 573 to 593 K and of x_{CO}^0 from 0.06 to 0.07, type II conditions.

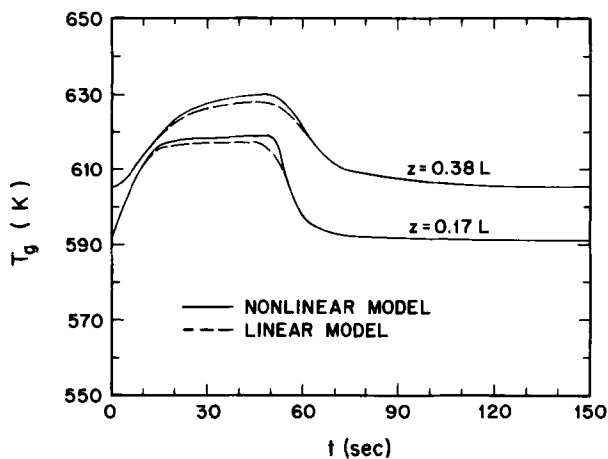


FIG. 24. Gas temperature dynamics during a 50-sec disturbance of T_0 from 573 to 593 K and of x_{CO}^0 from 0.06 to 0.072, type II conditions.

larger the deviation from the steady state. The important decision must be made as to how far from the steady state are the deviations still tolerable for control considerations. This decision will define the conditions under which relinearization is necessary and the usefulness of the linear model for control applications.

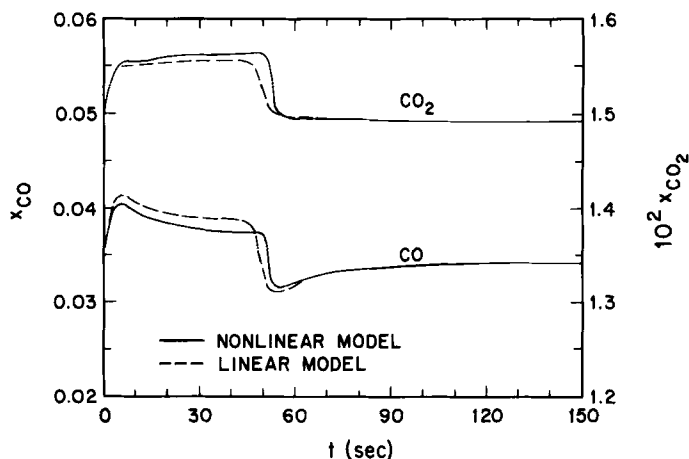


FIG. 25. Exit concentration dynamics during a 50-sec disturbance of T_0 from 573 to 593 K and of x_{CO}^0 from 0.06 to 0.072, type II conditions.

For start-up and disturbance simulations, the linearized model does predict an eventual return to the steady state around which the system was linearized. However, for step-input changes where the final steady state differs from the original, some minimal loss in accuracy is apparent in the final steady state reached using dynamic simulations of the linear model from the original steady state. This difficulty can easily be circumvented in the case of step changes by relinearizing about the new final steady-state conditions somewhere during the simulation.

Table VI shows a comparison of the solution times for the various dynamic simulations using the three models. As shown, the reduction in solution time is

TABLE VI
COMPARISON OF SIMULATION TIMES FOR
STANDARD TYPE II CONDITIONS

Simulation		Model		
		Nonlinear	Linear	Analytic
Step	$T_0 \rightarrow 593 \text{ K}$	2:54:24	12:54	00:36
	$x_{CO} \rightarrow 0.07$			
Step	$T_w \rightarrow 593 \text{ K}$	3:14:41	18:04	00:34
Start-up		4:43:26	28:39	00:29
Disturbance	$T_0 \rightarrow 602 \text{ K}$	4:58:42	23:10	00:31
(50 sec)	$x_{CO} \rightarrow 0.072$			

substantial when the linear model is used. With numerical integration of the linear state-space model, simulation times are reduced by a factor of 10. The analytical solution reduces simulation times by another factor of up to 100 (to a point where real-time solution is possible). As expected, the results using both the numerical and analytic solutions of the linear model are identical.

X. Dimensionality of the Linearized Model

Even after linearization, the state-space model often contains too many dependent variables for controller design or for implementation as part of the actual control system. Low-order models are thus required for on-line implementation of multivariable control strategies. In this section, we study the reduction in size, or order, of the linearized model.

A. MODEL DISCRETIZATION

The model discretization or the number of collocation points necessary for accurate representation of the profiles within the reactor bed has a major effect on the dimensionality and thus the solution time of the resulting model. As previously discussed, radial collocation with one interior collocation point generally adequately accounts for radial thermal gradients without increasing the dimensionality of the system. However, multipoint radial collocation may be necessary to describe radial concentration profiles. The analysis of Section VI,E shows that, even with very high radial mass Peclet numbers, the radial concentration is nearly uniform and that the axial bulk concentration and radial and axial temperatures are nearly unaffected by assuming uniform radial concentration. Thus model dimensionality can be kept to a minimum by also performing the radial concentration collocation with one interior collocation point.

In this section, the optimal choice for the number of axial collocation points is discussed. Obviously, if the number of axial collocation points is insufficient, the resulting axial solution for the temperature and concentration profiles will be inaccurate. On the other hand, one of the problems with fitting high-order polynomials to the axial profiles is that the polynomials, if of sufficiently high order, may begin to ripple along the curve. As pointed out by Jutan *et al.* (1977), this rippling can be extremely detrimental since the collocation formulas are used to approximate derivatives. Since there is a tradeoff between lowering the number of collocation points to reduce model dimensionality and reduce profile rippling and increasing the number of collocation points to retain high simulation accuracy, extreme care is required in the selection of the number of axial collocation points.

Figure 26 shows the predicted axial gas temperature profiles during reactor start-up for standard type I conditions with varying numbers of axial collocation points. Eight or more axial collocation points provide similar results, and even simulations with six collocation points show minimal inaccuracy. However, reducing the number of collocation points below this leads to major discrepancies in the axial profiles.

Although examining the results of simulations provides an indication of the optimal number of axial collocation for steady-state and dynamic simulations, Bonvin (1980) shows that the convergence pattern of the dominant eigenvalues of the model as the number of collocation points is increased can also be used as an important procedure for determining the optimal axial discretization. Since these dominant modes only describe the dynamic behavior of the linearized system, simulation of the full model should be used to verify the results for transient and steady-state analyses. Figure 27 shows the convergence of the dominant eigenvalues for the type I operating conditions. The eigenvalue analysis shows that fewer than six collocation points will lead to significant errors in the dynamic simulations as judged by the fact that the dominant eigenvalues are far from their true values. Seven collocation points would seem to be sufficient and six may be satisfactory. These results verify those obtained earlier using simulations with differing discretization (Fig. 26). With six interior axial collocation points, the full model would consist of 30 coupled, nonlinear ordinary differential equations along with their algebraic boundary conditions. The linear model would be a 30th-order state-space representation.

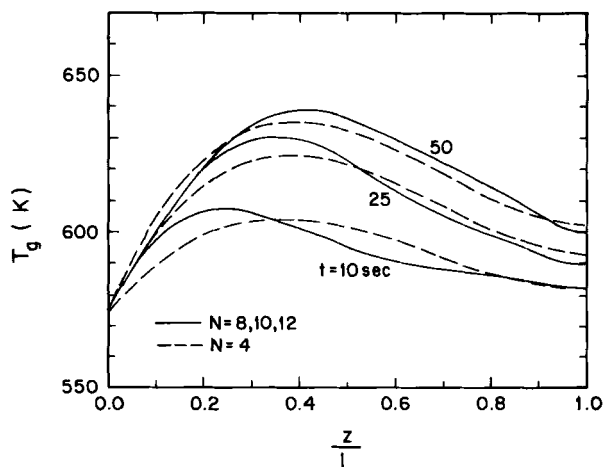


FIG. 26. Axial gas temperature profiles as a function of the level of axial discretization, type I conditions.

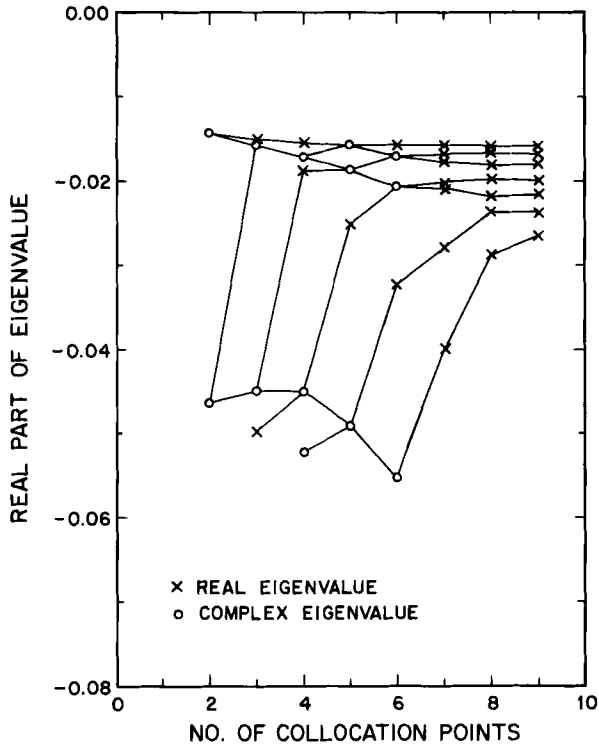


FIG. 27. Convergence pattern of dominant eigenvalues, type I conditions.

Under conditions where steep gradients exist within the reactor bed, collocation may lead to oscillatory axial profiles (rippling) due to the attempt to fit a simple N th-order smooth polynomial to the entire axial profile. Although these oscillations can often be reduced by decreasing the number of collocation points, significant errors in the profiles can then result. Simple trial and error can be used to determine the best number of axial collocation points to reduce rippling and retain accuracy. In extreme cases with very steep axial profiles or abrupt changes in the profiles, the OCFE procedure may be necessary. Using this technique, not only the number of collocation points in each element needs to be specified, but also the number and size of the elements.

B. MODEL REDUCTION

Regardless of whether orthogonal collocation or orthogonal collocation on finite elements is used for the discretization, the resulting linear state-space

representation is of high order (30–40 states)²⁶ due to the original system of five coupled partial differential equations and the accurate treatment of the gas, catalyst, and thermal well temperatures and concentrations. Although dynamic simulations using the state-space representation are very fast, difficulties still exist in developing multivariable feedback control algorithms owing to the relatively high order of the system. For such applications, an accurate reduced order model is desired.

Significant reduction in the order of the model is possible through the introduction of the approximations of quasi steady state for the concentrations, negligible accumulation of energy in the gas phase, or pseudo-homogeneity of the system. Although these approximations could have been made in the original model, doing so without a careful analysis of their effects on the model behavior is not advisable. Additionally, an analysis of the eigenstructure of the system shows that modal reduction techniques such as those presented by Bonvin (1980), Gould (1969), and Wilson *et al.* (1974) can lead to a low-order state-space model. Here we consider explicit modal reduction approaches to model reduction that result in an explicit reduced model formulation without statistical analysis of input–output data.

The basic strategy of modal reduction approaches is to retain only certain modes of the high-order model in the low-order model. Wilson *et al.* (1974) summarized these techniques and showed that many of the published modal approaches are equivalent since they produce identical reduced models. Bonvin (1980) also provides a comparison of the various modal techniques with respect to their steady-state and dynamic accuracies as well as to the dependence of the reduced models on the retained state variables.

According to Gould (1969), the central theme in modal reduction and control is

that the transient behavior of a process is predominantly determined by the modes associated with the smallest eigenvalues. If it is possible to approximate a high-order system by a lower-order system whose slow modes are the same as those of the original system, then attention can be focused on the attempt to alter the eigenvalues of the slow modes so as to increase the speed of recovery of the process from disturbances. It is essential to be aware of the fact that various disturbances excite the modes differently so that a scheme which is based on a lower-order model may be inappropriate if a disturbance injects most of its "energy" in a fast mode which has been neglected.

This basic approach is really divided into several distinct categories. Two of these, Davison's method and Marshall's method, provide suitable modal reduction for the state-space representation of the methanation reactor to a 12th-order model. Comparisons of the models and discussion of additional model reduction are presented in the next section.

²⁶ This is actually of very low order in comparison to traditional finite difference solutions.

1. Davison's Method

The principle of this method, proposed originally by Davison (1966), is to neglect eigenvalues of the original system that are farthest from the origin (the nondominant modes) and retain only dominant eigenvalues and hence the dominant time constants of the system. If we consider the solution of the linearized model

$$\mathbf{x}(t + dt) = e^{A dt} \mathbf{x}(t) + \mathbf{A}^{-1}(e^{A dt} - \mathbf{I}) \mathbf{W} \mathbf{w}(t) \quad (88)$$

and let

$$\mathbf{A} = \mathbf{S} \mathbf{\Lambda} \mathbf{S}^{-1} \quad (89)$$

where $\mathbf{\Lambda}$ is the diagonal matrix of eigenvalues

$$\mathbf{\Lambda} = \begin{bmatrix} \lambda_1 & 0 & \cdots & 0 \\ 0 & \lambda_2 & & \cdot \\ \vdots & \vdots & \ddots & \vdots \\ 0 & 0 & \cdots & \lambda_n \end{bmatrix} \quad (90)$$

and \mathbf{S} is the corresponding matrix of eigenvectors, the dynamic behavior of

TABLE VII
EIGENVALUES OF FULL 30TH-ORDER
LINEAR MODEL

Group	Real part	Imaginary part
I	-53.49	± 1.93
	-52.93	± 6.31
	-51.98	± 10.46
	-5.03	± 5.76
II	-2.12	± 10.38
	-1.37	± 10.35
	-6.27	± 1.89
III	-5.66	± 1.85
	-4.34	± 5.68
	-0.08	± 0.010
IV	-0.07	± 0.035
	-0.06	± 0.074
	-0.033	0.0000
V	-0.021	± 0.0011
	-0.018	± 0.0009
	-0.016	0.0000

the system is governed by the term

$$\begin{aligned} \mathbf{A}^{-1}(e^{\mathbf{A}dt} - \mathbf{I})\mathbf{W}\mathbf{w}(t) &= \mathbf{S}\mathbf{\Lambda}^{-1}(e^{\mathbf{\Lambda}dt} - \mathbf{I})\mathbf{S}^{-1}\mathbf{W}\mathbf{w}(t) \\ &= \mathbf{S} \begin{bmatrix} \frac{\exp(\lambda_1 dt) - 1}{\lambda_1} & \dots & 0 \\ \vdots & \ddots & \vdots \\ 0 & \dots & \frac{\exp(\lambda_n dt) - 1}{\lambda_n} \end{bmatrix} \mathbf{S}^{-1}\mathbf{W}\mathbf{w}(t) \end{aligned} \quad (91)$$

Obviously by neglecting the nondominant eigenvalues, the dynamic behavior of the approximate system will be similar to the original system, since the contribution of the unretained modes will only be significant early in the dynamic response.

Table VII shows the system eigenvalues for the full 30th-order linear state-space representation for type II conditions. As shown, the eigenvalues can be grouped into five distinct groups based on the real parts of the eigenvalues:

Group	—(Real)
I	≈ 50
II	1–5
III	4–6
IV	0.06–0.08
V	0.01–0.03

Further analysis shows that, for this particular example, the fastest modes (group I) correspond directly to the gas temperatures at the interior collocation points and those of groups II and III correspond to the concentrations. One should not infer from this conclusion that a general correspondence between the dynamical modes and the physical variables always exists. In this example, the correspondence results from the major differences in the magnitudes of the various groups.

It is evident that, of the 30 modes of the full linear model (with $N = 6$), 18 are very fast in comparison to the remaining 12 (by 2 orders of magnitude or more). Thus direct modal reduction to a 12th-order model using Davison's method should provide good dynamic accuracy. However, by simply neglecting the non-dominant modes of the system, the contribution of these modes is also absent at steady state, thus leading to possible (usually minor) steady-state offset. Several identical modifications (Wilson *et al.*, 1974) to Davison's

original method have been proposed by Davison and Chidambara (Chidambara and Davison, 1967a–c; Davison, 1968) and by Fossard (1970). In these methods, the states of the reduced model are artificially reconditioned to ensure the desired steady-state behavior.

2. Marshall's Method

Marshall's model reduction technique (Marshall, 1966) differs from Davison's in that the steady-state characteristics of the original system are retained in the reduced model. Since the response of any element of the state vector associated with a large eigenvalue is much faster than that of elements associated with the smaller eigenvalues (or larger time constants), the dynamics of the nondominant modes can simply be neglected.²⁷ This reduction is equivalent to approximating the response of the faster modes by an instantaneous step change. If the fast modes in the methanation model are taken as the gas temperatures and the CO and CO₂ concentrations, Marshall's procedure is a rigorous mathematical reduction identical to the assumptions of quasi steady state for the concentrations and negligible energy accumulation in the gas phase. An important advantage of Marshall's method over Davison's method is that the reduced-order model has the same steady state as the high-order model, since the time derivatives are identically zero for all state variables at steady state. However, the retained modes may no longer optimally represent the dynamic behavior.

Table VII shows that, for the methanation reactor model, the dynamic response of the gas temperatures and CO and CO₂ concentrations should be much faster (by two orders of magnitude) than the response of the catalyst and thermal well temperatures. This prediction is verified in the dynamic responses shown in Figs. 18 and 19 and the previous analysis of the thermal and concentration wave velocities.

Thus the state vector

$$\mathbf{x} = [\Theta_{s_i}, \Theta_{g_i}, \Theta_{t_i}, y_{1_i}, y_{2_i}]^T \quad (i = 1, \dots, N) \quad (92)$$

is partitioned into

$$\mathbf{x}_1 = \begin{bmatrix} \Theta_{s_i} \\ \Theta_{t_i} \end{bmatrix}, \quad \mathbf{x}_2 = \begin{bmatrix} \Theta_{g_i} \\ y_{1_i} \\ y_{2_i} \end{bmatrix} \quad (93)$$

The state-space representation

$$\dot{\mathbf{x}} = \mathbf{Ax} + \mathbf{Ww} \quad (94)$$

²⁷ That is, their time derivatives are set equal to zero.

where

$$\mathbf{A} = \begin{bmatrix} \mathbf{A}_{11} & \mathbf{A}_{12} & \mathbf{A}_{13} & \mathbf{A}_{14} & \mathbf{A}_{15} \\ \mathbf{A}_{21} & \mathbf{A}_{22} & \mathbf{A}_{23} & \mathbf{A}_{24} & \mathbf{A}_{25} \\ \mathbf{A}_{31} & \mathbf{A}_{32} & \mathbf{A}_{33} & \mathbf{A}_{34} & \mathbf{A}_{35} \\ \mathbf{A}_{41} & \mathbf{A}_{42} & \mathbf{A}_{43} & \mathbf{A}_{44} & \mathbf{A}_{45} \\ \mathbf{A}_{51} & \mathbf{A}_{52} & \mathbf{A}_{53} & \mathbf{A}_{54} & \mathbf{A}_{55} \end{bmatrix} \quad \text{and} \quad \mathbf{W} = \begin{bmatrix} \mathbf{W}_1 \\ \mathbf{W}_2 \\ \mathbf{W}_3 \\ \mathbf{W}_4 \\ \mathbf{W}_5 \end{bmatrix} \quad (95)$$

can then be partitioned into two sets of equations:

$$\dot{\mathbf{x}}_1 = \begin{bmatrix} \mathbf{A}_{11} & \mathbf{A}_{13} \\ \mathbf{A}_{31} & \mathbf{A}_{33} \end{bmatrix} \mathbf{x}_1 + \begin{bmatrix} \mathbf{A}_{12} & \mathbf{A}_{14} & \mathbf{A}_{15} \\ \mathbf{A}_{32} & \mathbf{A}_{34} & \mathbf{A}_{35} \end{bmatrix} \mathbf{x}_2 + \begin{bmatrix} \mathbf{W}_1 \\ \mathbf{W}_3 \end{bmatrix} \mathbf{w} \quad (96)$$

$$\dot{\mathbf{x}}_2 = \begin{bmatrix} \mathbf{A}_{21} & \mathbf{A}_{23} \\ \mathbf{A}_{41} & \mathbf{A}_{43} \\ \mathbf{A}_{51} & \mathbf{A}_{53} \end{bmatrix} \mathbf{x}_1 + \begin{bmatrix} \mathbf{A}_{22} & \mathbf{A}_{24} & \mathbf{A}_{25} \\ \mathbf{A}_{42} & \mathbf{A}_{44} & \mathbf{A}_{45} \\ \mathbf{A}_{52} & \mathbf{A}_{54} & \mathbf{A}_{55} \end{bmatrix} \mathbf{x}_2 + \begin{bmatrix} \mathbf{W}_2 \\ \mathbf{W}_4 \\ \mathbf{W}_5 \end{bmatrix} \mathbf{w} \quad (97)$$

Then we can let $\dot{\mathbf{x}}_2 = 0$ in light of the quasi-steady-state approximation and the assumption of negligible energy accumulation in the gas or in light of the significant differences in the magnitudes of the eigenvalues for the \mathbf{x}_1 and \mathbf{x}_2 states and solve for \mathbf{x}_2 as a function of \mathbf{x}_1 . Substituting this result into Eq. (96) results in a reduced state-space model

$$\dot{\mathbf{x}}_1 = \mathbf{A}' \mathbf{x}_1 + \mathbf{W}' \mathbf{w} \quad (98)$$

where the state variables are now the catalyst and thermal well temperatures at the collocation points and the new matrices \mathbf{A}' and \mathbf{W}' are simply related to the original matrices,

$$\mathbf{A}' = \begin{bmatrix} \mathbf{A}_{11} & \mathbf{A}_{13} \\ \mathbf{A}_{31} & \mathbf{A}_{33} \end{bmatrix} - \begin{bmatrix} \mathbf{A}_{12} & \mathbf{A}_{14} & \mathbf{A}_{15} \\ \mathbf{A}_{32} & \mathbf{A}_{34} & \mathbf{A}_{35} \end{bmatrix} \mathbf{A}_c^{-1} \begin{bmatrix} \mathbf{A}_{21} & \mathbf{A}_{23} \\ \mathbf{A}_{41} & \mathbf{A}_{43} \\ \mathbf{A}_{51} & \mathbf{A}_{53} \end{bmatrix} \quad (99)$$

$$\mathbf{W}' = \begin{bmatrix} \mathbf{W}_1 \\ \mathbf{W}_3 \end{bmatrix} - \begin{bmatrix} \mathbf{A}_{12} & \mathbf{A}_{14} & \mathbf{A}_{15} \\ \mathbf{A}_{32} & \mathbf{A}_{34} & \mathbf{A}_{35} \end{bmatrix} \mathbf{A}_c^{-1} \begin{bmatrix} \mathbf{W}_2 \\ \mathbf{W}_4 \\ \mathbf{W}_5 \end{bmatrix} \quad (100)$$

where

$$\mathbf{A}_c^{-1} = \begin{bmatrix} \mathbf{A}_{22} & \mathbf{A}_{24} & \mathbf{A}_{25} \\ \mathbf{A}_{42} & \mathbf{A}_{44} & \mathbf{A}_{45} \\ \mathbf{A}_{52} & \mathbf{A}_{54} & \mathbf{A}_{55} \end{bmatrix} \quad (101)$$

Of course, this technique does not actually eliminate the states Θ_{gi} , y_{1i} , and y_{2i} . Instead it retains their steady-state effects and relates their dynamic behavior to the gas and thermal well temperatures. The reduced model is then

of order $2N$, or of only 12th order for $N = 6$. Similarly, we could consider each assumption independently. If we retain the state variables Θ_g , the model is of $3N$ th order.

C. DISCUSSION OF REDUCED MODEL

The reduced-order model obtained using Marshall's method is an accurate $2N$ th-order approximation to the original $5N$ th-order model. Although the resulting model is equivalent to simply making the common assumptions of negligible energy accumulation in the gas and quasi steady state for the concentrations, we have provided a rigorous approach to these assumptions based on the eigenstructure analysis and have provided an accurate means of evaluating their applicability. The steady-state problems associated with Davison's method are eliminated, and the potential dynamic disagreement between the original and reduced models is minimal for the methanation reactor as verified by simulations.

Simulations using this reduced model show a reduction in computation time, along with storage space, without any significant loss in accuracy. Table VIII shows the computation times for various simulations using various models and solution techniques with $N = 6$. The $2N$ th-order model is considered using analytic solution of the equations, along with a $3N$ th-order model, where only the concentration dynamics have been neglected. Although the solution time advantages between the analytic solutions of the reduced models and the full linear model seem to be minimal, these analyses were conducted with a constant control and disturbance vector w over the periods of disturbance or simulation. If these values change frequently as may be the case in practice, the solution time savings for the reduced models will be increased.

TABLE VIII
COMPARATIVE SIMULATION TIMES OF MODELS

Simulation		Model				
		Nonlinear	Linear	Analytic	$2N$ th	$3N$ th
Step	$T_0 \rightarrow 593$ K	2:54:24	12:54	00:36	00:24	00:22
	$x_{co} \rightarrow 0.07$					
Step	$T_w \rightarrow 593$ K	3:14:41	18:04	00:34	00:22	00:20
Start-up		4:43:26	28:39	00:29	00:17	00:14
Disturbance (50 sec.)	$T_0 \rightarrow 602$ K	4:58:42	23:10	00:31	00:20	00:17
	$x_{co} \rightarrow 0.072$					

Figure 28 shows comparisons of the transient gas and solid axial temperature profiles for a step-input change with the full model and the reduced models. The figure shows negligible differences between the profiles at times as short as 10 sec. Concentration results (not shown) show even smaller discrepancies between the profiles. Additional simulations are not shown since all showed minimal differences between the solutions using the different linear models. Thus for the methanation system, Marshall's model reduction provides an accurate $2N$ th-order reduced state-space representation of the original $5N$ th-order linear model.

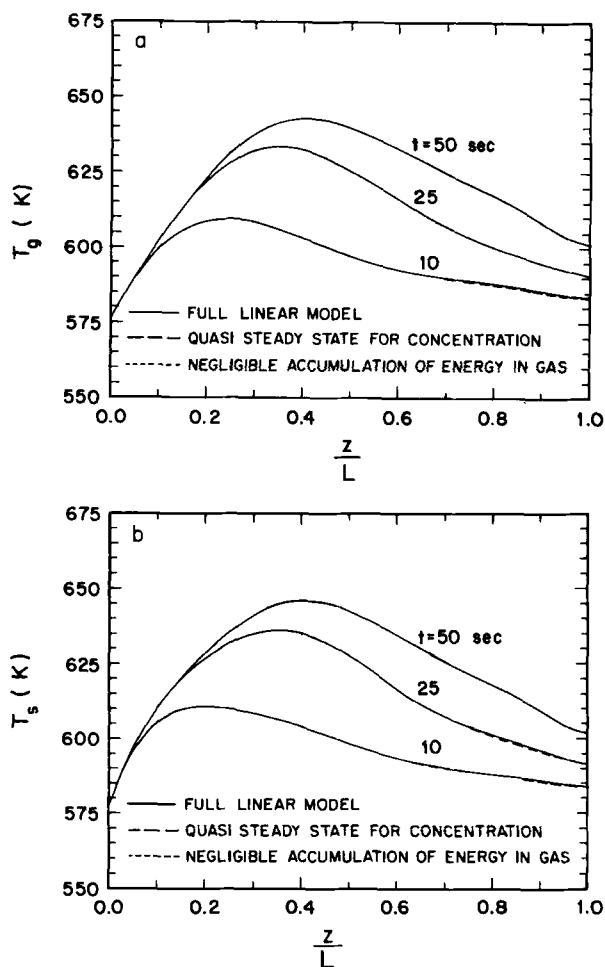


FIG. 28. Transient axial temperature profiles during start-up, type I conditions.

The excellent dynamic agreement between the original and reduced models (Fig. 28) can be explained by the eigenstructure of the reduced system. As shown in Fig. 29, the eigenvalues of the reduced model are nearly identical (with 1%) to the dominant eigenvalues of the original model. Thus the dynamic behavior is nearly identical to that which would result from modal reduction using Davison's method. The advantage then of Marshall's modal reduction for the methanation reactor model is that some contribution of the "fast" modes is still retained in the algebraic equations that result from the assumptions. These contributions lead to small deviations in the remaining eigenvalues and eliminate steady-state discrepancies without seriously affecting the dynamic responses.

Since the $2N$ th-order reduced model based on Marshall's reduction procedure accurately simulates the performance of the full linear model for a large range of input changes and disturbances, there is little or no incentive to attempt other techniques. If, however, further model reduction is desired or necessary for control studies, more powerful reduction techniques would be needed since the eigenvalues of the $2N$ th-order model are of similar magnitudes and simple elimination of the larger ones may lead to major errors.

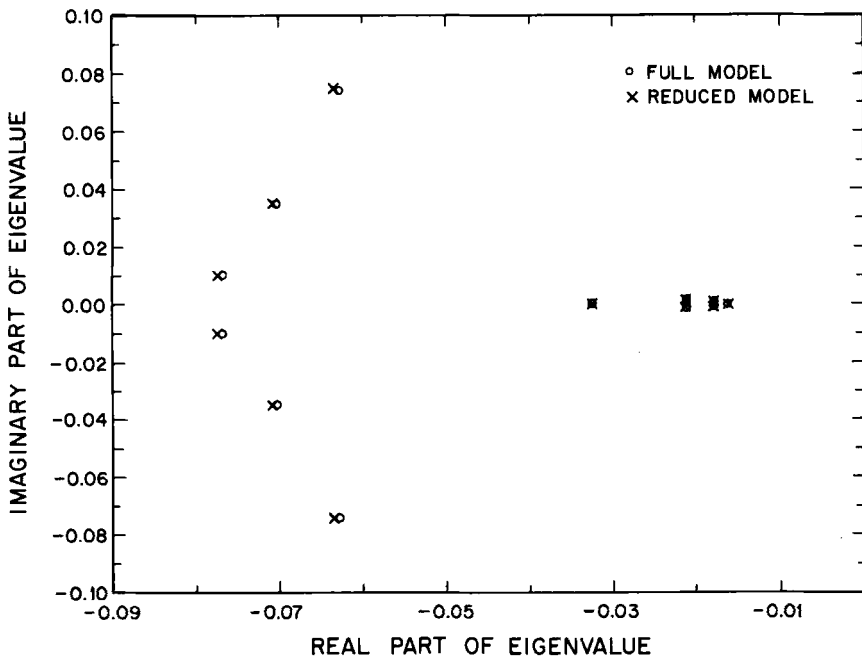


FIG. 29. Dominant eigenvalues of the full and reduced models, type II conditions.

One possible procedure for further reduction would be Litz's modal reduction described in detail by Bonvin (1980). Litz proposed that the contribution of the nondominant modes be taken as a linear combination of the dominant modes rather than simply being neglected. The appropriate linear combination is determined in order to minimize the error between the responses of the nondominant modes in the original and in the reduced-order models. Bonvin (1980) further explains that the eigenvalues of the reduced model are identical to the dominant eigenvalues of the original model, but the eigenvectors are given a new optimal orientation. Bonvin uses this technique to reduce a 24th-order model for a tubular autothermal reactor to a 5th-order reduced model. He concludes that Litz's procedure is superior to all other modal approaches.

XI. Nomenclature

A	State matrix	\hat{P}	Total pressure neglecting mole change, atm
A_{ij}, B_{ij}	Collocation weights for first and second derivatives	P_i	Partial pressure of species i , atm
B	Control matrix	Pe	Peclet number
c	Concentration, gmole/cm ³	r	Radial coordinate, cm
c_p	Heat capacity, cal/g K	r_c	Radial collocation point
d	Disturbance vector	R	Reaction rate, gmole/sec cm ³
d_i	Radial collocation weights	R_0, R_1	Radius of thermal well and outer wall, respectively, cm
D	Bulk molecular diffusivity, cm ² /sec	R'	Normalized reaction rate
E_a	Activation energy, cal/gmole	R_g	Universal gas constant, 1.987 cal/gmole K
f_1, f_2	Pressure-dependence constants for steam-shift reaction rate	t	Time, sec
h_{ij}	Heat transfer coefficient between phases i and j , cal/sec cm K	T	Absolute temperature, K
ΔH	Heat of reaction, cal/gmole	u	Control vector
k	Thermal conductivity	u_g	Interstitial velocity of gas, cm/sec
k_0	Reaction rate constant	U_{ij}	Overall heat transfer coefficient between phases i and j , cal/sec K
k_r, k_z	Radial and axial thermal conductivity, respectively, cal/sec cm K	v_g	Normalized fluid velocity, u_g/\bar{U}_{g0}
K_1, K_2	Methanation reaction rate constants, atm ⁻¹	v_z	Axial fluid velocity, cm/sec
K_p	Equilibrium constants for methanation, atm ⁻²	V	Volume, cm ³
L_i	Lagrangian polynomials	w_j	Weighting functions
L	Reactor length, cm	x	State vector
M_g	Molecular weight of gas, g/g-mole	x_i	Mole fraction of species i
N_i	Molar flux with respect to stationary coordinates, g-moles/cm ² sec	y	Output vector
		y_i	Normalized mole fraction, \hat{x}_i/\bar{x}_{CO}^0
		z	Axial coordinate, cm

Greek Letters

α	Dimensionless axial dispersion parameter	Λ	Diagonal matrix of eigenvalues
β	Dimensionless radial dispersion parameter	μ	Viscosity
δ	Moles CO reacted in methanation per total inlet moles	ω	Constants from radial collocation
ε	Void fraction of bed	ϕ_0	Normalized radius of thermal well, R_0/R_1
η	Dimensionless radius	ϕ_1, ϕ_2	Dimensionless heats of reaction
γ	Dimensionless heat transfer coefficient	ρ	Density, g/cm ³
κ	Dimensionless heat generation parameters	σ	Dimensionless reaction coefficients
λ	Eigenvalues	τ	Dimensionless pressure drop, $\hat{P}_{x=L}/\hat{P}_{x=0} - 1$
λ_{ijk}	Biot numbers	ϑ	Normalized time, $(tu_{g0})/L$
		Θ	Normalized temperature, T/\bar{T}_0
		ζ	Normalized axial coordinate, z/L

Subscripts and Superscripts

0	Value at inlet	s	Solid catalyst
b	Reactor bed	S	Steam-shift reaction
g	Gas	t	Thermal well
h	Heat	w	Cooling wall
m	Mass	z	Axial
M	Methanation reaction	\wedge	Based on inlet conditions
r	Radial	\sim	Steady state

ACKNOWLEDGMENTS

Acknowledgment is made to the donors of the Petroleum Research Fund, administered by the American Chemical Society, for partial support of this research. This work was also supported in part by National Science Foundation grant CPE-8315228. Finally, we wish to acknowledge support provided by Amoco Oil Company.

References

- Aris, R., "Mathematical Modelling Techniques." Pitman, London, 1978.
- Bird, R. B., Stewart, W. E., and Lightfoot, E. N., "Transport Phenomena." Wiley, New York, 1960.
- Bonvin, D., "Dynamic Modeling and Control Structures for a Tubular Autothermal Reactor at an Unstable State." Ph.D. thesis, University of California, Santa Barbara (1980).
- Brown, K. M., *Commun. ACM* **10**, 728–729 (1967).
- Carberry, J. J., "Chemical and Catalytic Reactor Engineering." McGraw-Hill, New York, 1976.
- Carberry, J. J., and Butt, J. B., *Catal. Rev.* **10**, 221 (1975).
- Carberry, J. J., and Wendel, M., *AIChE J.*, **9**, 129–133 (1963).
- Carey, G. F., and Finlayson, B. A., *Chem. Eng. Sci.* **30**, 587–596 (1975).
- Chidambara, M. R., and Davison, E. J., *IEEE Trans. Autom. Control* **AC-12**, 119–121 (1967a).
- Chidambara, M. R., and Davison, E. J., *IEEE Trans. Autom. Control* **AC-12**, 213–215 (1967b).
- Chidambara, M. R., and Davison, E. J., *IEEE Trans. Autom. Control* **AC-12**, 799–800 (1967c).
- Dahlquist, G., and Björke, A., "Numerical Analysis" (N. Anderson, trans.). Prentice-Hall, New York, 1974.

- Davis, M. E., "Numerical Methods and Modeling for Chemical Engineers." Wiley, New York, 1984.
- Davison, E. J., *IEEE Trans. Autom. Control* **AC-11**, 93–101 (1966).
- Davison, E. J., *IEEE Trans. Autom. Control* **AC-13**, 214–215 (1968).
- De Wasch, A. P., and Froment, G. F., *Chem. Eng. Sci.* **26**, 629–634 (1971).
- Fahien, R. W., and Stankovic, I. M., *Chem. Eng. Sci.* **34**, 1350 (1979).
- Ferguson, N. B., and Finlayson, B. A., *Chem. Eng. J.* **1**, 327–335 (1970).
- Finlayson, B. A., *Chem. Eng. Sci.* **26**, 1081–1091 (1971).
- Finlayson, B. A., "The Method of Weighted Residuals and Variational Principles." Academic Press, New York, 1972.
- Finlayson, B. A., *Catal. Rev. Sci. Eng.* **10**, 69–138 (1974).
- Finlayson, B. A., "Nonlinear Analysis in Chemical Engineering." McGraw-Hill, New York, 1980.
- Fossard, A., *IEEE Trans. Autom. Control* **AC-15**, 261–262 (1970).
- Froment, G. F., *Adv. Chem. Ser.* **109**, 1–34 (1972).
- Froment, G. F., *Chem. Ing. Tech.* **46**, 381 (1974).
- Froment, G. F., and Bischoff, K. B., "Chemical Reactor Analysis and Design." Wiley, New York, 1979.
- Gould, L. A., "Chemical Process Control: Theory and Applications." Addison Wesley, Reading, Massachusetts, 1969.
- Grad, J., and Brebner, M. A., *Commun. ACM* **11**, 12 (1968).
- Hlavacek, V., *Ind. Eng. Chem.* **62**, 8–26 (1970).
- Hlavacek, V., and Marek, M., *Chem. Eng. Sci.* **21**, 501 (1966).
- Hoiberg, J. A., Lyche, B. C., and Foss, A. S., *AIChE J.* **17**, 1434–1447 (1971).
- Jutan, A., Tremblay, J. P., MacGregor, J. F., and Wright, J. D., *AIChE J.* **23**, 732–742 (1977).
- Karanth, N. G., and Hughes, R., *Catal. Rev. Sci. Eng.* **9**, 169 (1974).
- Lee, A. L., *Symp. Clean Fuels Coal, Chicago, Sept.* (1973).
- McGowin, C. R., and Perlmutter, D. D., *Chem. Eng. J.* **2**, 125–131 (1971).
- Marshall, S. A., *Control* **10**, 642–643 (1966).
- Mears, D. E., *Ind. Eng. Chem. Fundam.* **15**, 20–23 (1976).
- Moe, J. M., *Chem. Eng. Progr.* **58**, 33–36 (1962).
- Paris, J. R., and Stevens, W. F., *Can. J. Chem. Eng.* **48**, 100 (1970).
- Perry, R. H., and Chilton, C. H., "Chemical Engineers' Handbook." McGraw-Hill, New York, 1973.
- Rabinowitz, P., ed., "Numerical Methods for Nonlinear Algebraic Equations." Gordon & Breach, New York, 1970.
- Schwartz, C. E., and Smith, J. M., *Ind. Eng. Chem.* **45**, 1209 (1953).
- Smith, J. M., "Chemical Engineering Kinetics." McGraw-Hill, New York, 1970.
- Stewart, W. E., *Chem. Eng. Prog. Symp. Ser.* **61**, 58, 61 (1967).
- Stewart, W. E., and Villadsen, J. V., *AIChE J.* **15**, 28 (1969).
- Valstar, J. M., Van Den Berg, P. J., and Oyserman, J., *Chem. Eng. Sci.* **30**, 723–728 (1975).
- Vatcha, S. R., "Analysis and Design of Methanation Processes in the Production of Substitute Natural Gas from Coal," Ph.D. thesis, California Institute of Technology, Pasadena (1976).
- Villadsen, J. V., and Michelsen, M. L., "Solution of Differential Equation Models by Polynomial Approximation." Prentice-Hall, New York, 1978.
- Villadsen, J. V., and Stewart, W. E., *Chem. Eng. Sci.* **22**, 1483–1501 (1967).
- Vortmeyer, D., and Schaefer, R. J., *Chem. Eng. Sci.* **29**, 485–491 (1974).
- Wei, J., Cwiklinski, R. R., and Tomura, J., *ISCRE* **8** (1984).
- Wilson, R. G., Fisher, D. G., and Seborg, D. E., *AIChE J.* **20**, 1131–1140 (1974).
- Yoon, H., Wei, J., and Denn, M. M., *AIChE J.* **25**, 429–439 (1979).
- Young, L. C., and Finlayson, B. A., *I&EC Fundam.* **12**, 412–422 (1973).
- Yu, W. C., Denn, M. M., and Wei, J., *ACS Symp. Ser.* (196) (1982).
- Yu, W. C., Denn, M. M., and Wei, J., *Chem. Eng. Sci.* **38**, 1467–1481 (1983).

This Page Intentionally Left Blank

KINPTR (MOBIL'S KINETIC REFORMING MODEL): A REVIEW OF MOBIL'S INDUSTRIAL PROCESS MODELING PHILOSOPHY

**Michael P. Ramage, Kenneth R. Graziani, Paul H. Schipper,
Frederick J. Krambeck, and Byung C. Choi**

**Mobil Research and Development Corporation
Paulsboro Research Laboratory
Paulsboro, New Jersey 08066**

I. Introduction

In the late 1960s, Mobil Research began the development of a mathematical simulation of the reforming process based on first principles of reaction chemistry, kinetics, and thermodynamics. The model was completed in 1974 and extended to include catalyst deactivation in 1979. Since 1974 the model has been used extensively throughout Mobil to optimize commercial reformer performance, to monitor Mobil's worldwide reformers, to evaluate commercial catalysts, to design new reformers, and to predict aromatics yield for petrochemical feedstocks. Because the model was developed from a fundamental basis, it has also been invaluable to Mobil's research efforts particularly in evaluating novel process designs, investigating catalyst improvements, and diagnosing commercial reformer problems. In addition, it has served as an excellent educational tool to teach personnel the interactions and trade-offs of the reforming process.

The model includes fundamental hydrocarbon conversion kinetics developed on fresh catalysts (referred to as start-of-cycle kinetics) and also the fundamental relationships that modify the fresh-catalyst kinetics to account for the complex effects of catalyst aging (deactivation kinetics). The successful development of this model was accomplished by reducing the problem complexity. The key was to properly define lumped chemical species and a minimum number of chemical reaction pathways between these lumps. A thorough understanding of the chemistry, thermodynamics, and catalyst

deactivation was necessary to reduce the problem to a manageable size without loss in accuracy. No model adjustment factors, commonly referred to as "tuning factors," are needed to simulate the wide range of conditions under which Mobil's commercial reformers operate.

Over 30 man-years of effort were involved in developing the model, which is named KINPTR, an acronym for *kinetic platinum reforming model*. Since its development, KINPTR has had a major impact in Mobil's worldwide operations. It can be accessed by personnel at each of Mobil's locations throughout the world. Input requirements are simple and convenient making it very user friendly. Only feed characteristics, product quality targets, process configuration information, and process conditions are required for input. Output is informative and detailed. Overall and detailed yields, feed and product properties, and reactor performance data are given in the output.

In this chapter the following topics will be reviewed: KINPTR's start-of-cycle and deactivation kinetics, the overall program structure of KINPTR, the rationale for the kinetic lumping schemes, the model's accuracy, and examples of KINPTR use within Mobil. As an example, the detailed kinetics for the C₆ hydrocarbons are provided.

II. Reforming Process

KINPTR is an overall process model; thus it simulates all important aspects of the process which affect performance. In order to lay a foundation for upcoming discussions related to KINPTR development, the important aspects of naphtha reforming—chemistry, catalysis, and reactor/hardware design—will be summarized. More extensive reviews are available in the literature (1–3).

A. CHEMISTRY

Commercial reformers upgrade virgin and cracked naphthas in the 5–12 carbon number range (in 310–490 K boiling range) to high-octane gasoline. Most virgin naphthas from crude oil have octane numbers below 65; this results from their high naphthene (cycloparaffin) and *n*-paraffin content. The reformer converts naphthenes and paraffins to high-octane aromatics and branched paraffins (Table I). In addition, low-carbon-number paraffins (C₅-) outside the gasoline boiling range are produced and there is a net generation of H₂ across the reformer. These transformations take place through a complex set of chemical reactions which involve over 300 chemical species, as

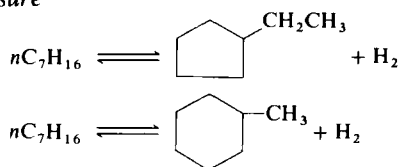
TABLE I
REFORMING CHARGE AND PRODUCT COMPOSITIONS^a

C ₅₊ composition (wt. %)	Mid-Continent		Arabian Light	
	Charge	Product	Charge	Product
<i>i</i> -Paraffins	27.2	21.4	33.1	26.0
<i>n</i> -Paraffins	28.0	10.0	34.3	12.4
Naphthenes	32.9	0.8	18.3	0.8
Aromatics	11.9	67.8	14.3	60.8
C ₅₊ research octane	64.2	99.1	<60	97.1

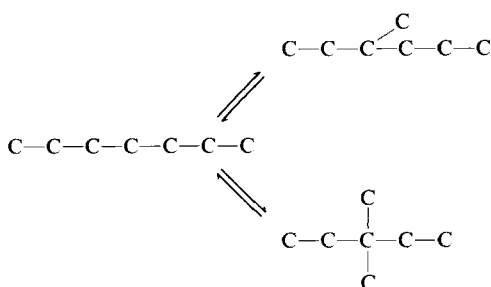
^a Reformer conditions: 3103 kPa, 783 K, 10/1 recycle ratio, 1.3 LHSV.

identified by gas chromatography. In general, reactions can be classified by type as shown here.

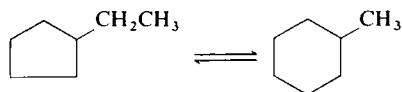
Paraffin Ring Closure



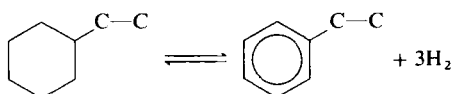
Paraffin Isomerization

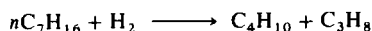
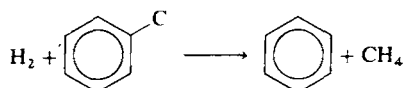


Naphthene Isomerization



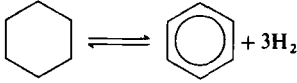
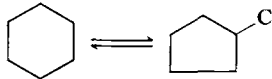
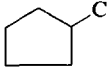
Naphthene Dehydrogenation



Paraffin Cracking*Aromatic Dealkylation*

Reaction parameters for the classes of reactions vary widely, as shown in Table II. As a result, different reaction classes dominate at various locations along the reaction pathway, as shown by the "zones" on Fig. 1 for reforming a mixture of C_6 components. The dehydrogenation reactions are very rapid and quickly approach equilibrium concentration, as indicated by an initial rapid increase of aromatics (zone A). These reactions are highly endothermic. In zone B, cyclopentanes are isomerized to cyclohexanes, which are in turn rapidly dehydrogenated to aromatics. Also, paraffins are isomerized to higher branched paraffins. Ring closure and paraffin cracking are slow steps in the reaction sequence (zone C). Paraffin reactions are critical in the reforming process. Paraffins are converted through three reactions; ring closure to five- and six-carbon-member naphthenes [cyclopentanes (N_5) and cyclo-

TABLE II
REACTION PARAMETERS FOR TYPICAL REFORMING REACTIONS

Reaction class	Relative reaction rate	ΔH_{RX} (kJ/mole)
Dehydrogenation		
	Very rapid (51)	400
Ring/paraffin isomerization		
	Rapid (2)	-27
Ring closure		
$C-C-C-C-C-C \rightleftharpoons$ 	Very slow (0.01)	120
Paraffin cracking		
$C-C-C-C-C-C \longrightarrow C-C-C-C + C-C$	Slow (0.03)	-37

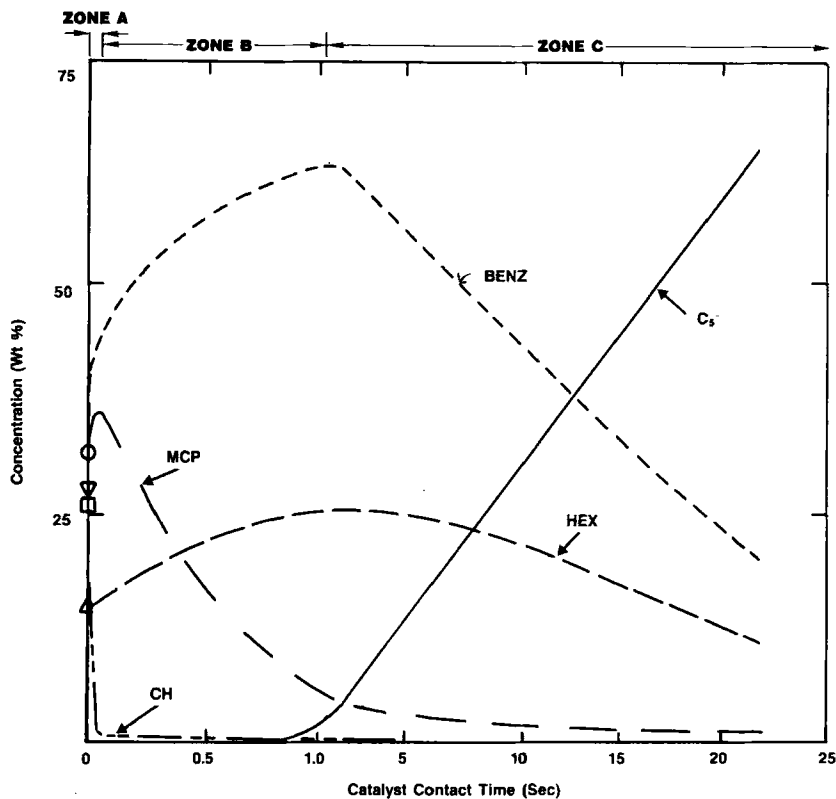


FIG. 1. Reaction composition profile. Reforming at 794 K, 2620 kPa. Zone A; dehydrogenation zone; zone B; isomerization zone; zone C; hydrogenation and cracking zone. [Charge stock: Δ , hexane (HEX); \square , benzene (BENZ); ∇ , cyclohexane (CH); \circ , methylcyclopentane (MCP).]

hexanes (N_6)], isomerization to branched paraffins, and cracking to lower-carbon-number paraffins. The ring closure reaction will increase octane the most since naphthenes in turn rapidly convert to aromatics. However, the ring closure rate is slow and approaches that of paraffin cracking. The similarity of these two reaction rates causes a significant gasoline yield loss when the reformer severity is "pushed" to make high octane (high aromatic yield). Also, thermodynamics has a pronounced effect on the benzene yields in zone C. Benzene concentration drops since the reaction sequence is reversible. Benzene, after being formed in zones A and B, is hydrogenated to naphthenes which ring open to paraffins. Paraffins can then ultimately crack to C_5 - light gas. Therefore, in general, process conditions which favor ring closure over cracking and ring opening are desirable. Such

TABLE III
AROMATIZATION SELECTIVITIES OF
PARAFFINS^a

Carbon number	1241 kPa	3103 kPa
6	0.26	0.04
7	0.41	0.19
8 ⁺	0.63	0.54

^a Weight of aromatic produced divided by weight of paraffin converted at 783 K.

conditions are, for example, low pressure, high temperature, and increased paraffin carbon number. Aromatization selectivities for paraffins as a function of pressure and carbon number are listed in Table III.

An important part of the model development was first defining a set of "lumped" chemical species from the 300 identified species and then defining

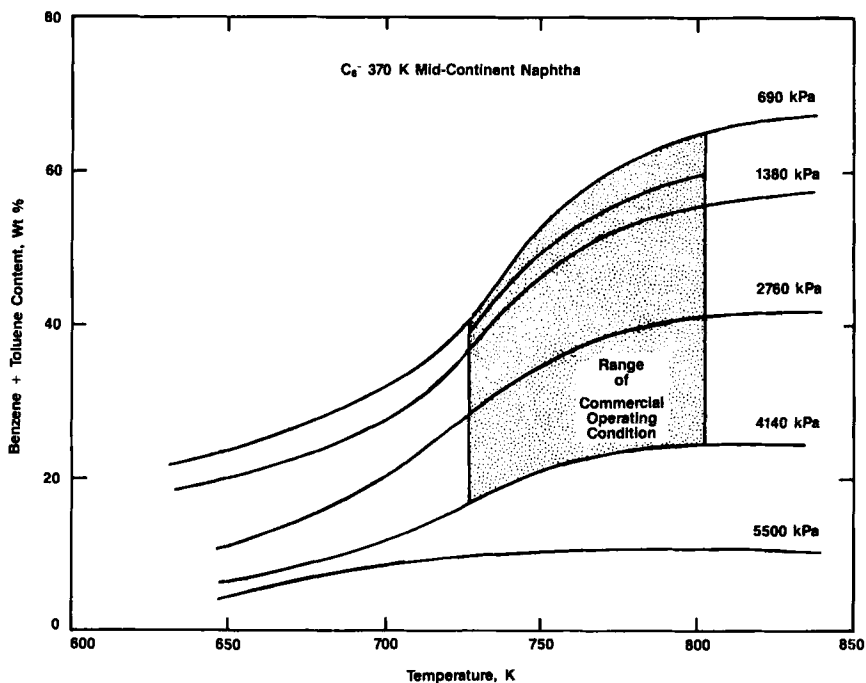


FIG. 2. Effect of operating conditions on aromatics formation.

the reaction pathways between the lumps so that reaction profiles, such as those shown in Fig. 1, could be predicted. Most reforming reactions are reversible. Thus, thermodynamic constraints play an important role in understanding the reforming chemistry and in model development. Aromatics formation as a function of pressure and temperature, from a C_6 - 370 K Mid-Continent naphtha is shown in Fig. 2. High yields of aromatics are favored by low pressures and high temperatures. Conditions which favor high aromatic yields also give high overall gasoline yield because side reactions to C_5 -paraffins are minimized. The window of operation for commercial reformers is indicated by the shaded area in Fig. 2. Pressures below 680 kPa are not yet feasible in commercial operation because of rapid catalyst deactivation. As shown in Fig. 3, the relative rate of aging increases significantly as the reformer pressure is reduced. Semiregenerative reformer designs operate in the pressure range of 1700 to 4100 kPa and have cycle lengths from 0.5 to 2 years. Universal Oil Products' (UOP's) continuous regeneration reformers and Exxon's cyclic reformers operate at lower pressures (~ 680 kPa for UOP's continuous

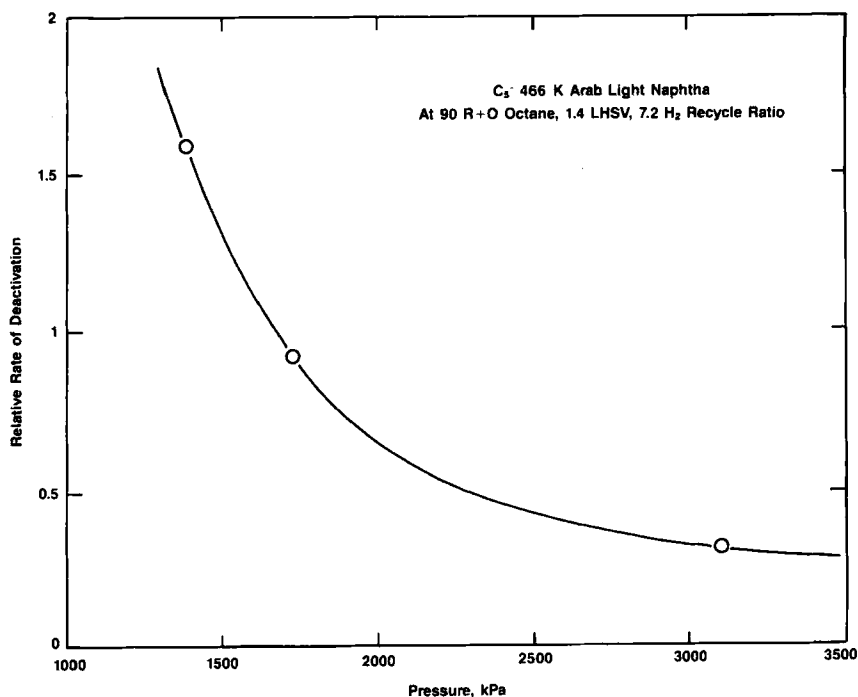
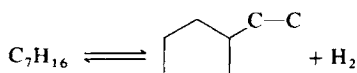


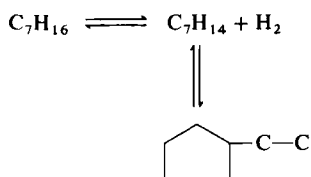
FIG. 3. Pressure effect on deactivation rate.

reformer) to increase the yield of high-octane components. The average catalyst cycle length is as short as 1 week for the continuous reformer. The trade-off between high yields and reasonable cycle lengths is one of the interesting and important optimization problems for a reforming model.

Although the reaction classes discussed earlier are sufficient to describe the hydrocarbon conversion kinetics, an understanding of the elementary reaction sequence is needed to describe catalyst deactivation. Several of the overall reactions require formation of olefinic intermediates in their elementary reaction sequence. Ultimately, these olefinic intermediates lead to coke formation and subsequent catalyst deactivation. For example, the ring closure reaction



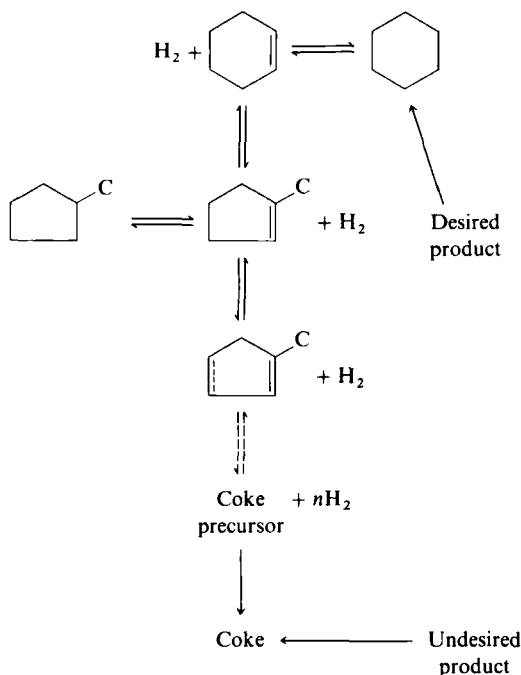
requires paraffin dehydrogenation to an olefin and, subsequently, carbon skeleton rearrangement to a cycloparaffin.



Also, a normal paraffin is converted to an isoparaffin first by dehydrogenation to a straight-chain olefin, then by rearrangement to form an isoolefin, and by hydrogenation to an isoparaffin.

For example, in the ring isomerization reaction, methylcyclopentane forms a methylcyclopentene intermediate in its reaction sequence to cyclohexane. The intermediate can also further dehydrogenate to form methylcyclopentadiene, a coke precursor. Bakulen *et al.* (4) states that methylcyclopentadiene can undergo a Diels–Alder reaction to form large polynuclear aromatic coke species. Once any olefinic intermediate is formed, it can either go to desired product or dehydrogenate further and polymerize to coke precursors. This results in a selectivity relationship between the desired products and coke formation as shown on the next page.

Catalyst deactivation is primarily caused by the blockage of active sites due to the coke formed from these olefinic intermediates. Higher hydrogen pressures suppress the diolefin formation, making the selectivity between olefinic intermediates and liquid products (in contrast to coke products) more favorable. However, higher pressures reduce selectivity to aromatics in the *desired* liquid product. Thus, a rigorous model must accurately predict not only the rates of product formation, but also the formation of coke precursors

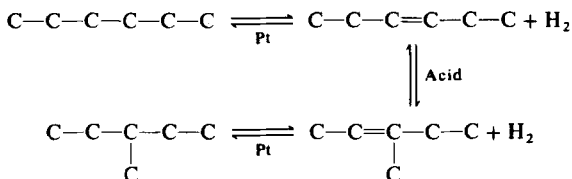


and their effect on catalyst deactivation over a wide range of reactor temperatures and pressures.

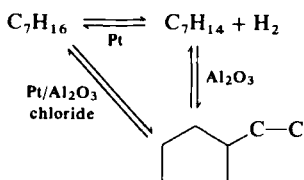
B. REFORMING CATALYSIS

Typical reforming catalysts are Pt/Re on Al_2O_3 and Pt/Ir on Al_2O_3 . Both metals and the support play key roles in the catalysis. The role of platinum is to catalyze dehydrogenation–hydrogenation reactions. Chlorided alumina acts as an acid and catalyzes carbon skeletal rearrangement through carbonium ion mechanisms. Proper acid activity is generally maintained by injecting trace amounts of a chloride compound with the feed. The second metal, either rhenium or iridium, acts as a stabilizer and suppresses catalyst deactivation. It can also affect reaction selectivity. The role of the second metal in catalyst stabilization is not fully understood and is the subject of current industrial and academic research.

Except for naphthalene dehydrogenation, which only requires a Pt site for catalysis, all the other major reactions require an interaction between sites. Ring and paraffin isomerization require the platinum function for dehydrogenation to olefin, the acid function for carbon skeletal rearrangement, and the metal function again for hydrogenation of the olefin.

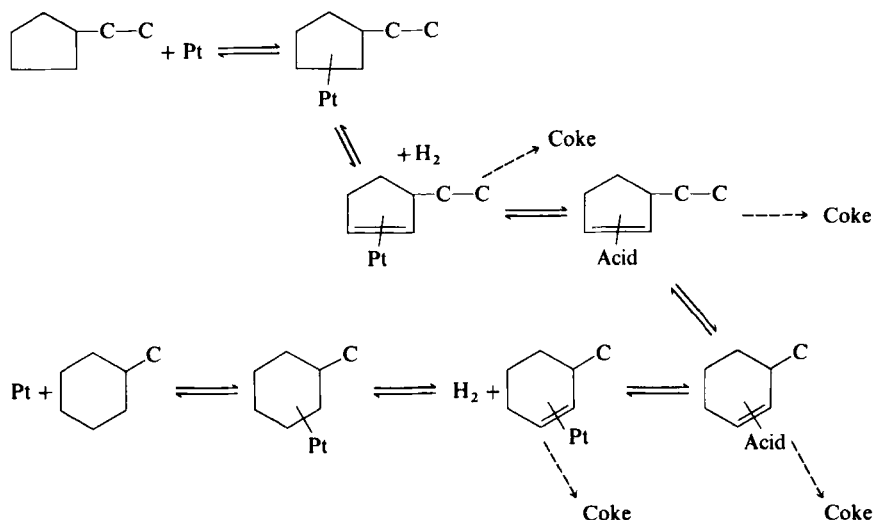


Ring closure can proceed through dehydrogenation of the paraffin on a platinum site followed by carbon skeletal rearrangement on an acid site. However, there is also evidence (5) that it can proceed directly on a single site composed of Pt, alumina, and chloride.



Cracking reactions can take place on either the acid site or the platinum site. Acid cracking is characterized by the formation of C_3 and C_4 paraffins due to the carbonium ion mechanism. Metal cracking (hydrogenolysis), as shown by Sinfelt (19), is random and forms more C_1 and C_2 gases relative to acid cracking.

As mentioned previously, the catalyst deactivates because of coke formation on the Pt and acid sites. The overall scheme for ethylcyclopentane is shown here.



It is commonly thought that the second metal, Re or Ir, lowers the formation rate of these coke precursors⁽⁶⁾.

A kinetic reforming model must properly represent these catalyst effects. Thus, catalyst composition and state factors such as metal type and activity, acid activity through chloride control and alumina type, and the role of the second metal must be built in to the kinetics.

C. REFORMER REACTOR CONFIGURATION

Commercial designs take into account the complex characteristics of the reforming reaction network. In order to show how these characteristics are factored into a design, a semi-regenerative reformer configuration with light gas recycle to the first reactor bed (Fig. 4) will be discussed here. In this design example, the catalyst fill is split between three adiabatic reactor beds of unequal size, with equal inlet temperatures. The catalyst fill in each reactor is primarily determined by the adiabatic temperature changes which take place during conversion. For optimal performance, catalyst deactivation is also a factor in establishing the fill ratios. The recycle stream is the light gas coming off a low-pressure separator and has a composition which is 65 to 95% H_2 . The composition of this gas can be changed by adjusting the conditions of the separator. It also will change with reformer severity, naphtha type, and catalyst age.

[Note: Typically in reformer design, liquid hourly space velocity (LHSV) is defined as fresh liquid charge volumetric flow rate divided by catalyst volume. Catalyst volume includes the void fraction and is defined by $W_c/\rho_p(-\epsilon)$.]

A typical reformer temperature profile for an inlet temperature of 783 K is shown in Fig. 5 for a three-reactor design. Only 15–20% of the total catalyst is used in the first reactor because of the rapid temperature decrease which results from naphthene dehydrogenation (Fig. 6). Note there is a 70 K temperature drop in this reactor. The activation energies are such that reaction rates are very low at the bottom of the first reactor. Thus, more catalyst in the first reactor would not provide additional conversion.

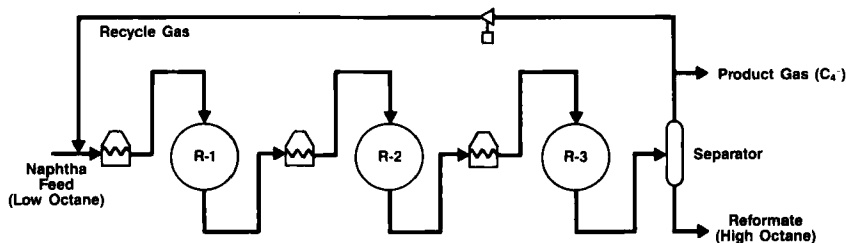


FIG. 4. Typical semi-regenerative catalytic reformer.

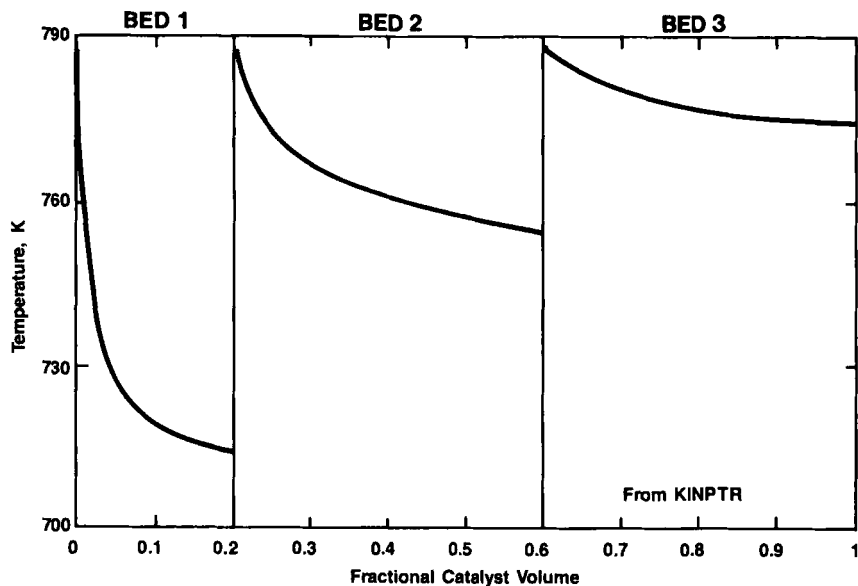


FIG. 5. Reactor temperature profiles.

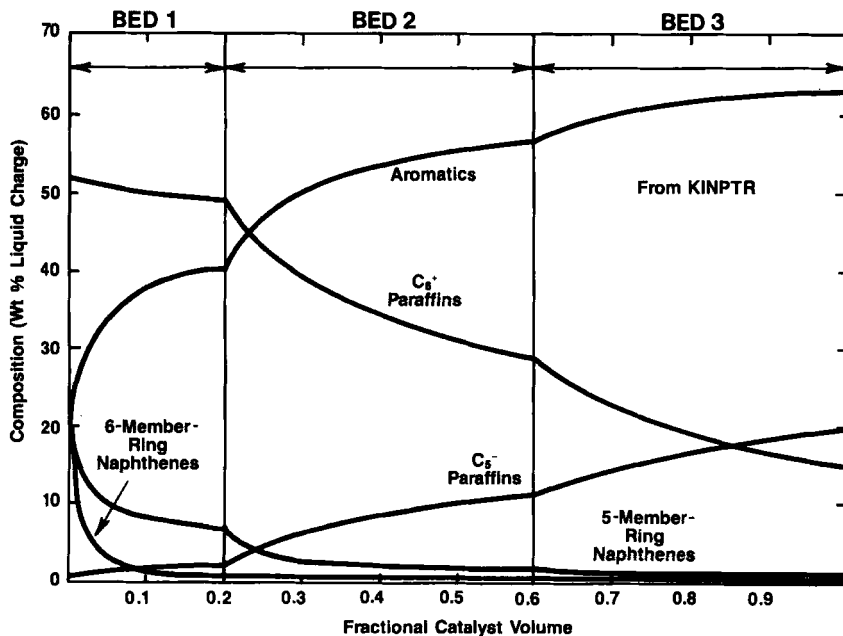


FIG. 6. Reactor composition profiles by molecular type.

After the product is reheated to 783 K for the second reactor inlet, the remaining five-member-ring naphthenes are isomerized to six-member rings, which are subsequently dehydrogenated to aromatics. Notice that this occurs in the "top" of the reactor bed, with a corresponding large temperature drop. Once the five-member ring naphthenes are reacted, equilibrium constraints on the paraffin ring closure reactions are relaxed and these reactions proceed. As mentioned earlier, paraffin cracking always proceeds at rates similar to ring closure.

Following a second preheat to 783 K, paraffin ring closure and cracking occur in the last reactor. Since the cracking rate is exothermic, there is only a small drop in temperature in the third reactor. Process conditions—temperature, pressure, space velocity, etc.—can have a significant effect on the selectivity between paraffin ring closure and cracking. In a refiner's language, conditions have a large impact on the yield-octane relationship. Since reformers are typically operated to give a target reformate octane, sufficient paraffin conversion must be obtained in the third reactor to meet the target.

As the catalyst deactivates, reactor inlet temperature must be increased to maintain the target octane. A typical temperature profile as a function of process stream time is shown in Fig. 7. The temperature increase further

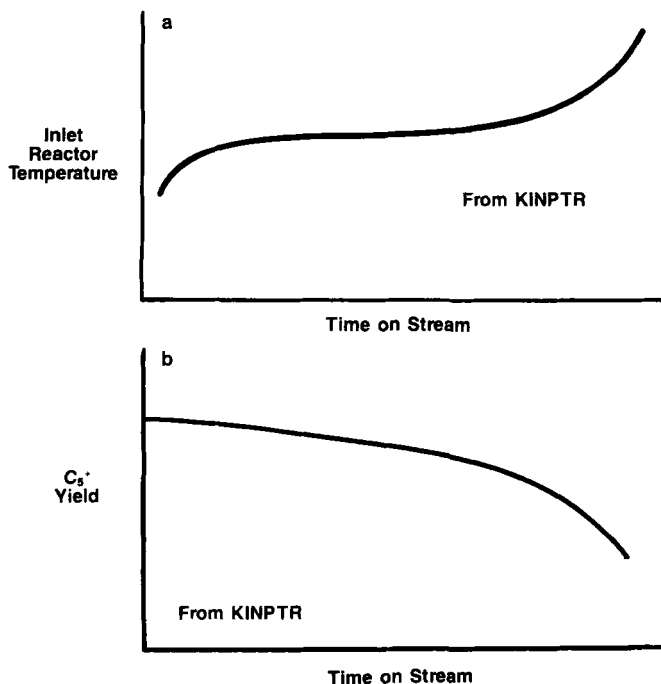


FIG. 7. Aging curve for typical semi-regenerative operation.

enhances the rate of deactivation. In addition, deactivation changes the catalyst acid-metal balance and thus its selectivity. With deactivation, more of the octane boost arises from cracking of paraffins (instead of aromatization), which lowers gasoline yield at target octane. When the temperature reaches the reactor metallurgy limit or the gasoline yield losses become too large, the catalyst must be regenerated. Cycle lengths between regenerations are typically 0.5–2 years in a semi-regenerative reformer.

III. Development of Reforming Kinetics

An effective kinetic reforming model must accurately represent the chemical interactions of a system which contains over 300 chemical species, as measured by gas chromatography. To model such a complex system with all species would be extremely difficult. However, if the correct assumptions are made, the size of the problem can be reduced without losing accuracy. The large number of chemical components can be reduced to a manageable, smaller set of kinetic lumps, each composed of chemical species which have sufficiently similar reaction characteristics. Weekman (7), Luss and Hutchinson (20), and Wei and Kuo (21) provide detailed discussions on the philosophy of defining kinetic lumps for complex reaction systems. We employed a similar strategy in developing KINPTR. The kinetics are defined in terms of a minimum set of lumped chemical species having a minimum, yet sufficient, number of reaction pathways between them. If the lumps and pathways properly describe the reforming system, the kinetic rate parameters will be independent of feedstock composition and will not require additional correlative adjustment factors for accurate predictions.

In the model development, the following strategies were employed.

1. The hydrocarbon lumps and reaction network for both the start-of-cycle and the deactivation kinetics were defined.
2. The start-of-cycle kinetic problem was uncoupled from the deactivation kinetics by taking advantage of their widely different time constants.
3. An experimental design was developed which uncoupled the overall problem into a number of smaller parameter estimation problems. This approach reduced confounding between parameters, for both start-of-cycle and deactivation kinetics.

For the start-of-cycle kinetics, the following assumptions were made.

1. The nonlinear rate expressions were of the pseudo-monomolecular form (8), which allowed the nonlinear parameter estimation problem to be split into two simpler linear problems.

2. The model followed mass action kinetics with Langmuir–Hinshelwood adsorption.

3. The model satisfied microscopic reversibility with the equilibrium constraints determined a priori from free energy data.

4. The reaction steps were consistent with known pure component behavior. For example, a benzene cracking reaction was not allowed.

5. Diffusional effects were combined into apparent kinetic rate constants by using commercial-sized catalysts in kinetic experiments. The experiments were designed so that no significant external transport and axial dispersion effects occurred.

For the deactivation kinetics, the following assumptions were made.

1. Catalyst activity loss was caused by coke formation only.

2. Deactivation could be modeled by using first-order irreversible aging rates.

3. The model followed single-site, nondissociative, Langmuir–Hinshelwood poisoning. This resulted in the same adsorption coefficients for deactivation and start-of-cycle kinetics.

In addition, based on pure component studies, the aging rates were found to depend on time and also on the local temperature, pressure, and composition in the vicinity of the catalytic site. Thus, aging rates for each reaction vary axially along the reactor length.

The validity of these assumptions will be demonstrated by KINPTR's ability to predict the wide range of commercial reformer performance and feedstock with no additional parameters.

A. LUMPING SCHEME AND REACTION NETWORK

The same criteria were used for start-of-cycle and deactivation lumping. Start-of-cycle lumping was based on thermodynamics and molecular–reaction similarity. The deactivation kinetic lumps contain the start-of-cycle lumps as a subset. The additional deactivation lumps were required to properly describe the effect of carbon number on aging rate.

1. *Start-of-Cycle Lumping Scheme*

Examples of thermodynamic equilibria are shown in Table IV. The conversion of five- and six-member ring naphthenes to aromatics is quite favorable. Methylcyclopentane conversion is the least favorable. Equilibria for aromatic formation improves with carbon number. For five-member ring naphthenes, the largest improvement occurs between the six-carbon

TABLE IV
 REFORMING EQUILIBRIA^a

Carbon number	A/N ₆ ^b	A/N ₅ ^b	(N ₅ ·N ₆)/P ^b
6	4.6	2.3	-3.7
7	5.4	4.2	-2.4
8	6.3	5.8	-1.4
9	7.1	7.0	-1.4

^a Conditions: 756 K and 1360 kPa.^b Natural log of weight ratio; A, aromatics; N₆, C₆ naphthenes; N₅, C₅ naphthenes; P, paraffins.

and seven-carbon components. The difference diminishes at higher carbon numbers.

Paraffin conversion to naphthenes is very unfavorable (last column of Table IV). For paraffins to be converted to naphthenes by ring closure, naphthenes must be at very low concentrations. If appreciable naphthenes exist, such as at short catalyst contact times, naphthene ring opening to paraffins can occur. Again, equilibria improve with carbon number. Eight- and nine-carbon paraffins behave quite similarly.

This wide variation in thermodynamic behavior requires that paraffins, cyclopentanes, cyclohexanes, and aromatics be treated separately in an accurate lumping scheme. Carbon number effects on the lumping scheme are indicated in Table IV, but are shown more clearly in Fig. 8. Aromatic selectivity (aromatic weight yield/weight hydrocarbon charged) for the molecular classes is presented as a function of carbon number and represents the effects of both thermodynamics and reaction kinetics. With carbon number, selectivity changes considerably between six-carbon, seven-carbon, and eight-carbon paraffins and cyclopentanes. For hydrocarbons containing eight or more carbon atoms, the selectivity within a molecular class does not vary significantly. Therefore, within a molecular class, the carbon number lumps C₆, C₇, and C₈₊ can be assumed.

Start-of-cycle kinetic lumps in KINPTR are summarized in Table V. A C₅-light gas lump is required for mass balance. Thirteen hydrocarbon lumps are defined. The reforming kinetic behavior can be modeled without splitting the lumps into their individual isomers (e.g., isohexane and *n*-hexane). Also, the component distribution within the C₅-lump can be described by simple correlations, as discussed later. The start-of-cycle reaction network that defines the interconversions between the 13 kinetic lumps is shown in Fig. 9. This reaction network results from kinetic studies on pure components and narrow boiling fractions of naphthas. It includes the basic reforming reactions

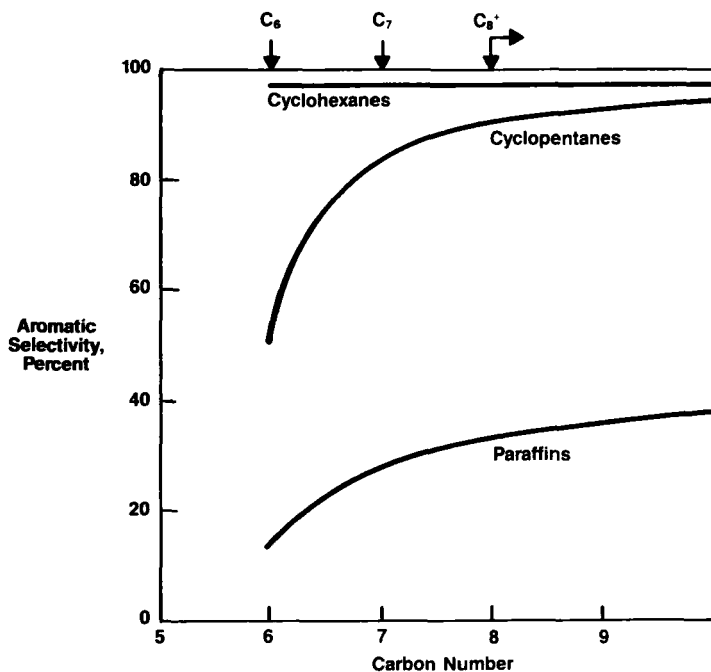


FIG. 8. Component reforming efficiencies at 756 K, 1379 kPa.

TABLE V

KINPTR START-OF-CYCLE KINETIC LUMPS (INDEX)

Carbon number	Six-carbon-ring naphthenes (N ₆)	Five-carbon-ring naphthenes (N ₅)	Paraffins (P)	Aromatics (A)
C ₈₊	C ₈₊ cyclohexanes (1)	C ₈₊ cyclopentanes (2)	C ₈₊ paraffins (3)	C ₈₊ aromatics (4)
C ₇	Methylcyclohexane (5)	Cyclopentanes (6)	Heptanes (7)	Toluene (8)
C ₆	Cyclohexane (9)	Methylcyclopentane (10)	Hexanes (11)	Benzene (12)
C ₅ -				C ₅ - hydrocarbons (13)

of cracking, ring closure, ring isomerization, and dehydrogenation. Those reactions between lumps of the same carbon number are reversible. Those reactions coupling carbon number levels (cracking) are irreversible. Note that for the six-carbon components, the reactions follow a simple, consecutive reaction sequence with no direct paraffin dehydrocyclization to six-carbon rings.

In general, the lumping scheme and reaction network of our model are considerably less complicated than that of Kmak (9).

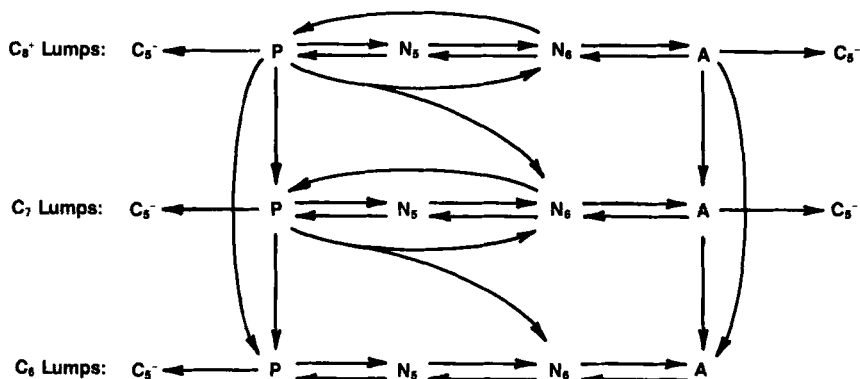


FIG. 9. Reforming lump reaction network. N, cyclopentane and cyclohexane naphthenes; P, C₆⁺ paraffins; A, aromatics; C₅⁻, pentane and lighter.

2. Deactivation Lumping Scheme

Experiments performed both in our laboratory and by others (4) show that aging is a strong function of boiling point, with the higher boiling components producing a much higher deactivation rate. The aging rate for a given class of reaction—such as ring closure—is a strong function of carbon number. For example, the effect of aromatic carbon number on the ring closure deactivation rate is given in Table VI. Therefore, while C₈⁺ components can be lumped together in the start-of-cycle kinetics, they must be delumped for the aging kinetics into C₈, C₉, C₁₀, and C₁₁ hydrocarbon types. However, the same molecular classes can be assumed. Components required in the deactivation kinetics are given in Table VII.

TABLE VI
EFFECT OF AROMATIC CARBON NUMBER ON
RING-CLOSURE AGING RATES

Aromatic carbon number	Contribution to ring closure aging rate ^a
C ₆	0
C ₇	1.0
C ₈	1.0
C ₉	1.0
C ₁₀	2.0
C ₁₁	14.0

^a Relative to C₇ aromatic contribution.

TABLE VII
COMPONENTS OF AGING

Component number	Component name	Component abbreviation
22	Hexanes	C ₆ P
21	Methylcyclopentane	C ₆ N ₅
20	Cyclohexane	C ₆ N ₆
19	Benzene	C ₆ A
18	C ₇ paraffins	C ₇ P
17	C ₇ cyclopentanes	C ₇ N ₅
16	C ₇ cyclohexanes	C ₇ N ₆
15	Toluene	C ₇ A
14	C ₈ paraffins	C ₈ P
13	C ₈ cyclopentanes	C ₈ N ₅
12	C ₈ cyclohexanes	C ₈ N ₆
11	C ₈ aromatics	C ₈ A
10	C ₉ paraffins	C ₉ P
9	C ₉ cyclopentanes	C ₉ N ₅
8	C ₉ cyclohexanes	C ₉ N ₆
7	C ₉ aromatics	C ₉ A
6	C ₁₀ paraffins	C ₁₀ P
5	C ₁₀ naphthenes	C ₁₀ N
4	C ₁₀ aromatics	C ₁₀ A
3	C ₁₁ paraffins	C ₁₁ P
2	C ₁₁ naphthenes	C ₁₁ N
1	C ₁₁ aromatics	C ₁₁ A

B. MATHEMATICS FOR DETERMINING KINETIC CONSTANTS

The general mathematical description for determining reforming kinetics is shown below for hydrocarbon conversion and deactivation rates, respectively,

$$\partial \bar{w} / \partial v = f_1(T, P_h, \bar{\alpha}, \bar{w}) \quad (1)$$

$$\partial \bar{\alpha} / \partial t = f_2(T, P_h, \bar{w}) \bar{\alpha} \quad (2)$$

where \bar{w} is the hydrocarbon composition vector and $\bar{\alpha}$ is the catalyst state vector (i.e., $\bar{\alpha} = 1.0$ signifies start-of-cycle activity). This set of highly coupled nonlinear partial differential equations describes both the catalyst deactivation and the hydrocarbon conversion through the reactor. Temperature, \bar{w} , and $\bar{\alpha}$ all vary with both fractional catalyst volume through the reactor v and with time on stream t . Also, the rate of deactivation ($\partial \bar{\alpha} / \partial t$) depends on hydrocarbon composition \bar{w} , and the rate of conversion ($\partial \bar{w} / \partial v$) depends on catalyst state $\bar{\alpha}$. This composition-dependent approach to aging differs significantly from other approaches (10, 11).

This complex system would be difficult to solve directly. However, the problem is separable by taking advantage of the widely different time scales of conversion and deactivation. For example, typical catalyst contact times for the conversion processes are on the order of seconds, whereas the time on stream for deactivation is on the order of days. [Note: Catalyst contact time is defined as the volume of catalyst divided by the total volumetric flow in the reactor at unit conditions, PV/FRT . Catalyst volume here includes the voids and is defined as $W_c/\rho_p(1 - \epsilon)$]. Therefore, in the scale of catalyst contact time, $\bar{\alpha}$ is constant and Eq. (1) becomes an ordinary differential equation:

$$d\bar{w}/dv = f_1(T, P_h, \bar{w}, \bar{\alpha}) \quad (3)$$

At start of cycle, $\bar{\alpha}$ equals 1 and

$$d\bar{w}/dv = f_1(T, P_h, \bar{w}) \quad \text{at } t = 0 \text{ (start of cycle)} \quad (4)$$

However, in handling the deactivation problem, Eq. (2) must still be solved in combination with Eq. (3).

1. Start-of-Cycle Kinetic Formulations

Reaction rates for the start-of-cycle reforming system are described by pseudo-monomolecular rates of change of the 13 kinetic lumps. That is, the rates of change of the lumps are represented by first-order mass action kinetics with the same adsorption isotherm applicable to each reaction step. Following the same format as Eq. (4), steady-state material balances for the hydrocarbon lumps are derived for a plug-flow, fixed bed catalytic reformer. A nondissociation, Langmuir-Hinshelwood adsorption model is employed. Steady-state material balances written over a differential fractional catalyst volume dv are the following:

$$d\bar{w}/dv = \phi \bar{K} \bar{w} \quad (5)$$

where

$$\phi = \frac{(PV/FRT)k_\phi}{[1 + K_h P_h + (PF_c/F)\bar{K}_w \cdot \bar{w}]} \quad (6)$$

and where P , P_h are the total and hydrogen pressures, respectively; V is the total catalyst volume [$W_c/\rho_p(1 - \epsilon)$]; v is the fractional catalyst volume; T is the temperature; F is the total molar flow rate; F_c is the mass flow rate of hydrocarbon charge; K_w , K_h are the adsorption equilibria coefficients; \bar{w} is the vector of hydrocarbon weight fractions; \bar{K} is the pseudomonomolecular selectivity rate constant matrix; and k_ϕ is the "real-time" rate constant. Hydrocarbon weight fraction w_j is defined on a H_2 -free basis, where

$$w_j = P_j F M_j / P F_c (1 - h) \quad (7)$$

h being the weight fraction yield of H_2 , typically 0.01 to 0.02. Therefore for added simplicity, we further assume that $1 - h \approx 1$. In Eq. (7), M_j and P_j are the molecular weight and partial pressure of lump j , respectively. Note that $\sum_{j=1}^{13} w_j = 1$, where H_2 is not included in the summation. The hydrogen yield h can be back-calculated from a hydrogen atom balance on the 13 hydrocarbon lumps.

The following features may be defined in this kinetic description of reforming. In Eq. (6), ϕ is the catalyst activity function incorporating the adsorption equilibria effects. Since each reaction rate expression employs the same adsorption term, it can be factored out of the general rate expressions and appears as a multiplying function on the matrix \bar{K} of Eq. (5); \bar{K} is the pseudo-monomolecular selectivity rate constant matrix. The elements in this matrix have the form k_{ji}/k_ϕ , where k_{ji} is the reaction rate constant for the reaction of the i th hydrocarbon lump to the j th lump. All elements in \bar{K} are defined relative to the real-time rate constant k_ϕ . As with the adsorption terms, k_ϕ is also factored out of the general rate expressions and appears as a matrix multiplier in ϕ . Since k_ϕ itself represents the rate constant of one of the reforming reactions, one element in \bar{K} will be $k_\phi/k_\phi = 1$, and k_ϕ may be chosen arbitrarily. In KINPTR, it is chosen to be the irreversible constant for heptane cracking to C_5 -.

The individual rate constants k_{ji} and k_ϕ follow the Arrhenius form and may be defined relative to a set of reference conditions. We define rate constants relative to the experimental conditions of 756 K and 1220 kPa. Their form is then

$$k = k^0 \exp \left[-\frac{E}{R} \left(\frac{1}{T} - \frac{1}{756} \right) \right] \left(\frac{P_h}{1220} \right)^n \quad (8)$$

where k is either k_{ji} or k_ϕ and k^0 is the rate constant at the reference conditions, E is the activation energy, and n is the reaction order in H_2 .

For reactions which are reversible, reverse rate constants k_{ij} satisfy microscopic reversibility and are given by

$$k_{ij} = k_{ji}(P_h)^{\gamma_{ji}} \exp[\Delta S_{ji}/R - \Delta H_{ji}/RT] \quad (9)$$

where ΔS_{ji} and ΔH_{ji} are, respectively, the entropy and enthalpy changes of reaction evaluated at reforming temperatures and γ_{ji} is the H_2 stoichiometric coefficient. Here ΔS_{ji} and ΔH_{ji} for each lump are calculated from heats of formation and free energies for the individual isomers in each lump.

The preceding equations can be used with appropriate experimental data to determine the kinetic parameters k_ϕ , E_ϕ , n_ϕ , k_{ji}^0 , E_{ji} , n_{ji} , \bar{K}_w , and K_h . The pseudo-monomolecular form of Eq. (5) can be used to simplify the parameter estimation into a selectivity problem (determine \bar{K}) and an activity problem (determine ϕ). This reduces the original highly nonlinear problem into two

simpler linear problems. The separation is accomplished by defining a new independent variable, τ , such that

$$d\bar{w}/d\tau = \bar{K}\bar{w} \quad (10)$$

where

$$d\tau = \phi dv \quad (11)$$

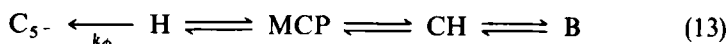
Equation (10) defines the selectivity kinetic problem since \bar{K} is the only parameter to be determined. Equation (10) can be integrated directly to give

$$\bar{w}(\tau) = \bar{X} \exp(\bar{\Lambda}\tau) \bar{X}^{-1} \bar{w}(0) \quad (12)$$

where \bar{X} is the matrix of eigenvectors and $\bar{\Lambda}$ the diagonal matrix of eigenvalues of the selectivity matrix \bar{K} .

As discussed earlier, the selectivity rate constant matrix \bar{K} contains one element that is unity, that is, $k_\phi/k_\phi = 1$. This property allows the elements of \bar{K} to be determined from composition data alone. The selectivity time τ , defined in Eq. (11), does not need to be independently known.

To illustrate the method of determining the selectivity rate constant matrix, it first must be shown that τ can be uniquely related to C_{5-} at any position in the reactor bed. This can be demonstrated using the C_6 system as an example (see Fig. 10):



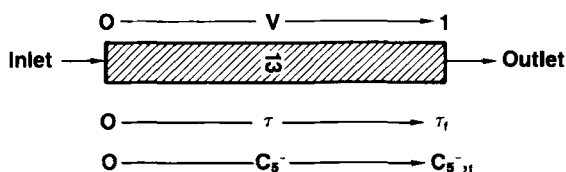
Note that k_ϕ in this example is defined as the real-time constant for hexane cracking to C_{5-} . In the selectivity matrix for this system this constant is unity. Thus, Eq. (10), written for C_{5-} formation, becomes

$$dC_{5-}/d\tau = H \quad (14)$$

In Eq. (14), C_{5-} monotonically increases with τ through the hexane concentration, and therefore is uniquely related to τ . Equation (14) allows the selectivity rate constant matrix to be fit in a selectivity space with the observed C_{5-} concentration as the independent variable and all C_{6+} compositions as the dependent variables.

During the selectivity kinetic parameter estimation, the relationship for τ in terms of C_{5-} is determined from Eq. (12). For an assumed set of rate constants \bar{K} , τ is calculated for each composition data point such that the experimentally measured C_{5-} equals that estimated from Eq. (12). Selectivity composition profiles as a function of C_{5-} are generated in this manner. The proper selectivity matrix \bar{K} will be that which minimizes the deviation between experimental and predicted profiles for the hydrocarbons other than C_{5-} , as illustrated in Fig. 10.

• **Reactor Hydrocarbon Profiles**



• **Selectivity Transformations: C_5^- Example**

$$d\tau = \phi \, dv \quad \text{Eq. (11)}$$

$$dC_5^- = \omega_1 \, d\tau \quad \text{Eq. (14)}$$

• **Parameter Estimation**

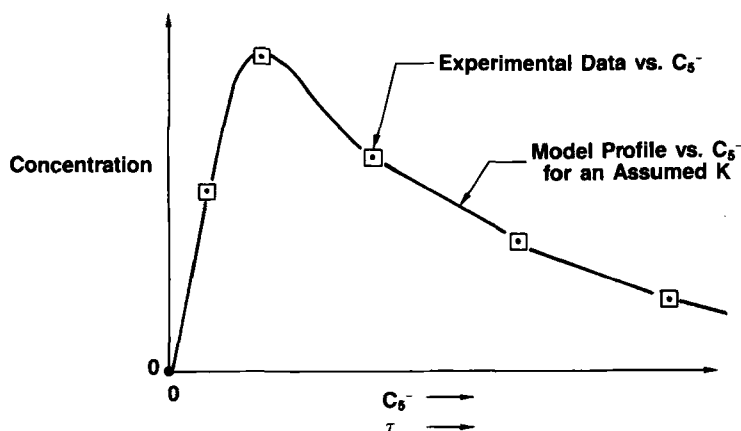


FIG. 10. Determining selectivity kinetics.

Solution to the activity kinetic problem ϕ requires integration of the selectivity transformation Eq. (11):

$$\int_0^{\tau_r} \frac{1}{\phi} \, d\tau = \int_0^1 dv = 1 \quad (15)$$

The right-hand integration is taken over the entire catalyst volume and equals one when defined in terms of fractional catalyst volume. The left-hand integration is carried out over the total extent of reaction as defined by total

C₅- yield. Here τ_f is the selectivity time when the C₅- yield at $v = 1$ (the reactor outlet) is equal to the experimental value of C₅-. It is determined from Eq. (12), as discussed earlier. Integration of Eq. (15) requires that the selectivity kinetics be previously determined. For isothermal reforming reactions, combining Eq. (15) with Eq. (6) gives

$$\frac{\bar{K}_w}{k_\phi} \int_0^{\tau_f} \frac{RTF_c}{V} \bar{w} d\tau + \frac{1}{k_\phi} \int_0^{\tau_f} \frac{RTF}{PV} d\tau + \frac{K_h}{k_\phi} \int_0^{\tau_f} \frac{RTF}{PV} P_h d\tau = 1 \quad (16)$$

Note that the total hydrogen molar flow F_h may be represented equivalently as

$$F_h = FP_h/P$$

Equation (16) can then be rearranged to be linear in the catalyst contact time parameters:

$$\bar{K}_w \cdot \bar{I}_1 + I_2 + K_h I_3 = k_\phi \quad (17)$$

where

$$\bar{I}_1 = \frac{F_c RT}{V} \int_0^{\tau_f} \bar{w} d\tau \quad (18a)$$

$$I_2 = \frac{RT}{PV} \int_0^{\tau_f} F d\tau \quad (18b)$$

$$I_3 = \frac{RT}{V} \int_0^{\tau_f} F_h d\tau \quad (18c)$$

In order to determine the activity parameters, values of \bar{I}_1 , I_2 , and I_3 must be calculated for each experiment. To accomplish this, only the selectivity kinetics and τ_f are required. Here τ_f is calculated from Eq. (12) by using the experimental value of C₅- at $v = 1$. Note that no other experimental compositional data are required.

Now \bar{I}_1 is determined by substituting the selectivity solution [Eq. (12)] for w into Eq. (18a):

$$\bar{I}_1 = \left(\frac{F_c RT}{V} \right) \bar{X} \int_0^{\tau_f} \exp(\bar{\Lambda} \tau) d\tau \bar{X}^{-1} \bar{w}_0 \quad (19)$$

As a result of irreversible reforming cracking reactions, the selectivity rate constant matrix \bar{K} contains one column of zeros. Therefore, \bar{K} will always yield one zero eigenvalue. Let λ_N , one of the elements in matrix $\bar{\Lambda}$, be set to 0 arbitrarily. After it is realized that $\lambda_N = 0$, the integration of the exponential diagonal matrix of Eq. (19) is done term by term. In matrix notation, the integration yields

$$\bar{I}_1 = (F_c RT/V) \bar{X} \bar{\Lambda}^* [\bar{I}^* - \exp(\bar{\Lambda} \tau_f)] \bar{X}^{-1} \bar{w}_0 \quad (20)$$

where $\bar{\Lambda}^*$ is a diagonal matrix whose elements are $1/\lambda_1, \dots, 1/\lambda_{N-1}, \tau_f$, and \bar{I}^* is a diagonal matrix whose elements are 1, 1, \dots , 2.

The analytical integrations for I_2 and I_3 [Eqs. (18b) and (18c)] are complicated by the dependence of F and F_h on composition and therefore on τ . Therefore, it was necessary to determine I_2 and I_3 numerically. A five-point Simpson's integration rule was used (12).

With a set of integrals (\bar{I}_1, I_2 , and I_3) calculated for each experiment, Eq. (17) can be used to determine k_ϕ and the adsorption coefficients. The form of k_ϕ was defined in Eq. (8). The adsorption coefficients are also defined relative to reference experimental conditions:

$$K_{wi} = K_{wi}^0 \exp \left[\frac{-H_{wi}}{R} \left(\frac{1}{T} - \frac{1}{756} \right) \right] \quad (21)$$

$$K_h = K_h^0 \exp \left[\frac{-H_h}{R} \left(\frac{1}{T} - \frac{1}{756} \right) \right] \quad (22)$$

where H_{wi} , H_h are the heat of adsorption (calories per mole) and K_{wi}^0 , K_h^0 are preexponential adsorption constants (parameters at base conditions).

To effectively determine the start-of-cycle reforming kinetics, a set of experimental isothermal data which covers a wide range of feed compositions and process conditions is needed. From these data, selectivity kinetics can be determined from Eq. (12). With the selectivity kinetics known, Eqs. (17) and (18a)–(18c) are used to determine the activity parameters. It is important to emphasize that the original definition of pseudomonomolecular kinetics allowed the transformation of a highly nonlinear problem [Eq. (5)] into two linear problems [Eqs. (12) and (15)]. Not only are the linear problems easier to solve, the results are more accurate since confounding between kinetic parameters is reduced.

2. Deactivation Kinetic Formulation

Following the general form of Eq. (3), hydrocarbon conversion with deactivation is given by

$$d\bar{w}/dv = \phi \bar{K}(\bar{\alpha})w \quad (23)$$

The elements of $\bar{\alpha}$ range in value from 0 to 1 and are the ratio of the reformer kinetic constants at time on stream t to the values at start of cycle. At any time on stream t , the deactivation rate constant matrix $\bar{K}(\bar{\alpha})$ is determined by modifying the start-of-cycle \bar{K} with $\bar{\alpha}$. From the catalytic chemistry, it is known that each reaction class—dehydrogenation, isomerization, ring closure, and cracking—takes place on a different combination of metal and acid sites (see Section II). As the catalyst ages, the catalytic sites deactivate at

different rates. Rather than attempt to determine the interaction of the sites during deactivation, each class of reaction is assumed to deactivate as if it took place on its own unique site, a combination of metal and acid catalytic sites (18). Thus, the deactivation can be lumped by the four reaction classes, resulting in a four-parameter catalyst state vector, $\bar{\alpha} = \alpha_D$ (dehydrogenation), α_I (ring isomerization), α_R (ring closure), and α_C (cracking). In addition, it is assumed that these four "sites" cannot distinguish between hydrocarbons of different carbon number. Therefore, $\bar{\alpha}$ is applied independent of carbon number, as shown in Fig. 11. The appropriate modification of \bar{K} by $\bar{\alpha}$ is defined by this figure. [For example, see Eq. (47) later in this chapter.]

With $\bar{\alpha}$ defined, the functional form for each rate of deactivation $d\bar{\alpha}/dt$ must be determined. The primary cause of catalyst deactivation under reforming conditions is the buildup of coke, which blocks active sites on the catalyst and prevents further reforming reaction.

In our mechanism, coke formation is due to the presence of olefins, which occur as intermediate species during the reforming reactions. As discussed in Section II, these olefins can go either to products or to coke precursors. The deactivation caused by feed poison, catalyst sintering during regeneration, or improper regeneration techniques is not considered in this development.

Reforming experiments at Mobil have shown that the aging rate due to coke formation is a function of the local composition at any position in the catalyst bed and varies with time on stream. Isothermal experiments were performed on mixtures of pure C_6 components over a fresh Pt-Re bimetallic reforming catalyst at accelerated aging conditions (low hydrogen partial pressure and high temperature). Aging data with time on stream are shown in Fig. 12a for a methylcyclopentane-hexane charge. The yield of benzene at a position 15% into the bed drops fairly rapidly from 55 wt. % initially to 12 wt. % in about 1 day. Further aging at this point in the bed does not occur because the bed

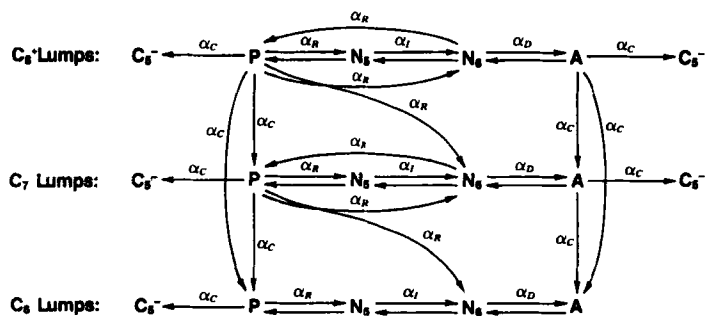


FIG. 11. Reforming reaction network modified by catalyst state vectors. N, cyclopentane and cyclohexane naphthenes; P, C₆⁺ paraffins; A, aromatics; C₅⁻, pentane and lighter.

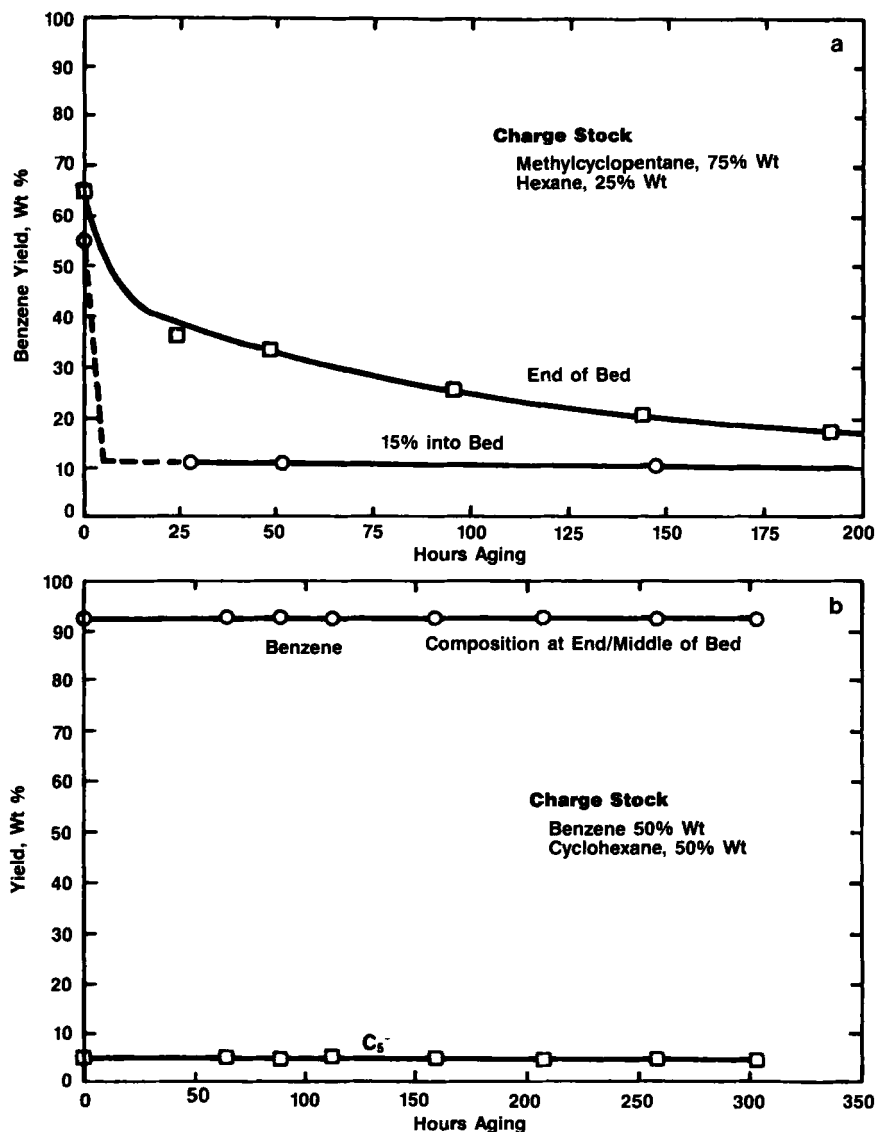
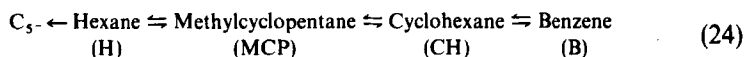


FIG. 12. C₆ aging on Pt/Re catalyst at 794 K, isothermal; 445 kPa HC partial pressure; 928.5 kPa H₂ partial pressure.

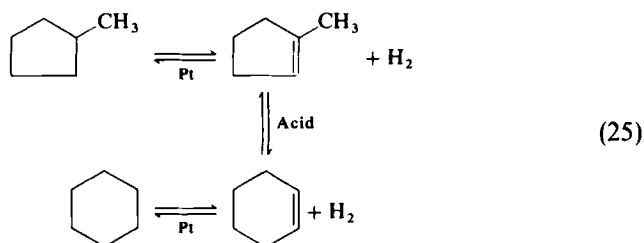
is deactivated. The end of the reactor, however, still has significant activity after 1 day of aging. Activity continues to decline with time on stream as the compositions of the severe aging precursors move farther into the bed. These results suggest bandwise aging in this isothermal experiment.

Further experiments were performed to investigate the effect of charge stock composition on catalyst aging. Aging data at the same conditions but with a feed of benzene and cyclohexane are also shown in Fig. 12b. This charge stock does not age the catalyst either in the initial part or at the end of the reactor bed. From these data and other similar aging studies, it was concluded that aging is a function of the local composition in the bed. As previously mentioned, start-of-cycle C_8+ lumps had to be delumped because of the rapid increase in aging with carbon number within the C_8+ lump.

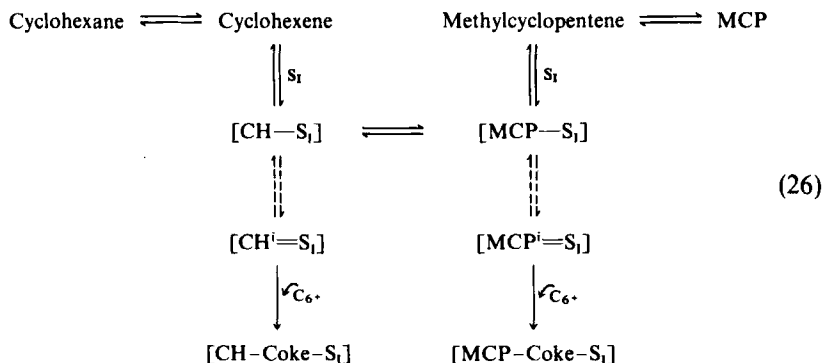
To illustrate how the functional form for the deactivation rate equation $d\bar{\alpha}/dt$ was developed, the C_6 component system will be presented here:



The C_6 component reaction sequence involves several elementary steps with adsorbed intermediates on both the metal and acid sites. An example is the reaction of methylcyclopentane to cyclohexane:



As mentioned previously, the catalyst ages because olefinic intermediates further dehydrogenate to form coke precursors. These coke precursors react further with other C_6+ hydrocarbon molecules to form an irreversible coke polymer. Therefore, each adsorbed molecule can react to form either a desired product or coke, as illustrated:



where MCP^i and CH^i are olefinic intermediates formed from MCP and CH, and S_i is a ring isomerization site (unique combination of acid-metal sites). Each intermediate that goes to coke blocks an active site, $[CH-coke-S_i]$ and $[MCP-coke-S_i]$.

Thus, the number of ring isomerization sites available for reaction is the total number of active sites minus those sites blocked by the formation of coke. Since the metal and acid sites can be used for reactions other than isomerization, intermediates from these other reactants adsorbed on the site also affect the ring isomerization reaction by reducing the number of active sites for the ring isomerization reaction. Since isomerization involves both metal and acid sites in a unique way, all intermediates from other reactions that utilize metal and acid sites in this manner have the potential to block these active sites. This is illustrated in Fig. 13.

In our start-of-cycle (SOC) model, the start-of-cycle rate constants for ring isomerization implicitly contained the total active ring isomerization site concentration:

$$K_1^0 = S_1^0 K_1 \quad (27)$$

where K_1^0 is the isomerization rate constant at SOC cycle, S_1^0 is the number of isomerization sites at SOC, and K_1 is the isomerization rate constant per site.

As the catalyst ages, the rate constants decrease since the number of active sites is reduced by coke formation:

$$K_1(t) = S_1(t) K_1 \quad (28)$$

The parameter, α_1 , defined in the following equation, relates the concentration of active ring isomerization sites at any time to the initial site

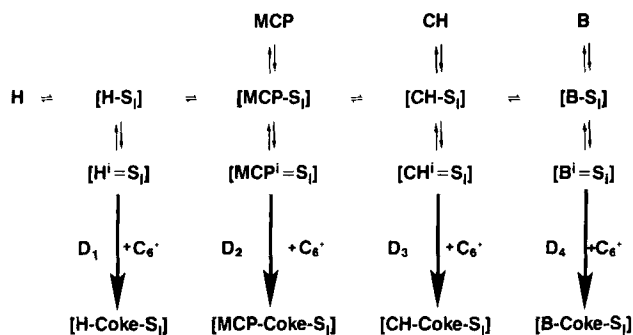


FIG. 13. C₆ aging mechanism: ring isomerization site deactivation.

the Langmuir–Hinshelwood type, the adsorption terms are the same as in the start-of-cycle model as shown in Eq. (33).

Identical equations can be written for the coke formed from the other adsorbed intermediates in the C_6 system of Eq. (24). Thus, the total rate of decrease in active ring isomerization site concentration can be solved by putting the solutions for the individual coke formation steps [similar to Eq. (33)] into Eq. (31). This can be expressed as

$$\frac{-d\alpha_1}{dt} = \sum_{i=1}^M \frac{D_i[P_h]^{-\delta_i}[P_i]\alpha_1}{1 + K_h P_h + (PF_c/F)\bar{K}_w \cdot \bar{w}} \quad (34)$$

where M is the total number of C_6 components.

Following the same arguments, the ring isomerization deactivation rate expression can be directly extended to include the effects of all kinetic lumps (defined in Table VII):

$$\frac{-d\alpha_1}{dt} = \sum_{i=1}^{22} \frac{D_i[P_h]^{-\delta_i}\alpha_1[P_i]}{1 + K_h P_h + (PF_c/F)\bar{K}_w \cdot \bar{w}} \quad (35)$$

Similar equations can be written for each of the four α 's:

$$\frac{-d\alpha_j}{dt} = \sum_{i=1}^{22} \frac{D_{ij}[P_h]^{-\delta_{ij}}\alpha_j[P_i]}{1 + K_h P_h + (PF_c/F)\bar{K}_w \cdot \bar{w}} \quad (j = D, I, R, C) \quad (36)$$

where

$$\alpha_j = \frac{K_i(t)}{K_i(t=0)} \Big|_j$$

and j is the reaction class.

Equation (36) can be recast in matrix notation as

$$\frac{d\bar{\alpha}}{dt} = \frac{\phi}{k_\phi} \bar{A} \bar{D}^P \bar{P} \quad (37)$$

where

$$\bar{D}^P = \begin{bmatrix} D_{1D}^P & \cdots & D_{22D}^P \\ D_{1I}^P & \cdots & D_{22I}^P \\ D_{1R}^P & \cdots & D_{22R}^P \\ D_{1C}^P & \cdots & D_{22C}^P \end{bmatrix}$$

and

$$D_{ij}^P = D_{ij}(P_h)^{-\delta_{ij}}$$

and \bar{P} is the 22-component vector of partial pressures for the deactivation kinetic lumps (Table VII).

Here, \bar{A} is a diagonal matrix whose elements are $\alpha_D, \alpha_I, \alpha_R, \alpha_C$:

$$\bar{A} = \begin{bmatrix} \alpha_D & 0 & 0 & 0 \\ 0 & \alpha_I & 0 & 0 \\ 0 & 0 & \alpha_R & 0 \\ 0 & 0 & 0 & \alpha_C \end{bmatrix} \quad (38)$$

Each component in the deactivation rate constant matrix D_{ij}^P is normalized to reference conditions:

$$D_{ij}^P = D_{ij}^0 \exp \left[\frac{-E_{ij}^d}{R} \left(\frac{1}{T} - \frac{1}{794} \right) \right] \left(\frac{P_{HC}}{344} \right)^{M_j} \left(\frac{P_h}{827} \right)^{-\delta_{ij}} \quad (39)$$

In order to solve the complete aging model, Eq. (37) must be solved with the start-of-cycle kinetic equations illustrated as follows:

$$\frac{d\bar{w}}{dv} = \phi \bar{K}(\bar{\alpha}) \bar{w}, \quad \frac{d\bar{\alpha}}{dt} = \frac{\phi}{k_\phi} \bar{A} \bar{D}^P \bar{P} \quad (40)$$

The matrix $\bar{K}(\bar{\alpha})$ is the start-of-cycle matrix \bar{K} at $t = 0$, appropriately modified by the $\bar{\alpha}$'s. Equation (40) represents the complete reformer model kinetic expressions.

C. EXTENSION OF KINETICS TO PREDICT PROCESS AND PRODUCT CHARACTERISTICS: DELUMPING

While the 13 hydrocarbon lumps accurately represent the hydrocarbon conversion kinetics, they must be delumped for the deactivation kinetics. In addition, delumping is necessary to estimate many of the product properties and process conditions important to an effective reformer process model. These include H_2 consumption, recycle gas H_2 purity, and key reformate properties such as octane number and vapor pressure. The following three lump types had to be delumped: the C_5 - kinetic lump into C_1 to C_5 light gas components, the paraffin kinetic lumps into isoparaffin and n -paraffin components, and the C_8+ kinetic lumps into C_8 , C_9 , C_{10} , and C_{11} components by molecular type.

The expanded set of 34 lumps necessary to define the reforming process is shown in Table VIII. Note that this 34-lump set is sufficient for both start-of-cycle and aging kinetics.

As an example of delumping, the kinetically predicted C_5 - lump is delumped by means of distribution correlations; C_5 - is distributed into C_1 , C_2 , C_3 , iso- C_4 , n - C_4 , iso- C_5 , and n - C_5 , as indicated in Table VIII. The

TABLE VIII

DELUMPED COMPONENTS

Component number	Component lump
1	Hydrogen
2	Methane
3	Ethane
4	Propane
5	Isobutane
6	<i>n</i> -Butane
7	Isopentane
8	<i>n</i> -Pentane
9	Isohexane
10	<i>n</i> -Hexane
11	Methylcyclo C ₅
12	Cyclohexane
13	Benzene
14	Isoheptane
15	<i>n</i> -Heptane
16	C ₇ cyclo C ₅
17	Methylcyclo C ₆
18	Toluene
19	Isooctane
20	<i>n</i> -Octane
21	C ₈ cyclo C ₅
22	C ₈ cyclo C ₆
23	C ₈ aromatic
24	Isononane
25	<i>n</i> -Nonane
26	C ₉ cyclo C ₅
27	C ₉ cyclo C ₆
28	C ₉ aromatic
29	C ₁₀ paraffin
30	C ₁₀ naphthene
31	C ₁₀ aromatic
32	C ₁₁ paraffin
33	C ₁₁ naphthene
34	C ₁₁ aromatic

Additional paraffin distribution lumps

2-Methyl pentane
 3-Methyl pentane
 Dimethyl butane
 2-Methyl hexane
 3-Methyl hexane
 Dimethyl pentane
 Monomethyl C₇⁺
 Dimethyl C₆⁺
 Normal C₈⁺

distribution correlation form for each light component is

$$\begin{aligned}
 C_i/C_{5-} = & A_{1i} + A_{2i} \times C_N + A_{3i} \times C_{5-} + A_{4i} \times P_h \\
 & + A_{5i} \times (1 - X_p) + A_{6i} \times C_N \times (1 - X_p) \\
 & + A_{7i} \times C_N \times P_h + A_{8i} \times P_h \times X_p + A_{9i} \times C_N \times (1 - X_p) \times P_h
 \end{aligned}
 \tag{41}$$

where C_i is the specific light gas component composition ($i = 1$ to 7), A_{ji} is the correlation coefficient for the i th component, C_N is the weighted average C_{6+} product carbon number, P_h is the reformer hydrogen partial pressure, and X_p is the C_{6+} paraffin weight fraction in product. The C_{5-} composition data generated as part of our kinetic data base studies were used to determine the correlation coefficients A_{ji} . A separate set of correlations has been developed for each reforming catalyst represented in our process model. Also, parameters to adjust light gas distribution for changes in catalyst environmental control have been incorporated.

The paraffin isomer and C_{8+} kinetic lumps are delumped in a more rigorous fashion than the C_{5-} . Semikinetic "delumping" equations have been developed for both the C_{8+} lumps and paraffin distribution (Table VIII). The paraffin distribution is constrained by known equilibrium.

IV. Experimental Design and Parameter Estimation

An isothermal, plug flow, fixed bed reforming pilot plant (shown in Fig. 14) was used to generate the kinetic data. The reactor was U shaped and contained roughly 70 ml of catalyst. Five sample taps were spaced along the reactor length to determine compositions over a wide range of catalyst contact times. The reactor assembly was immersed in a fluidized sand bath to maintain isothermal conditions.

On-line gas chromatographic analysis of the reaction mixture at each tap provided composition profiles of over 300 hydrocarbon components plus hydrogen through the catalyst bed. The sample acquisition system is shown in Fig. 15 (14). Reactor tap samples were analyzed by a Perkin-Elmer 900 Gas Chromatograph. Reactor tap samples are withdrawn through capillary flow restrictors into a heated manifold. Sample selection, line purging, and gas chromatograph injection were controlled by a PDP 8 computer. In addition to reactor sample tap analysis, an overall material balance was obtained by analyzing gas and liquid product streams. This provided an internal check on data consistency.

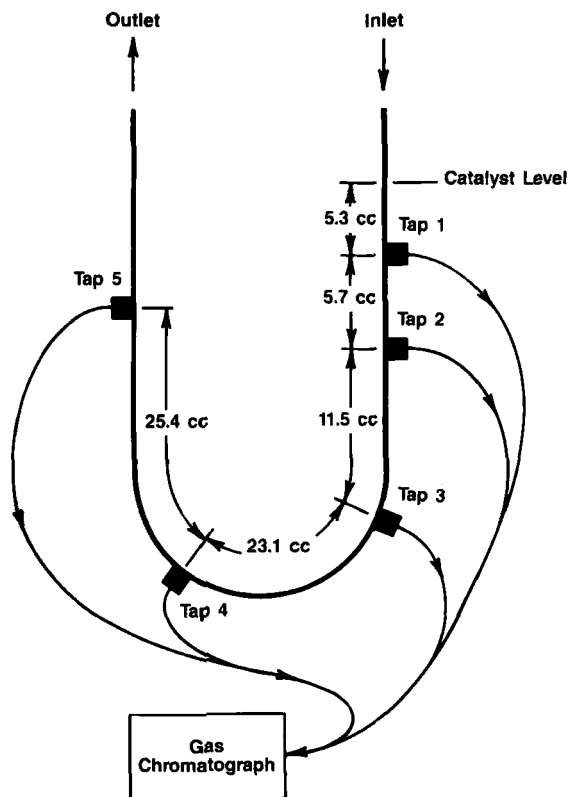


FIG. 14. Isothermal reformer reactor.

A. START-OF-CYCLE PARAMETER ESTIMATION

Data used to develop the start-of-cycle kinetics consisted of over 300 material balances on several commercial catalysts of three types: Pt/Al₂O₃, Pt-Re/Al₂O₃, and Pt-Ir/Al₂O₃.

Experimental conditions were 727, 756, and 794 K isothermal reactor temperature; 827-, 1220-, and 2619-kPa hydrogen pressure; 138- and 345-kPa hydrocarbon pressure; and 1 to 26 liquid hourly space velocity. (See Section II for definition.) Charge stocks consisted of three C₆ component blends (blends included 53/19/23/5, 25/75/0/0, and 0/0/50/50 wt. % hexane/methylcyclopentane/cyclohexane/benzene), C₆ to C₇ component naphthas (322–366 K TBP Kirkuk, Mid-Continent, and Nigerian), a C₆ to C₈ component naphtha (322–416 K TBP Mid-Continent), and C₆ to C₁₂ component naphthas (322–461 K TBP Arab Light, Mid-Continent, and

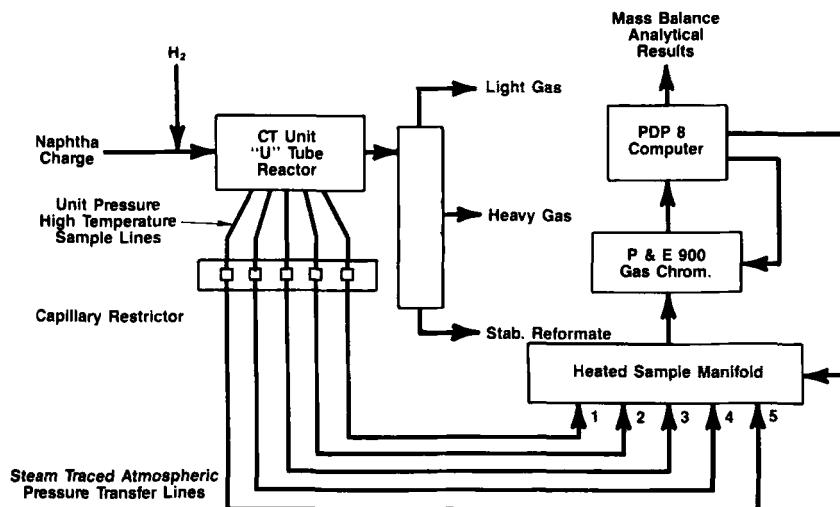


FIG. 15. Gas chromatograph sample acquisition.

Nigerian). In each experiment, single-pass hydrogen (100% H_2 feed without recycle) was used.

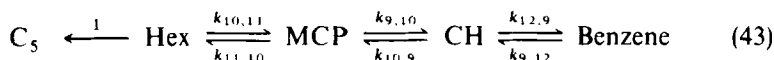
The start-of-cycle selectivity and activity kinetics were determined through a series of 22 separate parameter estimation problems. These separate estimating problems resulted from (1) uncoupling reactions of each carbon number by properly selecting the charge stock, (2) taking advantage of the mathematical form of the rate constants, and (3) translating the general nonlinear problem into two linear problems. This approach minimized the confounding between rate constant since no more than five kinetic parameters were determined at each step.

The fitting sequence is based on the following partitioning of the 13×13 selectivity rate constant matrix \bar{K} :

$$\bar{K} \equiv \begin{bmatrix} \begin{bmatrix} C_8+ \\ \text{reversible} \\ \text{subset} \end{bmatrix} & \begin{bmatrix} 0 \end{bmatrix} & \begin{bmatrix} 0 \end{bmatrix} & \begin{bmatrix} 0 \end{bmatrix} \\ \begin{bmatrix} C_8+ \\ \text{cracking} \\ \text{to } C_7 \end{bmatrix} & \begin{bmatrix} C_7 \\ \text{reversible} \\ \text{subset} \end{bmatrix} & \begin{bmatrix} 0 \end{bmatrix} & \begin{bmatrix} 0 \end{bmatrix} \\ \begin{bmatrix} C_8+ \\ \text{cracking} \\ \text{to } C_6 \end{bmatrix} & \begin{bmatrix} C_7 \\ \text{cracking} \\ \text{to } C_6 \end{bmatrix} & \begin{bmatrix} C_6 \\ \text{reversible} \\ \text{subset} \end{bmatrix} & \begin{bmatrix} 0 \end{bmatrix} \\ \begin{bmatrix} C_8+ \rightarrow C_5- \end{bmatrix} & \begin{bmatrix} C_7 \rightarrow C_5- \end{bmatrix} & \begin{bmatrix} C_6 \rightarrow C_5- \end{bmatrix} & \begin{bmatrix} 0 \end{bmatrix} \end{bmatrix} \quad (42)$$

for all 13 lumps as defined in Table V.

In general, each reversible subset is a 4×4 submatrix centered on the diagonal of \bar{K} and contains rate constants for the reversible reactions between components of the same carbon number. For example, the reversible subset for the C_6 system is



where $k_{11,10}$ represents the ring opening of methylcyclopentane (MCP) to hexane (HEX) and $k_{10,11}$ is the reverse, ring closure step. The C_6 reversible subset is

$$\begin{bmatrix} -k_{10,9} - k_{12,9} & k_{9,10} & 0 & k_{9,12} \\ k_{10,9} & -k_{9,10} - k_{11,10} & k_{10,11} & 0 \\ 0 & k_{11,10} & -1 - k_{10,11} & 0 \\ k_{12,9} & 0 & 0 & -k_{9,12} \end{bmatrix} \quad (44)$$

Constants below the diagonal can be determined by parameter fitting of the kinetic data. Parameters above the diagonal are calculated from microscopic reversibility, as discussed in Eq. (9). Other reversible subsets are of similar form. The remaining nonzero submatrices represent the irreversible cracking reactions.

Proper selection of charge stocks allows independent determination of each submatrix. Thus, the C_6 submatrices can be determined with a charge stock consisting of only C_6 components. A C_6 - C_7 charge stock allows the C_7 kinetics to be determined.

The selectivity parameters in \bar{K} were estimated in steps 1 to 15. With the experimental design, k^0 's, E 's, and n 's [Eq. (8)] were determined in separate fitting sequences. Initially the constants k_{ji}^0 (and k_{ij}^0 from microscopic reversibility) were estimated in five steps at the base conditions of 756 K and 1220 kPa H_2 partial pressure.

Step 1. Fit selectivity rate coefficients in the C_6 reversible submatrix relative to the hexane cracking to C_5 - rate coefficient using C_6 charge data ($k_{13,11}^0 = 1$).

Step 2. Fit rate coefficients in the C_7 reversible submatrix relative to the heptane cracking to C_6 - rate coefficient using $C_6 + C_7$ naphtha data.

Step 3. Fit rate coefficients in the C_{8+} reversible submatrix relative to the C_{8+} P cracking to C_7 - rate coefficient by using 416 and 461 K endpoint naphtha data.

Step 4. Fit rate coefficients for the cracking of C_7 components to C_6 and C_5 - with $C_6 + C_7$ naphtha data. The rate of heptane cracking to C_5 - was arbitrarily set to 1 for the selectivity matrix; thus $k_\phi = k_{13,7}$. The relative rate

of hexane cracking to heptane cracking was determined in this step to place the C_6 and C_7 kinetics on the same basis.

Step 5. Fit rate coefficients for the cracking of C_{8+} components to C_7 , C_6 , and C_{5-} . Also the relative rate of C_{8+} P cracking to that of heptane cracking was determined by using 416 and 461 K endpoint naphtha data.

Hydrogen pressure dependencies n_{ji} were fit in steps 6 to 10, using the same sequence as in steps 1 to 5. Data for n_{ji} determination were at 756 K and H_2 partial pressures of 827 and 2619 kPa. The activation energies E_{ji} were fit similarly in steps 11 to 15 by using data at 1226 kPa H_2 partial pressure and 727 and 794 K temperatures. This procedure completed determination of the selectivity matrix \bar{K} .

The activity kinetics were estimated in seven additional steps.

Step 16. Fit C_6 adsorption equilibrium constants (K_{wi} , K_h) at the base conditions by using C_6 data at 756 K and 1220 kPa H_2 partial pressure.

Step 17. Fit C_6 heat of adsorption ($\Delta\bar{H}_w$) by using C_6 data at 727 and 794 K.

Step 18. Fit C_7 base condition adsorption constants and real-time activity rate constant k_ϕ^0 by using base case condition data on C_6 and C_7 charge stocks.

Step 19. Fit C_7 heats of adsorption and k_ϕ activation energy by using data at 727 and 794 K.

Step 20. Fit hydrogen pressure parameter for the real-time activity constant k_ϕ from data at 827 and 2619 kPa. (Note: If only C_6 kinetics are to be determined, k_ϕ is the rate constant for C_6 cracking and must be determined in a procedure similar to steps 18 to 20.)

Step 21. Fit C_{8+} base case adsorption constants by using base case condition data.

Step 22. Fit C_{8+} heats of adsorption by using data at 727 and 794 K.

By following this multistep procedure, the kinetics were evaluated on a wide range of data (both conditions and feedstock) not used in the parameter estimation. The start-of-cycle kinetics were extended to other catalysts and catalyst states by defining an appropriate catalyst state vector ($\bar{\alpha} = \alpha_D, \alpha_I, \alpha_R, \alpha_C$), which is different from 1 at the start of cycle. A catalyst characterization test was developed to estimate parameters for new catalysts.

B. DEACTIVATION KINETICS PARAMETER ESTIMATION

Data used to develop the deactivation kinetics consisted of over 50 balances in the isothermal fixed bed reactor. Experimental conditions were 756 and 794 K isothermal reactor temperature, 551–1378 kPa H_2 partial pressure, 137–344 kPa hydrocarbon partial pressure, and 1–26 liquid hourly space

velocity. Charge stocks consisted of two C_6 component blends (25/75/0/0, and 0/0/50/50 wt. % hexane/methylcyclopentane/cyclohexane/benzene), a $C_6 + C_7$ component naphtha (322–372 K TBP Mid-Continent), a C_6 to C_9 component naphtha (322–416 K Mid-Continent), and a C_6 to C_{11} component naphtha (322–455 K Mid-Continent). As with the start of cycle, single-pass hydrogen (100% H_2 feed without recycle) was used.

In determining the deactivation kinetics, several observations and assumptions were made to reduce the number of deactivation kinetic lumps from that shown in Table VII. First, all six-carbon ring naphthenes have negligible effect on aging. These components react fast and their average concentration is low throughout the bed. (See Fig. 12.) Second, the aging coefficients for benzene are zero because experimental studies have shown that benzene does not age the catalyst significantly even under severe reforming conditions. With these assumptions, the number of component lumps for aging is reduced to 17.

The deactivation kinetics were determined through a series of seven separate parameter estimation problems. As with the start-of-cycle case, separate estimating problems resulted from uncoupling the reactions of each carbon number by properly selecting the charge stock. This allowed the independent determination of submatrices in the rate constant matrix \bar{D}^P [Eq. (37)].

For the C_6 system as an example,

$$\bar{D}^P = \begin{bmatrix} D_{19D}^P & \cdots & D_{22D}^P \\ D_{19I}^P & \cdots & D_{22I}^P \\ D_{19R}^P & \cdots & D_{22R}^P \\ D_{19C}^P & \cdots & D_{22C}^P \end{bmatrix} \quad (45)$$

where $19 = C_6A \cdots 22 = C_6P$. From the preceding assumptions, the deactivation rate constant matrix [Eq. (45)] reduces to

$$\bar{D}^P = \begin{bmatrix} 0 & 0 & D_{21D}^P & D_{22D}^P \\ 0 & 0 & D_{21I}^P & D_{22I}^P \\ 0 & 0 & D_{21R}^P & D_{22R}^P \\ 0 & 0 & D_{21C}^P & D_{22C}^P \end{bmatrix}$$

where each rate constant D_{ij} is defined relative to the reference conditions as defined in Eq. (39). At the reference conditions eight parameters D_{ij}^0 were determined from the C_6 pure component data.

The procedure for fitting the deactivation rate coefficients at reference conditions is as follows.

1. The C_6 rate coefficients were determined from benzene–cyclohexane and methylcyclopentane–hexane feed data.

2. The C_7 rate coefficients were determined from a C_6 - 372 K Mid-Continent naphtha which contained only C_6 and C_7 components.

3. The C_8 and C_9 rate coefficients were determined from a C_6 - 416 K Mid-Continent naphtha.

4. The C_{10} and C_{11} rate coefficients were determined from a C_6 - 455 K Mid-Continent naphtha.

Once the deactivation rate coefficients at reference conditions were determined, activation energy, hydrogen partial pressure, and hydrocarbon partial pressure parameters were estimated from data at 756 and 794 K, 551 to 1378 kPa hydrogen partial pressure, and 137 and 344 kPa hydrocarbon partial pressure.

V. C_6 Reforming Kinetics for R16H Bimetallic Catalyst

Complete reforming kinetics have been developed for several commercial catalysts, including those used in Mobil reformers. Since KINPTR affects Mobil's business strategy, the complete reforming kinetics are proprietary. However, as an example, KINPTR C_6 kinetics will be presented for UOP's R16H platinum-rhenium-alumina catalyst. Both the hydrocarbon conversion and the deactivation equations [Eqs. (36), (40)] can be directly applied to the C_6 system. For the C_6 hydrocarbon conversion, Eq. (40) becomes

$$d\bar{w}/dv = \phi \bar{K}(\bar{\alpha}) \bar{w} \quad (46)$$

with \bar{w} being (C_6N_6 , C_6N_5 , C_6P , C_6A , C_5^-). The C_6 system selectivity matrix modified for deactivation is

$$\bar{K}(\bar{\alpha}) = \begin{bmatrix} -k_{10,9}\alpha_I - k_{12,9}\alpha_D & k_{9,10}\alpha_I & 0 & k_{9,12}\alpha_D & 0 \\ k_{10,9}\alpha_I & -k_{9,10}\alpha_I - k_{11,10}\alpha_R & k_{10,11}\alpha_R & 0 & 0 \\ 0 & k_{11,10}\alpha_R & -\alpha_C - k_{10,11}\alpha_R & 0 & 0 \\ k_{12,9}\alpha_D & 0 & 0 & -k_{9,12}\alpha_D & 0 \\ 0 & 0 & \alpha_C & 0 & 0 \end{bmatrix} \quad (47)$$

where each

$$k_{ji} = k_{ji}^0 \exp \left[\frac{-E_{ji}}{R} \left(\frac{1}{T} - \frac{1}{756} \right) \right] \left(\frac{P_h}{1220} \right)^{n_{ji}} \quad (48)$$

As discussed previously, the reverse rate constants k_{ij} satisfy microscopic reversibility:

$$k_{ij} = k_{ji}(P_h)^{\gamma_{ji}} \exp \left[\frac{\Delta S_{ji}}{R} - \frac{\Delta H_{ji}}{RT} \right] \quad (49)$$

The C_6 system activity parameter ϕ is defined as

$$\phi = \frac{(PV_c/FRT)k_\phi^0 \exp\{(-E\phi/R)[(1/T) - \frac{1}{756}]\}(P_h/1220)^{n_\phi}}{1 + K_h P_h + (PF_c/F)\bar{K}_w \cdot \bar{w}} \quad (50)$$

where \bar{K}_w represents the five adsorption coefficients for N_6 , N_5 , P , A , and C_5 .

Each element of \bar{K}_w is

$$K_{wi} = K_{wi}^0 \exp\left[\frac{-\Delta H_{wi}}{R}\left(\frac{1}{T} - \frac{1}{756}\right)\right] \quad (51)$$

and

$$K_h = K_h^0 \exp\left[\frac{-\Delta H_h}{R}\left(\frac{1}{T} - \frac{1}{756}\right)\right] \quad (52)$$

The deactivation parameters α_j are determined by integrating the kinetic deactivation equations:

$$-\frac{d\alpha_j}{dt} = \sum_{i=1}^4 \frac{D_{ij}^P (P_h/827)^{-\delta_{ij}} (P_i) \alpha_j}{1 + K_h P_h + (PF_c/F)\bar{K}_w \cdot \bar{w}} \quad (53)$$

where α_j represents $(\alpha_D, \alpha_1, \alpha_R, \alpha_C)$ and i represents parameters defined for C_6 components ($6N_6$, $6N_5$, $6P$, $6A$). Also, each

$$D_{ij}^P = D_{ij}^0 \left(\frac{P_{HC}}{344}\right)^{M_{ij}} \exp\left[\frac{-E_{ij}^d}{R}\left(\frac{1}{T} - \frac{1}{794}\right)\right] \quad (54)$$

and K_h and \bar{K}_w are the same as Eqs. (51) and (52).

The selectivity and equilibrium parameters for the C_6 system are given in Table IX, the activity parameters in Table X, and the deactivation parameters in Table XI.

A. START-OF-CYCLE KINETIC PREDICTIONS

R16H selectivity and activity kinetics were fit over a wide range of temperature and pressure. Reforming selectivity is shown in Figs. 16 and 17, where benzene and hexane are plotted against C_5 , the extent of reaction parameter. The effect of pressure on reforming a 50/50 mixture of benzene and cyclohexane at 756 K is shown in Fig. 16. Selectivity to benzene improves significantly when pressure is decreased from 2620 to 1220 kPa. In fact, at 2620 kPa, hexane is favored over benzene when the C_5 yield exceeds 10%. This selectivity behavior can be seen in the selectivity rate constants:

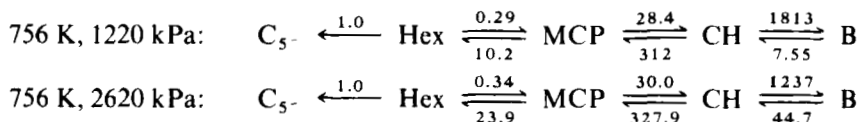


TABLE IX

KINPTR SELECTIVITY PARAMETERS FOR C₆ SYSTEM
[EQS. (47), (48)] AND EQUILIBRIUM CONSTANTS [EQ. (49)]

Reaction	k_{ji}^0	E_{ji} (kJ/mole)	n_{ji}
CH → BZ	1813	0	-1.5
CH → MCP	312	81.5	-0.94
MCP → HEX	10.2	-41.7	0.11

Reaction	$\Delta S_{ji}/R$	$\Delta H_{ji}/R$	γ_{ji}^a
CH ⇌ BZ	199.1	199.6	-2.8
CH ⇌ MCP	-20.2	-13.9	0
MCP ⇌ HEX	-39.6	60.6	+0.94

^a Note that these are slightly different than expected from stoichiometry (-3, 0, +1). It was found that these minor adjustments were necessary to fit the C₆ kinetics. Such adjustments were not necessary in the fitting of the C₇ and C₈ kinetics.

TABLE X

KINPTR REAL-TIME ACTIVITY PARAMETERS FOR C₆ SYSTEM [EQS. (50)–(52)] AND ABSORPTION CONSTANTS

k_{ϕ}^0 (sec ⁻¹)	E_{ϕ} (kJ/mole)	n_{ϕ}
4.9	130.6	0.05

Component	$K_{wi} \times 10^3$ (mole/g kPa)	ΔH_{wi} (kJ/mole)
CH	2.3	-54.1
MCP	16.5	-31.4
HEX	9.7	-30.6
BENZ	8.8	-121.4
C ₅ -	5.5	-82.0

Component	K_h^0	ΔH_h
H ₂	0	0

TABLE XI
KINPTR DEACTIVATION PARAMETERS FOR C₆ SYSTEM
[EQS. (53), (54)]

Component	α_D	α_I	α_R	α_C
a. Preexponential factors $D_{ij}^0 \times 10^5$ (kPa ⁻¹ sec ⁻¹)				
CH	0	0	0	0
MCP	1.83	1.66	0.41	0
HEX	0.85	0.81	0.23	0.17
BENZ	0	0	0	0
b. Activation energies E_{ij}^a (kJ/mole)				
CH	0	0	0	0
MCP	246.4	230.1	251.0	0
HEX	246.4	230.1	251.0	188.3
BENZ	0	0	0	0
c. Hydrogen partial pressure coefficients δ_{ij}				
CH	0	0	0	0
MCP	4	4	4	0
HEX	4	4	4	4
BENZ	0	0	0	0
d. Hydrocarbon partial pressure coefficients M_{ij}				
CH	0	0	0	0
MCP	1.45	1.45	1.45	0
HEX	1.45	1.45	1.45	1.45
BENZ	0	0	0	0

Note that due to the large cyclohexane dehydrogenation rate constant, the benzene yield increases very rapidly from the charge composition at both pressures. After the cyclohexane is converted to benzene, the reverse reactions from benzene through hexane to C₅- cause the benzene yield to decrease with extent of reaction. However, at higher pressures, the dehydrogenation equilibrium is less favorable and the reverse rate constants leading to C₅- are larger. Thus a lower yield of benzene is maintained over the conversion range, and the production of hexane is significantly higher.

Similar arguments can be made for the effects of temperature on the reforming of a methylcyclopentane-hexane mixture at 2620 kPa, as shown in Fig. 17. Higher temperatures favor the benzene formation.

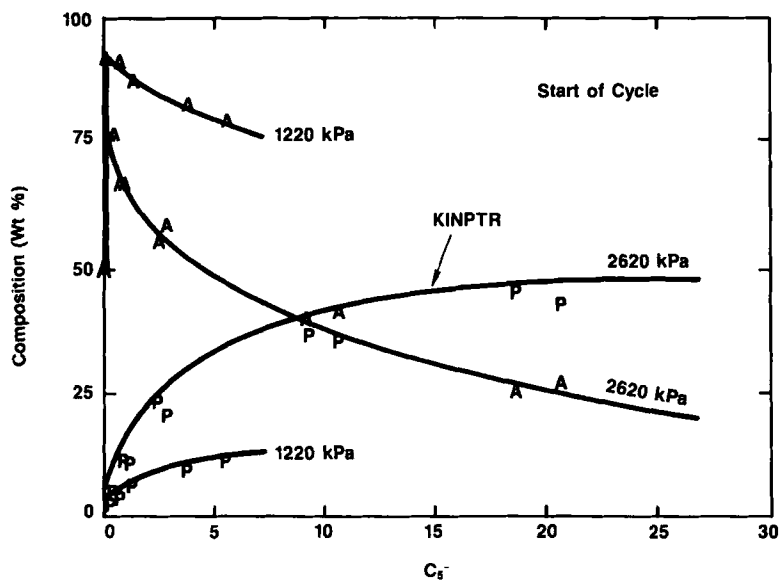


FIG. 16. Effect of pressure on C_6 reforming at 756 K, with benzene-cyclohexane feed (data: A, benzene; P, hexane).

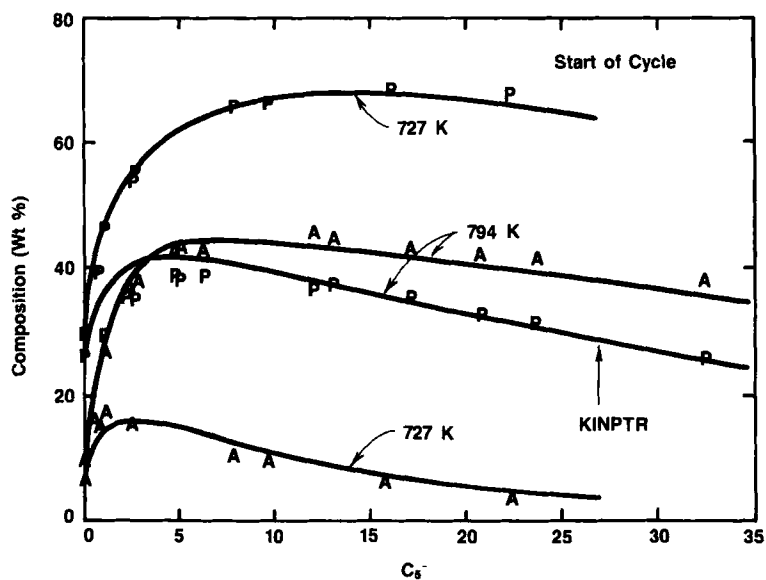


FIG. 17. Effect of temperature on C_6 reforming at 2620 kPa, with MCP-hexane feed (data: A, benzene; P, hexane).

With respect to catalyst contact time, the effects of temperature and pressure on the yields are shown in Figs. 18, 19, and 20. Activity (as measured by the C_5 - gas make) is a strong function of temperature, as shown in Figs. 18 and 19. Again, the higher-temperature operation favors benzene formation. KINPTR's prediction of activity as a function of pressure is shown in Fig. 20. Lower-pressure operation favors the yield of benzene.

Note that in Fig. 18, KINPTR's prediction of C_5 - falls below the data points. However, when one considers the large temperature and pressure effect on activity in the C_6 system and the fact that these same C_6 kinetics are used in KINPTR to make predictions for *all* reforming feedstocks (full-range naphthas, pure components, etc.), the predictions are certainly acceptable.

B. DEACTIVATION KINETIC PREDICTIONS

Methylcyclopentane and hexane dominate deactivation in the C_6 system, as shown in Fig. 21. At 77 hours of time on stream with a methylcyclopentane-hexane feed, the catalyst lost significant activity. However, with a cyclohexane-benzene feed at the same conditions, there was essentially no deactivation even after 304 hours on stream.

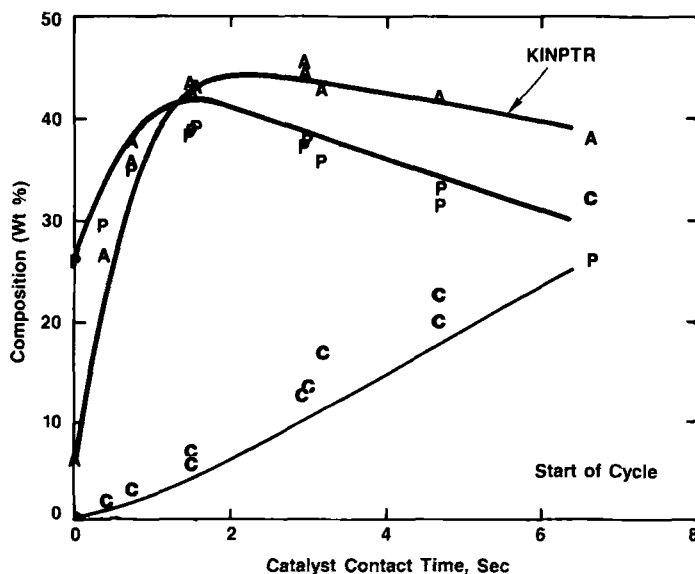


FIG. 18. Reforming composition profiles for C_6 system at 794 K, 2620 kPa, with MCP-hexane feed (data: A, benzene; P, hexane; C, C_5 -).

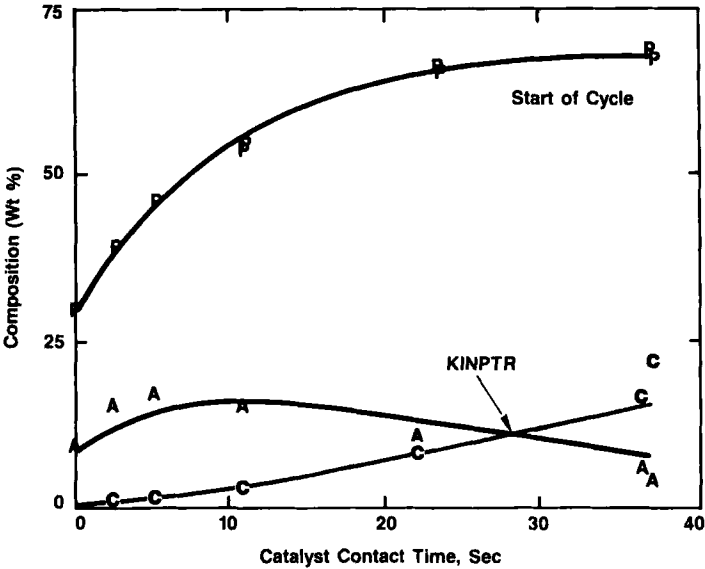


FIG. 19. Reforming composition profiles for C₆ system at 727 K, 2620 kPa, with MCP-hexane feed (data: A, benzene; P, hexane; C, C₅-).

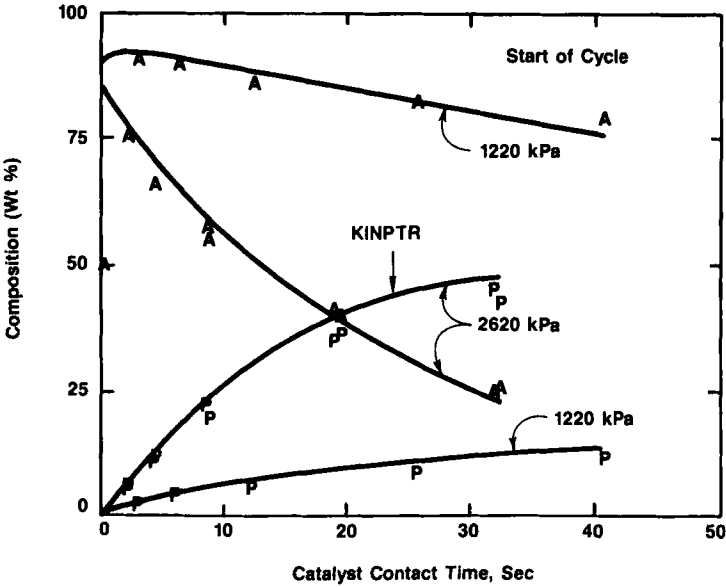


FIG. 20. Reforming composition profiles for C₆ system at 756 K, with benzene-cyclohexane feed (data: A, benzene; P, hexane).

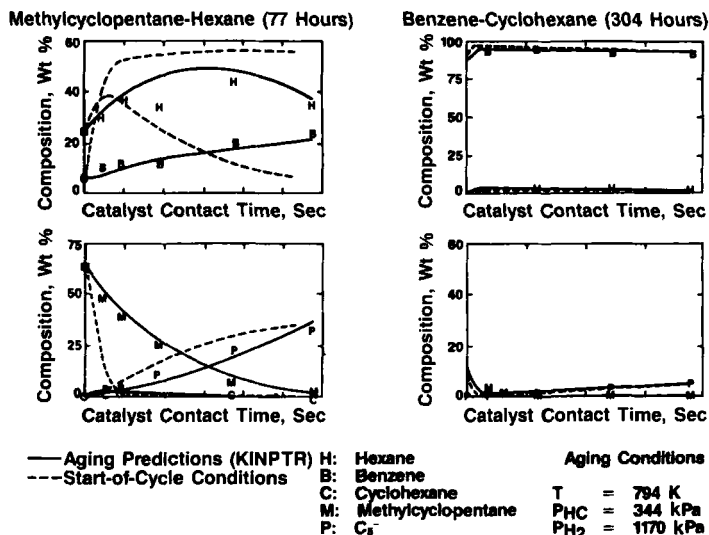


FIG. 21. Reforming composition profiles for C₆ system during deactivation.

As mentioned in the previous discussions of deactivation, catalyst aging is very composition dependent. Thus, catalyst state at a given time on stream will vary with axial distance in a plug flow reactor. This is shown in Fig. 22. Benzene and methylcyclopentane compositions as a function of time on stream are shown at 20% through the catalyst bed and at the end of the bed. KINPTR predicts the catalyst state gradient in the reactor.

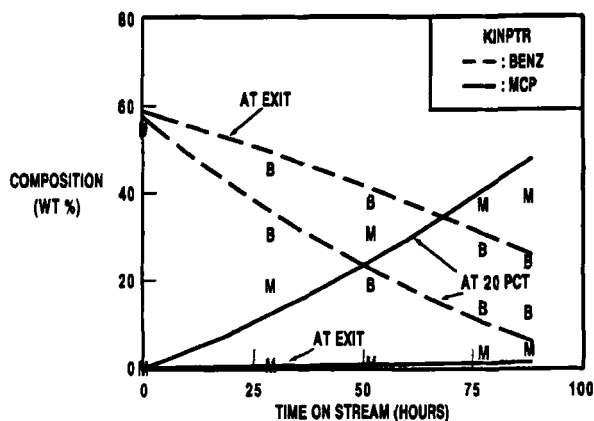


FIG. 22. Evidence for catalyst state vector gradient, isothermal pilot plant data, with methylcyclopentane-hexane feed (B, benzene; M, methylcyclopentane).

VI. Structure of Reforming Process Model

Kinetics for the C_7 and C_{8+} carbon number systems have been developed following procedures similar to those described in Sections III to V. The C_6 , C_7 , and C_{8+} kinetics comprise the complete reforming kinetics. However, these complete kinetics had to be incorporated into a reformer process model to simulate commercial operation. Mass and energy balances based on these kinetics were written to describe adiabatic commercial reactor behavior. The complete set of equations required for commercial reactor simulation is given in Table XII. In addition to providing for the kinetic changes, the process model also predicts product properties such as octane, vapor pressure, enthalpies, and other thermodynamic properties. It is capable of predicting for a wide variety of design configurations such as the number of reactors and recycle strategy. The process model description is shown in Fig. 23. The reactor and deactivation modules include the kinetics which are the heart of the model. However, as shown in Fig. 23, these modules are only a small part of the overall process model.

Each module performs one functional operation within the model. Modularization decreases program size by eliminating multiple coding of the same mathematical operation and enables new algorithms to be added with minimal program changes. Modular units also have general applicability and do not depend on one specific computer program. As a result, many of these modules have been used in Mobil's other process models.

The reforming process model is designed to predict the performance of many reactor configurations. The model can be run in four modes, combining adiabatic or isothermal reactors with recycle or single-pass (no recycle)

TABLE XII
EQUATIONS REQUIRED FOR COMMERCIAL REACTOR
SIMULATION

1. Differential hydrocarbon mass balance: Eq. (40)
2. Hydrogen balance:

$$h = \frac{\sum_{i=1}^N g_i(w_{i0} - w_i)}{1 - \sum_{i=1}^N g_i w_i}$$

3. Differential energy balance:

$$C_p(dT/dv) = (d\bar{w}/dv)\bar{H}(T)$$

4. Delumping as described in Section III: Eq. (41)
5. Catalyst deactivation: Eq. (37)

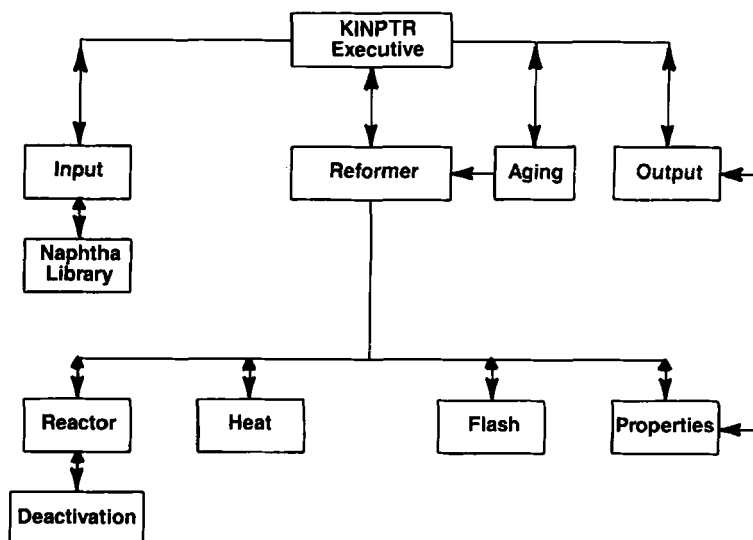


FIG. 23. KINPTR process model description (with module names).

operation. In the case of single-pass operation, the gas composition must be specified along with the charge stock information.

To use the model, only three types of input are required: charge stock characterization, process configuration, and product property targets. For charge stock characterization, the user can utilize a library which contains detailed compositional data on over 200 naphthas. If the charge stock is not in the library, a gas chromatographic composition is required. For the process configuration, the user specifies the number of reactors, the recycle gas separator conditions, the total feed rate, catalyst type and volume fill in each reactor, reactor pressure, and recycle ratio to each reactor. For product property targets, all key octane measurements can be specified along with a product cut point. In addition, vapor pressure can be specified.

A. MODULE DESCRIPTIONS

Module INPUT takes user-specified input and constructs proper initial conditions for the detailed mass and energy balance equations.

To specify charge stock characteristics, one of several options can be used: specify a detailed gas chromatographic composition; call the naphtha library; estimate composition from general charge stock properties, such as PONA (% paraffins, olefins, naphthenes, and aromatics) and gravity; or blend up to seven naphthas by utilizing the naphtha library.

The module REFORMER constructs the user-requested simulation and controls the numerical calculations. It simulates the process scheme and

supervises information flow between the modules—REACTOR, FLASH, HEAT, and PROPERTIES—as necessary. It also controls the convergence on the target property and recycle gas composition.

The module REACTOR contains the start-of-cycle kinetics discussed previously. It calculates the temperature and composition changes through each reactor by integrating the mass and energy balance equations. During the integration, the reaction rate constants can be constantly updated in the DEACTIVATION module (which contains the deactivation kinetics) to reflect catalyst deactivation. The composition changes through each reactor are determined for the 13 kinetic lumps. At the end of the reactor bed, the 13 lumps are delumped into the 34 property lumps (Table VIII) and passed back to the REFORMER, where the inlet conditions for the next reactor are developed.

The module FLASH simulates the reformer flash separator by using a modified Chao-Seader method. The necessary constants for the Chao-Seader correlation have been developed for the lumped components. The output from this module determines the liquid yield and the composition of recycle gas.

The module HEAT calculates stream enthalpies at any position in the reactor. It also calculates the necessary heat duties for interreactor heat exchange.

The module PROPERTIES calculates all the product properties listed in Table XIII. These are calculated by means of correlations based on the lumped components.

TABLE XIII
LIST OF PRODUCT PROPERTIES^a
CALCULATED IN MODULE
PROPERTIES

Octanes
Research clear octane (R + 0)
Research leaded octane (R + 3)
Motor clear octane (M + 0)
Motor leaded octane (M + 3)
Distributed clear octane (D + 0)
Front end clear octane (FE + 0)
Vapor pressures
Initial vapor pressure (IVP)
Reid vapor pressure (RVP)
Boiling point distribution
Specific gravity
Molecular weight

^a Calculated for C₅-, C₆-liquids.

The module OUTPUT generates a report (Tables XIV–XVII) summarizing input data, reactor operating conditions, product yields, properties of liquid products, recycle gas composition, and hydrogen production. Also, temperature and composition profiles are generated.

Input type	Input deck as edited
Documentation →	1 KINPTR Example Problem 200 01
Charge Stock →	{2900001 01000. 120-380 3900004 1500. 120-380 4 5 6 7 8 9 10 11 12 13 14
Process →	151000. 4 1 7.00 96.00 354.70 98.00 1.30 0.0
Reactors →	{16 2 0.115 364.7 0.0 10.00 0.0 17 0 0.227 18 0 0.324 19 0 0.334 20 21 22 23 24 25 26 27 28 29 30 31 32 33 34 35

TABLE XV
KINPTR CASE 1. KINPTR EXAMPLE PROBLEM

Naphtha charge composition									
Naphtha name	IBP-EBP		Vol. % of crude		Vol. % orig. naphtha				
Arab. Lt. (1974)	120-380		23.24		100.00				
Nigerian (41772)	120-380		29.90		100.00				
Component	MPH	Mol. percent	BPD	Volume percent	Lbs/Hr	Weight percent			
1 Hydrogen	0.0	0.0	0.0	0.0	0.0	0.0			
2 Methane	0.0	0.0	0.0	0.0	0.0	0.0			
3 Ethane	0.0	0.0	0.0	0.0	0.0	0.0			
4 Propane	0.0	0.0	0.0	0.0	0.0	0.0			
5 Isobutane	0.0	0.0	0.1	0.0	0.7	0.0			
6 <i>N</i> -Butane	0.3	0.3	2.2	0.2	19.0	0.2			
7 Isopentane	1.0	1.0	7.5	0.8	68.7	0.6			
8 <i>N</i> -Pentane	2.1	2.1	16.4	1.6	150.6	1.4			
9 Isohexane	4.9	5.0	44.1	4.4	426.3	3.9			
10 <i>N</i> -Hexane	4.9	4.9	43.4	4.3	420.0	3.8			
11 Methylcyclo C ₅	3.0	3.0	23.0	2.3	252.6	2.3			
12 Cyclohexane	3.2	3.2	23.4	2.3	266.7	2.4			
13 Benzene	0.8	0.8	4.9	0.5	63.1	0.6			
14 Isoheptane	4.2	4.3	42.1	4.2	423.3	3.8			
15 <i>N</i> -Heptane	4.4	4.4	43.9	4.4	440.7	4.0			
16 C ₇ cyclo C ₅	3.5	3.5	31.0	3.1	341.9	3.1			
17 Methylcyclo C ₆	5.9	6.0	51.6	5.2	582.4	5.3			
18 Toluene	2.4	2.8	20.1	2.0	256.0	2.3			
19 Isooctane	4.5	4.6	50.0	5.0	517.2	4.7			
20 <i>N</i> -Octane	3.7	3.7	40.6	4.1	418.3	3.8			
21 C ₈ cyclo C ₅	5.0	5.1	50.6	5.1	565.2	5.1			
22 C ₈ cyclo C ₆	5.2	5.2	50.7	5.1	583.8	5.3			
23 C ₈ Aromatic	4.7	4.8	39.4	3.9	501.1	4.6			
24 Isononane	4.9	5.0	60.1	6.0	630.6	5.7			
25 <i>N</i> -Nonane	3.2	3.2	39.1	3.9	411.0	3.7			
26 C ₉ cyclo C ₅	2.8	2.8	30.8	3.1	347.7	3.2			
27 C ₉ cyclo C ₆	5.1	5.2	55.6	5.6	645.2	5.9			
28 C ₉ Aromatic	4.0	4.0	37.2	3.7	476.8	4.3			
29 C ₁₀ Paraffin	5.1	5.2	68.5	6.8	732.5	6.7			
30 C ₁₀ Naphthene	3.4	3.4	41.2	4.1	479.8	4.4			
31 C ₁₀ Aromatic	1.6	1.6	15.4	1.5	207.4	1.9			
32 C ₁₁ Paraffin	2.9	3.0	42.5	4.2	461.0	4.2			
33 C ₁₁ Naphthene	1.5	1.5	19.6	2.0	229.5	2.1			
34 C ₁₁ Aromatic	0.5	0.5	4.8	0.5	79.4	0.7			
Total charge	99.2	100.0	1000.0	100.0	10998.2	100.0			
I-Paraffin	2MEC ₆	3MEC ₆	DMEC ₆	2MEC ₇	3MEC ₇	DMEC ₇	MMC ₈ ⁺	DMEC ₈ ⁺	<i>n</i> -C ₈ ⁺
Wt %	2.0	1.5	0.3	1.4	1.7	0.8	8.4	6.2	14.2

TABLE XVI

KINPTR CASE 1. KINPTR EXAMPLE PROBLEM^a

Process Conditions				
Average reactor pressure	364.7 psia			
Average H ₂ partial pressure	275.4 psia			
Separator pressure	354.7 psia			
Separator temperature	98.0 °F			
Total recycle ratio	12.4			
H ₂ recycle ratio	10.0			
Wt hourly space velocity	1.91 hr ⁻¹			
Liq hourly space velocity	1.30 hr ⁻¹			
C ₅ + octane severity	101.9 R + 3			
H ₂ O/HCl ratio	5.0 mole/mole			
Naphtha properties				
Specific gravity 60 °F	0.7546			
Average molecular weight	110.9			
Mean average boiling point	258.2 °F			
Composition, PCT	Vol	Wt	Mol	
Paraffins	50.06	46.55	46.60	
Naphthenes	37.76	39.05	38.91	
Aromatics	12.18	14.40	14.49	
ASTM distillation, °F	AS-IS	C ₆ +		
1P	171.	191.		
10	205.	212.		
30	237.	236.		
50	265.	267.		
70	298.	299.		
90	337.	338.		
EP	384.	384.		
Reid vapor pressure, psia	2.1	1.4		
Research octanes				
R + 0	63.6	63.2		
R + 3	81.6	81.3		
Reactor data				
	1	2	3	4
Catalyst type	R-16H	R-16H	R-16H	R-16H
Loading-vol. PCT	11.5	22.7	32.4	33.4
Cubic feet	20.7	40.9	58.3	60.1
1000 pounds	0.7	1.3	1.9	1.9
TONS/10MBPD	3.3	6.5	9.3	9.6
Inlet pressure psia	364.7	364.7	364.7	364.7
Inlet temperature, °F	909.9	909.9	909.9	909.9
Outlet temperature, °F	839.9	860.6	887.8	906.1
Delta temperature, °F	-70.0	-49.3	-22.2	-3.9
Heat of reaction, BTU/lb	-135.5	-95.8	-43.2	-7.5
Reheat MMBTU/hr	1.5	1.1	0.5	0.0
Inlet vapor viscosity, CPS	0.0199	0.0199	0.0200	0.0202
Inlet vapor density, CF	0.3813	0.3676	0.3566	0.3490

^a User specified the kinetic model with adiabatic reactors and recycle gas: R + O target is 96.0.

TABLE XVII

KINPTR CASE 1. KINPTR EXAMPLE PROBLEM^a

Product octanes	R + 0	R + 3	M + 0	M + 3	D + 0	D + 3	FE + 0	FE + 3				
C ₅ +	96.0	101.9	86.0	92.1	92.6	0.0	80.4	0.0				
C ₆ +	97.2	102.4	86.9	92.7	93.8	0.0	79.5	0.0				
Product properties	SG	MW	IVP	RVP	D-86	IBP	10	30	50	70	90	EP
C ₅ +	0.7939	98.8	4.7	4.4	128	156	156	197	243	284	333	397
C ₆ +	0.8121	101.9	2.2	2.0	169	187	187	211	253	290	337	398
Product yields	Volume	Weight	Molar	Miscellaneous								
Pentane plus	81.7	85.9	96.5	RG VPC C ₅ 1.3 RG Mole wt 7.6 RG Spec gr 0.264 SCF H ₂ /BBL 927								
Hexane plus	73.7	79.3	86.2									
Pentanes	8.0	6.7	10.2									
Butanes	6.0	4.6	8.7									
Dry gas	12.0 FOE	9.5	131.9									
Paraffins in C ₆ +	25.1	22.6	26.3									
Aromatics in C ₆ +	47.1	55.2	58.3									
Naphthene in C ₆ +	1.4	1.4	1.6									
Component	FOE 6.25	PCT	Volume CUMUL.	PCT	Weight CUMUL.	PCT	Molar CUMUL.	PCT	Molar CUMUL.	Recycle gas composition (percent)		
										VOL.	WT.	
Hydrogen	4.8			1.9	100.0	102.9	237.1			80.9		21.4
Methane	1.7			1.7	98.1	11.9	134.3			8.9		18.6
Ethane	1.9			2.0	96.4	7.5	122.4			4.3		16.8
Propane	3.5	5.7	93.4	3.9	94.4	9.7	114.9			3.3		19.0
Isobutane		2.0	87.7	1.5	90.5	2.9	105.2			0.5		4.1

<i>n</i> -Butane	4.0	85.7	3.1	89.0	5.9	102.3	0.9	6.6	
Isopentane	5.2	81.7	4.3	85.9	6.6	96.5	0.4	4.2	
<i>n</i> -Pentane	2.9	76.5	2.4	81.7	3.7	89.9	0.2	1.9	
Isohexane	8.4	73.7	7.4	79.3	9.5	86.2	0.3	3.0	
<i>n</i> -Hexane	4.1	65.3	3.6	71.9	4.6	76.7	0.1	1.0	
Methylcyclo C ₅	0.5	61.2	0.5	68.3	0.7	72.1	0.0	0.1	
Cyclohexane	0.0	60.6	0.0	67.8	0.1	71.4	0.0	0.0	
Benzene	3.4	60.6	4.0	67.7	5.6	71.3	0.1	0.7	
Isoheptane	6.1	57.2	5.6	63.7	6.2	65.7	0.1	0.7	
<i>n</i> -Heptane	1.9	51.1	1.8	58.1	1.9	59.5	0.0	0.2	
C ₇ cyclo C ₅	0.4	49.2	0.4	56.4	0.5	57.6	0.0	0.0	
Methylcyclo C ₆	0.1	48.7	0.1	55.9	0.1	57.1	0.0	0.0	
Toluene	11.6	48.6	13.4	55.8	16.1	56.9	0.1	0.8	
Isooctane	2.7	37.0	2.6	42.4	2.5	40.8	0.0	0.1	
<i>n</i> -Octane	0.6	34.3	0.6	39.9	0.5	38.3	0.0	0.0	
C ₈ cyclo C ₅	0.0	33.7	0.0	39.3	0.0	37.8	0.0	0.0	
C ₈ cyclo C ₆	0.0	33.6	0.0	39.3	0.0	37.7	0.0	0.0	
C ₈ aromatic	15.8	33.6	18.2	39.2	19.0	37.7	0.0	0.5	
Isononane	0.9	17.8	0.8	21.0	0.7	18.7	0.0	0.0	
<i>n</i> -Nonane	0.2	16.9	0.2	20.2	0.2	17.9	0.0	0.0	
C ₉ Cyclo C ₅	0.2	16.8	0.2	20.0	0.1	17.8	0.0	0.0	
C ₉ cyclo C ₆	0.0	16.6	0.0	19.8	0.0	17.6	0.0	0.0	
C ₉ aromatic	11.8	16.5	13.8	19.8	12.7	17.6	0.0	0.1	
C ₁₀ paraffin	0.1	4.7	0.1	6.0	0.1	4.8	0.0	0.0	
C ₁₀ Naphthene	0.0	4.6	0.0	5.8	0.0	4.7	0.0	0.0	
C ₁₀ Aromatic	3.7	4.6	4.5	5.8	3.8	4.7	0.0	0.0	
C ₁₁ paraffin	0.0	0.9	0.0	1.3	0.0	1.0	0.0	0.0	
C ₁₁ naphthene	0.0	0.8	0.0	1.3	0.0	1.0	0.0	0.0	
C ₁₁ aromatic	0.8	0.8	1.3	1.3	1.0	1.0	0.0	0.0	
I-Paraffin	2MEC ₆	3MEC ₆	DMEC ₆	2MEC ₇	3MEC ₇	DMEC ₇	MMC ₈ ⁺	DMC ₈ ⁺	<i>n</i> -C ₈ ⁺
WT. PC	3.4	2.6	1.5	1.8	2.3	1.5	2.4	1.1	0.8

^a User specified the kinetic model with adiabatic reactors and recycle gas: R + O target is 96.0

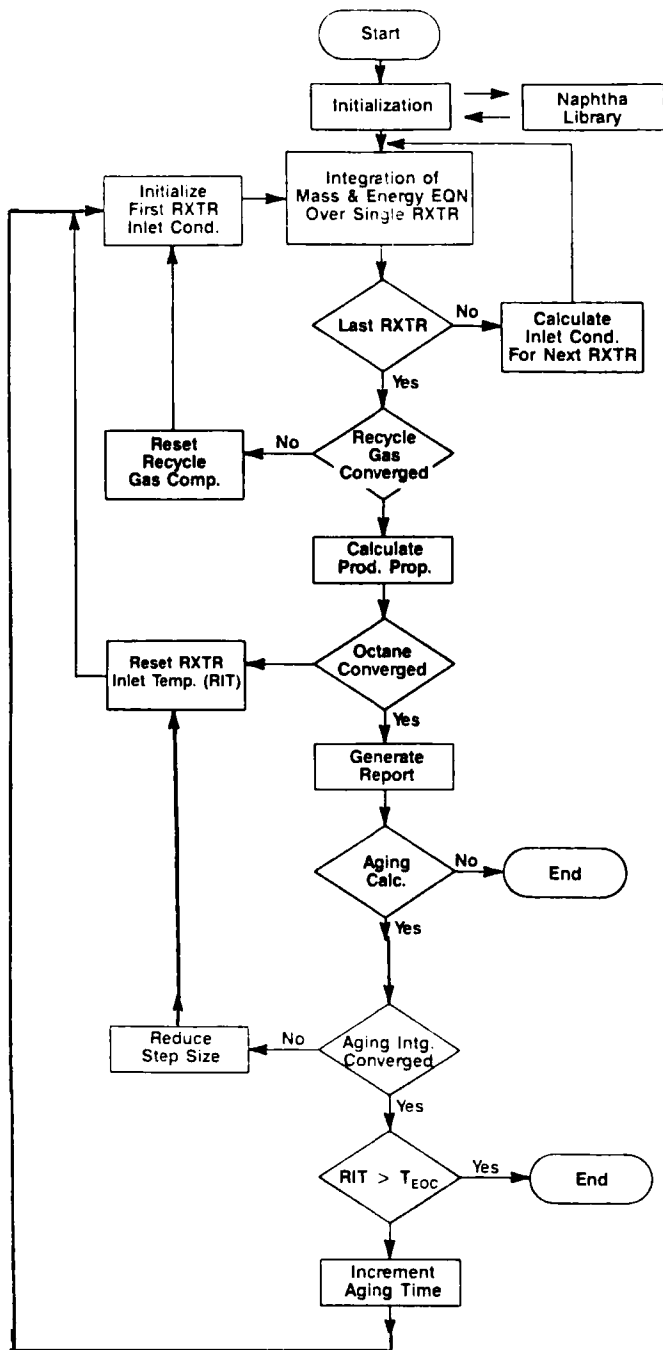


FIG. 24. KINPTR flow chart.

The model is user friendly and the input requirements are simple. An example of typical user input is shown in Table XIV, which contains all necessary information to run the model. In the example, charge stock information for a blend of two naphthas is produced by means of naphtha library codes; the detailed composition developed by the module INPUT for the specified naphtha codes is shown in Table XV. Optional output of yields, temperature, and octane at six points through each reactor can also be generated. The process and reactor conditions are summarized in Table XVI, and complete yields along with the product properties are shown in Table XVII.

B. LOGICAL STRUCTURE DIAGRAM

The logical structure of the model is shown in Fig. 24. To illustrate the logic flow, a typical commercial simulation is used as an example. In this case, the reactor inlet temperature is adjusted over an entire catalyst cycle to maintain target octane. The model must determine the recycle gas composition and inlet reactor temperature required to make octane as a function of time on stream. At the start of the model iteration, the reactor feed compositions are calculated on the basis of user-specified naphtha information and an assumed recycle gas composition. With an assumed reactor inlet temperature, mass and energy balance equations are integrated over each reactor. At the end of the last reactor, the effluent stream is flashed to calculate the recycle gas composition and checked for convergence. The octane number of the properly cut liquid product is calculated and checked for convergence to the target value. The entire calculation is repeated until both recycle gas and octane converge simultaneously. The converged solution will yield complete information on the reformer performance at a particular time on stream. After convergence, the time on stream is incremented, deactivation kinetics are solved, hydrocarbon conversion kinetics are properly modified, and the procedure is repeated.

The simulation continues until the temperature requirement exceeds a specified end-of-cycle limit.

VII. Predictions with the Complete Reforming Kinetics

The accuracy of KINPTR over a wide spectrum of conditions and feedstocks will be demonstrated in this section. KINPTR predictions will be compared to a variety of R16H start-of-cycle and aging data from pilot plant and commercial reformers. Pilot plant data were obtained in both adiabatic and isothermal reactors. These predictions required complete reforming

kinetics—that is, all fitted parameters in KINPTR—and a full set of mass and energy balances, as discussed in Section VI.

A. START-OF-CYCLE PREDICTIONS

KINPTR accurately predicts the start-of-cycle selectivity and activity for reforming of full-range naphthas. In Fig. 25, feedstock type—Arab Light versus Nigerian—is shown to have a dramatic effect on aromatic selectivity. As expected, the more naphthenic Nigerian naphtha results in increased aromatics compared to the more paraffinic Arab Light naphtha. Note that at higher conversion to C_5^- , the C_8^+ aromatics yield actually starts decreasing with a Nigerian feed, but not for an Arab Light feed. This behavior is a thermodynamic effect resulting from the widely different paraffin contents of the feeds. Reactor temperature also dramatically affects aromatic selectivity (Fig. 26). Higher temperatures improve the thermodynamics for aromatic production. Pilot plant compositional profiles as a function of catalyst contact time are shown in Figs. 27 and 28. Heptane and toluene profiles for a full-range, C_6^- 461 K Arab Light naphtha are shown in Fig. 27. Hexane and

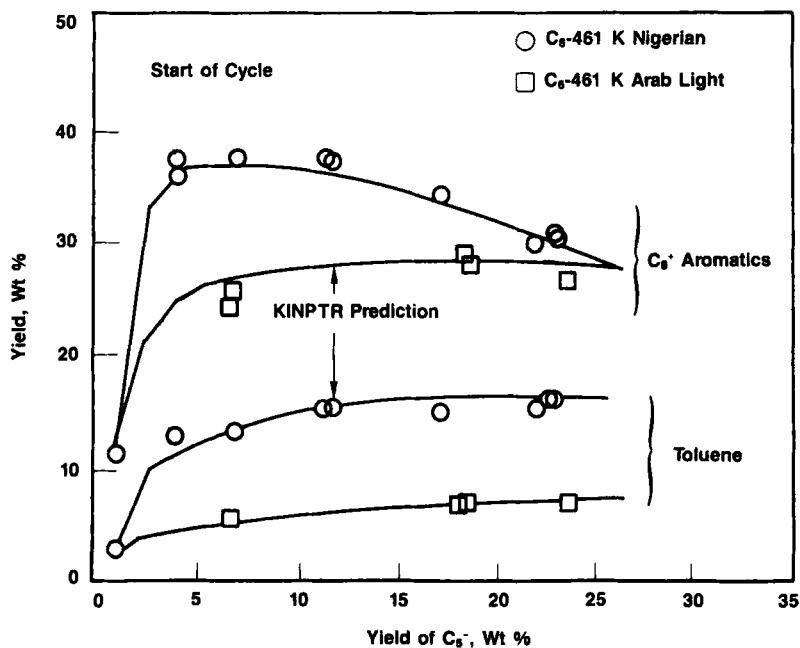


FIG. 25. Effect of charge stock type on aromatic selectivity.

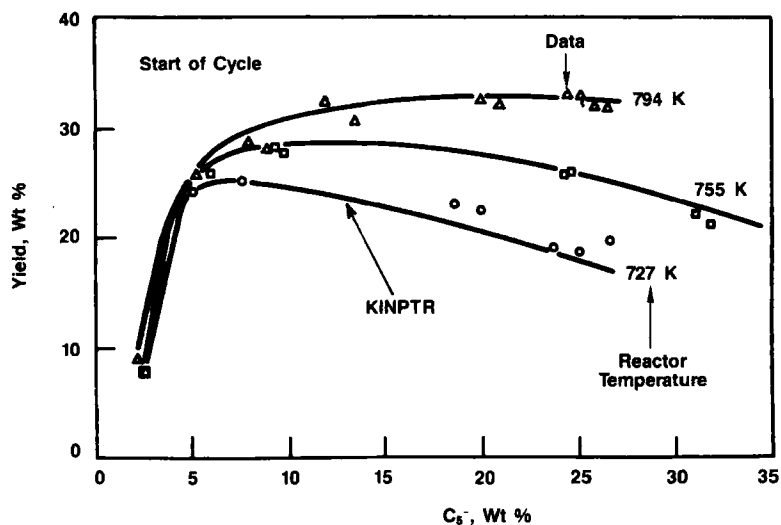


FIG. 26. Effect of temperature on C_{8+} aromatic selectivity at 2757 kPa, C_6 - 461 K Mid-Continent.

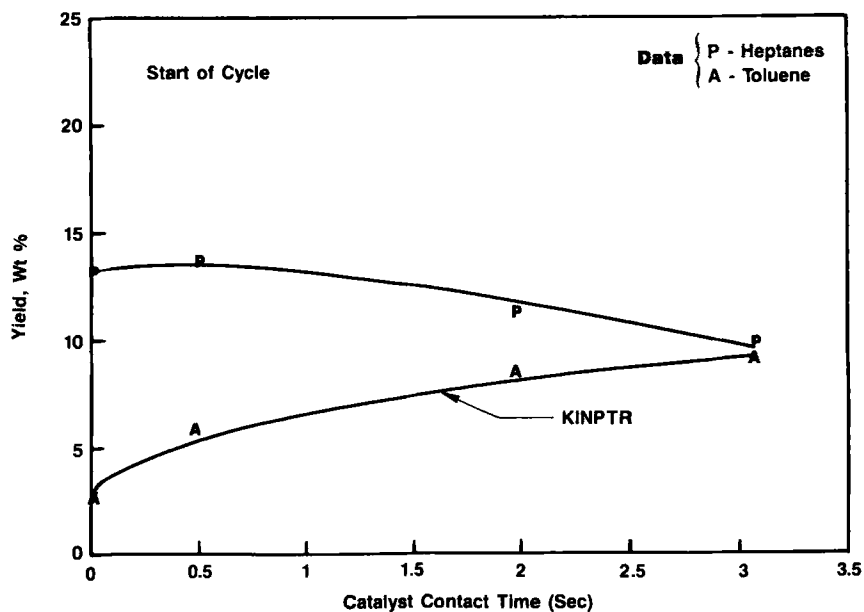


FIG. 27. Isothermal reforming composition profiles, at 782 K, 2620 kPa, C_6 - 461 K Arab Light.

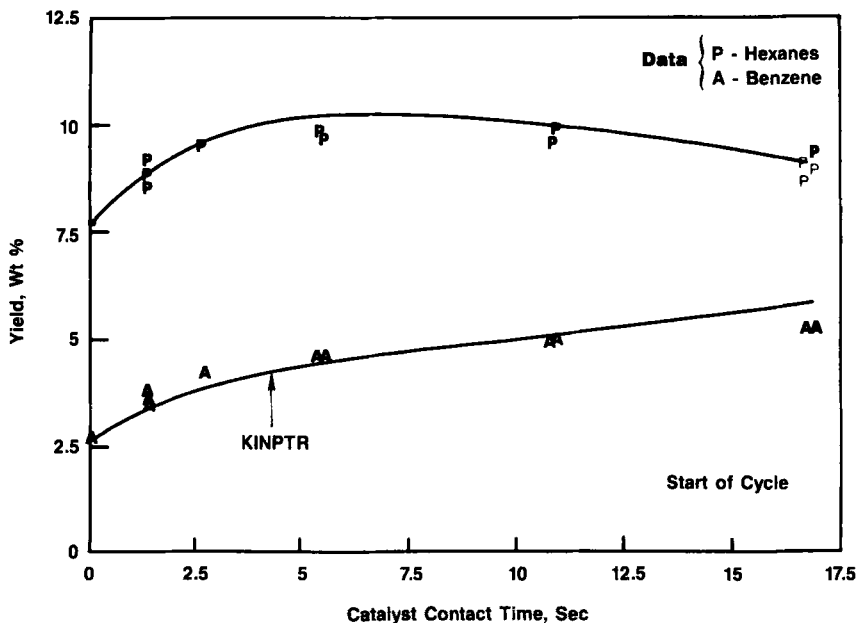


FIG. 28. Isothermal reforming composition profiles at 754 K, 1304 kPa, C₆- 461 K Mid-Continent.

benzene profiles for a C₆- 461 K Mid-Continent naphtha are shown in Fig. 28. KINPTR predicts the selectivity and activity profiles over the wide range of pressures and temperatures represented by these examples.

For commercial simulations, KINPTR's selectivity kinetics determine the reformate composition and overall yield at a target reformate octane. Reformer yield-octane behavior from pilot and commercial units are shown in Fig. 29a. The large variation in the reformate yields at a given octane, as much as 25%, results from the wide range of process conditions and naphtha feed quality used in Mobil reformers. As demonstrated in Fig. 29b, KINPTR accurately normalizes these reformate yields over a wide range of octanes, including those required for gasoline lead phaseout.

KINPTR's real-time activity kinetics determine the adiabatic reactor inlet temperature required to make a target octane. The accuracy of KINPTR's reactor inlet temperature predictions is shown in Fig. 30 for a wide range of process conditions. The average deviation is ± 3.8 K with no significant bias. This degree of accuracy is very reasonable considering the sensitivity of catalyst activity to start-up conditions and initial catalyst state (e.g., chloride added).

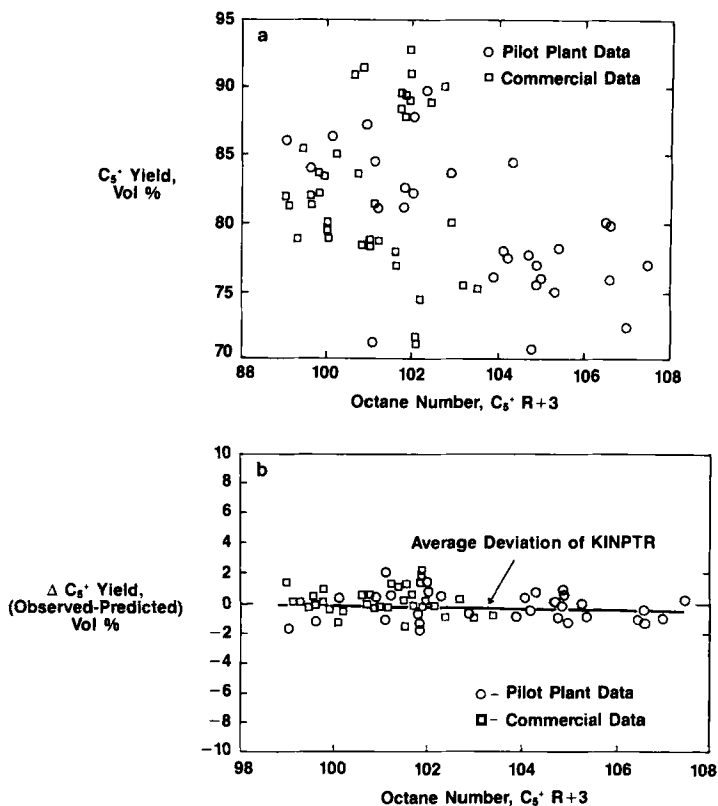


FIG. 29. (a) Actual reformate yield-octane data; (b) KINPTR yield comparisons.

B. DEACTIVATION KINETIC PREDICTIONS

KINPTR's deactivation model can be used to predict changes in composition and activity at any position in the reactor as a function of catalyst aging. The selectivity and activity gradients which occur in the bed during aging are illustrated in Figs. 31 and 32 for isothermal reforming. Owing to the large concentration of five-member ring naphthenes present in the early part of the reaction path, the initial portion of the catalyst bed ages faster than the back portion. As the catalyst in the initial portion deactivates, the naphthenes progress farther down the bed until they can react. Aging, therefore, occurs in a somewhat bandwise manner owing to the compositional gradients.

In commercial aging simulations, KINPTR's deactivation model is used to predict cycle lengths (time between catalyst regenerations) and reactor inlet temperature requirements with time on stream to maintain target reformate

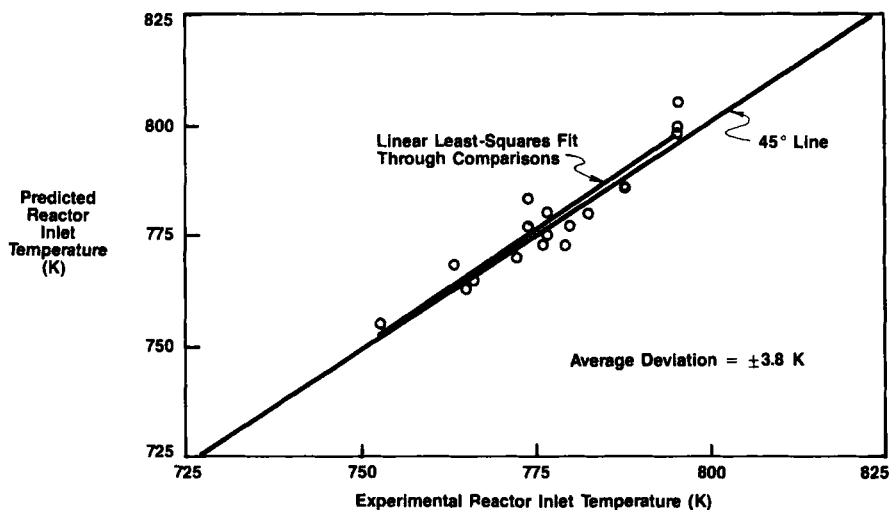
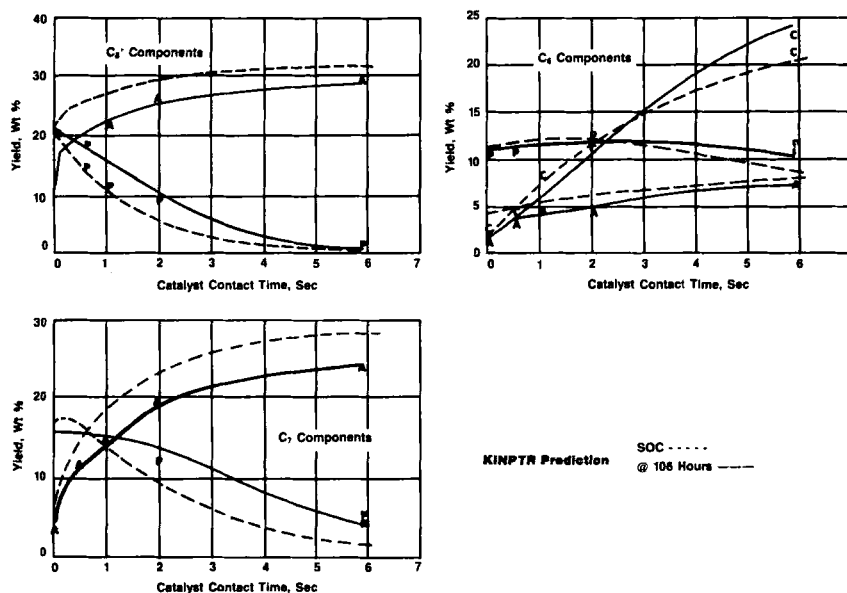


FIG. 30. KINPTR activity predictions, adiabatic pilot plant data.

FIG. 31. KINPTR isothermal aging predictions at 794 K, 928 kPa H_2 pressure, C_6 - 416 K Mid-Continent (P, paraffins; A, aromatics; C, C_3 -).

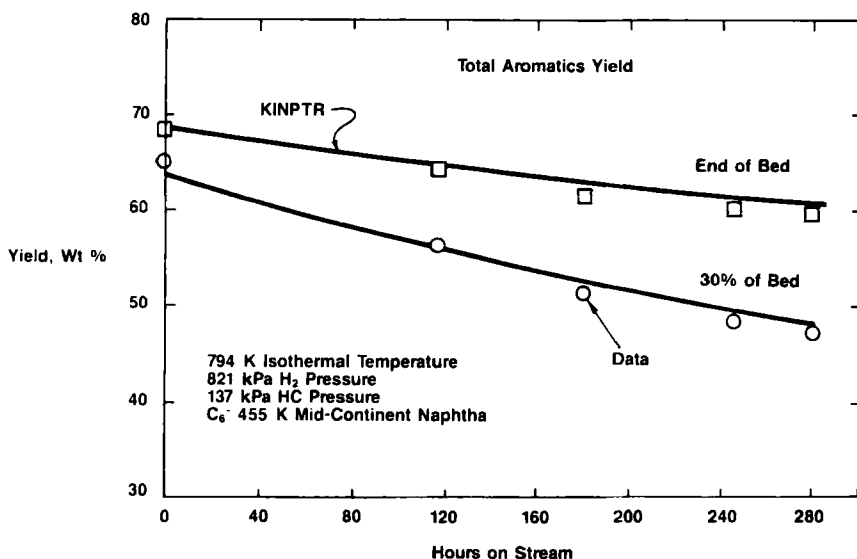


FIG. 32. KINPTR aging predictions.

octane. Cycle length predictions for a large number of adiabatic pilot plant and commercial cycles are shown in Fig. 33. Over the wide range of process conditions, catalyst types, and cycle lengths (up to 700 days on stream), KINPTR accurately predicts the data within $\pm 10\%$. A typical commercial cycle prediction is shown in Fig. 34. Not only does KINPTR predict overall cycle lengths, it also predicts the proper shape of the temperature aging curve. In addition, KINPTR predicts C₅+ yield loss (aging selectivity shift) with a standard deviation of 0.87 and no significant bias (Fig. 35).

C. SENSITIVITIES TO PROCESS CONDITIONS

KINPTR simulations of commercial reforming (Table XVIII) will be used in this section to demonstrate process sensitivity. In the base case, a full-range Mid-Continent naphtha (55 wt. % paraffins) is reformed to a constant octane of 90 R + 0 over the entire cycle. With a reactor pressure of 1695 kPa and a 7.2 H₂ recycle ratio, the start-of-cycle reactor inlet temperature to achieve target octane is predicted to be 759 K. The deactivation simulation shows that it would take about 1 year to reach the end-of-cycle temperature of about 798 K. The start-of-cycle C₅+ yield for this case is 86 vol %. The model predicts that the yield would decline by 4.8 vol % over the cycle.

If the pressure of the reformer is doubled with the same feedstock and octane target (case 1), the start-of-cycle inlet temperature is unaffected (760 K).

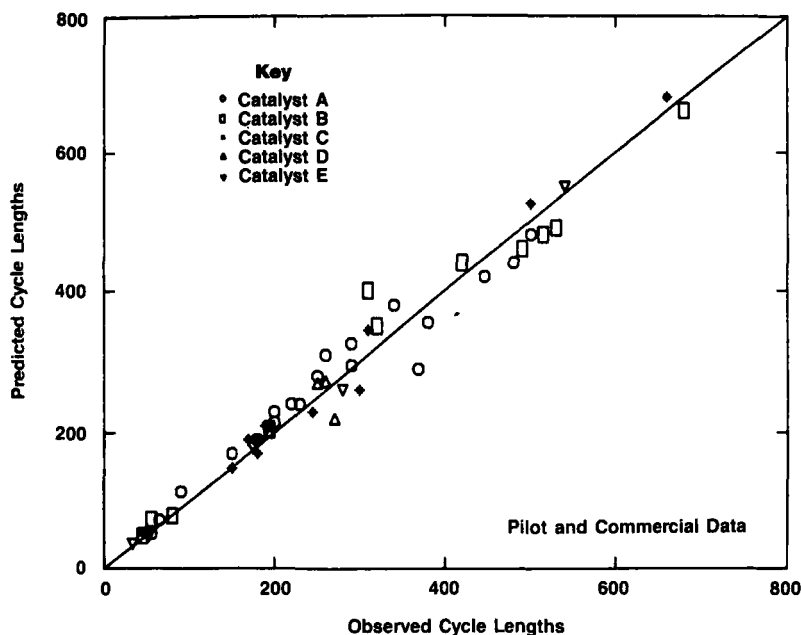
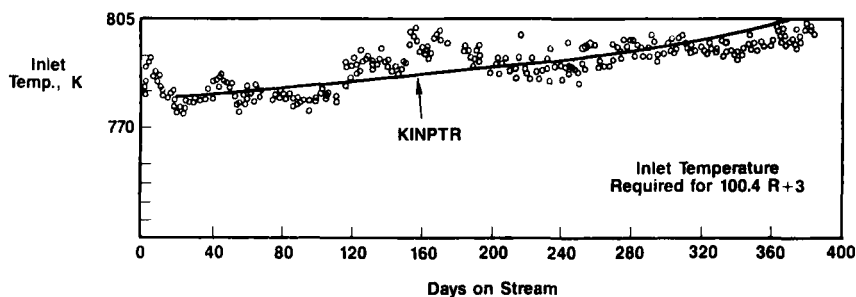


FIG. 33. KINPTR aging predictions.

FIG. 34. KINPTR commercial cycle length prediction. Average cycle conditions: 2.3 LHSV, 5.8 H₂ recycle ratio, 3685 kPa pressure, C₆- 455 K Mid-Continent.

Despite the same start-of-cycle temperature, the aging rate is significantly reduced due to the higher-pressure operation. KINPTR predicts that doubling the pressure will triple the cycle length and reduce start-of-cycle C₅+ yield to 83.8 vol %. The yield shift results from less favorable aromatization equilibrium. Over the cycle, the C₅+ yield drops by 4 vol %. This example clearly illustrates the trade-off between cycle length and yields discussed in Section II.

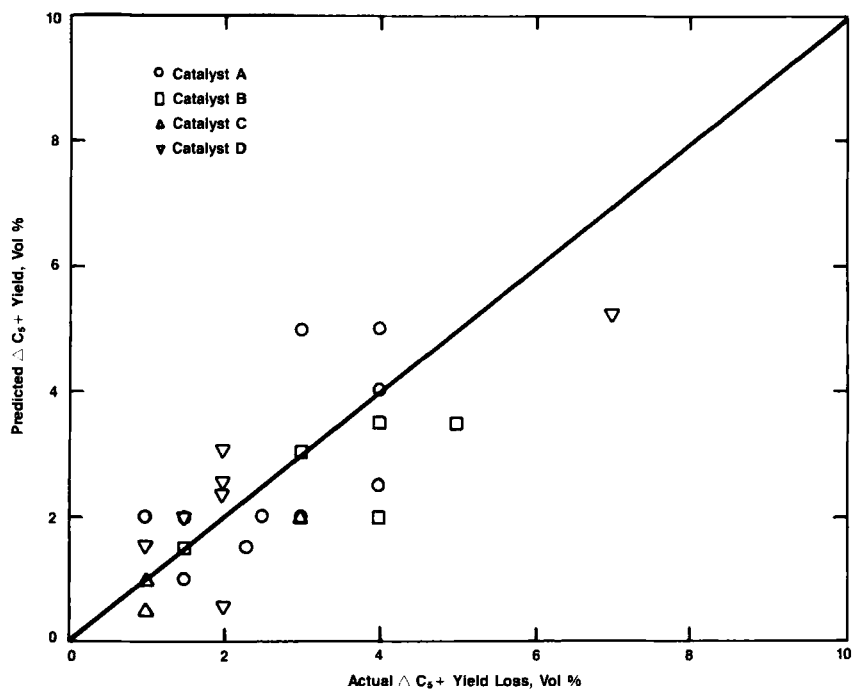
FIG. 35. KINPTR aging predictions, C_5+ yield loss.

TABLE XVIII

KINPTR SIMULATIONS OF COMMERCIAL OPERATION: PROCESS VARIABLE EFFECTS^a

Variable	Base case	Case 1	Case 2	Case 3	Case 4	Case 5
		Reactor pressure	Octane	Recycle ratio	Charge stock	Space velocity
Octane (R + 0)	90	90	98	90	98	98
Reactor pressure (kPa)	1695	3051	1695	1695	1695	1695
H ₂ recycle ratio	7.2	7.2	7.2	10	7.2	7.2
Paraffins (wt. %)	55	55	55	55	71	55
LHSV	1.43	1.43	1.43	1.43	1.43	0.70
Temperature (K) (SOC)	759	760	779	758	782	768
Temperature (K) (EOC)	798	791	794	797	798	797
Cycle length (days)	385	1000	100	595	47.5	250
C_5+ yield (SOC)	86.0	83.8	79.5	85.9	74.2	79.5
C_5+ yield (EOC)	81.2	79.8	76.6	81.3	70.9	73.7

^a SOC, start of cycle; EOC, end of cycle.

If the target octane is increased to 98 R + 0, keeping the base case pressure and recycle ratio (case 2), the start-of-cycle temperature must be increased significantly (779 K). Because of the higher temperature and the higher level of aromatics required for octane, cycle length is reduced to 100 days. The 98 R + 0 operation results in a start-of-cycle C_{5+} yield of 79.5 vol %, 6.5 vol % lower than that of the base case. The reforming reactions required to increase octane from 90 to 98 R + 0 consist mainly of ring closure and cracking. Since the ring closure and cracking rates are similar, the higher-octane operation gives lower C_{5+} yields. During the reforming cycle, the C_{5+} yield is estimated to decrease by 2.9 vol %.

When recycle ratio is increased over the base case, maintaining other variables constant (case 3), the start-of-cycle temperature is unaffected. However, because of the lower hydrocarbon partial pressure, the deactivation rate is significantly reduced. KINPTR estimates a 595-day cycle length to reach 798 K. This is due to the presence of more inerts in the reformer, which reduces the partial pressure of the coke-forming reactants. The C_{5+} yields with hydrogen recycle rates remain similar to those of the base case over the entire cycle length because hydrogen partial pressure remains essentially the same. As discussed previously, hydrogen partial pressure significantly affects the aromatization equilibrium. While higher recycle ratios favor longer cycle lengths, increased utility costs result owing to increased compression requirements for the additional recycle gas. Thus, in this case, there is a trade-off between utility costs and cycle length.

If an Arab Light naphtha (71% paraffins) is charged to the reformer instead of Mid-Continent (55% paraffins) at 98 R + 0 (case 4 versus case 2), start-of-cycle temperature increases only about 3 K. However, the temperature profiles through each reactor bed are less endothermic for the more paraffinic stock, resulting in a higher average reactor bed temperature. Since the Arab Light naphtha contains more paraffins and less naphthenes than Mid-Continent naphtha, additional ring closure activity is required to make target octane. As mentioned during the discussion of target octane effects, cracking also increases, resulting in a lower C_{5+} yield. The increased ring closure requirement leads to a higher concentration of five-member ring naphthene on the catalyst and the aging rate is substantially increased. The cycle length is only 47.5 days and the start-of-cycle yield is 5.3% lower than in case 2.

The last column in the table shows a decrease in space velocity to 0.7 hour^{-1} at the higher octane, 98 R + 0. The model results show that the inlet temperature decreases to 768 K owing to the increased catalyst volume. Because of the lower space velocity and temperature, the aging rate is significantly reduced so that the cycle length is 250 days. The C_{5+} start-of-cycle yield is 79.5% with a 5.8 vol % yield loss over the cycle.

These case studies show the versatility of KINPTR to optimizing unit performance in terms of cycle length, feedstock, yield, product octane, and operating costs.

VIII. Examples of Model Applications

As shown in Section VII, KINPTR accurately predicts the effects of wide variations in unit operating conditions and feedstock. Therefore, it is a very valuable asset to reforming operations, allowing unit performance to be optimized in terms of cycle length, yield, feedstock type, product octane, and operating costs.

KINPTR is used several thousand times a year for both research and commercial reformer estimates. The model has four principal uses: commercial monitoring, reformer diagnostics, optimization, and research and development guidance.

A. MONITORING APPLICATIONS

The model provides a performance reference to evaluate commercial reformer operation by taking into account the wide variation in operating conditions, feedstocks, and product octane typically experienced commercially. Such variations in reformate yield have already been discussed in Fig. 29, where the model effectively predicts the yield variations. As a monitoring tool, the model is routinely used to assess reformer yield and activity losses due to catalyst deactivation relative to fresh catalyst model estimates. When commercial yield and/or activity losses relative to the model are uneconomical, a decision to regenerate the catalyst is made. A typical monitoring trend (Fig. 36) illustrates the use of the model as a performance reference.

B. REFORMER DIAGNOSTICS: A COMMERCIAL EXAMPLE

Occasionally, routine commercial monitoring finds significantly larger deviations from the model than expected. We have successfully used the model as a diagnostic tool to troubleshoot these situations. Table XIX is an example of a model diagnosis of a damaged commercial reformer catalyst. Commercial data taken after only 9 days on stream compare reasonably well to the model estimate. At constant octane, the yields agree. The inlet temperature requirement is 9 K higher than expected, but this is not sufficient to require commercial corrective action.

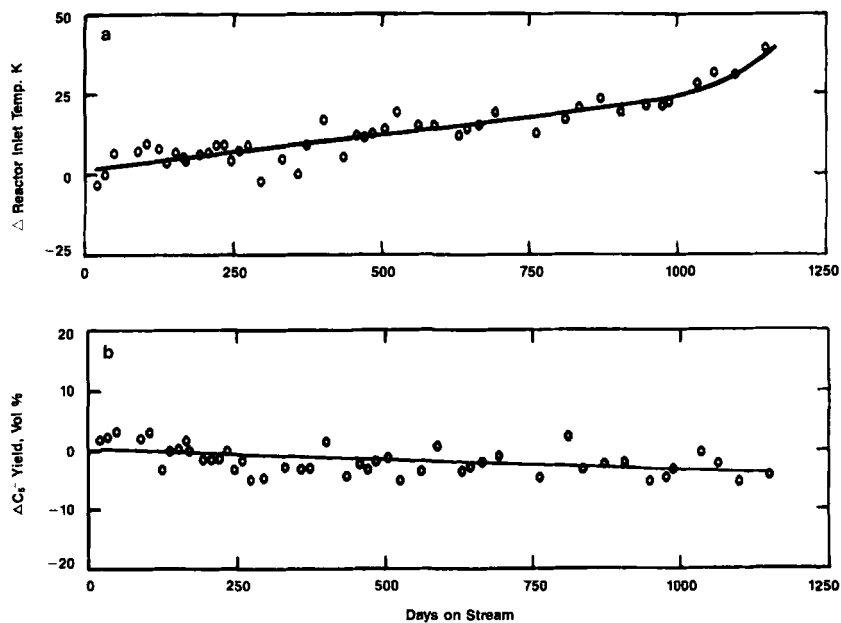
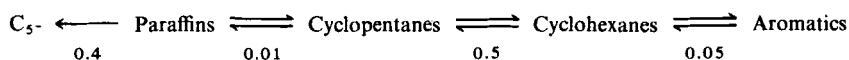


FIG. 36. Commercial reforming monitoring using KINPTR: Shifts in temperature and yields relative to start of cycle KINPTR.

TABLE XIX
KINPTR DIAGNOSIS OF DAMAGED REFORMER CATALYST

Variable	Commercial data	KINPTR	Commercial data	KINPTR
Days on stream	9	Start of cycle	27	Start of cycle
Octane ($C_5 + R + 0$)	95.1	95.1	83.6	83.6
C_5 yield (vol %)	75.0	76.0	75.5	84.4
Average reactor inlet temperature (K)	768	759	767	726

Fraction of fresh catalyst rate constants at 27 days:



However, at 27 days on stream, the comparison has changed dramatically. While about the same temperature was maintained, the reformer octane fell roughly 12 numbers to 83.6, but yields stayed constant. At the same octane, the model predicts a 41 K lower inlet temperature and 9 vol % higher reformat

yield. Such a shift signals significant catalyst damage, since under normal operation the catalyst should last more than 6 months. Several operating factors could account for such damage, one example being sulfur poisoning. However, standard commercial investigations did not find anything abnormal in the operation. Further, an acceptable catalyst regeneration is indicated by the good comparison to the model at 9 days on stream.

To provide a more fundamental diagnosis of the problem, the model was used to characterize the state of the commercial catalyst at 27 days on stream. The rate constants representing the four basic reactions—cracking, ring closure, ring isomerization, and dehydrogenation—were adjusted to match commercial performance. The necessary shifts are shown as fractions of the fresh catalyst rate constants in Table XIX. Although all reaction rates have been deactivated, dehydrogenation and ring closure, which depend strongly on catalyst metal function, are nearly completely deactivated. This analysis clearly pointed to platinum metal deactivation. Troubleshooting activities focused on the naphtha pretreater, although normal naphtha analysis did not indicate unusual levels of sulfur in the naphtha. Upon closer examination, a periodic flooding of the pretreater stripper which slugged H_2S into the reformer was detected. The periodic nature of the H_2S slugging made detection by naphtha analysis subject to random chance. Correction of the stripper operation and catalyst regeneration restored expected reformer performance. Such use of the model quickly eliminated several other possible factors (e.g., chloride environmental control) and facilitated a resolution of the problem, thus saving costly commercial downtime.

C. OPTIMIZATION

KINPTR is also used extensively for commercial planning guidance and reformer operation optimization. The model has been used to improve linear program accuracy for short-range refinery planning and crude oil supply and distribution studies. It is also used to optimize reformer economics by proper selection of operating conditions within refinery constraints.

In Mobil's short-range planning activities, reformer objectives such as octane target and naphtha distillation cutpoints are determined in view of the overall refinery operation using large linear programs (LPs). The model was used to improve the reformer representation in these LPs. Because the LPs require very large matrices of process information during their execution, executing the highly nonlinear kinetic model several thousand times for each LP run is time-consuming and cumbersome. Therefore, to more efficiently generate this information, numerous correlations of the kinetic model results were developed over a wide range of conditions and feedstocks for each of

Mobil's reformers. These consisted of more than a quarter of a million correlation coefficients. The improved LP reformer representation has been used in Mobil's refinery LPs successfully since the mid-1970s.

Also, the optimization and planning of crude allocations in Mobil's worldwide refinery system is the principal objective of Mobil's supply and distribution planning group. Overall corporate profits can be maximized by proper crude allocations to the various refineries. Similar to the refinery LPs, the reformer representation in the crude supply and distribution LP was improved. Table XX gives an example of how sensitive reformer operation can depend on the type of naphtha reformed. A significant improvement in performance and octane potential results from processing a naphthenic stock compared to a paraffinic stock. This improved performance must be balanced against differences in crude cost.

Finally, the model has been coupled with Mobil's process equipment models and economic analysis programs to create the overall Reformer Operations Model (ROM) for each of Mobil's reformers. The ROM allows us to study the effects of process conditions and design configurations on reformer economics. The ROM calculates mass and energy balances, reformer yields and cycle length, and utility consumptions for all major reformer equipment (compressors, towers, exchangers, etc.). Economic analysis allows optimization of the individual reformer's profitability. The effect of various design configurations on profitability can also be determined.

D. RESEARCH AND DEVELOPMENT GUIDANCE

The model has also provided Mobil with a fundamental understanding of reforming because it is based on the fundamental thermodynamics and kinetic reactions. It has been used extensively to provide guidance in Mobil's research and development efforts, particularly in developing and evaluating leads for

TABLE XX
EFFECT OF CHARGE STOCK ON REFORMER PERFORMANCE

Charge stock	Start-of-cycle at 98 R + 0 octane		Estimated cycle length to 794 K (days)
	Temperature (K)	Yield	
Paraffinic naphtha (70% P)	778	73.2	48
Naphthenic naphtha (34% P)	764	86.3	148

new reforming process and catalyst research directions. This has reduced the necessity for costly laboratory experiments.

We have evaluated and developed new process modifications using the model. The concept of staggering the reactor inlet temperatures to equalize the aging rates in all three reactors (15) was evaluated with the model. Model simulations, to quantify the benefits of this modification, could be carried out in a day. Corresponding experiments showing similar effects would have required months to complete. With minimal modifications to the model, the benefits for splitting the reformer feed among the three reactors (16) were also determined.

Also, the deactivation kinetics development gave Mobil leads for novel, more stable reforming catalysts. It was discovered in 1978, using the model, that increased rhenium content improved catalyst stability. This discovery arose during the determination of the deactivation kinetics for catalyst C (Table XXI). Initially, the deactivation kinetics for catalysts A and B were determined. Both catalysts had different catalyst densities and rhenium contents (Table XXI). As Table XXI illustrates, catalyst B had increased stability. Catalyst C is essentially the same catalyst as catalyst A but with a higher rhenium content. Mobil found that it could fit the commercial and pilot plant aging data for catalyst C by using the start-of-cycle kinetics of catalyst A (same catalyst density, platinum content, manufacturer) and the deactivation kinetics of catalyst B (roughly the same rhenium content).

Given the excellent fit of the data (Fig. 37), Mobil researchers hypothesized that further increases in rhenium content would further improve catalyst stability. To test this hypothesis, a series of Pt-Re reforming catalysts were prepared with increasing rhenium content and evaluated under accelerated aging conditions. As Fig. 38 shows, increasing the rhenium content significantly decreased the aging rate, confirming the original hypothesis developed

TABLE XXI
PROPERTIES AND AGING RATES
FOR COMMERCIAL REFORMING CATALYSTS

	A	B	C
Pt	0.375	0.35	0.375
Re	0.20	0.35	0.375
Catalyst density	32	39-40	32
Catalyst type	Spheres	Extrudates	Spheres
Relative stability	Base	Improved	Improved
Catalyst kinetics used			
Start of cycle	A	B	A
Deactivation	A	B	B

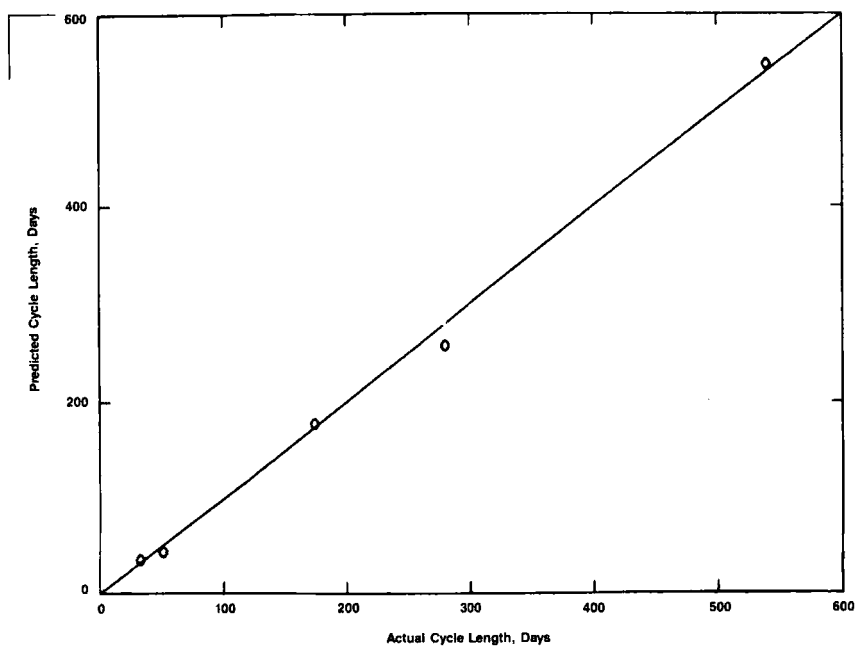


FIG. 37. KINPTR cycle length predictions for catalyst C.

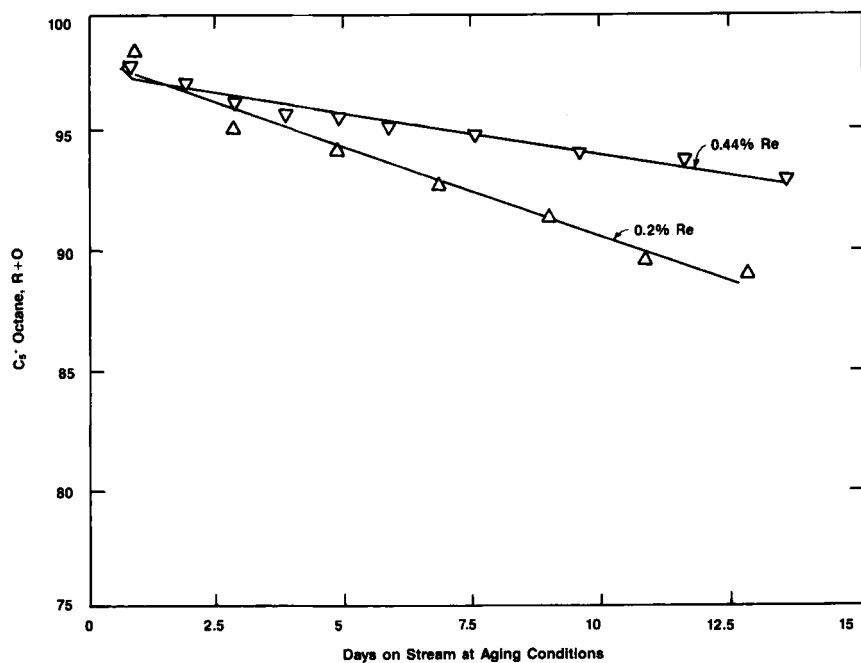


FIG. 38. Effect of higher rhenium content on catalyst stability, experimental confirmation.

from the reforming model. Recent developments in commercial reforming catalysts use higher rhenium contents and are claimed to increase catalyst stability (17).

IX. Nomenclature

\bar{A}	Diagonal matrix of catalyst state vector	M_j	Hydrocarbon partial pressure exponent in deactivation kinetics
A_{ji}	Correlation coefficient for C_5 -light gas delumping	n	Hydrogen pressure reaction order
C_N	Weight average C_6 -product carbon number	P	Total pressure, kPa
C_p	Heat capacity, kJ/gmole K	\bar{P}	Hydrocarbon partial pressure vector in deactivation kinetics
\bar{D}	Deactivation rate constant matrix	P_h	Hydrogen partial pressure, kPa
D_{ij}	Deactivation rate constant for i th component, j th catalyst state parameter	P_{HC}	C_6 -hydrocarbon partial pressure, kPa
E	Activation energy, kJ/gmole	R	Ideal gas constant
E^d	Deactivation activation energy, kJ/gmole	S_i	Catalyst site concentration for isomerization
EOC	End of cycle	S_t	Total catalyst sites
F	Total molar flow rate, gmole/sec	S_v	Liquid hourly space velocity
F_c	Hydrocarbon charge weight flow rate, g/sec	ΔS_{ji}	Entropy of reaction, kJ/gmole K
F_h	Hydrogen molar flow rate, gmole/sec	SOC	Start of cycle
g_i	Combined hydrogen of hydrocarbon species i	t	Time on stream, sec
h	Weight fraction yield of H_2	T	Temperature, K
\bar{H}	Heat of formation vector, kJ/gm	v	Fractional catalyst volume
H_h	Heat of adsorption for hydrogen, kJ/gmole	V	Total catalyst volume, liters [$V = W_c/\rho_p(1 - \epsilon)$]
H_{wi}	Heats of adsorption for hydrocarbon i , kJ/gmole	\bar{w}	Vector of hydrocarbon weight fractions for specific hydrocarbons used in text: H, hexane MCP, methylcyclopentane CH, cyclohexane B, Benzene A, aromatics P, paraffins C, C_5 -light gas N_5 , five-carbon-member-ring naphthenes N_6 , six-carbon-member-ring naphthenes
ΔH_{ji}	Enthalpy of reaction, kJ/gmole	\bar{w}_0	Hydrocarbon charge composition vector
ΔH_{RX}	Heat of reaction, kJ/mole	W_c	Catalyst weight, g
k_ϕ	Real-time rate constant, sec^{-1} (defined in terms of catalyst contact time)	\bar{X}	Matrix of eigenvectors of \bar{K}
\bar{K}	Pseudomonomolecular selectivity rate constant matrix (each element is k_{ij})	X_p	C_6 -paraffin weight fraction
K_h	Hydrogen adsorption constant, kPa^{-1}		
\bar{K}_w	Hydrocarbon adsorption equilibria vector, gmole/kPa g		
M	Molecular weight, g/gmole		

Greek Letters

$\bar{\alpha}$	Catalyst state vector	ϵ	Catalyst void fraction
γ_{ji}	Hydrogen pressure stoichiometric coefficient	$\bar{\Lambda}$	Diagonal matrix of eigenvalues of \bar{K}
γ_R	Molar feed ratio hydrogen to hydrocarbon	ρ_c	Hydrocarbon charge density, g/liter
δ_{ij}	Hydrogen partial pressure exponent in deactivation kinetics	ρ_p	Catalyst particle density, g/liter
		τ	Selectivity time
		ϕ	Catalyst activity function

ACKNOWLEDGMENTS

We wish to acknowledge C. D. Prater, J. J. Wise, and V. W. Weekman, Jr., for their valuable guidance and critical support of the KINPTR research and development program. Their strong commitment, both technically and managerially, to the development of a reforming process model based on fundamental reaction kinetics was instrumental to KINPTR's success.

We also wish to acknowledge the efforts of many others who contributed to KINPTR: D. G. Tajbl and K. A. Hill for their contributions to the development of the kinetic data base and various aspects of the kinetics; J. C. W. Kuo, S. B. Jaffe, and W. H. Speaker for their key software contributions to the KINPTR process model; J. S. Hicks for his efficient numerical algorithms; and the many technicians and analytical personnel whose dedication to generating very accurate kinetic data ultimately led to the successful development of KINPTR.

References

1. Ciapetta, F. G., *Catal. Reform. Petro/Chem. Eng.* **May**, C-19-C-31 (1961).
2. Haensel, V., *Ind. Eng. Prod. Res. Dev.* **15**, 3 (1976).
3. Gates, B. C., Katzer, J. R., and Schuit, G., "Chemistry of Catalytic Processes" pp. 184-324. McGraw Hill, New York, 1979.
4. Bakulin, R. A., Levinter, M. E., and Unger, F. G., *Int. Chem. Eng.* **18**, 89 (1978).
5. McHenry, K. W., Bertolacini, R. J., Brennan, H. M., Wilson, J. L., and Seely, H. S., *Proc. Int. Congr. Catal.*, 2nd, *Davis* **117**, 2295 (1960).
6. Burch, R., *Platinum Metals Rev.* **57**, 20 (1978).
7. Weekman, V. W., *AIChE Monogr. Ser.* **75**, 11 (1979).
8. Wei, J., and Prater, C. D., *Adv. Catal.* **13**, 203 (1962).
9. Kmak, W. S., *AIChE Nat. Meet. Prepr.*, Houston (1971).
10. Marin, G. B., and Froment, G. F., *Chem. Eng. Sci.* **37**, 759 (1982).
11. Henningson, G., and Bundgaard-Nielson, M., *Br. Chem. Eng.* **15**, 1433 (1970).
12. Graziani, K. R., and Ramage, M. P., *A.C.S. Symp. Ser.* **65**, 282 (1978).
13. Ramage, M. P., Graziani, K. R., and Krambeck, F. J., *Chem. Eng. Sci.* **35**, 41 (1980).
14. Stockinger, J. H., Callen, R. B., and Kaufman, W. E., *J. Chromatogr. Sci.* **16**, 418 (1978).
15. U. S. Patent No. 3563883, Texaco, Inc., Feb. 16, 1971.
16. U. S. Patent No. 4401554, Mobil Oil Corp., Aug. 30, 1983.
17. British Patent No. 2018278, Englehard Corp., 1983.
18. Schipper, P. H., Graziani, K. R., Choi, B. C., and Ramage, M. P., *Int. Chem. Eng. Symp. Ser.* **87**, 33 (1984).
19. Sinfelt, J. H., *Adv. Catal.* **23** (1974).
20. Luss, D., and Hutchinson, P., *Chem. Eng. J.* **2**, 172 (1971).
21. Wei, J., and Kuo, J. C. W., *Int. Chem. Eng.* **8**, 114 (1969).
22. Weisz, P. B., *Adv. Catal.* Vol. **13** (1964).

INDEX

A

- Abbot Laboratories, 4
- Activity
 - function of pressure, 237-238
 - function of temperature, 237
 - gradients, 253
 - prediction by KINPTR, 250, 253-254
- Adams-Moulton predictor-corrector technique, 139
- Adsorption coefficients
 - defined, equations, 217
- Aging rate, *see also* Deactivation
 - boiling point and, 210
 - C, on Pt/Re, 219
 - charge stock composition and, 220
 - components of, 211
 - deactivation kinetics, 193
 - effect of carbon number, 207, 210
 - prediction by KINPTR, 254-257
 - pressure effect on, 199
 - ring closure, 210
- Algebraic method, 15-54
 - accuracy of, 44
 - cubic for mixed convection, 54
 - versus exact solution, 28
 - and integral method compared, 41-42
 - quadratic in penetration theory, 54
 - renewal models and, 49-50
- Aromatization
 - hydrogen partial pressure and, 258
 - selectivities, 198, 250
- Aspect ratios, 127
- Assisting convection, 30
- Automatic clinical analyzer, 6
- Average mass transfer coefficient
 - equation for, 88-89, 94
 - multiple, 91
- Axial aspect ratio, 118

- Axial collocation, 135-138, 178
 - assumed axial profiles, 136
 - catalyst energy balance, 136
 - gas energy balances, 137
 - mass balances, 137
 - overall continuity, 138
 - thermal well energy balance, 137
- Axial dispersion, 127

B

- Biot numbers, 128
- Blake-Kozeny equation, 125
- Blasius expansions, 35, 44
- Blasius expression, 49, 65
- Blasius flow, 35, 37, 106
- Boundary layer thickness
 - elasticity and, 18
 - velocity and, 18
 - viscosity and, 18
- Brown's algorithm, 139
- Bulk concentration
 - profiles, 148
- Buoyancy factor, 29

C

- Carson transformation, 96
- Catalyst aging, *see* Aging rate
- Catalyst characterization test, 230
- Catalyst contact time
 - defined, 212
 - pressure and temperature effects, 237-238
 - reforming compositional profiles and, 251-252
- Catalyst damage, 260-261
- Catalyst deactivation, *see also* Aging rate
 - coke formation and, 200, 202

- Catalyst regeneration
 - cycle lengths, 206
 - Catalyst state gradient, 239
 - predicted by KINPTR, 239
 - Cell number, 100
 - Chambre-Young solution, 35
 - Chao-Seader method, 242
 - Coke formation
 - concentration of components and, 222
 - deactivation from, 200, 202
 - olefins and, 218
 - Collocation, 130
 - axial, 135-138
 - orthogonal, 132-133
 - radial, 133-135
 - Combined convection in internal flows, 31-32
 - Concentration wave velocity, 167-168
 - Continuity equation, 120, 125, *see also*
 - Total mass conservation
 - Continuum transport theory, 118
 - Control model development
 - model linearization, 171-174
 - control and disturbance variables, 173
 - simulations with linearized model, 174-178
 - concentration dynamics, 175
 - gas temperature dynamics, 175-176
 - steady-state concentration profile, 176
 - state-space representation, 170-171
 - Control theory, modern multivariable, 179
 - convective diffusion equation, 12, 24, 64, 78,
 - near liquid interface, 86
 - roll cell model and, 95
- D**
- Damköhler number, 35, 45
 - Danckwerts renewal model, 55, 57
 - Danckwerts theory, 86-91, *see also* Physical
 - model approach
 - Danckwerts equation, 89
 - statistical model, 107
 - Davison's method, for reduced model, 182-184, 186
 - Deactivation kinetics, *see also* Aging rate
 - assumptions, 207
 - in C_s system, 237, 239
 - coke formation, 200, 202, 218
 - hydrocarbon conversion with, 217
 - kinetic formulation, 217-224
 - lumping scheme, 210-211
 - number of lumps, 231
 - parameter estimation, 230-232
 - rate coefficients, 231
 - rate constant, 222
 - rate equation, 220
 - for C_s component system, 220
 - predictions, 237-239
 - Deborah number, 18
 - Delumping, 224-226
 - delumped components, 225
 - semikinetic "delumping" equations, 226
 - Dimensional analysis, 11
 - based on two scales, 12-15
 - micro- and macroscales, 13
 - Drag coefficient, 18, 19
 - Du Pont
 - agricultural products, 3-4
 - basic research, 2, 4
 - biomedical products, 4
 - AIDS antibody test, 4
 - catalysts, 3
 - composites, 5
 - dyes, electrochemicals, 2
 - electronics, 3-4
 - engineering plastics, 4
 - explosives, 2
 - General Motors, 2
 - neoprene, nylon, 2
 - N. V. Philips, joint venture with, 4
 - petroleum-based raw materials, 2
 - polymer science, 2
- E**
- "Effective" parameters, 162
 - Ergun equation, 120, 125
 - Euclidian norm, 174
 - Euler's equations, 16
 - Exxon
 - cyclic reformers, 199
- F**
- Falkner-Skan flows, 36, *see also* Wedge
 - flows
 - Finite difference technique, 130-131
 - Fisher-Tropsch processes, 117
 - methanation, 116
 - Fourier number, 43
 - Free-stream velocity, 18, 36
 - zero free-stream flow, 37

G

Galerkin method, 130–131
 Galileo number, 69
 Gallium arsenide, 5
 General Motors, 2
 Global rate expression, 117
 Granular bed filters, 50

H

Harshaw Ni-0104T nickel-Kieselguhr catalyst, 117
 Heats of reaction, 128
 Heat transfer, 11
 boiling, from horizontal surface, 75–76
 between bubble bed and vertical wall, 74
 between fluid flowing through fixed or fluidized bed and wall, 70–74
 Heat transfer coefficient, 12, 18, 19
 local, defined, 28
 Hessenberg matrix, 174
 Higbie–Danckwerts approach, 91
 Higbie equation, 94
 Higbie penetration theory, 86
 “Hot spot,” 141, 144, 145
 Householder’s method, 174

I

Image force, 51
 Insulin, 6
 Interfacial turbulence
 Marangoni effect and, 104
 Interferon, 6

K

Kinetic platinum reforming model, 193–265
 accuracy of predictions, 249–255
 inlet temperature, 252–253
 applications, 259–265
 diagnostics, 259–261
 monitoring, 259
 optimization, 261–262
 research and development, 262–265
 deactivation model, 253
 activity predictions, 253–254

 aging predictions, 253–255, 256
 composition changes predicted, 253
 cycle length predicted, 253–257, 264
 deactivation parameters, 235
 example problem, 243–247
 experimental design and parameter estimation, 226–232
 activity kinetics, 230
 gas chromatograph sample acquisition, 228
 hydrogen pressure dependencies, 230
 isothermal reformer reactor, 227
 flow chart, 248
 kinetic lumps in, 208–209
 nomenclature, 265
 to predict reformer performance, 207
 process model description, 241
 real-time activity kinetics, 252
 real-time activity parameters
 for C_4 system, 234
 selectivity kinetics, 252
 selectivity parameters for C_4 system, 234
 KINPTR, *see* Kinetic platinum reforming model
 Kmak, 209

L

Laminar convection, forced and free,
 26–31
 free, equations for, 20–22
 Prandtl numbers, 20–22, 26
 velocity, 26
 Laminar flow
 transition to turbulent flow, 15
 Laminar motion, 11
 Laminar natural convection, 47
 Langmuir–Hinshelwood adsorption, 207,
 212, 223
 Langmuir–Hinshelwood rate law, 117
 Leveque solution, 32
 Life sciences
 chemical engineering in, 5–6
 controlled release drugs, 6
 dermal penetration drugs, 6
 drugs, 6
 microbial processing, 6
 Linearized model, 171–187
 accurate near steady state, 175
 start-up and disturbance simulations, 177

Linearized model, dimensionality of
 178–189
 model discretization, 178–180
 axial collocation points, 178–180
 OCFE, 180
 rippling, 178, 180
 model reduction, 180–186
 Davison's method, 182–184
 Marshall's method, 184–186
 modal reduction approach, 181, 188,
 189
 Linear stability theory, 73
 Liquid hourly space velocity (LHSV)
 defined, 203
 Lithium niobate, 5
 Litz's modal reduction, 189
 "Lumped" heat transfer parameters, 162
 Lumping scheme
 deactivation, 210–211
 start-of-cycle, 207–210
 Lumps
 delumping, 224–226
 lumped chemical species, 206

M

Marangoni effect, 55
 circulation patterns, 102
 influence on mass transfer between
 phases, 101–107
 interfacial turbulence, 104
 mass transfer coefficient, 103
 numerical calculations of, 106–107
 Reynolds number, small values of, 101
 Marshall's model reduction technique,
 184–186
 advantage of, 184
 state-space representation, 184
 state vector, 184
 Mass diffusivities
 axial, defined, 123
 radial, defined, 123
 Mass transfer, 11
 to a continuous phase from single
 spherical drop, 39–41
 through free surface of stirred liquid,
 92–93
 surface tension, 92
 viscosity, 92
 in liquid film in turbulent motion, 91–92
 to separated flows, 76–78

turbulent, with first-order chemical
 reaction, 46–49
 unsteady-state, to rotating disk, 41–44
 Mass transfer coefficients, 12, 22–25, 33,
 48, 53, 64, 91
 algebraic equation for, 12
 local, 31
 in a semiinfinite liquid, 22–26
 Mathematical models of packed bed
 reactors, mathematical models of
 Methanation
 Langmuir–Hinshelwood rate law, 117
 nickel catalyst, 117
 reaction system
 high exothermicity, 114, 115
 nickel on alumina catalyst, 116
 reactions in, 116
 side reactions, 115
 synthetic natural gas production, 140
 Mixing length, 55
 Mobil, 193–265 *passim*
 Mobil Research, 193
 Modal reduction
 central theme in, 181
 Davison's, 188
 Litz's, 189
 Marshall's, 188

N

Naphtha reforming
 chemistry, 194–201
 classification of reactions, 195–196
 paraffin reactions, critical, 196
 reforming charge and product composi-
 tions, 195
 National Academy of Sciences, "Opportun-
 ities in Chemistry," 1, *see also*
 Pimentel Report
 Natural convection velocity, 31
 Navier–Stokes equations, 11, 16
 Newtonian fluids, 19, 54
 Nusselt number, 37–38, 45, 53

O

OC, *see* Orthogonal collocation
 OCFE, *see* Orthogonal collocation on
 finite elements
 Opportunities in chemical engineering, 1–9
 OR double-step iterative process, 174

Orthogonal collocation, 115
 drawback of, 152
 and OCFE compared, 158–159
 orthogonal polynomials, defined, 132
 for packed bed reactors, 132
 solution, 157
 Orthogonal collocation on finite elements,
 131, 152–159, 180
 discretization analysis, 154
 formulation of, 153–158
 global indexing system, 154–155
 Lagrangian functions versus Hermite
 polynomials, 153
 local indexing system, 154–155
 and OC compared, 158–159

P

Packed bed modeling, simplifications
 approximations in, 160
 as bundle of tubes, 71
 dispersion effects, 161–162
 axial thermal diffusion, 162
 Peclet numbers, 161
 “rippling,” 162
 evaluation of physical simplifications,
 160–169
 homogeneous versus heterogeneous,
 162–166
 combined energy balance, 163
 exothermic reactions, 164
 steady-state profiles, 165
 negligible energy accumulation in gas
 phase, 168–169
 quasi-steady-state approximation for
 concentration, 166–168
 concentration wave velocity, 167–168
 reactor configuration and conditions,
 168
 thermal wave velocity, 167–168
 Packed bed reactor
 configuration, 116
 control model development, 170–178
 differential equations describing, 120–124
 continuity equation, 120
 energy balance for catalyst, 121–122
 energy balance for gas, 120–121
 energy balance for thermal well, 122
 mass balance in reactor section,
 122–123
 $H_2 + O_2$ on platinum, 163

typical parameters, 140
 Packed bed reactors, mathematical models
 of, 113–189
 adiabatic conditions, 149–150
 analysis of model behavior, 139–152
 catalytic reactor, 114
 for designing control systems, 113
 dimensionless equations
 energy balance for catalyst, 126
 energy balance for gas, 125–126
 energy balance for thermal well, 126
 mass balance in reactor section, 127
 total mass conservation, 125
 dimensionless quantities
 aspect ratios, 127
 axial dispersion, 127
 Biot numbers, 128
 heats of reaction, 128
 heat transfer, 128
 radial dispersion, 128
 reaction coefficients, 128
 reaction rates, 128
 dynamic behavior, 142–144
 effect of thermal well, 150–152
 formulation of model, 118–128
 heterogeneous, 114
 major assumptions, 119–120
 methanation reaction system, 114
 nomenclature, 189
 nonadiabatic, 115
 numerical simulation, 138–139
 numerical solution, 129–139
 operating conditions and reactor
 behavior, 144–146
 pseudohomogeneous, 114
 radial concentration profiles, analysis of,
 146–148
 solution techniques, 129–132
 finite difference, 130
 weighted residuals, 130
 steady-state behavior, 141–142
 “hot spot,” 141, 144, 145
 radial temperature profiles, 143
 axial profiles, 142–144
 two-dimensional, two-phase, 118
 Particle deposition, rates of
 under combined flow and assisting
 electrostatic field, 50–53
 Peclet numbers, 40, 53, 100, 178
 radial concentration profiles and, 148
 radial gas, 161

Penetration theory, 105
 Higbie, 86
 mass transport equation, 32
 rate of diffusion with chemical reaction, 32–34
Perturbation solutions, 46
Philips, N. V., 4
Physical model approach, 84–86, *see also* Danckwerts theory
 physicochemical and hydrodynamic parameters separated, 85
 renewal and, 85–86
Physical scaling, 11
Pimentel Report, 1, 6, *see also* National Academy of Sciences, “Opportunities in Chemistry”
Polymers, 2
 alloys, 5
Powell’s algorithm, 139
Prandtl’s evaluation procedure, 15–17
Prandtl numbers, 19, 20–22, 29, 37, 44
 laminar free convection and, 20–22, 26
Process sensitivity, 255–259
Process technology, 7

Q

Quasi-steady model, 66
 laminar, 70, 74

R

R16H platinum-rhenium-alumina catalyst, 232
 activity kinetics, 233
 selectivity rate constants, 233
Radial collocation, 133–135
 discretization in radial dimension, 133
 radial concentration profiles, 134
 radial temperature profiles, 133
Radial concentration profiles
 analysis of, 146–148
 Peclet numbers and, 148
Radial dispersion, 128
Radial temperature files
 in catalyst, 150–151
Reaction coefficients, 128
Reaction rates, 128
Reduced model, 180–189
 computation time reduced, 187
 methanation, 187–188

Reformer Optimization Model (ROM), 262
Reformer yield-octane behavior, 252–253
Reforming catalysis, 201–203
 interaction between sites, 201
 Pt/Ir on Al_2O_3 , 201
 Pt/Re on Al_2O_3 , 201
Reforming kinetics
 C_6 , for R16H catalyst, 232–239
 pressure effects, 236
 temperature effects, 236
 delumping, 224–226
 equilibria, 208
 kinetic lumps, 206
 kinetic reforming model, 206
 strategies employed, 206
 lumping scheme and reaction network, 207–211
 mathematics for kinetic constants, 211–224
 deactivation, 211, 217–224
 hydrocarbon conversion, 211, 217
 predictions with, 249–259
 process and product characteristics, 224–226
 process sensitivity, 255–259
 rate constants defined, 213
 selectivity, 214
 start-of-cycle formulations, 212–217
Reforming process
 equations for reactor simulation, 240
 mathematical simulation, 193
 reactor configuration, 203–206
 aging curve, 205
 reactor composition profiles, 204
 reactor temperature profiles, 204
 yield-octane relationship, 205
Reforming process model
 logical structure diagram, 249
 module descriptions, 241–249
 product properties calculated, 242
 structure of, 240–249
 13 kinetic lumps, 242
Reforming reactions
 aromatization selectivities of paraffins, 198
 high octane (high aromatic yield), 197
 reaction composition profile, 197
 reaction parameters, 196
Renewal frequency, 74, 91–92
Renewal models
 algebraic method and, 49–50
 Danckwerts, 55, 108
 hydrodynamic rotating structures and, 93

Reynolds analogy, 67
 Reynolds number, 11, 18, 19, 39, 69, 71
 critical, 61
 Marangoni effect and, 101
 strong turbulence, 14
 vanishingly small, 14
 Rhenium
 catalyst stability and, 263–265
 Richardson and Zaki equation, 72
 Ring isomerization
 deactivation rate, 223
 start-of-cycle rate constant, 221
 “Rippling,” 162, 178, 180
 Roll cell model
 average mass transfer coefficient, 94
 convective diffusion equation, 95
 quantitative formulations of, 94–101
 Schlieren arrangement and, 94
 for turbulent mass transfer, 93–94
 Roll cell pattern, 58
 Runge-Kutta-Gill method, 139

S

Scale, changes in
 effectiveness of chemical products, 8
 physical piece of equipment, 8
 Scaling transformations, 12
 Schlieren arrangement, 94, 104
 Schmidt number, 15, 37, 39, 65
 depth of penetration by diffusion and, 35
 high values of, 22, 35
 Selectivity
 aromatic 198, 250
 effect of charge stock type, 250
 effect of temperature, 251
 gradients, 253
 kinetic parameter estimation, 214
 kinetic problem, 214–216
 rate constant matrix, 214, 216, 230
 for C_s system, 232
 time, 216
 transformation, 215
 Shear stress
 equation for, 68
 Sherwood numbers, 11, 14, 34, 53, 54
 local, 35
 Similarity solution, 38
 similarity transformation, 100
 similarity variable, 28, 86
 Simpson's integration rule, 217
 “Smart” chemicals, 8

SOC, *see* Start-of-cycle
 Space charge effect, 51
 Start-of-cycle kinetics
 assumptions, 206–207
 defined, 193
 formulations, 212–217
 lumping scheme, 207–210
 lumps in KINPTR, 208–209
 in module REACTOR, 242
 predictions, 233–237, 250–253
 ring isomerization, 221–223
 Start-of-cycle parameter estimation,
 227–230
 Steady laminar flow, 34–36
 along a plate, 58–61
 Steady stagnation laminar flow, 61
 Steam-shift reaction, 116–117
 rate expression for, 117
 Stokes equations, 50–51
 Successive scaling, 81
 Suction of fluids, 36–39

T

Temperature field
 equation for, 44
 Thermal boundary layer, 26
 Thermal wave velocity, 167–168
 Thermal well, 122, 126
 effect of, 150–152
 Total mass conservation, 120, *see also*
 Continuity equation
 Transfer coefficient, 38
 Transient model, 66
 Transport phenomena, analysis with scaling
 and physical models, 11–109
 Tube and separated flow cases, 78–81
 average mass transfer coefficient, 79
 mass flux, 79
 “Tuning factors,” 194
 Turbulent diffusivity, 46–48, 81–83,
 equation for, 55–56
 Turbulent flow
 near solid boundary, 55–58
 theory of turbulence, 55
 turbulent transport equations, 55
 very large Schmidt numbers, 56, 59
 Reynolds number and, 15
 transition from laminar flow, 15
 Turbulent heat and mass transfer, 54–108
 “local,” 60
 in stirred vessel, 68–70
 in tube, for Sc or $Pr > 1$, 66–68

Turbulent kinematic viscosity, 56
 Turbulent mass transfer
 coefficient
 for large Schmidt numbers, 83
 in tube, for Sc or $Pr > 1$, 66–68
 deterministic approach, 107–108
 Danckwerts statistical model and,
 107–108
 near liquid–fluid interface, 81–83
 physical model approach, 84–86
 in stirred vessel, 68–70, 83–84
 viscosity and surface tension, 83–84
 Turbulent motion, 11
 Turbulent transport, 46

U

Universal Oil Products
 continuous regeneration reformers, 199
 R16H bimetallic catalyst, 232
 Unsteady heat transfer to liquid in steady
 laminar flow, 44–45

Unsteady laminar motion and turbulent
 transport, 62–66
 Unsteady-state transport equation, 41, 109
 UOP, *see* Universal Oil Products

V

Velocity profile of forced flow, 31
 Viscoelastic fluid, boundary layer for,
 17–20
 Viscous limit, 20

W

Wall shear stress
 equation for, 65
 Wedge flows, *see also* Falkner–Skan flows
 transport phenomena in, 36–39
 Weighted residuals, 130, 131
 collocation, 130
 Galerkin method, 130